



EUROPEAN  
COMMISSION

Community research

# RECOSY

(Contract Number: **FP7-212287**)

## DELIVERABLE (D-N°:1.2) Report on the scientific state of the art

Author(s): **All project beneficiaries**

Reporting period: e.g. 01/04/2011 – 30/03/2012

Date of issue of this report : **03/09/2012**

Start date of project : **01/04/2008**

Duration : **48 Months**

<b>Project co-funded by the European Commission under the Seventh Euratom Framework Programme for Nuclear Research &amp; Training Activities (2007-2011)</b>		
<b>Dissemination Level</b>		
<b>PU</b>	Public	X
<b>RE</b>	Restricted to a group specified by the partners of the <b>RECOSY</b> project	
<b>CO</b>	Confidential, only for partners of the <b>RECOSY</b> project	







The objective of this deliverable is to document the state of the art of the research subjects within Recosy at the end of the project. This will facilitate the identification of the contribution that the Recosy work programme and outcome have made to the improvement of the knowledge in each one of the research issues included in the project:

- WP2. Development of redox determination methods (page 4)
- WP3. Redox response of defined and near-natural system (page 37)
- WP4. Redox reactions of radionuclides (page 77)
- WP5. Redox processes in radionuclide transport (page 123)
- WP6. Redox reactions affecting the spent fuel source-term (page 144)

The harmonization and documentation of the advance of the project is developed within WP1 and many of the activities within this WP are related with each other to ensure that the project is consistent from a documentation perspective.

The detailed texts on the state of the art of each research subject are presented in the following sections where all the beneficiaries working in the project have contributed describing the work performed by each other from the beginning of the project.

## WP2. Development of redox determination methods

The redox state of a system is a key parameter for the safety assessment of a nuclear waste disposal. Existing determination methods and models are limited due to poisoning of electrode material, diffusion potentials in electrode bridges, drift through catalytic reactions on electrode material, drift through changes in electrolytes via diffusion, analytical difficulties in determining concentrations of redox sensitive system components or state of involved solids/minerals, and insufficient/inadequate thermodynamic data for calculation of the redox state of natural systems. The redox state of such complex systems can only be properly assessed based on a sound combination of chemical analysis and associated thermodynamic modelling.

The aim of WP2 was to improve the necessary scientific-technical basis for redox determination in environments relevant for nuclear waste disposals. Therefore, the application and modification of existing methods as well as the development of advanced methods for determination of the redox state of relevant systems were pursued. In order to provide trust in the outcome of the studies an inter-laboratory comparison exercise (ICE) on samples selected from the relevant host rocks in the project (granitic and clayey rocks) where the different methods are foreseen to be applied was performed and the outcome was assessed in the Interlaboratory Comparison Exercise (ICE) report. A broad scientific-technical basis for the future application was provided by the use of different types of electrodes as well as optical sensors. The various individual developments were tested against each other and evaluated for their applicability under different conditions (ICE). Based on the results tools to improve the information base for the interpretation of the system conditions were (are being → ongoing research) developed for selected examples.

### I. Redox speciation using selected redox pairs as probes

#### I.1 Kinetics and thermodynamics of Np and Tc in homogenous and heterogeneous systems

In order to investigate whether there is a well-defined redox potential or pe value ( $pe = 16.9 E_h$  at 25°C) for the reduction of  $NpO_2^+(aq)$ , the redox behaviour of  $3.5 \cdot 10^{-5}$  M Np(V) solutions in 0.1 M NaCl was studied in the pH range of  $5 < pH < 10$  under Ar atmosphere. To cover a wide range of chemically different reducing systems, including homogeneous solutions and heterogeneous suspensions, several different inorganic and organic reducing agents were

---

(D-N°:1.2) – [Report on the scientific state of the art](#)

Dissemination level :PU

Date of issue of this report : **03/09/2012**

used. The reduction process was monitored spectroscopically and by the decrease of the aqueous Np(V) concentration determined after removal of colloidal Np(IV) by 10 kD ultrafiltration. A “borderline” ( $E_h = 0.01 \pm 0.02$  V;  $pe = 0.15 \pm 0.40$ ) for Np(V) reduction has been identified. Above this line, samples with initially Np(V) are not reduced, samples falling below this line do show Np(V) reduction.

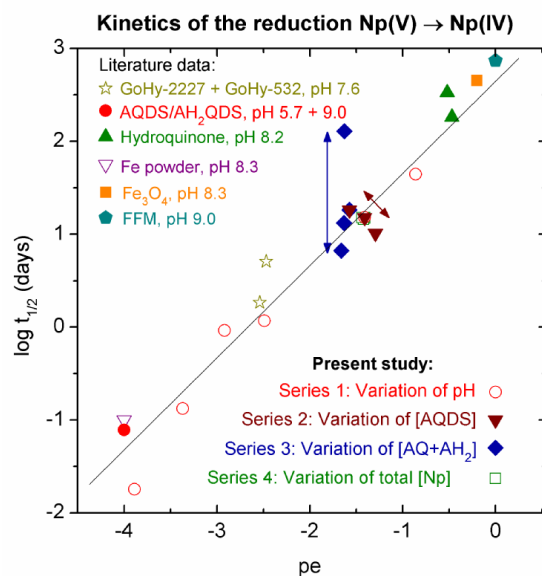


Figure I.1.1: Dependence of the half-life ( $\log t_{1/2}$ ) of Np(V) reduction on the redox potential ( $pe$ ).

Moreover, the possible kinetic control on the redox reactions was investigated under comparable experimental conditions. The Np(V) reduction in several series containing anthraquinone / anthrahydroquinone (2,6)-disulfonate (AQDS, AH<sub>2</sub>QDS) buffer was analysed systematically over an extended period of time.

Independent of homogenous system or heterogeneous suspensions and the kind of chemical used to fix the redox conditions, a general trend is apparent as shown in Figure I.1.1. The more negative the measured redox potential ( $pe$ ) in the system, the faster the Np(V) reduction takes place. In one set of experiments containing anthraquinone / anthrahydroquinone (2,6)-disulfonate ([AQDS] = [AH<sub>2</sub>QDS]) buffer (Series 3 in Fig. I.1.1), a dependence of the half-life of reduction on the concentration of reducing chemicals was observed. When keeping  $pe$  and  $pH$  constant ( $pH = 5.73 \pm 0.04$ ,  $pe = -1.62 \pm 0.04$ ) and varying only the concentration of the redox buffer (from  $6.7 \cdot 10^{-5}$  M to  $1.2 \cdot 10^{-3}$  M), a direct dependence of reduction kinetics on the redox buffer concentration *at the same*  $pe$  was

observed. By increasing the buffer concentration by a factor of 10 the half-life of reduction is decreased by a factor of 10. This indicates that only pH and pe are insufficient to characterize reduction kinetics and calls for more elaborate chemical models to be developed.

Furthermore, the solubility of Np(V) was investigated in dilute to concentrated NaCl-NaOH solutions ( $0.1 \text{ M} \leq I \leq 5 \text{ M}$ ,  $10 \leq \text{pH}_c \leq 14$ ) with special focus on the characterization of neptunium solubility-limiting solid phases in equilibrium with supernatant solutions. Composition, stoichiometry and structure of these solid phases need to be understood as a basis for improved thermodynamic descriptions. Complementary studies in  $\text{NaClO}_4$  were conducted to assess the effect of the background electrolyte. A very significant decrease in the solubility of Np(V) was observed increasing the concentration of  $\text{NaClO}_4$  from 1 M to 3 M. This observation was previously explained as an aging effect of the forming  $\text{NpO}_2\text{OH}(\text{am})$ . For NaCl, only the solubility data at low ionic strength (0.1 M NaCl) were consistent with the  $\text{NaClO}_4$  system. Under increasing ionic strength conditions, significant changes in Np solubility were observed: a pronounced drop in the solubility was observed in the  $\text{pH}_c$  region of 11.5 – 12.0. Further increase of  $\text{pH}_c$  to strongly alkaline conditions resulted in an increased neptunium solubility. XRD, XANES, chemical analysis and SEM-EDS of the solid phases showed that with increasing  $\text{pH}_c$  and NaCl concentration, Np(V) hydroxide undergoes significant phase transformation to Na-Np(V) phases, which are currently not considered in thermodynamic models. The solubility controlling solid phases were characterized by XRD, chemical analysis and SEM-EDS, which indicated the prevalence of a solid phase with a Na:Np ratio 1:1, likely  $\text{NaNpO}_2\text{O}(\text{OH})(\text{cr})$  (or  $\text{Na}_2\text{Np}_2\text{O}_7 \cdot \text{H}_2\text{O}$ ). EXAFS further indicated the predominance of a neptunate-like structure with significantly short Np– $\text{O}_{\text{ax}}$  and Np– $\text{O}_{\text{eq}}$  distances ( $1.76 \pm 0.02 \text{ \AA}$  and  $2.12 \pm 0.03 \text{ \AA}$ , respectively).

In all the systems studied ( $0.1 \text{ M} \leq I \leq 5.0 \text{ M}$ ), the solubility curve can be divided into three different regions (see Figure I.1.2): (a)  $\sim 7 \leq -\log[\text{H}^+] \leq \sim 9.5$ , showing a steep decrease in the Np solubility with a slope between  $-2$  and  $-3$ ; (b)  $\sim 9.5 \leq -\log[\text{H}^+] \leq \sim 11$ , with a nearly pH-independent [Np] and (c)  $\sim 11 \leq -\log[\text{H}^+] \leq \sim 13.5$ , showing an increase in the solubility with a well-defined slope of  $+1$  (see Figure 1). The slope analyses of these solubility data, together with the stoichiometries determined for the solid phases as well as direct analogies with U(VI), led to the definition of the equilibrium reactions  $\text{NaNpO}_2\text{O}(\text{OH})(\text{cr}) + \text{H}_2\text{O} = \text{Na}^+ + \text{NpO}_2(\text{OH})_3^-$  and  $\text{NaNpO}_2\text{O}(\text{OH})(\text{cr}) + 2\text{H}_2\text{O} = \text{Na}^+ + \text{NpO}_2(\text{OH})_4^{2-} + \text{H}^+$  to prevail in the regions (b) and (c) of the solubility curves. Two characteristic features were observed for

those samples in region (a): first, the Np concentration is unexpectedly high (with regard to previous U(VI) study under similar conditions); second: a continuous decrease of the  $E_h$  with time was found (from +800–1000 mV to +500–700 mV). This is probably related to the degradation of NaClO and might be linked with a partial reduction of Np(VI) to Np(V). The solubility of  $\text{Np}^{\text{V}}\text{O}_2\text{OH}(\text{am})$  under these  $-\log[\text{H}^+]$  and  $I$  conditions is significantly higher; this suggested that the equilibrium reaction  $\text{NaNpO}_2\text{O}(\text{OH})(\text{cr}) + 3\text{H}^+ + \text{e}^- = \text{Na}^+ + \text{NpO}_2^+ + 2\text{H}_2\text{O}$  is controlling both  $E_h$  and  $[\text{Np}]$  in the system (slope of  $-3$  to be expected), although other interpretations may also apply (*i.e.* partial formation of  $\text{Np}^{\text{VI}}\text{O}_3(\text{s})$  or  $\text{NaNp}^{\text{V}}\text{O}_2(\text{OH})_2(\text{s})$ ). This hypothesis is to be experimentally assessed by solid phase characterization and VIS–NIR spectroscopy of the aqueous phase.

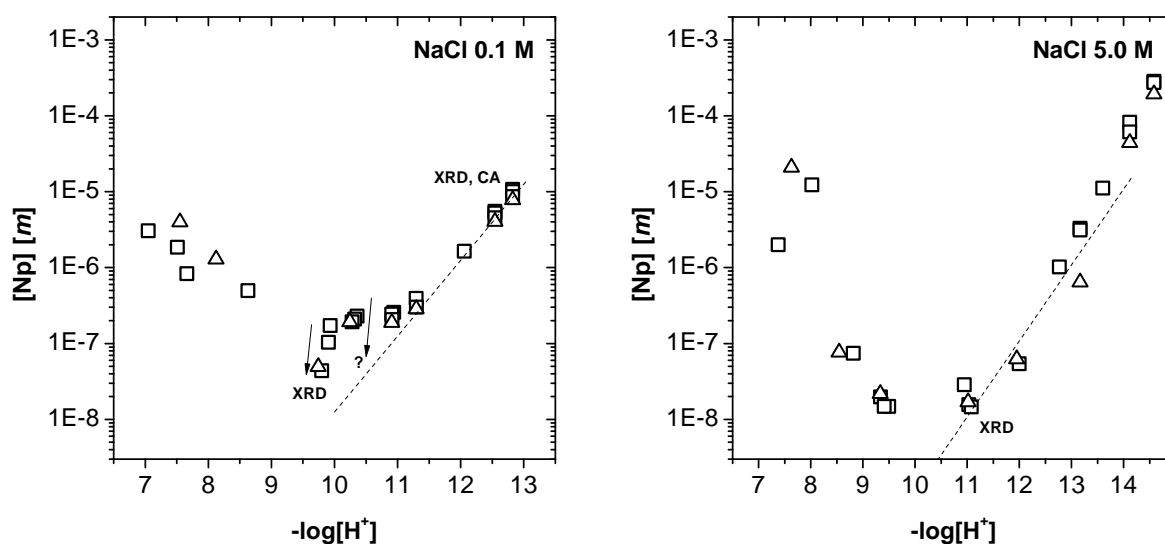


Figure I.1.2: Np(VI) solubility data determined for 0.1 M and 5.0 M NaCl. Samples equilibrated for 74 – 305 days. Samples for which solid phase analysis was performed are marked in the figures. Triangles indicate the results from the last sampling. Solubility data for 0.5 M, 1.0 M and 2.5 M NaCl not shown.

The specific ion interaction theory (SIT) was considered to derive  $\log^{\circ}K_{s,1,4}^*$  and  $\Delta\varepsilon$  for the equilibrium reaction  $\text{NaNpO}_2\text{O}(\text{OH})(\text{cr}) + 2\text{H}_2\text{O} = \text{Na}^+ + \text{NpO}_2(\text{OH})_4^{2-} + \text{H}^+$  (region (c)). Region (b) was disregarded in this step because thermodynamic equilibrium had not been reached (even after 305 days). The combination of experimental  $\Delta\varepsilon$  with  $\varepsilon(\text{H}^+, \text{Cl}^-) = 0.12 \text{ kg}\cdot\text{mol}^{-1}$  and  $\varepsilon(\text{Na}^+, \text{Cl}^-) = 0.03 \text{ kg}\cdot\text{mol}^{-1}$  allowed the calculation of  $\varepsilon(\text{Na}^+, \text{NpO}_2(\text{OH})_4^{2-}) = -0.16$ , whereas  $\log^{\circ}K_{s,1,4}^* = -19.4$ . These results underline the relevance of Na–Np(VI) solid

phases in controlling Np(VI) solubility in cementitious and NaCl-dominated saline environments.

The redox chemistry of Np(V/VI) under hyperalkaline conditions was also investigated in TMA-OH solutions. Despite the use of TMA-OH, the high total Np concentration ( $[\text{Np}]_{\text{tot}} = 2 \cdot 10^{-3} \text{ M}$ ) gave rise to the precipitation of solid Np phases in some of the samples. The carbonate concentration (as impurity of TMA-OH) was  $2 \cdot 3 \cdot 10^{-3} \text{ M}$ . Redox conditions were defined by the absence or presence of  $\text{ClO}^-$  as oxidizing agent and pH ranged between 9 and 13.5. UV spectra obtained from the supernatant in TMA-OH solutions and in absence of  $\text{ClO}^-$  showed very clear Np(V) features, identified as  $\text{NpO}_2^+$ ,  $\text{NpO}_2(\text{CO}_3)^-$  and  $\text{NpO}_2(\text{OH})_2(\text{CO}_3)^{3-}$ . XANES of these samples confirmed the predominance of Np(V). No UV features were observed within 800-1300 nm for samples with  $\text{ClO}^-$ , even though Np(VI) is expected to occur. This different behaviour was explained by the lower Np concentration in some of the samples, but is also indicative of the possible formation of centrosymmetric Np(VI) species (e.g.  $\text{NpO}_2(\text{OH})_4^{2-}$ ) with lower absorption coefficients. XANES data of this second set of samples confirmed the predominance of Np(VI), in accordance with reference spectra. A similar Np redox distribution was observed for the solid phases based on XANES and EXAFS measurements. Moreover, EXAFS spectra indicative of  $\text{Np}^{\text{V}}\text{O}_2\text{OH}(\text{s})$  and  $\text{Np}^{\text{VI}}\text{O}_3 \cdot x\text{H}_2\text{O}(\text{s})$  were obtained and the formation of a Na-Np(VI) solid phase in  $5 \cdot 10^{-2} \text{ M ClO}^-$  at  $\text{pH} \approx 12$  was indicated from both EXAFS and chemical analysis. These results confirm the relevance of Np(VI) in hyperalkaline systems even under mildly oxidizing conditions. Anionic species analogous to U(VI) are expected to be formed in the pH range  $10 < \text{pH} < 14$ . Indications of a Na-neptunate formation at  $[\text{Na}] = 0.01 \text{ M}$  suggest the potential relevance of Na-Np(VI) (and Ca-Np(VI)) solid phases in cementitious and saline environments.

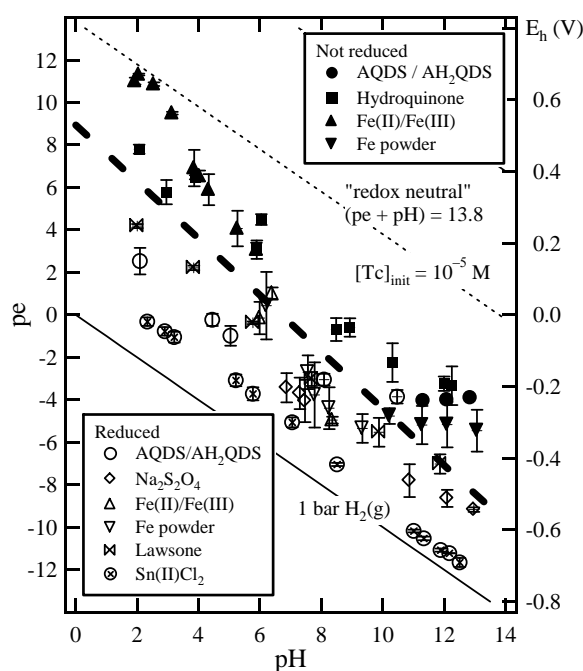


Figure I.1.3: Reduction of Tc(VII) in 0.1 M NaCl/NaOH solutions. Open symbols indicate Tc(VII)/(IV) reduction, filled symbols indicate no Tc(VII) reduction within up to 1.5 months. The dashed line represents the experimental borderline for Tc(VII)/Tc(IV) reduction.

The behavior of Tc in the environment critically depends on its oxidation state. In the +VII oxidation state, Tc forms highly soluble solids and exists as an anionic  $\text{TcO}_4^-$  ion in aqueous systems. On the other hand, in +IV oxidation state, Tc is easily hydrolyzed to form sparingly soluble hydroxide solids and aqueous hydrolysis species, and considered to be relatively immobile. It is, therefore, needed to clarify the Tc(VII)/Tc(IV) redox processes and to predict the redox state distribution and respective stability fields as function of basic geochemical parameters (pe, pH, ionic strength) under the reducing redox conditions relevant for deep geological repositories. The systematization of Tc redox processes in both homogenous and heterogenous systems within the established  $E_h/pH$  concept offered a robust approach and allowed conclusions on main reaction mechanisms. Aliquots of  $\text{TcO}_4^-$  stock solution were added to the sample solutions which were pre-equilibrated with different reducing agents at certain pHs in 0.1 M NaCl/NaOH solutions. The reductants used in this study were sodium anthraquinone / anthrahydroquinone disulfonate redox buffer solutions (AQDS / AH<sub>2</sub>QDS), hydroquinone solutions, Fe(II) / Fe(III) solutions and precipitates, Na<sub>2</sub>S<sub>2</sub>O<sub>4</sub> solutions, Fe powder suspensions, 2-hydroxy-1,4-naphthoquinone (Lawsone) redox buffer solutions, and

the Sn(II) system. The initial  $\text{TcO}_4^-$  concentration after spiking the pre-equilibrated samples was set to  $10^{-5}$  M. After given a period of time the pH and  $E_h$  values were measured and Tc concentrations were determined in solution after 10kD (2 nm) ultrafiltration using Liquid Scintillation Counting (LSC, LOD~ $10^{-8}$  M). The concentrations of Tc(VII) and reduced Tc(IV) species were determined using solvent extraction technique (tetracosylchloride extraction). The Tc concentrations in the aqueous phases decreased in  $\text{Na}_2\text{S}_2\text{O}_4$ , Sn(II), Lawsons, Fe powder (neutral pH range), and AQDS /  $\text{AH}_2\text{QDS}$  (acidic pH range) systems, indicating the reduction of Tc(VII) and the formation of the expected sparingly soluble Tc(IV) solid phases. In contrast, the initial Tc concentrations did not change in the systems of AQDS/ $\text{AH}_2\text{QDS}$  (alkaline pH), hydroquinone, Fe(II)/Fe(III) (acidic pH) and Fe powder (alkaline pH). The reaction kinetics did not show any pronounced differences related to homogenous or heterogenous system characteristics and rather suggested a dependence on overall  $E_h$ /pH conditions. The results are summarized quantitatively in the pe-pH diagram (Fig. I.1.3). Samples in which no Tc(VII) reduction was observed are plotted as filled symbols, samples in which Tc(VII) was reduced are plotted as open symbols. The dashed line represents the experimental borderline for the reduction, which was found to be independent of the reducing chemicals or the presence of iron solid phases. This systematic trend of the Tc(VII)/(IV) redox behaviors depending on the  $E_h$ /pH conditions agrees well with the predictions from thermodynamic calculations considering a known effect of solid phase particle size on the solubility and redox equilibria. Well defined stability fields for dominant Tc(VII) and Tc(IV) redox states were established for the given experimental parameters ( $E_h$  and pH conditions).

### I.2 Speciation of iodine

The sorption behaviour of iodine species from  $\text{NaClO}_4$ -solution by kaolinite (KGa-1b) and humic acid (HS, Sigma Aldrich) was examined. Samples in the pH range of  $2 < \text{pH} < 10$  were prepared with a kaolinite concentration of 4 g/L. After the pre-equilibration time (2 weeks) the solutions were spiked with iodine species (iodide or iodate,  $c = 10$  mg/L). After a contact time of 14 days the iodine species content remaining in the solutions were determined by ICP-MS (see Figure I.2.1 and Figure I.2.2).

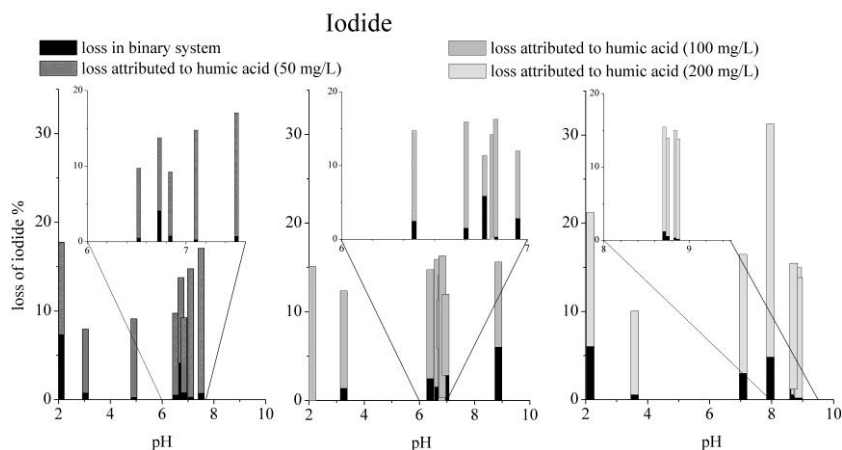


*Figure I.2.1: Iodide systems investigated by ICP-MS*

Both, iodide and iodate had a low sorption capacity below 8% and 21% on kaolinite. The pH of the solutions had an effect on the sorption capacity of the species only at pH < 4. After determination of the iodine loss due to sorption on kaolinite, ternary systems were prepared by adding different amounts of HS to samples containing the equilibrated iodine-kaolinite systems (concentrations of HS = 50, 100, and 200 mg/L, respectively).

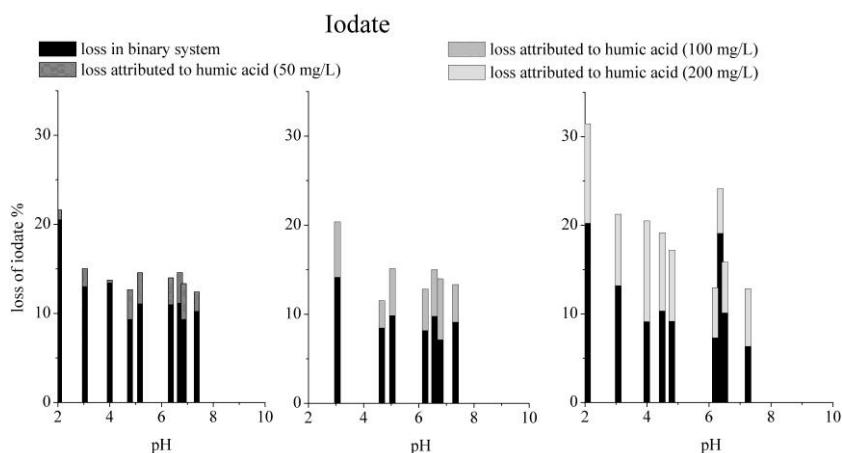


*Figure I.2.2: Iodate systems*

Compared to the binary systems an additional loss of iodine from the solutions attributed to reactions with humic acid was observed for both species which was higher for iodide (up to 26%) than for iodate (<14%).

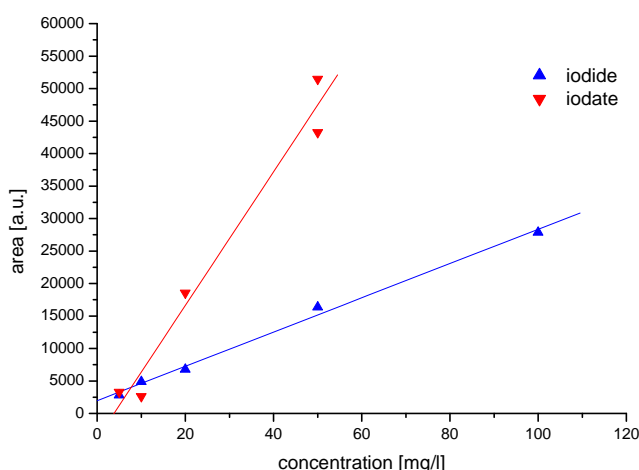


Figure 1.2.3: Calibration of iodine and iodate by CE-ICP-MS

Figure 1.2.3 shows the calibration of iodide and iodate in CE-ICP-MS measurements (note: free iodine samples for calibration could not be prepared under similar conditions in the electrolyte system, only standards in organic solvents were prepared but the sensitivity of the ICP-MS signal is different and cannot be compared to aqueous electrolyte systems). Ion chromatography can be used as alternative separation technique for the determination of distribution of iodine species. Adjusting the ionic strength using  $\text{NaClO}_4$  the pH values of solutions were set between  $2 < \text{pH} < 10$ . Two sets of samples were prepared. Solutions with only iodine species were compared with binary iodine species-kaolinite systems. The effect of the presence of kaolinite on the equilibrium between the iodine species was investigated over a period of 3 months. During that time the species were stable in presence of kaolinite as well as without it. After 3 months for both species a loss of approx. 10% was measured in the samples without kaolinite. This suggests sorption on the glass or the formation of free iodine. Losses in the binary systems were not significantly higher. Therefore, in addition to our earlier investigations, it can be assumed that the no significant sorption can be observed in the binary iodine species-kaolinite systems that could be assigned to kaolinite.

### 1.3 Speciation of Se

The speciation of Se was evaluated as a probe for redox state determination in hyperalkaline solution. UV/Vis spectrophotometry is the efficient technique for the characterisation of Se(-II) species but its sensitivity is too low for determining concentrations lower than  $10^{-4}\text{M}$ .

Therefore, the *in fine* analytical approach was applied to establish a speciation technique (ion chromatography) *off line* coupled with a very sensitive analytical technique (ICP-MS). A specific electrosynthesis of a selenide ions source (sodium selenide) was developed and characterized by X-Ray Diffraction as well as X-Ray Photoelectron Spectroscopy (XPS). The deconvolution of the XPS peaks showed contributions between 52 eV and 54.25 eV which can be assigned to Se(-II) species (3d5/2 and 3d3/2 transitions). The solid was kept in a glove box under inert atmosphere. Solutions of sodium selenide ( $6.2 \cdot 10^{-4}$  M) were prepared by dissolving the solid in sodium hydroxide solutions ranging from 0.5 to 8 M in order to investigate the whole range of stability of Se(-II) monomer species. UV/Vis spectra were acquired for all solutions. Results show that the major specie is  $\text{HSe}^-$  ( $\lambda_{\text{max}} = 245$  nm) for NaOH concentrations lower than 1 M and  $\text{Se}^{2-}$  ( $\lambda_{\text{max}} = 274$  nm) for concentrations higher than 2 M in accordance with literature.

Speciation experiments were conducted on  $\text{HSe}^-$  solutions using ion chromatography. The redox potential of the solution was -0.655V/ESH. The separation protocol was optimized for *on line* detection of the following species ( $\text{HSe}^-$ , Se(IV) and Se(VI)) related to different redox states in order to get simultaneous informations on a potential reoxidation during the analysis. For that purpose, two different detectors (a UV-visible single wavelength detector and a conductimetric one) were coupled to an ion chromatograph for detecting  $\text{HSe}^-$  with UV/Vis spectrometry at  $\lambda = 245$  nm and oxidized species with conductimetry. The eluent solution (KOH = 20 mM) and all the separation apparatus were flushed continuously with ultrapur Helium for maintaining an anoxic environment during the analysis. The flow rate and temperature were set at 1mL/min and 30°C, respectively.

Figure I.3.1 shows the analysis of a  $\text{HSe}^-$  solution in 0.05 M NaOH. UV-visible detection shows only one peak at 12.6 min which is assigned to  $\text{HSe}^-$ .

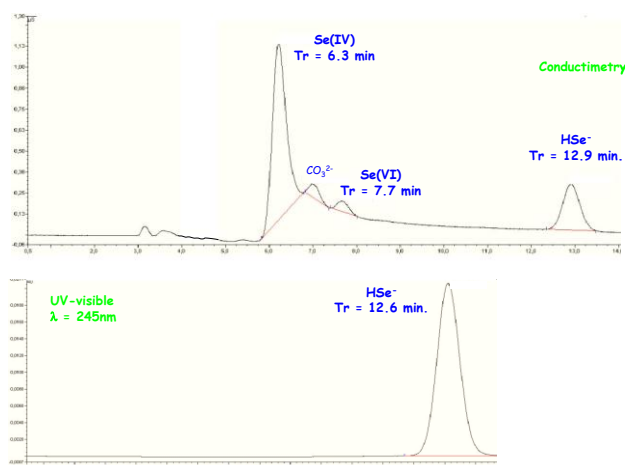


Figure I.3.1: Chromatograms (top: conductimetric detection ; bottom: UV/Vis detection at  $\lambda = 245\text{nm}$ ) of a  $\text{HSe}^-$  solution in  $0.05\text{ M NaOH}$

Because of the time shift related to the coupling of the two detectors, the peak at 12.9 min can then be assigned to this species in conductimetry detection. The other peaks are assigned to Se(IV) and Se(VI) at 6.3 min and 7.7 min, respectively. The presence of those oxidized species showed, that despite the precautions, some traces of  $\text{O}_2$  were still trapped in the chromatographic system. However, this contamination remains at a low level since Se(IV) and Se(VI) concentrations were found to be less than 5 % and 0.2 % of the total Se concentration, respectively. The additional peak at 7.0 min is due to the presence of carbonate ions in the eluent. This result showed that HPAEC is sensitive enough for identifying and quantifying  $\text{HSe}^-$  at millimolar level. The quantification limit is determined to  $5 \cdot 10^{-5}\text{ M}$ . Coupling subsequent *off line* ICP-MS analysis (after fraction collection) decreases drastically the quantification limit to  $10^{-9}\text{ mol/L}$ .

Attempts for separating a mixture of  $\text{HSe}^-$  and  $\text{Se}^{2-}$  species with a adapted protocol (gradient elution mode from 0.05 to 0.5 mol/L KOH at 0.4 ml/L ;  $T = 45^\circ\text{C}$ ) were unsuccessful. The two peaks remained only partially resolved (retention time are separated by only 40 s). The retention time for  $\text{Se}^{2-}$  species (slightly greater than this of  $\text{HSe}^-$ ) was consistent with the retention of a higher charged species (stronger interaction with the functional groups of the anion resin). Nevertheless, Gaussian deconvolution of the peaks allow to quantify the two species at a millimolar level (ie:  $3 \cdot 10^{-3}\text{ M}$ ).

A mixture of polymer species was synthesized by adding a known mass of Se(0) to a Se(-II) solution with a 1:1 molar Se(-II)/Se(0) ratio, in 4 mol/L KOH. The analysis was based on the previous described protocol. Improvements were obtained with an isocratic elution (0.5 M

KOH). Figure I.3.3 shows the chromatogram of this mixture and was representative for polymer species. Two peaks can be distinguished at 10.72 min and 11.31 min which meant that the analyzed species had a real chemical interaction with the functional groups of the resin. Despite the analytical efforts, only partial separations were obtained because of very similar interactions of both species towards the anion exchange columns. Based on these results, new route making use of aminoacids as cationic complexants, should be tested in the near future to improve the separation of Se reduced species.

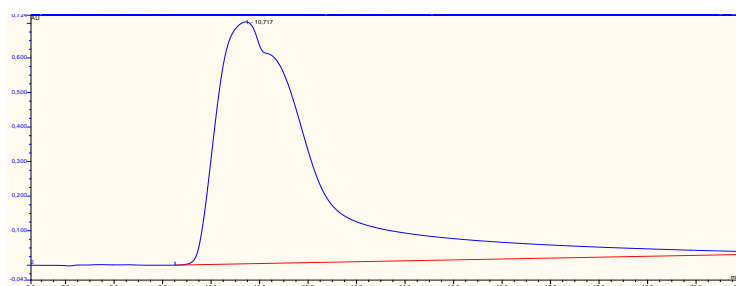


Figure I.3.2: Chromatogram of a 1:1 Se(-II)/Se(0) molar ratio mixture of polymer species.  
Flow rate = 0.4 mL/min ; T = 45°C ; UV detection at  $\lambda = 360$  nm

#### I.4 Speciation of Fe

In a fully equilibrated aqueous system the oxidation state of system components is determined by the redox potential  $Eh$ . In solutions that contain the redox couple Fe(II) and Fe(III) it may be expressed by the Nernst equation (I.4.1).

$$E = E^0 + 0.05916 \log \frac{a_{Fe^{3+}}}{a_{Fe^{2+}}} \quad (I.4.1)$$

Unfortunately, only in dilute solutions conventionally measured  $Eh$  values have a well-defined physical meaning. In brines the Nernst equation (equation 1), is not applicable for two reasons.

Firstly, the liquid junction potential at the interface between reference solution (e.g. 3 M KCl) and sample solutions cannot be regarded as constant. Thus, the standard redox potential  $E^0$ , which is normally taken as constant, becomes a function of the ionic strength  $I$ . Secondly, the single ion activity coefficients  $\gamma$  that are part of the activity  $a$  can only be determined with reasonable accuracy in dilute solutions. In concentrated solutions, only combined or mean ion activity coefficients and activities have a physical meaning and are accessible through

measurements. Thus, the single ion activity in equation (1) has to be substituted by a combined activity, for example by expanding equation (1.4.1) with the activity of the corresponding anion (such as chloride or sulphate).

Taken these two aspects into account, the cell potential can be described with the following equation:

$$E = E^0 + \Delta E_{LJ} + 0.05916 \log \frac{a_{Fe^{3+}} a_{Cl^-}^3}{a_{Fe^{2+}} a_{Cl^-}^2} - 0.05916 \log a_{Cl^-} \quad (1.4.2)$$

The last term contains the inaccessible individual activity coefficient of chloride. It is combined with the equally immeasurable liquid junction potential to the deviation  $\Delta Rx$ .

$$\Delta Rx = \Delta E_{LJ} - 0.05916 \log a_{Cl^-} \quad (1.4.3)$$

The remaining constant or calculable terms are combined to  $Rx$ :

$$Rx = E^0 + 0.05916 \log \frac{a_{Fe^{3+}} a_{Cl^-}^3}{a_{Fe^{2+}} a_{Cl^-}^2} \quad (1.4.4)$$

An analogous formulation was derived for sulphate media:

$$Rx = E^0 + 0.05916 \log \frac{a_{Fe^{3+}} a_{SO_4^{2-}}^{1.5}}{a_{Fe^{2+}} a_{SO_4^{2-}}} \quad (1.4.5)$$

$$\Delta Rx = \Delta E_{LJ} - 0.05916 \log a_{SO_4^{2-}}^{0.5} \quad (1.4.6)$$

Only if the element specific redox potential  $Rx$  is known conclusions about the oxidation state of system components can be drawn.

*The spectrophotometric method:* One method for accessing the element specific redox potential  $Rx$  is by species analysis. In the study spectrophotometric techniques with the UV/Vis probes phenanthroline and thiocyanate were carried out. Those probes are well established in water analysis but only little was known whether these methods were also suitable for concentrated salt solutions.

It could be shown that the Fe(III) determination with thiocyanate was not significantly influenced by chloride concentrations even at high ionic strength. On the other hand a deviation of up to 30% was observed in a 1.3 m  $Na_2SO_4$  solution. Furthermore, the dependence on time, pH and  $SCN^-$  concentration was demonstrated. Because of these disadvantages it was decided to switch to the phenanthroline method.

The influence of NaCl, Na<sub>2</sub>SO<sub>4</sub>, MgCl<sub>2</sub> and CaCl<sub>2</sub> on the performance of the phenanthroline method for Fe(II) and total iron determination was tested at 25°C. Samples with increasing salt concentration up to near saturation (except CaCl<sub>2</sub>) were prepared and measured with a regular two beam spectrometer. We could show that the background ions had no significant influence on the determination method. The lower detection limit with 1 cm cuvettes was 5·10<sup>-4</sup> g/l. The long pass flow cell worked well only for the analysis of Fe(II) species. Determinations of total iron and Fe(III) were not possible with the capillary spectrometer due to effects emerging by the use of a long pass flow.

The activities of redox sensitive species in saline solutions can be calculated by geochemical modelling tools. This is possible if the concentrations of these species as well as the inorganic salts are determined and thermodynamic data of the redox sensitive species are available. In that case, the redox potential  $R_x$  can be calculated with equations (I.4.4) and (I.4.5).

*The potentiometric method:* If a redox electrode will be used for the determination of the redox potential  $R_x$  in saline solutions, the measured cell potential  $E$  has to be corrected for the saline media induced bias  $\Delta R_x$  according to equation (I.4.7).

$$E = R_x + \Delta R_x \quad (I.4.7)$$

To obtain a function for  $\Delta R_x$ , the potential  $E$  of known FeCl<sub>3</sub>/FeCl<sub>2</sub> or Fe<sub>2</sub>(SO<sub>4</sub>)<sub>3</sub>/FeSO<sub>4</sub> activity ratios has to be analysed in specified saline solutions. Measurements were carried out with a combined Pt ring electrode. The reference electrode was an Ag|AgCl with 3M KCl as electrolyte. The salt concentration (NaCl, KCl, and MgCl<sub>2</sub> as well as Na<sub>2</sub>SO<sub>4</sub>, K<sub>2</sub>SO<sub>4</sub>, and MgSO<sub>4</sub>) was varied from about 0.1 mol/kg till near saturation. All samples contained 0.01 M HClO<sub>4</sub> and about 5·10<sup>-5</sup> M FeCl<sub>2</sub> and 5·10<sup>-5</sup> M FeCl<sub>3</sub>.

In most electrolyte solutions the cell potential  $E$  declined with increasing salt concentration. Only in MgSO<sub>4</sub> solutions  $E$  run through a minimum at 0.7 mol/kg chloride followed by a continuous increase. In chloride and sulphate systems the potassium salts had the strongest influence on the redox potential followed by sodium and magnesium. In chloride solutions the decline was maximal 43 mV. A comparison with sulphate solutions exhibits an even much more significant effect. At  $I = 0.1$  mol/kg, redox potentials were already 60 mV lower than in

dilute chloride solutions. Between 0.1 and salt saturation redox potential further decreased up to 40 mV.

Generally, a decline of the redox potential with increasing salt concentration has to be expected. Although the Fe(II)/Fe(III) ratio was kept constant the free concentrations and also activities of  $\text{Fe}^{2+}$  and  $\text{Fe}^{3+}$  decrease due to interaction and complexation with chloride or sulphate. Since the  $\text{Fe}^{3+}$  complexation is much stronger than for  $\text{Fe}^{2+}$  the activity ratio  $a\text{Fe}^{3+}/a\text{Fe}^{2+}$  and therefore, the potential according to equation (I.4.2) will decrease.

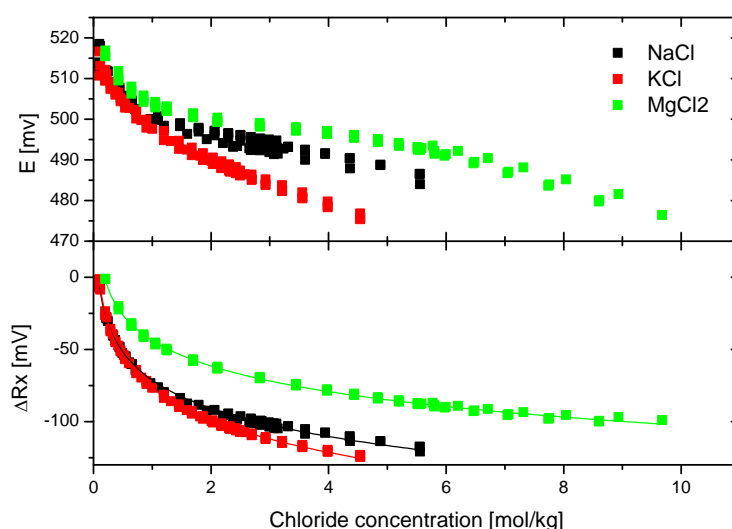


Figure I.4.1: Measured redox potential  $E$  of chloride solutions with  $\text{Fe(II)} = \text{Fe(III)} = 5 \cdot 10^{-5} \text{ M}$  and  $\text{HClO}_4 = 0.01 \text{ M}$  above and the calculated  $\Delta R_x$  values below

The correction factor  $\Delta R_x$  can be calculated from the difference between the apparent potential  $E$  and  $R_x$ , which is given by equation (I.4.4) and (I.4.5). The calculation of the required activities is specified further down. The correction data were fitted with the following function to describe the concentration dependence.

$$\Delta R_x(m_x) = a \log m_x + b \cdot m_x + c \quad (I.4.8)$$

Here,  $m_x$  represents the concentration (molality) of the main anion (chloride or sulphate). For chloride solutions the second term could be omitted. Parameters were calculated by means of a multilinear regression based on a least square optimization. The correction functions are summarized in the following table.

Table I.4.1: Parameters for the media dependency of  $\Delta Rx$  (Hagemann et al. 2012a)

Electrolyte solution	Function for $\Delta Rx$	Medium absolute deviation ( $\Delta Rx - \Delta Rx_{calc}$ )	Maximum exp. scattering between repeated runs	Concentration range
NaCl	$-64.8 (\pm 0.5) \log m_{Cl} - 71.3 (\pm 0.3)$	1.6 mV (95%: 3.1 mV)	$\pm 2$ mV	0.1-5.5
KCl	$-74.1 (\pm 0.3) \log m_{Cl} - 76.8 (\pm 0.1)$	0.86 mV (95: 1.8 mV)	$\pm 1$ mV	0.1-4.5
MgCl <sub>2</sub>	$-58.8 (\pm 0.3) \log m_{Cl} - 43.8 (\pm 0.2)$	0.88 mV (95%: 2.0 mV)	$\pm 1$ mV	0.2-11.5
Na <sub>2</sub> SO <sub>4</sub>	$-124.9 (\pm 1.5) \log m_{SO_4} + 27.7 (\pm 1.1) m_{SO_4} - 237.7 (\pm 1.2)$	1.1 mV (95%: 1.8 mV)	$\pm 3$ mV	0.1-1.9
K <sub>2</sub> SO <sub>4</sub>	$-136.2 (\pm 2.7) \log m_{SO_4} - 246.3 (\pm 1.4)$	3.9 mV (95%: 6.2 mV)	$\pm 5$ mV	0.65
MgSO <sub>4</sub>	$-112.4 (\pm 0.8) \log m_{SO_4} + 29.8 (\pm 0.5) m_{SO_4} - 202.9 (\pm 0.6)$	0.8 mV (95%: 1.9 mV)	$\pm 1$ mV	0.56-2.6

*Comparison of methods:* Both described methods have specific strengths and limitations. The potentiometric method is based on the widely used standard procedure for the measurement of redox potentials with commercially available redox electrodes. Principally, the method is applicable for all salt media and pH values. However, correcting factors  $\Delta Rx$  have been derived only for simple salt, not for mixed salt solutions. It still needs to be tested for slightly acidic to near neutral solutions. The spectrophotometric method is applicable to all pH values. It allows the determination of total Fe(II) and Fe(III) concentrations in simple as well as in mixed electrolyte solutions and is not limited to 25°C. The drawback of this method is that the interpretation of Fe(II) and Fe(III) concentrations with regard to redox potentials depends on the availability of a thermodynamic model for the original test solution. Currently, such a model is only available for acidic solutions in the system Na-K-Mg-Cl-SO<sub>4</sub>-H<sub>2</sub>O at 25°C. Moreover, the total Fe(III) and Fe(II) concentrations must be higher than the detection limit of the spectrophotometric method. Measuring with the long path flow cell would extend the applicability of the method but still is challenging.

*Thermodynamical model for Fe in saline solutions:* Calculation of the  $Fe^{2+}$  and  $Fe^{3+}$  activities are required for the spectrophotometric as well as for the potentiometric method. This was done with the geochemical modeling tool EQ3/6. Pitzer interaction parameters for the system Na-K-Mg-Ca-Cl-SO<sub>4</sub>-OH-HCO<sub>3</sub>-CO<sub>3</sub>-CO<sub>2</sub>-H<sub>2</sub>O were taken from literature including binary interaction parameters for Fe(II) and Fe(III) in chloride and sulphate solutions. Ternary parameters for Fe(II) and Fe(III) in Na-K-Mg-Cl-SO<sub>4</sub>-H<sub>2</sub>O systems were newly developed. The used model describes the activities of iron sufficiently well although it does not include complexes explicitly. A first step for the development of a thermodynamic model that takes into account hydroxo and chloro-complexes as well as possible mixed complexes was developed. Here, pH titration with saline solutions (NaCl, MgCl<sub>2</sub> or CaCl<sub>2</sub>) including Fe(II) and Fe(III) were carried out. Beside the pH value also the redox potential and UV-spectra were recorded.

It could be shown that the decrease of redox potential is directly connected to the decrease of free  $Fe^{3+}$  concentration. At a constant concentration of background ions redox potential is only depending on the formation of hydroxo complexes. Without knowing the exact composition of hydroxo ("FeOH") and chloro complexes ("FeCl<sub>n</sub>") the relative concentration of hydroxo complexes can be calculated according to formula (I.4.9).

$$\frac{C_{FeOH}^n}{C_{FeCl_n}^n} = 1 - 10^{\frac{\Delta E_{Rx}}{0,05916}} \quad (I.4.9)$$

Figure I.4.2 summarizes the results of the model calculation for the fraction of hydroxo complexes in relation of total Fe(III) in MgCl<sub>2</sub> solutions as a smoothed contour diagram.

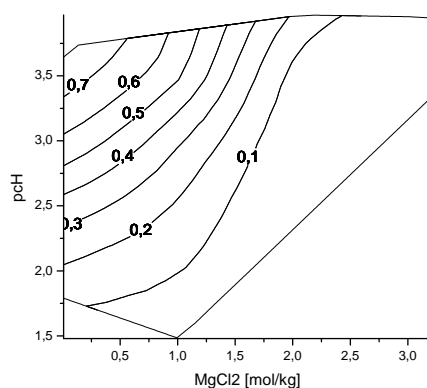


Figure I.4.2: Calculated fraction of hydroxo complexes in relation of total Fe(III) in MgCl<sub>2</sub> solutions

The UV-spectra were evaluated using the information about relative concentration of hydroxide complexes. Based on this the single species spectrum it could be concluded that up to chloride concentrations of 4 mol/kg and  $-\log cH^*$  values of 4 the monohydroxo complex  $FeOH^{2+}$  is the first and only monohydroxo complex to form. It was shown that  $FeOH^{2+}$  is the only hydroxo complex in chloride concentrations between 1 and 4 mol/kg. No evidence was found for mixed chloro hydroxo complexes.

## II. Advanced redox measurements in natural systems

### II.1 Development of optodes for fiber-based chemical sensing of redox-relevant parameters

Research on the development of optodes was focused on i) the implementation of an improved dual-phase modulation-based fiber optode for the determination of oxygen concentrations in the sub-ppm range and ii) the development of a luminescence decay time based pH-sensor. The challenges of these research topics are highly different. The development of the optode for trace level oxygen measurements requires an optical sensor with a very long luminescence decay time in order to have a sufficient dynamic range at low oxygen concentrations. Technical requirements such as sensitivity of the detection system, adaption of the modulation frequencies and polymer matrix used for immobilisation are major aspects that need to be considered in the development. Moreover, for pH measurements the luminescence probes available show mostly spectral alterations, have fluorescence decay times in the nanosecond range (hence require a completely different electronics for light modulation and detection) and show only limited pH sensitivity when immobilized in a polymer matrix.

The electronic and optical setup including fiber tip was distinctly miniaturized to improve handling for in field applications. The characterization of different pH-sensitive fluorescence probes for fiber-based optical sensing was carried out including the integration of pH-sensitive probes in different polymer materials and determination of the optical response functions. With respect to the measurement of oxygen novel luminescence probes were tested, depth profiles in biofilms were collected, and a comparison with electrochemical methods was carried out in detail. In order to increase the applicability of the set up for

multiparameter sensing, the accessible modulation frequency range was increased as well. This increases the number of potential fluorescence probes to be used within the optodes. A novel luminescence probe with a luminescence decay time of several hundred  $\mu\text{s}$  was implemented for improved oxygen detection using fiber-optical two-modulation luminescence detection. Different chromophores can now be used in the oxygen sensor in order to address different concentration ranges with a high precision. The novel Pd-probe has a very high dynamic range with respect to the decay time change due to the presence of oxygen (gain of a factor of  $>10!$ ) compared to the established oxygen sensor. For the implementation of the novel probe a thorough calibration in the ppm concentration range was indispensable and turned out to be a demanding task. The calibration experiments were carried out in the low vol% range. With the Pd-based probe the determined LOD for oxygen in aqueous solution is 1 ppb and around 7 ppb for the Pt-based sensor type. For both optode types outstanding accuracies in the data acquisition were achieved. A major factor for the excellent sensitivity, accuracy and reproducibility is the fact, that the measurements were performed at two different frequencies, which significantly reduced any contribution from background luminescence and scattered light.

In the development of multiparameter FOCS the determination of pH was investigated with emphasis on a time-resolved detection scheme using dual frequency phase modulation spectroscopy. The fundamental aspects of pH sensing based on luminescence decay time measurements were further evaluated by testing different pH-sensitive probes and by optimizing the polymer matrix to improve the proton-selectivity and reduce cross-sensitivity for other cations. The experiments were focused on different fluorescein derivatives as probes and their potential for luminescence decay time based pH-sensing was evaluated in batch as well as fiber-based experiments. In the later case the probes were immobilized in a novel polymer, which shows very high proton permeability. For calibration purposes a series of citrate and TRIS buffer solutions with fixed pH-values were used. The phase shift at pH 1 was used as reference point and the change of the phase shift at all other pH compared to pH 1 was recorded. From these relative phase shift the change in decay time was calculated. With the current optode, a pH range between one and five can be addressed. Finally, the miniaturized electronic and optical set up was further successfully developed for multiparameter sensing by the combination of the oxygen and pH optodes.

## II.2 Comparative electrochemical and fiber-optic oxygen sensor measurements in uranium contaminated biofilms

*Electrodes:* Electrochemical microsensors of the micro-Clark design from Unisense (Denmark) were used to measure concentration profiles of oxygen in biofilms. The oxygen microsensors are based on the diffusion of oxygen through a silicone membrane to an oxygen reducing cathode which is polarized against an internal Ag/AgCl anode. The sensors used had a sensing tip diameter of 10  $\mu\text{m}$ . The stirring sensitivity of < 2% and the response time of < 1 s was specified from Unisense (Denmark). During the measurements the sensors were fixed in a holder on a motor-driven micromanipulator stage. For automated measurements of 20  $\mu\text{m}$  steps the micromanipulator was connected with a motor controller. This enabled the positioning of the microsensors in a precise small-scale. The motor controller communicated with a PC via the RS-232 serial port and was controlled from the PC with the program PROFIX (Unisense, Denmark). The current was measured by a picoammeter which was connected with an A/D converter for data acquisition.

*Optodes:* Due to the specific electronic nature of molecular oxygen, the phosphorescence of sensor dyes is quenched by ambient oxygen molecules. With increasing oxygen concentrations, both, phosphorescence decay time and intensity decrease. It is favorable to measure the decay time  $\tau$  instead of the intensity, since  $\tau$  is independent of sensor concentration, absorption and scattering properties of the sample. For real-time measurements,  $\tau$  is determined by phase modulation, in which the sensor is excited with sinusoidal modulated light. The temporal delay of the phosphorescence signal results in a phase shift  $\phi$  between the excitation and phosphorescence light. In the case of a single exponential decay, the relation between  $\tau$ ,  $\phi$ , and the modulation frequency  $\omega$  is given by  $\tan \phi = \omega \tau$ . The corresponding oxygen concentration was evaluated from  $\tau$  or  $\phi$  by use of a temperature-corrected calibration curve, which is based on the Stern-Volmer equation. In praxis, sinusoidal interference signals, e.g. fluorescence arising from the sample or optical components as well as residual excitation light, which unintentionally reaches the detector, superpose the sensor signal. These in-phase signals lead to a corruption of  $\phi$  and therefore, to incorrect oxygen values. A straightforward approach to mask the interference of in-phase signals is to measure the respective phase shifts at two different modulation frequencies. This technique is based on the fact that the time delays of all sinusoidal interference signals can be assumed to be zero compared to the microseconds decay time of sensor's phosphorescence.

The first studies were performed in stable multispecies biofilms, grown in the laboratory biofilm reactors at the air/liquid interface and were exposed to uranium in ecologically relevant concentrations ( $1 \times 10^{-5}$  and  $1 \times 10^{-6}$  M), e.g., in seepage water of Schlema/Saxony, Germany. Numerous oxygen microsensor profiles were measured versus depth at different points. The microsensor profile measurements exposed to uranium showed that the oxygen concentration decreased faster with increasing biofilm depth compared to the uranium free biofilms (Fig. II.2.1). The fast decrease in the oxygen concentrations in the biofilm profiles showed that the bacteria in the top region of the biofilms, i.e., the metabolically most active biofilm zone, battle the toxic effects of aqueous uranium with an increased respiratory activity. This increased respiratory activity results in oxygen depleted zones closer to the biofilm/air interface which may trigger uranium redox processes, since suitable redox partners, e.g., extracellular polymeric substance (EPS) and other organics (e.g., metabolites), are sufficiently available in the biofilm porewaters. Such redox reactions may lead to precipitation of uranium (IV) solids and consequently to a removal of uranium from the aqueous phase. Both sensor methods showed almost identical curve progressions within the absolute error from the top to a biofilm depth of approximately 680  $\mu\text{m}$  and 480  $\mu\text{m}$ , respectively. At this depth the electrochemical sensor measurements had to be stopped in order to avoid the destruction of the very fragile sensor tip when reaching the solid microscope glass slide on the bottom of the biofilm. Due to the high stability of the optodes against consolidated materials, laser-based microsensor measurements were continued over an additional range of approximately 1 mm down to the biofilm/solid glass slide interface within the same biofilms. Thus, additional information of the oxygen concentration of the lower zone was obtained and showed that the oxygen concentration within the biofilm exposed to uranium decreased rapidly.

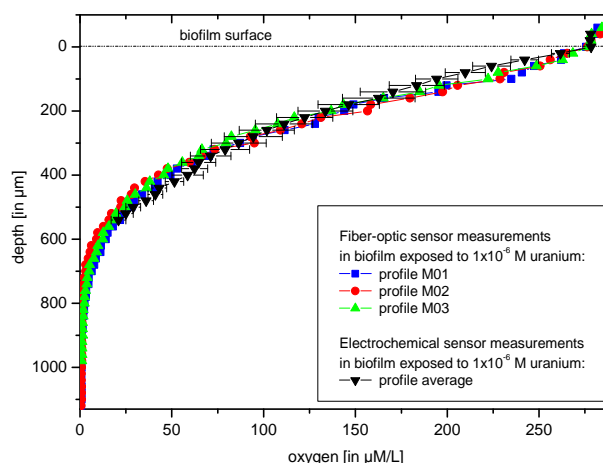


*Figure II.2.1: Oxygen concentration profiles of fiber-optic sensor and electrochemical sensor measurements in a biofilm, exposed to a uranium concentration of  $1 \times 10^{-6}$  M U(VI) in the surrounding bulk solution.*

It was the aim to use microsensors for field-measurement in radionuclide contaminated environments, e.g. former uranium mining sites, to verify redox processes in in-situ biofilms, the improved miniaturized laser-based fiber-optic oxygen microsensor equipments proved to be very suitable. Comparative studies have been carried out in stalactite-like biofilms from the uranium mine Königstein (Germany), where the mining activities had been stopped in 1990 and the uranium mine has been partially flooded for remediation. In the acidic, sulphate-rich waters with high concentration of heavy metals and radionuclides (uranium) as contaminants, biofilms are formed and occur as gelatinous filaments, and as stalactite-like snotites. Numerous stalactite-like biofilms with a maximum length of 45 cm were hanging from the ceiling of a gallery of pit +50 m above sea level of the uranium mine. During a sampling campaign in June 2010, some of them were sampled and transported in sterile boxes to the laboratory for microsensor studies. AMD water, which was dripping down the stalactite-like biofilm was collected in sterile glass bottles. The water was used during the microsensor measurements to simulate the in situ condition in a self-constructed holder for fixing the biofilm vertically. Due to the heterogeneity of biofilms numerous electrochemical and fiber-optic microsensor profiles were recorded starting from the biofilm surface/bulk solution interface. At this position the oxygen concentration profiles measured by electrochemical sensors showed high concentrations of oxygen ( $272.73 \pm 1.36 \mu\text{mol/L}$ ).

Similar values ( $272.27 \pm 6.05 \mu\text{mol/L}$ ) were detected by fiber-optic microsensors. By further penetration of the sensors into the biofilm the oxygen concentrations decreased slightly (Fig. II.2.2).

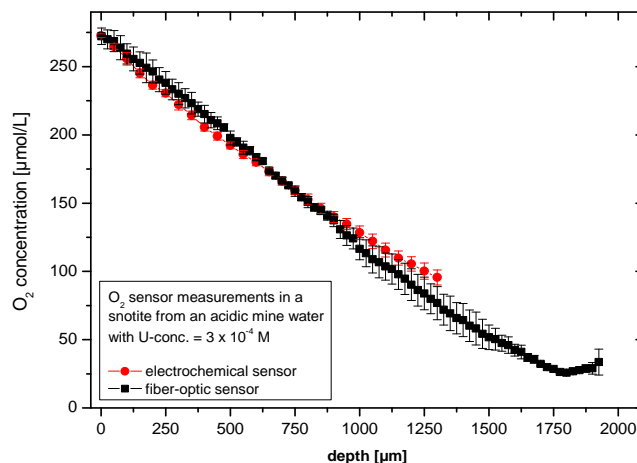


*Fig. II.2.2. Oxygen concentration profiles in a stalactite-like biofilm from the uranium mine Königstein (Germany), exposed to a uranium concentration of  $3 \times 10^{-4}$  mol/L U(VI) in the bulk solution. The data were obtained by electrochemical and fiber-optic microsensor measurements.*

At a biofilm depth of approximately 1.3 mm measurements by electrochemical sensors were stopped and further measurements in deeper layers of the biofilm were avoided due to the risk of destructing the very fragile sensor tip. From the border of the stalactite-like biofilm to this depth, the values obtained by electrochemical sensors were in good agreement with the profiles obtained by fiber optic sensors. At the depth of 1.3 mm  $95.6 \pm 5.56 \mu\text{mol/L}$  oxygen were detected by electrochemical sensors. In contrast, measurements by fiber-optic sensors showed at the same depth a higher oxygen concentration of  $76.76 \pm 12.11 \mu\text{mol/L}$ . We assume that the difference is due to the penetration of the sensors at different locations. Further measurements were performed down to a depth of 1.8 mm by fiber-optic sensors, exclusively. These sensors in general allow measurements in deeper regions of the biofilm, i.e. close to the biofilm/solid surface interface due to their higher stability of the optode against consolidated materials. At a depth of 1.8 mm an oxygen concentration of  $25.74 \pm 0.97 \mu\text{mol/L}$  was detected. Since the following measurements showed an increase of the

oxygen concentration, we were able to locate the centre of the stalactite-like biofilm at a depth of 1.8 mm.

The two independent methods allowed measurements of geochemical relevant gradients of oxygen in very small sample volumes and subsequently also with a high spatial resolution. In case of optode measurements, laser excitation and the two-frequency phase modulation technique allowed the use of miniaturized optodes with tip diameters  $< 10 \mu\text{m}$  without the need to any fluorescence-shielding opaque layer. The use of fiber-optic oxygen microsensors in the field of environmental microbiology is a good alternative to electrochemical microelectrodes, because they can be applied in an almost non-invasive fashion, independent from pH and ionic strength.

### III. Development of amperometric and potentiometric tools for redox measurements

#### III.1 Development of amperometric tools

*Potential internal and external redox indicators for the amperometric determination of redox potentials:* During this work, it was tried to make use of the higher sensitivity of ultramicroelectrodes (UMEs) to measure very low concentrations of redox indicators in order to determine redox potentials by monitoring voltammetrically the concentrations of the reduced and oxidized forms of a redox indicator.

The compounds investigated were compounds likely to be employed in workpackages WP3 and WP4 to provoke redox disturbances (soluble species of selenium and iodide as well as oxygen/oxygen peroxide mixtures), minor electroactive constituents of Callovo-Oxfordian argillite porewater (Fe) or NaCl brines (I, Fe) and potential potentiometric indicators to be added in the system (hydroquinone, quinhydrone).

Investigation of the  $\text{I}_2/\text{I}^-$  and Fe(III)/Fe(II) couples in chloride media: the  $\text{I}_2/\text{I}^-$  couple appeared as an interesting possibility, however, in chloride media the couple to be considered is  $\text{ICl}/\text{I}^-$  or  $\text{ICl}_2/\text{I}^-$ . Problems appeared with the Fe(III)/Fe(II) couple, even in acidic media (pH 3), because of the formation of insoluble Fe(III) species during the Fe(II) that passivate the electrodes surface even if rapid scan rates or pulsed methods are employed.

Hydrogen peroxide is just as well oxidizable as reducible. Its cathodic wave is very close to the reduction of dissolved oxygen, and the two signals cannot be distinguished from each other. In the presence of  $\text{HCO}_3^-$  ions, a strong corrosion current appears that indicates the catalysis of the  $\text{H}_2\text{O}_2$  decomposition by the electrode material.

Selenate ions are not electroactive at a platinum electrode, and the electrochemical kinetics for the selenite ions reduction is quite slow.

All the attempts for the quantitative determination of hydroquinone or quinhydrone, even using very low amounts ( $< 10^{-6}$  M) of these compounds failed because partial passivation of the electrode in relation with adsorption phenomena on the platinum surface. These phenomena remained even when transient voltammetric techniques (rapid cyclic voltammetry, normal pulse, difference pulse or square wave voltammetry) were used.

During our researches for the determination of redox potentials of solutions or suspensions of minerals (COx) by means of the voltammetric determination of soluble electroactive species concentrations using platinum UMEs, we observed that, very often, relatively large currents flow through the UME when it is maintained at the rest potential (OCP) measured beforehand with a classic platinum potentiometric electrode. In this way, especially when the electroactive species are insoluble or their concentration is very low, the difference between the OCP measured potentiometrically, and the potential where effectively no current flows through the UME can reach few hundred millivolts!

*Investigations for finding an effective method complementary to potentiometry:* Investigations of a simple method for determining the potential where effectively no current flow through the indicator electrode were carried out. The method adopted was very close to the "opposition method" used formerly. A high impedance voltammetric detector for chromatography, 10  $\mu$ m diameter platinum UMEs (Pt UMEs) as well as a classic millivoltmeter, a platinum rotating disk electrode (Pt RDE) 2 mm in diameter and a saturated calomel electrode were used. Before each measurement, both types of electrodes, PtRDE and PtUMEs, were wet-polished using abrasive sheets P#2400 and P#4000 then abundantly rinsed with MilliQ water.

First step: the potential that has been previously measured potentiometrically at the PtRDE (P0) is applied to the PtUME through the analog potentiostat with a lower current range of 100 pA full-scale. If the current measured is null, the amperometric determination is in good agreement with the potentiometric one and the procedure stops here. If not, we proceed to the second step. Second step: a voltammetric scan is started from P0 in the negative direction if the current is positive (or in the positive direction if the current is negative). After, we determine the potential (P1) where the voltammetric curve crosses the potentials axis and the PtUME is polished again. Third step: P1 is applied to the PtUME and, if the current measured is null P1 is taken as the redox potential and the procedure stops here. If not, we pass to the forth step. Fourth step: a new voltammetric scan is started from P1 in the

negative or positive direction (according to the sign of the current value) and the potential where the voltammetric curve crosses the potentials axis (P2) is determined and the PtUME is polished again. Fifth step: P2 is applied to the PtUME and, if the current measured is null P2 is taken as the redox potential and the procedure stops here. If not, we go back to the fourth step. The fourth and fifth steps are repeated until the current measured reaches the value zero.

*Tests performed with a series of commercial instrument*: In order to check if the nature of the apparatus used for the potentiometric determinations could have an influence on the measurements performed, a dozen of commercial instruments were tested by measuring the current that flows through the instruments when they operate. Two kinds of experiments were carried out: First, the flowing current was measured by connecting directly a femtoammeter to the instrument under test. Then, an electrochemical cell was inserted in series in the preceding electrical circuit. During the first kind of measurements the presence of oscillations of about 10 nA for the worst instrument and less than 5 pA for the best one (factor of 1000!) were detected. The relatively high currents that flow when certain devices are used, which can polarize the electrodes, must be taken into account during the interpretation of potentiometric measurements.

#### Researches for fabricating ultramicroelectrodes compatible with concentrated brines

When it was tried to make use of the higher sensitivity of UMEs to measure very low concentrations of redox species in concentrated NaCl solutions, the attempts completely failed. Actually, the voltammetric response of UMEs –that perfectly work in diluted media or pure water– becomes completely meaningless once immersed in NaCl brines. Nine platinum UMEs having diameters ranging between 10 and 50 $\mu$ m in NaCl solutions whose concentration varied from 5.84 to 29.22% (w:w) were tested. The UMEs used were either commercial or homemade, and their insulating body was formed of various glasses (Pyrex, soft glass, quartz, quartz suprasil...) or polymeric resins (epoxy, polyester, PTFE). For convenience, dissolved oxygen was used as the main electroactive species but several experiments were also carried out with the model species ferrocene dimethanol. The results achieved with the different UMEs were compared with those obtained using a routine 2mm diameter platinum rotating disc electrode. The voltammetric response of the platinum UMEs that were tested strongly depended on the nature of the insulating material used to make the body of the electrodes. And the more concentrated the solution was, the more the resulting

voltammetric signal was distorted. This distortion was particularly noticeable during the reverse scans. The UMEs that the insulating part was made of "quartz-suprasil" were the less affected by the brines. However, the fabrication of such an electrode was quite difficult because the melting point of platinum (1772°C) and the softening point of quartz-suprasil (~1600°C) are relatively close. The use of platinum wires insulated with PTFE was an interesting alternative but there were problems with their mechanical behaviour and then with polishing. The UMEs were classified as a function of the insulating materials in the following order, from least to most resistant: quartz fiber < epoxy, softglass < polyester, Pyrex < quartz-suprasil, PTFE.

The distortions of voltammograms that were observed when the UMEs were immersed in brines are linked with phenomena occurring at the metal/insulating material interface. The same phenomena must occur when millimetric electrodes are used, but they are not detected because of the much higher distance between this interface and the main surface area of the platinum disc.

One of the major objectives in 2009 was to carry out robust geochemical (Eh-pH) sensor concepts being able to be devoted (after adaptation or development and/or implementation) to the observation and monitoring of the underground components of a nuclear waste storage. These sensors must answer precise specifications related to the requirements and constraints of observation and monitoring of the storage components (geological environment and associated phenomenology). In addition to the technical aspects, the major constraint seems to be the operation life, which will have to be based on the robustness and the perseverance of the principle of the sensors. Among the geochemical parameters to be followed, the most significant are temperature, pH, conductivity, redox potential, the speciation of certain elements, and measurement of H<sub>2</sub>, O<sub>2</sub>, CO<sub>2</sub> and H<sub>2</sub>S. The inventory and the assessment of the currently available methodologies and tools for these parameters indicate that today there are not suitable geochemical sensors for monitoring nuclear waste storing systems. Based on this report, BRGM proposes some realistic pathways of research and development to be initiated to mitigate the lack of geochemical sensors dedicated to the underground storage of nuclear waste. For that purpose, R&D pathways will be the development and manufacture of geochemical sensors made of robust and unalterable material (gold, platinum, glassy carbon). They must possess active principles everlasting, or protected or restored easily.

Moreover, solid-state sensors fabricated with a few component of the argillaceous formations (raw Callovo-Oxfordian argillite (COx ) or purified argillite K119, or pyrite) for measuring pH and redox potential can be designed for use. Response characteristics of these sensors must be tested in aqueous samples with compositions similar to those present inside an underground repository and results were compared with those obtained with commercial electrodes obtaining a good agreement between commercial and the sensors. Electrochemical methods will be in the base of the sensors assessments. These approaches will be consisted in the continuous or semi-continuous analysis of large surface electrodes (pyrite, argillite, ) immersed in solutions with or without oxidant (nitrate, selenate and selenite) or reducer (sulfide,  $\text{Fe}^{2+}$ , ). The electrochemical behavior of these electrodes was compared to those of known inert and unattackable electrodes (Pt, Au, glassy carbon) positioned in the same operating conditions. Measurements realized by voltammetry (at open circuit potential and cyclic voltammetry), by Tafel polarization analysis and by electrochemical impedance spectroscopy (EIS) were used to identify, monitor and compare the electrochemical reactions and kinetics occurring during immersion, both in solution and on the surface of electrodes. The combination of chemical and electrochemical approaches appears to be an appropriate method to investigate the redox reactivity of COx components versus predicted redox perturbations.

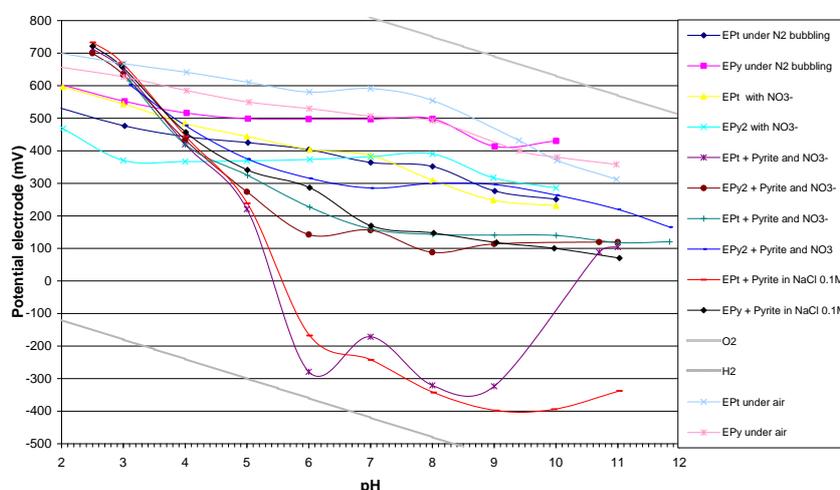
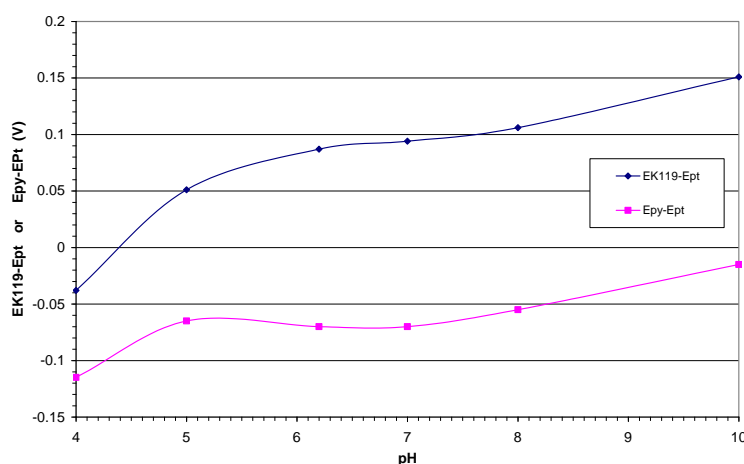


Figure III.2.1: Measurement of free electrode potential of Pyrite and Platinum electrodes immersed in different media (different pH, and presence or absence of nitrate and or pyrite in grains).



*Figure III.2.2: Measurement of the difference of free electrode potential between two couples of electrodes (purified COx and Pyrite versus Platinum electrode) as a function of pH.*

As example, Figure III.2.1 presents the measurements of electrode potentials (versus KCl-Saturated Calomel Electrode, SCE) for Pyrite and Platinum electrodes immersed in different media (different pH and composition). With responses in potential of this type, it is obvious that it will be possible to manufacture systems of solid and robust electrodes where the reference electrode is unnecessary. It will be also possible, provided that the potential difference is known, to deduce the pH of the solution, as it is demonstrated in figure 2.

At BRGM in WP2 another major objective in 2009 was the determination of the redox potential using complementary approaches: geochemical modelling and continuous potential measurements on multi-electrodes. Among other experiments, the ICE was an occasion to put this complementary approach into practice.

*Background and objectives:* Redox potential value  $E_h$  versus Normal Hydrogen Electrode (NHE) is generally approached by voltage measurement between an inert indicator electrode and a reference electrode. Indicator electrodes, that ideally acts as a site for reactions occurring in the local environment by functioning as a source or a sink of electrons without undergoing chemical changes itself, therefore adopts a potential that is determined by the electron demand or availability at its interface with the surrounding solution. In practice, however, numerous problems can arise. Those related to the voltage measurement fall into two categories, (i) those related to the non-ideal behaviour of electrode materials and (ii) those associated to redox species and reactions.

*Problems related to the non-ideal behaviour of electrode materials:* Inert indicator electrodes such as gold (Au), platinum (Pt) or glassy carbon (GC) have been favoured for redox potential measurements but their respective responses depend on both the electrode nature and surface properties. Measurement difficulties associated with indicator electrodes can nevertheless be partly addressed by ensuring suitable electrode preparation (polishing, cleaning, conditioning), and calibration before use. Concerning reference electrodes, Ag/AgCl/KCl<sub>sat</sub> saturated by AgCl<sub>(s)</sub> or Saturated Calomel, they often remain suitable for laboratory work with the appropriate maintenance.

*Problems related to Redox species and reactions:* Two or more redox couples frequently occur in solution, in equilibrium or not. Redox species that are not in equilibrium each other give rise to "mixed potential" measurement. Species involved in irreversible and kinetically slow reactions do not participate in the redox measurement. Those involved in reversible but kinetically slow reactions are responsible for weak and unstable potential signals. It is thus rarely possible to relate the measured  $E_h$  to the activities of reduced and oxidized species present for most actual systems by a single measurement. The purpose of the study was (i) to investigate the semi-continuous monitoring of the redox potential with multi electrodes (Au, Pt and GC electrodes) and (ii) to compare the acquired results with those obtained by geochemical modeling.

*Experimental approach:* The multi-electrode and continuous measurement approaches were considered in order to examine both the stability of the signal and the convergence of various electrode responses in order to be sure that an equilibrium of the system as a whole was obtained. The acquired results were compared to those obtained by geochemical modelling in order to identify the redox reactions that could control the measured potential and to test different hypotheses in order to reconcile, if needed, measured and theoretical values. The robustness of the complementary approaches was investigated in no organic matter content samples, at different ionic strength, where the iron redox-active species dominated the redox reactions. All aliquots were taken from the Ar inert gas glove-box and transferred to the workbench. Transfer, that took less than one minute, was ensured in hermetically closed electrochemical cells ensuring minimum perturbation generated by atmospheric O<sub>2</sub> and CO<sub>2</sub>. Electrochemical cells were placed under Ar bubbling for 3 min before incorporating any electrode. Electrodes immersion was realised under argon bubbling. All measurements were then conducted under gently and continuous stirring with a magnetic stirrer and under argon

atmosphere without bubbling to avoid CO<sub>2</sub> depletion from the samples. pH and temperature were followed by a SenTix 41 pH-electrode from WTW (Germany) with automatic temperature compensation. Potentiometric measurements were performed by a 10 mm-disk shaped Pt electrode (78.54 mm<sup>2</sup>), 2 mm-disk shaped Au electrode (3.14 mm<sup>2</sup>) and a 2 mm-disk shaped Gc electrode (3.14 mm<sup>2</sup>). Each electrode was successively polished with diamond pastes (3 μm and 1 μm), rinsed with milli-Q water and dried before use. Potentials were measured versus SCE, which consisted in a commercial SCE protected with a KCl 3 mol L<sup>-1</sup> junction. Three SCE reference electrodes, that were stored in KCl 3 mol L<sup>-1</sup> when not used, were utilised during experiments: two for the experimental analyses; the third one served as a reference in order to check the drift of the others. The two first electrodes were checked once a day versus the first one. No drift was observed over the four days of experiments. All indicator-electrode potentials were checked at the beginning of each experiment with a redox buffer solution (190 mV/NHE at 23.9°C). Nevertheless, it is worth noting that a problem with the use of such standards reference solutions could be their high poise. As they produce such a stable potential they are probably not capable of distinguishing between small differences in the indicator electrodes performance, such as might arise due to adsorption of chemicals onto the surface of the electrode or the formation of surface oxide layers. Such effects could however have influence the measured potential. Potentiometric measurements were recorded continuously with a data acquisition system (Keithley instruments, 2700 data acquisition system) for 25 minutes at least. PHREEQC geochemical code was used to determine E<sub>h</sub> and aqueous speciation by thermodynamic methods with the appropriate associated Thermodynamic database (THERMODEM® thermodynamic database generated by BRGM). Redox potential calculated values were obtained by speciation measurements given by INE. Redox potential calculated values were obtained from the initials conditions given by INE or speciation measurements, when they were given by PSI. Only two reference solutions are discussed here, *Ref 01 (II/III) b and Ref 02 Na c.*

**Table III.2.1: Initial conditions as well as experimental and geochemical data**

<b>Initial conditions</b>				
<b>Ref 01 (II/III) b:</b> NaCl 0.1 mol L <sup>-1</sup> ; FeCl <sub>2</sub> 10 <sup>-4</sup> mol L <sup>-1</sup> ; FeCl <sub>3</sub> 4.10 <sup>-4</sup> mol L <sup>-1</sup> , pH fixed with HCl (2)				
<b>Ref 02 Na c:</b> NaCl 5 mol L <sup>-1</sup> ; FeCl <sub>2</sub> 10 <sup>-4</sup> mol L <sup>-1</sup> ; FeCl <sub>3</sub> 4.10 <sup>-4</sup> mol L <sup>-1</sup> , pH fixed with HCl (2)				
<b>Experimental measurements</b>				
	<b>Ref 01 (II/III) b</b>		<b>Ref 02 Na c</b>	
T (°C)	23.4		23.9	
pH	2.18		1.1	
Fe(II) (mol L <sup>-1</sup> )*	1 10 <sup>-4</sup>			
Fe(III) (mol L <sup>-1</sup> )*	5.6 10 <sup>-5</sup>			
	E (mV/NHE)	Equilibration time	E (mV/NHE)	Equilibration time
E Pt	697.0 ± 0.1	30 s	690.0 ± 0.4	0
E GC	688 ± 3	12 min	683 ± 2	3 min
E Au	647 ± 1	30 min	666 ± 1	10 min
E <sub>h</sub> *	690.00 ± 0.05			
<b>Geochemical modelling</b>				
E <sub>h</sub> (mV/NHE)	700		-	

\* Results coming from LWM: Laboratory for waste management, PSI, Switzerland

The influence of the ionic strength was investigated in NaCl samples in acidic media (pH fixed to 2), in which processes controlling the concentration of the redox sensitive elements are kinetically fast reactions, and thus shorter stabilization times should have been encountered. Figure III.2.3 presents the experimental measurements versus time obtained in *Ref 01 (II/III) b* and *Ref 02 Na c* samples. Table III.2.1 summarizes pH, temperature, Fe speciation measurement as well as equilibrium (E<sub>h</sub>) and calculated (by geochemical modeling) potentials from the given samples. It is worth noting that no Pitzer database was

available for Fe(III), therefore, activity coefficient correction was carried out. Consequently, thermodynamic calculation was not achieved for *Ref 02 Na c*.

Potential voltages obtained by the others partners who investigated measurements into the glove box are also given. All potential values are expressed in Volt (V) with respect to the NHE.

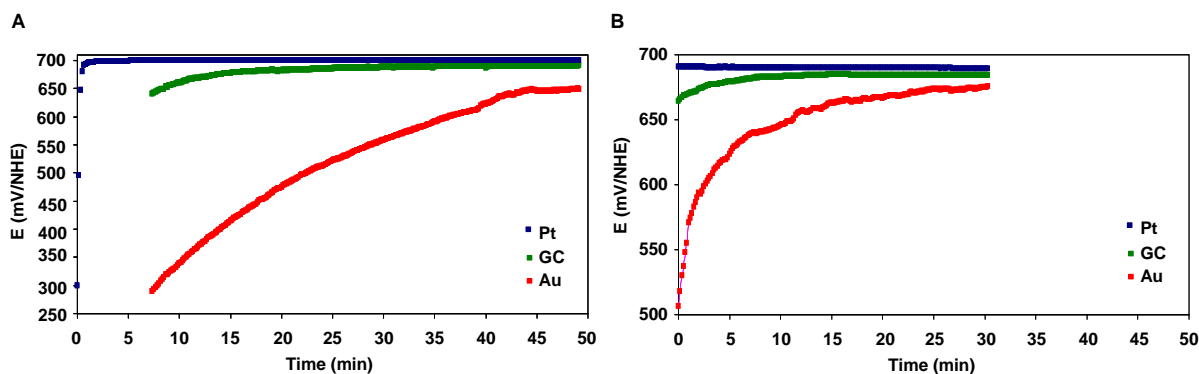


Figure III.2.3: *Ref 01 (II/III) NaCl (0.1 mol L<sup>-1</sup>) and Ref 02 Na c (5 mol L<sup>-1</sup>) multi-electrode potential voltage (Eh (V/NHE)) versus time.*

As expected, potential stabilization times fluctuated as a function of electrode nature and sample composition. In comparison with Au or GC electrodes, Pt electrode stabilization time was generally faster. Indeed, platinum has the higher exchange current density (10 mA/cm<sup>2</sup> in comparison to 0.3 mA/cm<sup>2</sup> for Au), leading to a reasonable response time. Moreover, the higher the conductivity the faster the stabilization time. During the experiments, the general convergence of the stabilization potential of all the immersed inert electrodes demonstrated (i) the outcome of an equilibrium state under the experimental conditions and (ii) the interest in using multiple inert electrodes in order to ensure measurement reliability. It is worth noting that the equilibrium potential was not or little influenced by NaCl concentration. Potential voltages were comparable to those obtained by other partners (see table 1). Potential voltages are in a good agreement with the geochemical modelling: Fe(II) and Fe(III) concentrations were controlled by equilibrium between aqueous Fe(II) and Fe(III) species. Measurements, geochemical modeling as well as “speciation measurements” (concentrations in solution, identification of precipitated solid etc...) are necessary for redox determination and interpretation. The interest in continuous monitoring of voltage measurements using multiple redox electrodes has clearly been demonstrated to ensure reliable qualitative measurement.

## WP3. Redox response of defined and near-natural system

### 1. Response of crystalline environment to redox perturbation

#### a. Redox Eh - pH pair field measurements and computations (UNIZAR)

The work carried out on this topic by the Geochemical Modelling Group of the University of Zaragoza (UNIZAR) is based on the observations and interpretations done in the two sites proposed in Sweden for hosting a deep repository for spent nuclear fuel: Forsmark and Laxemar-Simpevarp, in the eastern coast of Sweden. The general description of the Swedish candidate sites for underground deep disposal of nuclear waste has been extensively provided elsewhere (Ström *et al.*, 2008; Laaksoharju *et al.*, 2008). For the explorative analysis and modelling of the redox systems in Forsmark and Laxemar-Simpevarp, two types of data are considered in this work: 1) selected hydrochemical groundwater data from packed sections of core-drilled boreholes covering a wide range of depths and representative of the different hydrochemical conditions and 2) potentiometrically-measured Eh by using the sophisticated methodology developed by SKB (already presented in Auqué *et al.*, 2008 and Gimeno *et al.*, 2009a, among others). The measurement and selection of both types of data and the procedures for ensuring their quality and representativity are a major concern and have already been presented elsewhere (Gimeno *et al.*, 2009b and references therein). With regard to the potentiometric Eh measurements, they can have both technical and interpretative problems (Auque *et al.*, 2008 and references therein). These problems are, among others, the existence of mixed-potentials, the presence of non-electroactive species, problems of electrode poisoning, presence of low concentrations of redox species or lack of electrochemical equilibrium. SKB has developed over the last 25 years one of the best available methodologies for the measurement of this parameter (e.g. Grenthe *et al.*, 1992; Christensen *et al.*, 2000; Auque *et al.*, 2008 and references therein) and its careful use is, at the very least, extremely helpful information for the study of something as complex as the redox system. The SKB methodology for the potentiometric measurement of Eh in deep groundwaters is based on an integrated system for: (1) sealing off a borehole section by inflatable packers and pumping of groundwater from the section; (2) sampling of pumped

groundwater as well as sampling *in situ* in the section to obtain groundwater samples at maintained pressure and (3) on-line long-term measurements (weeks or months; in this last case, usually with several logging periods) of chemical and physical parameters in the unbroken sample water line both at the surface and at depth downhole. Eh is measured and logged simultaneously by three different electrodes (gold, platinum and glassy carbon electrodes) downhole as well as at the surface, against Ag/AgCl double junction gel-filled reference electrodes in both cases. Together with Eh, each probe measures pH and water temperature and the cell at the surface measures also electrical conductivity and dissolved oxygen. This allows checking whether Eh variability is related to variations in the chemical composition of the waters, which makes easier the selection of Eh-values. From a careful analysis of these logs an Eh value for the groundwaters from the borehole section can be determined. The continuous logging of the redox potential during weeks allows the attainment of stable readings in waters with low concentrations of the redox active species. Moreover, coincident measurements obtained by different electrodes corroborate the existence of electrochemical equilibrium. Hence, those values can be used as reference in geochemical modelling. In order to ensure the quality and representativeness of the potentiometrically measured Eh values, these values are only accepted for explorative or modelling purposes when corresponding to logs longer than 3 days that produce stable and coincident readings (in a range smaller than 50 mV) by at least two electrodes in the long term and that have simultaneous and stabilised pH logging (to minimize the uncertainty associated with the pH). The results obtained by applying this methodology to the study of the Forsmark and Laxemar-Simpevarp groundwater systems indicate that Eh values range from -143 to -281 mV in Forsmark and from -210 to -310 mV in Laxemar-Simpevarp. Even though Eh-pH plots show a general trend of decreasing Eh values as the pH increases, no clear trend with depth is observed. This behaviour was already noticed by Nordstrom and Puigdomenech (1986) in their work on different Swedish groundwaters down to 600 m depth but it is clearly different to the observed evolution in Palmottu, Finland (where a similar measurement methodology has been applied) and in most aquifers elsewhere, where a marked decrease of redox potential is observed as the residence time and depth of the waters increase (e.g. Drever, 1997; Blomqvist *et al.*, 2000). All the Eh values from both studied sites are located in a clearly reducing zone, even for the samples in the shallowest parts of the systems, where possible perturbations of the original redox environment may have taken place during the measurements. This would indicate the redox-buffering ability of

microbial or water-rock interaction processes. Moreover, most of the measured Eh values are in the range defined by Drever (1997) for groundwaters buffered by sulphate-reduction. There is a strong heterogeneity in the distribution of Eh data with depth both in Forsmark and in Laxemar-Simpevarp. This behaviour could be the result of a modification in the original redox state in some groundwaters (perturbation of the system). But, most probably, it can be the consequence of the complex hydrological setting and palaeohydrogeological evolution of the Laxemar-Simpevarp area, where the redox-sensitive elements, the potentials calculated from redox couples or the microbiological populations do not show a clear trend with depth either. Calculated Eh values for both studied systems have also been obtained with the assistance of the PHREEQC code and using a modified version of the WATEQ4F database; Parkhurst and Appelo, 1999, Ball and Nordstrom, 2001, Gimeno *et al.*, 2009b). As also described in similar systems elsewhere in the Scandinavian Shield (see Gimeno *et al.*, 2008, 2009b and references therein), the calculated redox pairs that have performed better among the many considered for Laxemar-Simpevarp and Forsmark have been the dissolved  $\text{SO}_4^{2-}/\text{HS}^-$  and  $\text{CO}_2/\text{CH}_4$  redox pairs, and the heterogeneous couples  $\text{Fe}^{2+}/\text{Fe}(\text{OH})_3$ ,  $\text{HS}^-/\text{S}_{(c)}$ ,  $\text{SO}_4^{2-}/\text{FeS}_{\text{am}}$  and  $\text{SO}_4^{2-}/\text{pyrite}$ . The calculated potential for most of these pairs usually agree within a range of  $\pm 50$  mV with the potentiometrically measured Eh values, except for  $\text{HS}^-/\text{S}_{(c)}$  which systematically provides higher potential values (Gimeno *et al.*, 2009b) and they do not show any clear trend with depth.  $\text{Fe}^{2+}/\text{Fe}(\text{OH})_3$  is completely reasonable as ferric oxyhydroxides (mainly hematite) have been found in the fracture fillings and it is an electroactive pair for potentiometric measurements. The calculated Eh values are generally within the range of values obtained by assuming a clearly crystalline iron oxyhydroxide (similar to goethite or hematite, where the equilibrium constant proposed by Grenthe *et al.*, 1992 has been used) and assuming a low-crystallinity iron oxyhydroxide (the constant value proposed by Banwart, 1999 is used). This situation is consistent with the expected features in these clearly reducing systems, characterised by the presence of crystalline ferric oxyhydroxides under pristine conditions and long-residence time groundwaters but perturbed during the brief oxygen intrusions associated to drilling and sampling activities, which would lead to the precipitation of poorly crystalline ferric oxyhydroxides.

b. Possible controls on measured Eh (UNIZAR)

Once again, the work carried out on this topic by the Geochemical Modelling Group of the University of Zaragoza (UNIZAR) is based on the observations and interpretations done in the two sites proposed in Sweden for hosting a deep repository for spent nuclear fuel: Forsmark and Laxemar-Simpevarp. The present hydrochemistry of groundwaters in these sites is the result of a complex mixing process driven by the input of different recharge waters at least since the last glaciation. As a general trend, in both Forsmark and Laxemar-Simpevarp, there is a more or less clear trend towards more saline waters with depth from the shallowest and more dilute groundwaters to intermediate brackish groundwaters and finally to the deepest and more saline (Laaksoharju *et al.*, 2008a). The possible controls on the measured Eh values have been evaluated by means of redox pairs calculations for both Forsmark and Laxemar-Simpevarp. These calculations have shown that potentiometrically measured Eh values, clearly reducing, are consistent with the calculated redox potentials with the  $\text{Fe}^{2+}/\text{Fe}(\text{OH})_3$  redox couple, with most of the feasible sulphur redox pairs and with the  $\text{CO}_2/\text{CH}^+$  couple. Moreover, the widespread presence of S(-II) (although low) in many of the sampled sections at different depths provide indisputable evidence of microbiological sulphate reduction. These observations are very consistent with the described mineralogy in the bulk rock and in the fracture fillings (e.g. frequent presence of hematite and pyrite) from the Laxemar-Simpevarp deep bedrock system and are indicative of the important role played by the iron and sulphur redox systems in the buffering of its redox conditions.

c. Redox response of Äspö and Grimsel FFMs to oxygen input (CTM)

The nuclear waste repositories are constituted by host-rock systems which can contain iron-bearing mineral phases such as iron sulphides or iron silicates. The redox buffer capacity of the host-rocks and their behaviour under the infiltration of oxidizing groundwaters or other perturbations are of primary importance. In this way, the redox buffer capacity of pyrrhotite and pyrite (which could be present as accessory mineral in igneous rocks) and two fracture filling materials (one from Grimsel and another from Äspö) have been studied. In addition, the condition imposed by host-rock may perturb the redox state of uranium, leading to a immobilization of uranium under its tetravalent form [U(IV)]. With this intention, hexavalent uranium U(VI) has been introduced in a pyrrhotite system to know if the redox environment

imposed by pyrrhotite can lead to the reduction of uranium to its tetravalent state [U(IV)]. During the whole Reosy project, CTM has designed and performed at laboratory scale the studies mentioned, even a data acquisition system was developed to monitor pe/pH remotely, and also has interpreted the results with some modelling with hydromedusa code [Puigdomenech 2009]. Natural pyrrhotite was obtained from Gualba (NE Spain). A characterization of the pyrrhotite sample by X-ray diffraction (XRD) indicated the presence of subordinate amounts of quartz, pyrite, calcite, kaolinite, chlorite, and muscovite. Powder pyrrhotite at a particle size of 100-150 microns and with a specific surface area of 0.83 m<sup>2</sup>/g (determined by BET) was used. Pure natural pyrite (from Arnedo, N Spain) triturated at 100-150 microns with a BET surface area of 0.17 m<sup>2</sup>/g was used in the experiments. The fracture filling materials (FFMs) studied were facilitated by Partner 1. Grimsel FFM and Äspö FFM used were in the fraction 0.5-1 mm and their surface areas were respectively of 0.187 and 0.259 m<sup>2</sup>/g. XRD indicated that both FFMs were composed by quartz, microcline, biotite, albite and muscovite. All experiments were performed in batch reactor with a S/L ratio between 2 and 13 g/l of solid in NaClO<sub>4</sub> 0.01 M at 25°C and 1 atm. Three kinds of experiments have been performed: a) experiments carried out under N<sub>2</sub> atmosphere and perturbed with an oxygen injection, b) experiments started with an initial dissolved O<sub>2</sub> concentration and monitoring its consumption with time (named also EC), and c) experiments carried out under N<sub>2</sub> atmosphere and perturbed with an uranium injection. Type a experiments were performed bubbling N<sub>2(g)</sub>. Type b experiments were performed in the absence of a free gas phase, reducing the volume of the reactor during sampling. Type c experiments were carried out inside a glovebox (Jacomex) with N<sub>2</sub> atmosphere. Continuous monitoring of pH, Eh (Pt and Au electrodes) and dissolved oxygen (DO) was carried out with combined-glass electrodes and with an optical sensor. Calibration of pH and Au and Pt Eh electrodes (Crison, models 5221, 5262 & 5269 respectively) were performed against commercial standard buffers before and after each experiment. Additionally, Eh electrodes were mechanically cleaned before each experiment. DO concentrations were measured only in type b experiments with an optical sensor (Ocean Optics, FoxyOR125GT & red eye) calibrated at two points: 0 % in 20 % Na<sub>2</sub>SO<sub>3</sub> or N<sub>2(g)</sub> and 20.9% in open air. Aliquots were taken at elapsed times to follow the aqueous concentrations of iron (Fe(II) and Fe(total)) by UV-ferrozine method [Gibbs,1996] (Shimadzu, 1600), anions (SO<sub>4</sub><sup>2-</sup>, S<sub>2</sub>O<sub>3</sub><sup>2-</sup>, Cl<sup>-</sup>) by IC with ion suppression (Dionex, ICS2100) and total uranium and trace metals by ICP-MS (Agilent 7500cx). For the U(VI) TRLFS measurements, a Nd:YAG laser (Polaris II, New Wave

Research) was used. Samples were filtered through 0.45  $\mu\text{m}$  pore size filters before analysis. Solid samples examination was done by BET (Micromeritics Flowsorb II 2300), SEM-EXD (ZEISS UltraPlus), XRD ( PANalytical  $\theta/\theta$ ) and XPS (ESCA).

#### *Redox buffer capacity of pyrrhotite*

The evolution of pH and pe as a function of time during one of the type a experiment with pyrrhotite showed that the system evolves from initial values of pH = 6.0 and pe = 6.0 to values of pH = 8.6 and pe = - 5.7 (17 days), thus pyrrhotite buffers the system to these values. If at this point NaOH is added the increase of pH is counteract with a decrease of pe, therefore reaching values of pH = 9.5 and pe = - 7.4, which appear to remain constant after 60 days. In addition, the initial solution is supersaturated with respect to Fe(III) oxyhydroxide, and subsequently evolve towards equilibrium state among FeS (pyrrhotite), Fe(III) oxyhydroxide and the aqueous solution.

#### *Kinetics of oxygen consumption*

In the type b experiments the oxygen evolution as function of time performed with pyrrhotite was monitored. In some cases more than one oxidation cycle has been carried out. Experiments EC137 and EC194 are duplicate experiments for pyrrhotite. The slope of oxygen evolution for these two experiments is quite different for the first oxidation cycle, as well as iron and sulphate concentrations in solution (data not shown). In fact, pyrrhotite dissolution seems to be congruent in experiment EC194 while seems to be incongruent in EC137, where concentrations of sulphate exceed several orders of magnitude those of dissolved iron. This different behaviour can be explained for a different freshness of the pyrrhotite used. By SEM-EDX and XPS techniques, Fe(III) oxyhydroxides have been identified in all pyrrhotite experiments; even three distinctive Fe(III) oxyhydroxides layers have been observed on pyrrhotite surface as consequence of three oxidation cycles. From XRD, goethite has been identified as an iron oxyhydroxide crystalline phase in the final pyrrhotite, however, other different oxidation products, such as  $\alpha\text{-S}_8$  and biothite, have been also identified on the pyrrhotite surface, suggesting a complex mechanism of pyrrhotite oxidation. Chemical analysis of solution also supports complex oxidation dissolution as thiosulphate was determined as another different species involved. It is important to note that measured pe values in these experiments should be considered with caution because they could be result of mixed potentials due to the different redox pairs involved in the system:

O(0)/O(-II), S(-II)/S(VI), and Fe(II)/Fe(III). No significant differences have been observed between Pt and Au electrodes, although a more rapid response of Pt electrodes versus Au electrodes have been observed. A drawback of the combined glass pH/pe electrodes used is the contamination of the solution with KCl coming from the internal electrolyte. Table 1 summarizes the oxygen scavenger capacities calculated as rate of oxygen consumption for experimental data. Table 1 also includes some literature data in order to contrast. It is observed that the pyrrhotite oxidation rate is one or two order of magnitude higher compared with the results from other materials tested (pyrite and the Äspö/Grimsel FFM). Pyrrhotite oxidation rates ranged from  $1.2 \cdot 10^{-7}$  to  $1.1 \cdot 10^{-6}$  molO<sub>2</sub> kg<sup>-1</sup> s<sup>-1</sup>, with an average value of  $5.7 \cdot 10^{-7}$  molO<sub>2</sub> kg<sup>-1</sup> s<sup>-1</sup>. These values are clearly higher than oxidations rates for other sulphides such as pyrite, galena [Acero, 2007] and chalcopyrite [Acero, 2009]; thus highlighting the great oxygen capacity of pyrrhotite.

**Table 1.** Comparison of oxygen consumption measurements performed by CTM with literature data (OC: oxygen cycle).

Reference	Experiment	Material	Oxidation rate (mol O <sub>2</sub> kg <sup>-1</sup> s <sup>-1</sup> )
This work	EC008	Pyrrhotite	$2.5 \times 10^{-7}$
This work	EC070	Pyrrhotite	$1.5 \times 10^{-7}$
This work	EC137	Pyrrhotite	$1.2 \times 10^{-7}$ (1 <sup>st</sup> OC), $1.1 \times 10^{-6}$ (2 <sup>nd</sup> and 3 <sup>rd</sup> OC)
This work	EC194	Pyrrhotite	$1.3 \times 10^{-6}$ (1 <sup>st</sup> OC), $4.8 \times 10^{-7}$ (2 <sup>nd</sup> OC)
This work	EC193	Pyrite	$2.6 \times 10^{-8}$
Sracek 2006		Pyrite	$6.7 \times 10^{-8}$
Domènech 2002*		Pyrite sludge	$2.5 \times 10^{-7}$
Acero 2007*		Galena	$6.7 \times 10^{-8}$
Acero 2009*		Chalcopyrite	$2.0 \times 10^{-8}$
This work	EC175	Äspö FFM	$2.5 \times 10^{-8}$
This work	EC243	Grimsel FFM	$6.7 \times 10^{-9}$
Giménez 2006*		Olivine	$2.1 \times 10^{-8}$

\*: Oxidation rate has been calculated as an average value of the different experiments reported and considering the final BET value in case was indicated in the reference.

The pyrite oxidation rate obtained is slightly lower than the values reported in literature [Sracek, 2006] [Domènech, 2002]. This could be explained by the formation of an oxidation layer (observed by SEM-EDX) on the pyrite surface that would probably passivate the pyrite surface for further reaction. The pH and pe conditions at the end of the experiment (at 1000h) were oxidants with values of 3.5 and 9.2 respectively, which could be indicative that the redox potential is governed by the hydroxide layer. Comparing FFM's oxidation rates, the oxidation rate obtained for the Äspö FFM is higher than the one from the Grimsel FFM. This is attributed to the fact that Grimsel FFM was not received under N<sub>2</sub>-atmosphere, therefore as somehow oxidized material. However, the value of  $2.5 \cdot 10^{-8}$  mol O<sub>2</sub> kg<sup>-1</sup> s<sup>-1</sup> for the Äspö FFM is in perfect concordance with the ones reported for other silicate minerals [Giménez 2006]. In these experiments kinetic dissolution of the minerals is observed. In the case of the Äspö experiment, for example, the steady state is achieved at pH 6.1 and pe 6.4, and at 2000h of experimentation the higher concentrations in solution are attributed to Ca<sup>2+</sup>, Si, NH<sub>4</sub><sup>+</sup> and SO<sub>4</sub><sup>2-</sup> with concentrations of  $1.4 \cdot 10^{-4}$ ,  $3.1 \cdot 10^{-5}$ ,  $2.6 \cdot 10^{-5}$  and  $1.1 \cdot 10^{-5}$  M. Lower concentrations of metals have also been determined: Zn/Al/Ni in 10<sup>-6</sup> M concentration and Mn/Rb/Sr/Pb/Ba in 10<sup>-7</sup> M concentration. One new crystalline phase, clinocllore, has been identified by XRD in the final FFM Äspö solid.

#### *Uranium behaviour under pyrrhotite environment*

Two series of experiments have been conducted adding U(VI) once the pyrrhotite was equilibrated with 0.01 M NaClO<sub>4</sub>. In one series equilibrium pH (around 5.3) was kept, while in the second series pH was adjusted with NaOH at around 7.8. Spikes of U(VI) at three different initial concentrations were considered ( $2 \cdot 10^{-7}$ ,  $6 \cdot 10^{-7}$ , and  $2 \cdot 10^{-6}$ ). In series one, pH and pe remains practically equal after 100 days of re-equilibration time. On the contrary, series two evolves towards pH 6.4 and pe around 1 to equilibrate with Fe<sup>2+</sup> and Fe(OH)<sub>3(s)</sub> phase, thus achieving an equilibrium state different than in type a experiments. In accordance, all iron analyzed in solution is in the form of Fe(II), being its concentration at the end of the experiments around  $4 \cdot 10^{-4}$  M for series one or one order of magnitude below ( $5 \cdot 10^{-5}$  M) for series two. TRLFS measurements have been made in order to check if part of the U(VI) added have been reduced. However, the presence of sulphates, chloride and iron precludes any spectra acquisition due to the quenching effect. In addition, total uranium determination in solution by ICP-MS has showed a decrease of the uranium concentration in experiments. This could be explained by uranium precipitation or sorption on the pyrrhotite

surface. SEM analysis has not been conclusive identifying uranium on pyrrhotite surface, probably due to the detection limit of the EDX technique. However, the experimental data clearly show that U(VI) can not be reduced to U(IV) under the redox conditions achieved.

## 2. Response of clay environment to redox perturbation

### a. Boda claystone: voltammetric characterization (CNRS-Nancy)

A large part of the activities in WP3 were devoted to the electrochemical characterization of clays using three techniques: Voltammetry of Microparticles (VMP), Voltammetry of Microparticles in Thin Layer (VMPTL), and Clay Matrix Voltammetry (CMV). VMP is now quite widespread in the electrochemistry community. It allows the characterization of electroactive microparticles, conducting or not conducting after their immobilization on the surface of a graphite electrode. The VMPTL technique is derived from VMP and has been developed in the laboratory. The device is more much complex than VMP. Its principle consists in entrapping a very small amount of electroactive material and a thin layer of solution between the cross sections of two graphite rods. Therefore, it allows the characterization of the immobilized microparticles and of the soluble species released during their electrochemical transformation and has high sensitivity and resolution. Before the beginning of the Reosy project only a prototype was available. A more elaborate device was constructed but unfortunately, the new device as the prototype were accidentally broken during the test period. A supplemental device was constructed; however, it is still in the finalization phase. Therefore VMPTL was only sparingly employed during the project. CMV was developed during the last year of the project (*paper submitted to Electrochemistry Communications*). Its major advantage is the possibility of almost in-situ characterizing of soils with the only addition of the minimum humidity required for electrolytic conduction. The humidification is provided by a water-saturated argon gas flow.

#### Voltammetric characterization of Boda Albitic Claystone

We have chosen samples from the Boda Albitic Claystone to develop a methodology using VMP for the characterization of soils envisaged for the underground storage of nuclear waste because a recent study performed with Mössbauer spectroscopy (cf. Károly Lazar) has shown the high stability of all the samples examined against oxidation. The voltammograms

recorded using VMP in acidic media with different samples that have been previously characterized by Mössbauer spectroscopy pointed out the voltammetric signals for all the iron containing species, i.e.  $\text{Fe}^{2+}$  and  $\text{Fe}^{3+}$  ions associated with clays and hematite. Moreover, the measurements have allowed us to clear up an uncertainty that remained about the presence of pyrite in certain samples. The cathodic signal for reduction of hematite in certain conditions is split into two peaks. The amount of  $\text{Fe}^{2+}$  and  $\text{Fe}^{3+}$  ions that are released when the clays are immersed in aqueous solutions decreases with time elapsing. And moreover, generally, the higher the acidity the faster is the release. The identification of pyrite can be accomplished using its anodic peak, which is independent of the pH, or the cathodic one that shifts to higher potentials when the pH decreases. In the presence of soluble  $\text{Fe}^{2+}$  ions it is preferable to use the cathodic peak because there is considerable overlap between the signal for  $\text{Fe}^{2+}$  oxidation and the anodic peak of pyrite. Along this study, we were quite bothered by the evolution of the iron (II) containing samples. The evolution of the i-E curves relative to pyrite containing samples with the time elapsed after grinding is impressive: the amount of  $\text{Fe}^{2+}$  ions associated to clays progressively increases, while the signal of pyrite decreases and finally disappears into the peak for  $\text{Fe}^{2+}$  oxidation. The explanation of the observed phenomena probably lies in the adsorption of molecular oxygen on the clay particles after grinding and the size of  $\text{FeS}_2$  particles in the clays. Recently, the characterization of Boda clays with SEM showed that in the most of Boda samples pyrite is present as nanometric particles. This fact explains its high reactivity in aqueous solutions.

#### Voltammetric characterization of Callovo-Oxfordian argillite (COx)

The voltammograms for COx recorded using VMP are simpler than those for Boda clays. The main electroactive species is pyrite that exhibits two peaks: an anodic one at 0.86 V vs. SCE that is not dependant on the pH value and a cathodic peak that is pH dependant (-0.59 V at pH 2, -0.66 V at pH 1 and -0.74 V at pH 0). Iron species associated to clays (essentially Fe(II)) is hardly detectable. The voltammetric curves obtained with the VMPTL device has allowed us to detect the iron species released during the oxidation of  $\text{FeS}_2$  and thus to determine the ratio of the charges required for the oxidation of Fe(II) and S(-I). This ratio argues for the electrooxidation of  $\text{FeS}_2$  into sulphur oxyanions. The i-E curves for "dry COx" recorded with the CMV device also show the presence of soluble Fe(II) and pyrite that are both quantitatively oxidized. If successive cycles are performed, additional signals appear on the voltammetric curves. Their interpretation requires further investigations. Chlorite and

glaucinite minerals as well as kerogen issued from CO<sub>x</sub> were also characterized electrochemically in this part.

b. Boda claystone: response to redox perturbation (II-HAS)

Redox responses of Boda Claystone were investigated under i/ natural, and ii/ artificial conditions. The changes in the redox state of stone were followed by monitoring the Fe<sup>2+</sup>/Fe<sup>3+</sup> ratios in clay minerals (predominantly in chlorite) and comparing their portions to the amount of hematite present in the sample.

1. On natural systems the effects of conditions of diagenesis and influence of weathering were demonstrated. The effects of conditions of diagenesis were demonstrated by comparing the amounts of chlorite with the amounts of hematite in samples obtained from strata formed under different conditions. The exclusive iron bearing mineral was only chlorite and it contains iron exclusively in ferrous form in the strata formed under reducing conditions. In further layers, hematite is the main mineral containing the larger part of iron. Additionally, in chlorite and other clay minerals iron occurs both in Fe<sup>3+</sup> and Fe<sup>2+</sup> forms. Effects of weathering were studied on samples collected from Boda Claystone strata located close to ground surface, thus the surface layers were exposed to weathering. Samples were collected from different distances from the surface. The effects of weathering were followed by measuring the Fe<sup>2+</sup>/Fe<sup>3+</sup> ratios in clay mineral (chlorite). The phenomenon was clearly demonstrated, in the top ~ 20 m thick layer the Fe<sup>2+</sup>/Fe<sup>3+</sup> ratio in the chlorite decreased continuously by approaching the surface.

2. Effects of redox treatments in aqueous media were also studied under two conditions. i) ***Influence of various oxidants*** on Fe<sup>2+</sup>/Fe<sup>3+</sup> ratios were measured in samples containing iron mostly in chlorite, in ferrous form. The exposure to oxidants was 10 days, the oxidants were hydrogen peroxide, hypochlorite and perchlorite anions. No effect of treatments could be detected. ii) ***Influence of reducing agents*** was also studied on samples containing iron in ferric form partly in chlorite and in hematite. Hydroxyl-amine, hidrazine, formaldehyde and dithionite agents were used. The first three reagent did not have any influence on the original Fe<sup>2+</sup>/Fe<sup>3+</sup> ratio. The latter agent reacted with hematite. The amount of this mineral constituent was decreased significantly by a reductive dissolution, significant part of iron could be found in the aqueous solution. Further on, a part of reduced ferrous hydrated iron

ions was taken back to the solid phase by incorporation them into novel sites which were not present formerly in the starting minerals.

c. COx claystone: characterization by new voltametric techniques (BRGM)

Particular equipment has been purchased and methodology has been developed and/or adapted for the investigation (in WP2), including the design of various specific electrodes and the use of diverse electrochemical techniques, in order to explore the electrochemical kinetics of the COX system in contact with different plausible redox perturbations (e.g. nitrate plume, contact with atmosphere before the closure of the system, H<sub>2</sub> perturbation...). Material under investigation includes massive and/or paste claystone rock samples (COx) as well as individual mineral contributors to the redox reactivity already identified in the media, provided we could meet the necessary conductivity limits (e.g. pyrite, clay paste, Fe(II) clays included chlorite, sorbed Fe(II) on various surfaces, sphalerite,..) (Ignatiadis, 2009; Ignatiadis et al., 2010).

d. COx claystone: characterization of natural OM/kerogen (INE)

Studies on natural claystone organic matter by partner KIT-INE were twofold and focused on a) the characterization of the organic matter carbon functionality and its radiation sensitivity as well as b) the isolation of the kerogen and the characterization of redox sensitive groups. Kerogen extractions performed on Opalinus Clay (OPA) revealed > 78 wt. % organic matter, using the extraction protocol established in the petroleum industry (Vandenbroucke and Largeau, 2007) with pyrite impurities in the range of ~12 wt. % . Throughout the project different extraction protocols were tested to isolate the sedimentary organic matter (Grasset et al., 2010) or to mimic the clay-organic interaction by synthesis using the Maillard reaction (Vilas et al., 2010). Spectroscopic Fe L-edge studies on the isolated kerogen of the Callovo-Oxfordian argillite (COx) and OPA showed predominantly ferrous iron and sulfur K-edge measurement a majority of reduced sulfur species. We have observed that kerogen is a minor component in the OPA system (Schäfer et al., 2009a), but this organic pool through the strong association with pyrite and organo- bond sulfur contributes to around 50% of the total redox buffer capacity (TRC) of ~4 meq/g. The second activity focused on the redox perturbation through  $\gamma$ -irradiation. Synchrotron based (C-, K-, Ca-, O- and Fe-edge XANES) scanning transmission X-ray microscopy (STXM) and FT-IR microspectroscopy was used to identify under high spatial resolution the distribution of clay-organic matter with different

functionality using principal component and cluster analysis (Schäfer et al., 2009a; Schäfer et al., 2009b). After radiation of 1.7GGy under helium atmosphere the same rock sample area (COx) was investigated for radiation damage. Radiation damage in the smectite and illite–MLM associated organic matter is comparably low with 20–30% total oxygen mass loss and 13–18% total carbon mass loss. A critical dose  $d_c$  of 2.5GGy was calculated under room temperature conditions. C(1s) XANES show a clear increase in C=C bonds especially in the illite–MLM associated organics. This results suggests a combination of the formation of C=C bond due to crosslinking via polymerization and mass loss due to bond breaking (scissioning) in the main chain or in side groups of the organic macromolecules upon irradiation. Further studies under more relevant conditions (e.g., presence of porewater) are underway to draw final conclusions on radiation induced changes of kerogen/bitumen present in potential high-level nuclear waste host rock formation.

e. COx claystone interactions with soluble I and Se species (CNRS-Nancy)

*Anaerobic conditioning of COx samples with soluble iodine and selenium species*

Solution aliquots were sampled during the conditioning and analyzed by ICP-AES, ion chromatography and UV-visible spectroscopy. After reaction, the COx particles were separated from the liquid phase, rinsed, dried and then characterized voltammetrically. Sorption experiments were performed in the dark, at room temperature and under argon atmosphere with 0.5% (w:w) solid/liquid ratio. COx lumps, instead of powder, were used in order to limit the oxidation of the clay by the atmospheric oxygen. The suspensions were stirred by means of a come and go movement shaker. The conditioning of COx suspensions has been performed at 'natural' pH and without pH control in the following conditions:  $[I^-] = [IO_3^-] = [SeO_3^{2-}] = [SeO_4^{2-}] = 1$  or 0.1 mM; with elemental iodide, we used a saturated  $I_2$  solution (solid  $I_2$  was always present) or the liquid phase sampled from an iodine suspension in 1 mM  $I^-$ . After reaction, the solid particles were taken out, washed with deaerated osmosed water, filtered or centrifuged, and then characterized by different techniques.

f. Calcite interaction with Fe(II) and Se(IV) (CNRS-Grenoble)

*1. Sorption and catalytic oxidation of Fe(II) at the calcite surface*

In this study, the effect of sorption and co-precipitation of Fe(II) with calcite on the kinetics of Fe(II) oxidation was investigated. After 24 h, Fe(II) sorption isotherm depicts the S-shape

curve typical of a continuum between adsorption and co-precipitation processes. A Langmuir type adsorption predominates at low Fe(II) aqueous concentrations, while a surface coprecipitation process dominates at higher concentration. The curve inflection points lead to a concentration of surface functional groups of  $4.0 \times 10^{-6} \text{ mol g}^{-1}$ , i.e. 1.0 sites  $\text{nm}^{-2}$ , in coherence with site density values reported in various structural and spectroscopic investigations. The sorption of Fe(II) on calcite occurred in two distinguishable steps: a rapid adsorption step (seconds–minutes) was followed by a slower incorporation (hours–weeks). The incorporated Fe(II) could not be remobilized by a strong complexing agent (phenanthroline or ferrozine) but the dissolution of the outmost calcite layers with carbonic acid allowed its recovery. Based on the results of the dissolution experiments, a stoichiometry of 0.4 mol% Fe:Ca and a mixed carbonate layer thickness of 25 nm (after 168 h equilibration) were estimated. Fe(II) sorption on calcite could be successfully described by a surface adsorption and precipitation model (Comans & Middelburg, 1987) and surface complexation modeling (Van Cappellen et al., 1993; Pokrovsky et al., 2000). The surface complex model required the consideration of two adsorbed Fe(II) surface species,  $> \text{CO}_3\text{Fe}^+$  and  $> \text{CO}_3\text{FeCO}_3\text{H}^0$ . For the formation of the latter species, a stability constant is being suggested. The oxidation kinetics of Fe(II) in the presence of calcite depended on the equilibration time of aqueous Fe(II) with the mineral prior to the introduction of oxygen. If pre-equilibrated for  $>15$  h, the oxidation kinetics was comparable to a calcite-free system ( $t_{1/2} = 145 \pm 15$  min). Conversely, if Fe(II) was added to an aerated calcite suspension, the rate of oxidation was higher than in the absence of calcite ( $t_{1/2} = 41 \pm 1$  min and  $t_{1/2} = 100 \pm 15$  min, respectively). This catalysis was due to the greater reactivity of the adsorbed Fe(II) species,  $> \text{CO}_3\text{FeCO}_3\text{H}^0$ , for which the species-specific rate constant was estimated. The effect of oxygen addition on the Fe(II)–calcite system was investigated. The presence of calcite accelerated Fe(II) oxidation relative to an equivalent calcite-free system. Based on a surface complexation model, and in analogy to the study by King (1998) about the acceleration of the Fe(II) oxidation by carbonate species (in particular by the species  $\text{Fe}(\text{CO}_3)_2^{2-}$ ), the species-specific oxidation rate constant for the surface species  $> \text{CO}_3\text{FeCO}_3\text{H}^0$  was determined,  $\log k(> \text{CO}_3\text{FeCO}_3\text{H}^0) = 0.72 \pm 0.15 \text{ M}^{-1}\text{s}^{-1}$  at  $I = 0$ . However, if Fe(II) and calcite were equilibrated several hours before exposure to oxygen, the measured oxidation rate constant was lower than in the absence of calcite. These results suggest that Fe(II) is progressively incorporated in the calcite lattice, where it is no longer susceptible to oxidation. In both

cases, the measured oxidation rate constants could be reproduced by speciation and kinetics calculations (not shown).

## 2. Sorption and Fe(II)-induced reduction of selenite at the calcite surface

The findings of the present investigations are directly linked to key geochemical processes that govern mobility of toxic Se in the environment. The anoxic groundwater is often oversaturated with respect to calcite, leading to the formation of various Fe(II) bearing calcites. Depending on whether sorbed Fe(II) is located on the surface or in the bulk of calcite will condition its reactivity and thus the reactive transport of Se. The reactivity of Fe(II) sorbed on calcite can also be used in engineered permeable reactive barriers (PRBs) using Fe<sup>0</sup>, which induce the release of a large amount of Fe(II) and, due to the resulting pH increase, the precipitation of carbonate minerals. The Fe-rich calcite produced therefore an in situ Se attenuation mechanism which applies both to PRB treatment of contaminated sites and to nuclear repositories where canister corrosion releases Fe(II) while calcite is formed due to (i) the interaction between bicarbonate-rich groundwater and cement phases, (ii) the in situ degradation of organic waste components, and (iii) the microbial process in cement in the repository. Results of this work are also applicable to further investigations on the mobilization/immobilization of other redox-sensitive contaminants like As, Cr, Tc, U, and Np. The reductive immobilization of Se(IV) by micrometer-sized (100 - 200 µm) calcite containing sorbed or co-precipitated Fe(II) was investigated at pH 7 under anoxic conditions ( $O_2 < 1$  ppmv) using X-ray absorption near-edge structure (XANES) spectroscopy to determine the reaction products. The Se(IV) sorption on calcite increased in the presence of sorbed Fe(II) compared to that of Fe-free pure calcite. XANES spectra of Se K-edge shows that, within 24 h, nearly half of the total Se(IV) was reduced to Se(0) by Fe(II) sorbed on calcite. The extent of reduction decreases with increasing the equilibration time of the calcite with Fe(II) solution, before Se(IV) addition. The combined results of field emission scanning electron microscopy and x-ray diffraction have shown that needle-shaped red monoclinic elemental Se, with diameters of 30 - 50 nm and lengths of up to 100 nm, precipitated on the calcite surface. On the other hand, Fe(II) co-precipitated calcite did not lead to Se(IV) reduction within 72 h. The non reactivity is attributed to the incorporation of Fe(II) into the calcite structure, by cation substitution. XANES spectra in the present study provides evidence of reduction from Se(IV) to Se(0), the possibility of iron selenides (e.g., FeSe<sub>2</sub>, Fe<sub>7</sub>Se<sub>8</sub>) as Se reduction product cannot be excluded without good quality EXAFS data, which is limited in our study due to the

low amount of sorbed Se (0.02 - 0.2 wt%). Se in solution did not show any reduction of Se(IV) to Se(0) or Se<sup>2-</sup> by aqueous Fe(II) up to 72 h. Therefore, the observed reduction of Se(IV) by Fe(II) occurs only in the presence of calcite surface and is strongly influenced by the location of Fe(II) on or in calcite and to a lesser extent by the pre-equilibration time of calcite with Fe(II) solution. Such understanding is important to predict the transport, transformation, and attenuation of Se in subsurface and in nuclear waste repositories.

### 3. Role of Fe/S system in buffering redox

#### a. Reduction by Hydrogene of pyrite into pyrrhothite (BRGM)

Nuclear waste repositories are being installed in deep excavated rock formations in some places in Europe to isolate and store radioactive waste. In France, the Callovo-Oxfordian formation (COx) is a potential candidate for a nuclear waste repository. The COx formation contains pyrite (FeS<sub>2</sub>), which would, a priori, react to Hydrogen gas (H<sub>2</sub>). After the closure of the underground nuclear waste repository, aqueous corrosion of the steel canister and, to a lesser extent, radiolysis of water should produce significant amounts of H<sub>2</sub>. This H<sub>2</sub> can interact with materials from the repository and with the surrounding clay host formation. This work aims at understanding these interactions. Given the mineralogical complexity of clay formation, this work focused on the study of the interaction of FeS<sub>2</sub> alone with H<sub>2</sub>, using electrochemical techniques and the analysis of solutions and interfaces. After pyrite electrodes had been assembled, various electrochemical disturbances were applied to this material (and to platinum for comparison) while it was submerged in a partially reconstituted solution of COx pore water, enclosed in a High Pressure Thermo-Reactor (HPTR) at 90 °C, or in a Low Pressure Thermo-Reactor at 25°C in the absence and in the presence of pyrite grains (particle size between 40 and 63 µm) and H<sub>2</sub> (0 partial pressure or 1 bar). In addition to the electrochemical behaviour of the platinum and the pyrite, the pH, temperature and pressure of the liquid medium were monitored. The principal result of this work is the elucidation of the mechanism governing the reduction of the sulphur S<sup>0</sup> of the FeS<sub>2</sub>. Indeed, at 90°C, the S<sup>0</sup> is reduced to sulphide (HS<sup>-</sup>/S<sup>2-</sup>), which is freed in solution, whereas the pyrite turns superficially into pyrrhotite (FeS<sub>1+x</sub> with 0<x<0.125), forming a layer that slows down the reduction process (Betelu et al., 2012). At 25°C the S<sup>0</sup> is metastable and simultaneously reduced to sulphide and oxidized to thiosulphate, both are freed in solution, whereas the pyrite turns superficially into pyrrhotite (Ignatiadis et al. 2012). All of the measurements

agree, and the qualitative exploitation of these data (open circuit electrode potential, Tafel curves, and electrochemical impedance measurements on platinum and pyrite electrodes) and surface analyses, made it possible to provide evidence of the reduction of pyrite into pyrrhotite and to create a large electrochemical database. The future exploitation of this electrochemical database will make it possible to determine the kinetics of the reaction of reduction of pyrite by  $H_2$  in a HPTR and in a LPTR and, by extrapolation, to storage conditions.

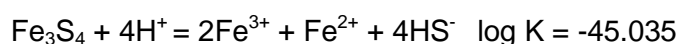
*b. Reduction by pyrite of nitrate, selenite and selenate: electrochemistry (BRGM)*

Abiotic pyrite reactivity versus nitrate, selenate and selenite using chemical and electrochemical methods. The main objective of this work is the sound understanding of redox phenomena controlling the long-term release/retention of radionuclides in nuclear waste disposal and providing tools to apply the results to performance assessment/safety case. Redox is one of the main factor affecting speciation and mobility of redox-sensitive radionuclides. Thus, it is of a great importance to investigate the redox reactivity of the host radioactive waste formations, particularly when exposed to redox perturbations. Callovo-Oxfordian formation (COx), a clay rock known as an anoxic and reducing system (Gaucher et al., 2004), was selected in France as the most suitable location to store nuclear waste. Iron (II) sulfide, mostly constituted of pyrite ( $FeS_2$ ), iron (II) carbonate, iron(II) bearing clays and organic matter are considered to account almost entirely for the total reducing capacity of the rock. We report here the redox reactivity of pyrite upon exposure to nitrate (N(V)), selenate (Se(VI)) and selenite (Se(IV)) that possibly occur in the nuclear storage. Both, chemical and electrochemical kinetic approaches were simultaneously conducted such as to (i) determine the kinetics parameters of the reactions and (ii) understand the kinetic mechanisms. In order to reach similar conditions that are encountered in the storage system, all experiments were realised in NaCl 0.1 M, near neutral pH solutions, and an abiotic glove box ( $O_2$  less than  $10^{-8}$  M). Chemical approach has consisted to set in contact pyrite in grains with solutions containing respectively nitrate, selenate and selenite. Reactants and products chemical analyses, conducted at different contact times, allowed us to assess the kinetics of oxidant reduction. Electrochemical approach has consisted in the continuous or semi-continuous analysis of large surface pyrite electrodes immersed in solutions with or without oxidant (nitrate, selenate and selenite). The electrochemical behavior of these electrodes was compared to those of known inert and unattackable electrodes (Pt, Au, glassy carbon)

positioned in the same operating conditions. Measurements realized by voltammetry (at open circuit potential and cyclic voltammetry), by Tafel polarization analysis and by electrochemical impedance spectroscopy (EIS) were used to identify, monitor and compare the electrochemical reactions and kinetics occurring during immersion, both in solution and on the surface of pyrite electrodes. The nitrate and nitrite evolutions during pyrite-nitrate chemical interaction versus time were monitored. With a rate equation of the type  $-d[\text{NO}_3^-]/dt = k [\text{NO}_3^-]^n$ , our results give an order  $n$  equal to zero and a kinetic constant  $k$  equal to 0.015 mM/day, demonstrating the slow denitrification kinetics in anaerobic conditions. A comparison between our kinetics and those of the literature show that (for Le Bideau (1996)  $n=0$ ,  $k=0.005$  mM/day; for Postma et al. (1991)  $n=0$ ,  $k= 0.1$  to  $0.32$  mM/day; for Pauwels et al. (1998)  $n=1$ ,  $k=1.61$  to  $4.83$  mM/day) our  $k$  value is 3 times greater than the one obtained by Le Bideau (1996), probably due to our greater pyrite grains specific surface. It is worth noting that our kinetic experiment will be continued during one year. Tafel polarization analysis and EIS were used to determine the corrosion rates and charge-transfer resistances associated with  $\text{NO}_3^-$  removal by  $\text{FeS}_2$ . Although  $\text{NO}_3^-$  is an oxidant,  $\text{FeS}_2$  oxidation rates were not proportional to the aqueous  $\text{NO}_3^-$  concentrations due to anodic control of  $\text{FeS}_2$  oxidation. Results obtained confirm the slow kinetics of denitrification by  $\text{FeS}_2$  and show that the zero order removal kinetics can be explained by anodic control of  $\text{FeS}_2$  oxidation and the concomitant anodic control of  $\text{NO}_3^-$  reduction. Contrary to the results obtained with nitrate and in agreement with those reported in literature (Myreni et al., 1997), both selenate and selenite reductions by  $\text{FeS}_2$  grains (pH 4.5-5.0) prove to be fast reactions. With a rate equation of the type  $-d[\text{Se(IV)}]/dt = k [\text{Se(IV)}]^n$ , our preliminary results gave an order  $n$  equal to 1 and a kinetic constant  $k$  equal to  $2.0 \cdot 10^{-5} \text{ s}^{-1}$ . Similar order and kinetic constant were obtained for Se(VI) reduction. However, it is worth noting that, Naveau et al., 2007 have established the pH dependence of Se(IV)- and Se(VI)-adsorption on pyrite surfaces. Electrochemical measurements are thus in progress to appreciate the different redox and adsorption-desorption processes for Se(IV) and Se(VI) and to establish these mechanisms at the pyrite surface. The combination of chemical and electrochemical approaches appears to be an appropriate method to investigate the redox reactivity of COx components versus predicted redox perturbations.

c. Reduction by natural pyrite and synthetic nano-sized pyrite/greigite mixture of selenite: spectroscopy (CNRS-Grenoble)

Nano-pyrite was synthesized upon reaction of  $\text{FeCl}_3$  and  $\text{NaHS}$  in the ratio of 1:2. Following this protocol, 28% of greigite ( $\text{Fe}^{2+}\text{Fe}^{3+}_2\text{S}_4$ ) was found in the solid phase. Greigite is an important precursor for pyrite formation, and its occurrence in the present study may originate from  $\text{HS}^-$  loss during the synthesis. Batch reactor experiments were performed upon adding selenite or selenate to the nano-sized pyrite-greigite suspension at different pH values and with or without the addition of extra  $\text{Fe}^{2+}$ . Both XANES and EXAFS (not shown) spectroscopy revealed, for the first time, the formation of ferroselite ( $\text{FeSe}_2$ ), the thermodynamically most stable species, as the predominant reaction product along with elemental Se. The nucleation and growth of  $\text{FeSe}_2$  is believed to occur at the nano-pyrite/greigite surface via several steps and reaction kinetics and aging time may play a significant role. The present study demonstrates that, in  $\text{Fe}^{2+}$ /sulfide-bearing environment, Se can be immobilized in its most insoluble form, which leads to its reduced mobility in the environment. Thermodynamic modeling was performed with PHREEQC software package. The equilibrium constant for greigite was obtained from the Wateq4f database with the following equation:



The results of the calculations for pyrite suggest that under acidic to neutral condition  $\text{Se}(0)$  is the unique/predominant reaction product, while, in the neutral to slightly alkaline range,  $\text{FeSe}_2$  becomes the thermodynamically favored species with approximately the same molar fraction of  $\text{Se}(0)$ . In strongly alkaline conditions, part of the  $\text{Se}(0)$  can further be reduced to  $\text{HSe}^-$ , leading to  $\text{FeSe}_2$  as the predominant solid species. For greigite, PHREEQC calculations indicated that  $\text{FeSe}_2$  is the main equilibrium product, except at acidic ( $\text{pH} < 4$ ) and strong alkaline ( $\text{pH} > 12$ ) conditions, where elemental Se and  $\text{FeSe}$  become the predominant species, respectively. Therefore, the observation of  $\text{FeSe}_2$  formed on the pyrite-greigite nanocomposite in the pH range of  $\sim 5.9$  to  $\sim 10.3$  considered in this study is thermodynamically allowed. Both thermodynamic calculations and experimental observations (spectroscopic and aqueous analysis) indicate that pyrite can significantly attenuate the mobility of Se by reductive precipitation. This study reports the abiotic formation of  $\text{FeSe}_2$  in

laboratory experiments for the first time, suggesting that stabilization of selenium in its most insoluble form is possible in Fe<sup>2+</sup>/sulfide-bearing environment.

d. Oxidation of pyrrhotite and pyrite by oxygen: kinetics (Amphos)

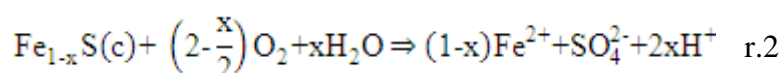
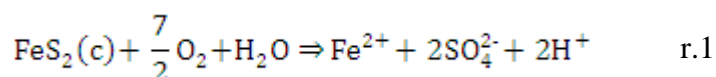
In the context of the stability of the waste radioactive repositories, the study of the redox state of the system is one of the most fundamental aspects. The spent nuclear fuel is mainly composed by UO<sub>2</sub>, and its corrosion increases with the redox potential (U(VI) species are mobile in contrast with the U(IV) species, which are preferentially retained into solid phases). To typical depths of repositories, groundwater shows reducing conditions. But certain geochemical and hydrological processes can generate oxidizing species (flow through open fractures, dissolution of Mn-carbonates, among others). For this reason, in the repository designs, it is essential to characterize the redox buffer capacities of the host-rock. In this way, some geological environments and mineral paragenesis have been studied related to its redox buffer capacity. The main task within the WP3 of RECOSY project of Amphos21 has been focused on the role of Fe/S system in buffering the redox state in natural systems. The main objective of Amphos 21 has been to evaluate both the experimental work performed by CTM and available data from literature with the aim at developing a conceptual model able to be incorporated in reactive transport codes for the calculation of the redox buffering capacities. During the first year, a literature review was done. During the following 3 years, Amphos 21 has collaborated with CTM in the design of the experiments and has studied, treated and modelled the experimental data obtained. A conceptual model has been defined and experimental data modeled. The redox state of a system is given by the ratio between the main electron donors and acceptors. In this way, different authors (Scott and Morgan, 1990; among others) have proposed the concepts of OxiDising and ReDucing Capacities (OXC and RDC), due to the difficulty to obtain redox potentials from field data. The RDC is defined as the amount of electrons available for reduction over a defined reference state. The RDC of a system gives an estimation of its capacity to accept oxidants, and it is formally defined as:

$$RDC = \sum_i n_i \times [Red] - \sum_j n_j \times [Ox]$$

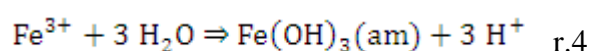
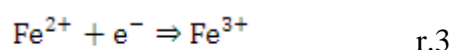
where [Red] and [Ox] are the concentration of reducing and oxidizing species present in the system, respectively, and n<sub>i</sub> and n<sub>j</sub> are the number of electrons involved in the redox reactions. The RDC concept has been previously developed for a hypothetical HNLW

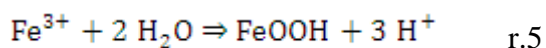
repository system, where the  $\text{UO}_2$  was the main contributor to the RDC (Bruno et al., 1996). This concept was been also applied by Bruno and Duro (1996) to a hypothetical natural system, with the Fe(II) as the main contributor to the RDC of the system. The main determinants of OXC and RDC in bedrocks are Fe-oxides, Fe-sulphides and Fe-bearing silicates. In most deep groundwaters the redox state is governed by electron transfer between Fe(II) and Fe(III) species and therefore, the largest reductive capacity of such systems is given by their content in Fe(II). Particularly pyrite, siderite, biotite and chlorite dissolution have been traditionally considered to be the main source of electron donors. The mechanisms of these reactions are strongly dependent of pH and  $\text{O}_2$  concentrations (Thomas et al., 2000). They are commonly reproduced by considering kinetic assumptions. The kinetic rates of dissolution depend on pH, temperature, and reactive surface areas of solid phases and even in some cases, on the presence of microbes (Nordstrom and Southam, 1997). Kinetic rates are determined from analytical experiments. They are commonly reproduced by simplistic numerical models in order to describe the evolution of the redox state. These types of experiments have been done for the most common Fe-bearing minerals, as olivine (Duro et al., 2005; Giménez et al., 2006; Malmström et al., 1995), pyrite, siderite, chlorite and biotite. Minerals as pyrrhotite (found in massive sulfide deposits associated with pyrite), magnetite, hematite and goethite (as accessory minerals in igneous and metamorphic rocks and iron deposits) are not traditionally included in this type of study. The kinetic laws of this type of Fe-sulfides and oxides have not been extensively studied, and are not commonly included in the most of the kinetic databases. To simulate the presence of one of these minerals, it is frequent that numerical models include the kinetic laws of an alternative mineral phase (pyrite,  $\text{Fe}(\text{OH})_3$ , e.g.), or consider them under equilibrium assumptions. After pyrite, pyrrhotite is the most common iron sulphide in nature. The factors affecting pyrite and pyrrhotite oxidation are similar, but pyrrhotite has not been too much analyzed. Because of this, experimental work was focused to increase the knowledge on kinetic behavior of pyrrhotite. Kinetic experiments to evaluate the oxygen uptake capacity of pyrrhotite or pyrite have been performed at two initial dissolved oxygen concentrations, 70 and 20%, at  $25 \pm 0.2$  °C. Pyrrhotite and pyrite were from with natural samples from the skarn sulphide deposit of Gualba (NE Spain) and from Arnedo (N Spain), respectively. The solids were crushed and sieved to a 100-150  $\mu\text{m}$  particle size. Experiments were carried out in a batch reactors where a volume of  $350 \text{ cm}^3$  of  $\text{NaClO}_4$   $10^{-2} \text{ mol dm}^{-3}$  was saturated with  $\text{O}_2(\text{g})$  at the initial dissolved oxygen concentration desired (70% or 20%

respectively). Between 0.5 and 3 g of pyrrhotite or pyrite were added (except in the case of the blank), and the free gas phase was eliminated. Stirring was provided by orbital shaker at 90 rpm in order to keep the solution as homogenous as possible while minimising the risk of solid grinding. pH, Eh and DO were continuously monitored and aqueous samples were periodically analysed. Solid samples have also been characterized by SEM-EDX, DRX and XPS. DRX indicated that the rock is composed mainly of pyrrhotite (identified as  $\text{Fe}_7\text{S}_8$ ) and quartz, with some minor impurities like clays (chlorite and kaolinite), phyllosilicates and calcite. SEM images and EDX measurements show Fe-rich secondary phases formed that have grown homogeneously, which lead to an incongruent dissolution between Fe and S. In all kinetic studies, mineral dissolution has been observed. Experiments with pyrrhotite and pyrite shows Fe, sulphate and thiosulphate aqueous concentrations increase with time. In both cases,  $[\text{O}_2]$  decreases and  $\text{SO}_4^{2-}$ , Fe(II) and  $\text{Fe}_{\text{total}}$  aqueous concentrations increase with time. In the case of pyrrhotite, faster processes are observed. According to the information found in the literature (Nicholson, 1994, Belzile et al. 2004; Murphy and Strongin, 2009) the presence of ordered vacancies within the Fe lattice in the non-stoichiometric pyrrhotite crystal structure ( $\text{Fe}_{1-x}\text{S}$ , x from 0.125 to 0), may be the reason accounting for the faster oxidation rate of pyrrhotite when compared with pyrite. Oxidation of both pyrite and pyrrhotite generates protons and hence, cause a decrease in pH (r.1 and r.2). However, due to the different crystal structure of both minerals, pyrrhotite oxidation generates less acidity than pyrite oxidation (Nicholson, 1994).



From the experiments, the precipitation of Fe-oxyhydroxides onto the pyrrhotite surface can be observed. The results indicate that although pyrite or pyrrhotite dissolution processes are kinetically driven and control the pH of the solution, the redox potential is controlled by the redox pair  $\text{Fe}^{2+}/\text{Fe(III)}$ -oxyhydroxides.  $\text{Fe}^{2+}$  generated in r.1 and r.2 is oxidized to  $\text{Fe}^{3+}$  (r.3) which under the favourable conditions of neutral to alkaline pHs leads to the precipitation of amorphous Fe-oxyhydroxides which, in turn, may evolve to more crystalline phases (r.4, r.5).





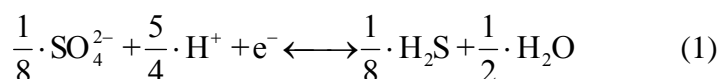
Experimental data have been modeled with the code PHREEQC (Parkhurst and Appelo, 1999) and the sit.dat database supplied with the code (without considering SIT coefficients for ionic strength corrections). In the case of pyrite kinetic experiment pyrite is assumed to be dissolved according to the rate of Williamson and Rimstidt (1994) and that  $\text{Fe}^{2+}$  generated oxidises kinetically to  $\text{Fe}^{3+}$  according to the kinetic law of Singer and Stumm (1970). Ferrihydrite is left to precipitate in equilibrium. Initial  $\text{O}_2$  aqueous concentration corresponds to that in equilibrium with 70%  $\text{O}_2(\text{g})$  in the gas phase ( $10^{-3} \text{ mol dm}^{-3}$ ). Diffusion of  $\text{O}_2$  is also considered.

e. Reduction of Uranium as a function of sulphate reduction in PPG (UniCYP)

The study is related to the effect of redox conditions existing within the tailings dump on the stability of phosphogypsum (e.g sulphate reduction) and uranium(VI). Phosphogypsum sampling and in-situ measurements were carried out at a coastal tailings dump in Vasiliko Cyprus, pH,  $E_{\text{H}}$  and solubility experiments were performed in-situ and in simulated laboratory systems, and thermodynamic calculations using MINTQA2. Generally, in the open tailings dump oxidizing conditions predominate stabilizing sulphur and uranium in their hexavalent oxidation states. On the other hand, after the application of a soil/vegetative cover and in the presence of natural organic matter, anoxic conditions prevail ( $E_{\text{H}} < -70 \text{ mV}$ ) resulting in S(VI) and U(VI) reduction to S(-II) and U(IV), respectively.

The research reported here covers the phosphogypsum tailings dump (about 50 000  $\text{m}^2$ ) at the Vasilikos site, which is a coastal area in front of a former fertilizer plant in Cyprus. Several observation boreholes have been drilled into the tailings dump (to a maximum depth of 5 meters) and tailings dump solutions were sampled from the boreholes using a submersible pump and filtered in the field immediately after collection. Since spring 2008, the tailings dump has been covered by a 1 metre topsoil and dense vegetative cover, which will affect the redox conditions within the tailings dump. Because the cover is relatively young the effects due to the soil/vegetative cover are observed only close to the soil-phosphogypsum interface. Therefore, solid material samples were obtained from phosphogypsum adjacent to the topsoil and affected by organic run-off. The respective samples have a pale-brown to dark-brown colour, in contrast to non-affected phosphogypsum, which is white. The redox potentials in the tailings dump solutions prior to vegetative cover have been determined

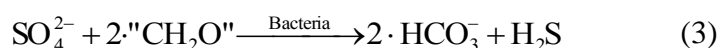
using a previously calibrated platinum  $E_H$  electrode. For the anoxic conditions (after application of the vegetative cover) the redox potential ( $E_H$ ) was calculated based on the S(+VI)/S(-II) redox couple, because the redox measurements “under anoxic conditions” are strongly affected by the presence of oxygen, which enters the system during borehole drilling and sampling. The S(+VI)/S(-II) redox couple was selected for the redox potential calculations because sulphur is the predominant redox sensitive species in the system and other possible redox couples such as Fe(III)/Fe(II) are present in trace amounts and difficult to analyze in the phosphogypsum matrix and solutions. The [S(-II)]/[S(+VI)] ratio in the suboxic material was determined after extraction of the sulphate and sulphide from the solid material by de-ionized water under a nitrogen ( $N_2$ ) atmosphere. The sulphate concentration in solution was determined by ion chromatography, whereas the sulphide concentration was measured by potentiometric titration using a sulphide ion selective electrode and a Hg(II) standard solution. Experimental and calculated data are graphically correlated and discussed in order to assess the redox conditions existing in the phosphogypsum tailings dump before and after the application of a soil/vegetative cover. The impact of the corresponding redox potential on the chemical behaviour of the redox sensitive species playing a key role in the phosphogypsum chemistry (sulphur and uranium) is also considered. The redox potential data associated with the open tailings dump have been determined experimentally, whereas the suboxic data have been calculated based on the following redox semi-reaction Eq. (1) and the corresponding Nernst equation Eq. (2):



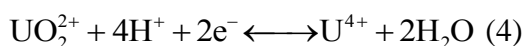
$$E_H = E_H^{\circ} - 59.2 \cdot \log \left( \frac{[H_2S]^{1/8}}{[SO_4^{2-}]^{1/8} \cdot [H^+]^{5/4}} \right) \quad (2)$$

where  $E_H^{\circ}$  is the standard redox potential for the above reaction, equal to 303.5 mV. Calculation of the redox potentials is necessary, because  $E_H$  measurements within the suboxic tailings dump are strongly affected by oxygen that diffuses in the phosphogypsum body during borehole drilling and sampling works. The redox potentials of the open tailings dump vary between +500 mV and +600 mV, indicating that sulphate and uranium(VI) are the predominant species in solution for sulphur and uranium, respectively. Regarding uranium speciation in the pH range relevant to this study, the U(VI) aquo ion and the  $UO_2CO_3$  dominate in solution. The increased redox potentials found in the open tailings dump are

attributed to the unrestricted oxygen diffusion within the tailings dump and are in agreement with corresponding literature data. On the other hand, after application of the soil/vegetative cover, the redox conditions are determined principally by runoff containing increased natural organic matter, bacterial activity and restricted oxygen diffusion within the tailings dump, resulting in more or less suboxic conditions below the vegetative cover. Because of the restricted oxygen diffusion and the continuous supply of natural organic matter, the redox potential decreases dramatically (down to -95 mV). At such low redox potentials (from -75 mV to -150 mV) bacterial reduction of sulphate to sulphide begins. Natural organic matter acts as an energy source for the bacterially assisted sulphate reaction described by the following general equation:



The consumption of protons during sulphate reduction (Eq. 1) results in increased pH values in the corresponding systems. In the studied system the pH increase is about 1 pH unit, indicating that sulphate reduction was proceeding. Nevertheless, the redox potential values ( $-70 \text{ mV} < E_H < -75 \text{ mV}$ ) calculated for the studied tailings dump are notably higher than corresponding values ( $-250 \text{ mV}$ ) found in the literature. This could be attributed to the fact that the measurements were performed in a relatively short time (about one year) after the application of the soil/vegetative cover on the phosphogypsum tailings dump, whereas a redox potential of  $-250 \text{ mV}$  corresponds to highly anoxic conditions. Nevertheless, in the long-term (even in the real system) a further decrease of the redox potential is expected because of the continuous supply of organic matter from the top-soil cover. Due to the activity of sulphate reducing bacteria, uranium(VI) is reduced to U(IV), and  $\text{U}(\text{OH})_4$  becomes a predominant uranium species in the suboxic tailings dump. The reduction of U(VI) to U(IV) described by Eq. 4 is favoured under the given conditions, because of the low solubility of the  $\text{U}(\text{OH})_4$  solid phase.



However, despite its low solubility, U(IV) in colloidal form can be highly mobile, particularly in an extensively weathered matrix like an anoxic phosphogypsum tailings dump. Phosphogypsum dissolution and migration of its associated contaminants into the surrounding environment is expected to be more effective in the case of the Vasiliko tailings dump because the disposal site is adjacent to the sea, exposed to waves and receiving large amounts of seawater, particularly in winter time.

#### 4. Role of microbes

##### a. Sulphate Reducing Bacteria (SRB) in deep groundwater Äspö hard rock laboratory under various energy and carbon load and hydrogen effect on microbial sulphate reduction (MICANS)

Microbial Analytics Sweden AB (Micans) is a company performing research and analyses (www.micans.se). MICANS was founded 2005 by scientists at Göteborg University, Sweden. One very important mission of the company is to perform and deliver microbiological analyses of groundwater with ISO 9001 and ISO 14001 quality grade for the radioactive waste disposal organisations in Belgium, Finland, Japan and Sweden. The company also takes on research missions related to radioactive waste disposal. Micans had a very well equipped laboratory for the purpose of the tasks at start of ReCosy. Microelectrode systems for redox, sulphide, oxygen and pH from Unisense A/S were available. The lab also had two gas chromatographs, and one mass spectrometer, 2D-autoradiography system, fluorescent microscopes, anaerobic boxes and all items needed for cultivation of anaerobic microorganisms such as a gas mixing bench and anaerobic tube systems. Basic equipment for all types of microbiology was at hand. There was a complete set-up for DNA technology work such as polymerase chain reaction (PCR) amplifier, quantitative PCR, temporal gradient gel electrophoresis (TTGE), cloning, digital gel documentation system, laminar air flow box, and -85 C freezer. In the field, 450 m underground, Micans had a set up 6 independent, remotely controlled biofilm flow cell circulation systems that communicated under in situ pressure and chemistry with aquifers in the granitic rock of Äspö hard rock laboratory. Within work package 3 Micans focussed laboratory research on the effect from microbial processes on redox reactions. Many redox reactions in natural systems are in disequilibrium due to the activity of microorganisms. Micans studied their laboratory and field systems under sterile and non-sterile conditions. A microbial process identified to be of particular importance for safety cases in radioactive waste disposal was the reduction of sulphate to sulphide, where microorganisms are a prerequisite for the process to occur at low and intermediate temperatures. This process have been investigated in both laboratory environments and in natural environments 450 m underground in the Äspö hard rock laboratory and the ONKALO tunnel in Olkiluoto.

The overall objectives for year 1 were to quantify and develop process understanding for redox buffer capacity and kinetics of response to redox perturbations of defined and near-

natural systems. Until summer 2008, Micans worked in the laboratory with pilot tests of how microbial cultures of sulphate reducing bacteria (SRB) influenced the redox potential in the culture media. Site investigation data on the relation of microbial numbers and redox were also evaluated. Field experiments in the Äspö tunnel generated data on the relation between sulphide, ferrous iron and microbes. Pressure resistant (1-25 Bars) *in situ* microelectrodes for pH and redox were developed to be used in field work in the Äspö hard rock laboratory tunnel environment. Micans performed analysis of redox and microbial data from the site investigations for a future radioactive waste repository in Forsmark and Laxemar (Pedersen et al, 2009, 2012). Sulphate reducing bacteria was demonstrated to be an important component for the measured redox state in the studied deep groundwater. Methods for analysis of the effect from microbial processes on the redox potential in the Äspö hard rock laboratory at 450 m depth were designed. A conceptual model that outlined how microbial and inorganic processes are involved in iron and sulphur transformations were tested and confirmed in the Äspö hard rock laboratory tunnel. This model served as a base for the Recosy research of Micans during the remaining part of the project. The objectives from year 1 were kept, i.e. to quantify and develop process understanding for redox buffer capacity and kinetics of response to redox perturbations of defined and near-natural systems. Specifically, *in situ* field work with pressure resistant microelectrodes were performed with deep groundwater microorganisms and laboratory experiments with sulphate and nitrate reducing bacteria and their influence on redox were performed in batch and continuous cultures. Five underground circulation systems with flow cells for biofilm development were installed in the Microbe Laboratory at 450 m depth in the Äspö hard rock laboratory. Two different groundwater systems were used. They connected directly to aquifers at the *in situ* pressure of approximately 24 bars and biofilms developed on the rock or glass surfaces in the flow cells. The systems were isolated from the aquifer and groundwater with indigenous microbes was then circulated through the flow cells without contact with the aquifer. These systems were used to investigate the effect of microbial processes on groundwater chemistry, pH and redox potential. Pressure resistant *in situ* microelectrodes for redox were installed. Treatments with acetate and lactate and hydrogen were performed. The evolution of gas composition, pH redox, chemistry and microbiology was followed over a two months period. A first set of experiments comprised three circulation systems that operated in the Micans laboratory with groundwater from the Microbe laboratory. These experiments were used to set the conditions for the underground laboratory experiments. In addition, a set of 36

inoculated and sterile, anaerobic culture bottles (100 mL) with sulphate reducing bacteria and acetogenic bacteria was prepared and delivered in October to be used in the Recosy ICE. Pressure resistant microelectrodes were tested under pressure conditions and calibrated versus HACH multi-instrument redox electrodes and laboratory Scott electrodes with a good outcome. Two series with growth of sulphate reducing consortia from 450 m depth of the Äspö hard rock laboratory under various energy and carbon load were performed and analysed in relation to redox. A third series of experiments with six circulation systems were started in March 2010 with three different hydrogen concentrations and with acetate and hydrogen on two different groundwater types at 450 m depth. The influence of oxygen on redox in the circulation systems above will be analysed as will, directly after the anaerobic experimental cycle has been completed. This experiment aimed at understanding redox buffering capacity of microbial ecosystems. Biological life systems are non-equilibrium systems and in most cases, they will never reach equilibrium. The overall influences of microbial activity on the Eh are complex and dependent on availability of sources of energy and carbon, either inorganic or organic compounds, and the nature of these. In the work performed year 3, pressure resistant Pt and Ag/AgCl reference electrodes were constructed and installed into pressurized (2 MPa) circulation systems. Investigations of the relations between Eh and microorganisms growing with different electron donors (lactate or hydrogen) and electron acceptors (nitrate or sulphate) were performed. The influence of pulses of oxygen on the redox stability under different growth conditions was analysed. It became clear that microbial activity was very important for how the Eh developed in the studied systems. Microbial lactate and hydrogen oxidation, sulphide production and oxygen reduction occurred and the effect from introduction of oxygen on Eh was mitigated by microbial activity. The presence and activity of microorganisms consequently could be demonstrated to have a great influence on Eh in natural water systems. The effect of varying concentrations of hydrogen and acetate on microbial sulphate reduction was documented and quantified. The influence of microbial activity on redox as a function of the hydrogen load on oxygen reduction was demonstrated to be significant (Pedersen et al. 2011). Microbial populations appeared to have a strong redox buffering capacity. Simulation of the microbial processes was initiated with a program denoted Microbe. This program simulated the microbial processes well. New series of experiments with three circulation systems was started in March 2011 with different hydrogen and methane concentrations with microbial populations from 360 m depth in ONKALO, Finland. The influence of microbial metabolism of hydrogen,

methane and oxygen on redox in the circulation systems discussed above was analysed. Oxygen was used to inactivate the microbial populations. This experiment aimed at understanding redox buffering capacity of microbial ecosystems with high concentrations of methane and hydrogen. The addition of hydrogen lowered the redox significantly as expected. Methane had no initial effect but once microbial processes started there was a significant lowering of the redox compared to the inactivated control. Analysis and interpretation of the results is ongoing.

**b. Characterization of the products of microbial U(VI) reduction (UNIUTR)**

Microbial reduction of U(VI) to U(IV) is expected to result in the precipitation of solid  $\text{UO}_2$  at neutral pH. However, in preliminary incubation experiments at relatively low U / bacteria ratios, we did not observe the formation of black precipitates. In order to elucidate the fate of U(VI) in these experiments we performed incubations with the organism *Shewanella putrefaciens* to which U(VI) was added. The samples of these experiments were analysed by X-ray absorption spectroscopy (XAS) at the Advanced Photon Source, Argonne, IL, USA (APS experiment GUP-9160: U(IV) speciation at bacterial cell walls and its role in uraninite formation. April 1-4, 2009). EXAFS analyses revealed that enzymatic reduction of U(VI) did not instantaneously lead to the formation of an  $\text{UO}_2$  precipitate but that U(IV) was monomerically associated with the bacterial cells. Indications were obtained that U(IV) in this form is very susceptible for reoxidation. A manuscript on these findings is in preparation.

**c. Microbial S(-II) production and mobility of U(VI) adsorbed onto iron oxides (UNIUTR)**

The mobility of U during reductive dissolution of iron oxide by S(-II), a product of microbial sulfate reduction was investigated. In preceding experiments the activity of sulfate reducing organisms was mimicked by adding S(-II) solution to suspensions containing the iron oxide lepidocrocite with adsorbed U(VI). It turned out that the interaction of various abiotic processes cause a high complexity in the investigated system (Alexandratos V., Behrends T., and Van Cappellen P. (2009) Effect of S(-II) driven conversion of iron oxides to FeS on uranium mobility. *Wissenschaftliche Berichte - Forschungszentrum Karlsruhe, (FZKA 7461)205-212*). Hence, it was decided to focus on the abiotic reaction network and not to include sulfate reducing organisms because the presence of living organism would have further increased the complexity. Without a thorough understanding of the abiotic processes simultaneous acting in the systems it would have not been possible to appropriately evaluate

the role of bacteria and to obtain unequivocal interpretation of the results. Past results showed intermediate mobilization of U(VI) and a partial reduction of U(VI) to U(IV) in systems where lepidocrocite had been transformed into FeS through incremental addition of S(-II). However, lepidocrocite is an iron oxide with high intrinsic reactivity and it became of question as to how data would compare to systems where a more crystalline iron oxide is present. For this reason, batch experiments were performed with hematite suspensions in an O<sub>2</sub>-free glovebox, at a steady pH 8 and ionic strength of 0.1M. Addition of S(-II) was used to drive reductive dissolution of hematite and U mobility was followed throughout the duration of the experiments. Additionally, the reversibility of the reduction processes was investigated to evaluate the potential release of U upon re-oxidation of the products. For this, suspensions of lepidocrocite which had reacted with S(-II) were introduced to atmospheric conditions. Both solid and solution samples were collected for an overall analysis of the suspension. Solid samples specifically were prepared for XAS analysis. Samples from both experimental series were analyzed during two experiments at the European Synchrotron Radiation Facility (ESRF) in Grenoble, France. (ESRF experiment 26-01- 845: Effect of S(-II) on the U(VI) oxidation state and coordination environment in the presence of hematite, BM26A, April 30– May 4, 2009 and ESRF experiment EC- 279: Adsorption of U(VI) onto FeS and its subsequent reduction. June 25 – 30, 2008). The instant reaction that was seen previously between lepidocrocite and S(-II) is not observed in the case of hematite. Reaction of hematite and S(-II) was much slower compared to that of lepidocrocite; S(-II) consumption was completed within the first five hours, especially for suspensions reacted with lower S(-II) concentrations. Just as in the case of lepidocrocite, production of Fe(II) was observed in both solution and solid.

- Concentration of dissolved uranium (U(aq)) in suspensions before S(-II) addition were below detection limit, indicating quantitative adsorption of U(VI) onto the hematite surface. An acute release of U(aq) into solution was observed at the timing of S(-II) introduction to the system, comparable to lepidocrocite. However, instantaneous release of U(VI) in the case of hematite reached much higher numbers than those of lepidocrocite. U(VI) remained for very little time in solution as the concentrations immediately decreased. Throughout the rest of the experiments U concentration levels were observed at a 3% of the initial added amount. This persistent amount can be attributed to the transformation of substrate to FeS, having a lower affinity for U compared the iron oxide it was before.

- For hematite samples, XAFS analysis surprisingly showed a decrease of the coordination number of axial oxygens -indicative for the formation of U(IV)- as soon as the first hour of reaction. This indicates faster reduction of U(VI) compared to what was seen in experiments with lepidocrocite. In addition to that, the amount -almost all- of the U added in the suspension has been reduced as early as the first hour of reaction, something that is very different from the gradual U reduction that had been observed in lepidocrocite.
- Reoxidation experiments showed that U reduction is a reversible process, however, not as fast as initially estimated. Reversibility was related to the amount of S(-II) added in suspension; the lower the amount of S(-II) added, the higher the amount of U(VI) going back into solution.
- XAFS analysis in all cases, and in samples reoxidised as long as 200 hours, revealed a continuous presence of U(IV) in the system. Reductive dissolution of iron oxides results in the formation of FeS nanoparticles; it is speculated that when these nanoparticles reoxidise, they may maintain their size but also aggregate, thus trapping U(IV). It's quite possible that this may be a fraction of U(IV) being maintained as such, due to its difficulty to access oxygen.

Sulfide, as a product of microbial respiration and occurring naturally in subsurface environments, may play an important role in the mobility of U when adsorption of U(VI) to iron oxides controls U mobility. Irrespective of the iron oxide characteristics, presence of S(-II) in the solution and transformation into FeS decreases U(VI) adsorption to the solid phase. That is, U(VI) is partially mobilized due to the appearance of S(-II). Reduction of U(VI) to U(IV) was more emphasized when hematite instead of lepidocrocite was used. This suggests that the lower reactivity of the iron oxide facilitates U(VI) reduction, possibly by competing less efficiently with U(VI) as an oxidant for S(-II). Reoxidation of suspensions containing FeS and reduced U indicate that U(VI) reduction is a reversible process, however, aggregation of reoxidising FeS nanoparticles may form clusters which can trap U(IV) and maintain it as such for longer timescales.

*d. Uranium interaction with magnetite surface Fe(II) (INE)*

Experimental studies on sorption and/or reduction of U(VI) in presence of magnetite are still accumulating, mostly motivated by the importance of elucidating effective immobilization processes of (U(VI) => U(IV)) and the role of aqueous, surface sorbed or structural bound Fe(II). U data of sorption and reduction studies with magnetite in presence of carbonate at

---

(D-N°:1.2) – [Report on the scientific state of the art](#)

Dissemination level :PU

Date of issue of this report : **03/09/2012**

pH values representative for granitic ground-waters (pH 8-9) for contact times up to 150 days were presented by (El Aamrani, 1999). These authors applied X-ray photoelectron spectroscopy (XPS) to identify the U surface species on magnetite and found evidences for a coupled reduction-oxidation process of U(VI) and Fe(II), respectively in the presence of bicarbonate. Though, they found no U(IV) at slightly acidic pH (4.81) in the absence of carbonate. XPS results presented by (Missana et al., 2003a; Missana et al., 2003b) and (Scott et al., 2005) indicate U reduction in the presence of structural bound Fe(II) in mineral phases. U(VI) reduction is also feasible by means of sorbed ferrous iron in presence of an Fe(III) containing solid phase (nanoparticulate hematite) as shown by (Liger et al., 1999). Here, a surface-catalyzed process for the U reduction by sorbed Fe<sup>(II)</sup> is proposed. The influence of bicarbonate in the system uranyl-magnetite for pH 6, 8 and 10 with contact times of 42 days using XPS was investigated by (Regenspurg et al., 2009). A facilitated U(VI) reduction attributed to the formation of siderite representing an additional Fe<sup>(II)</sup> pool was found. Most recently, Ilton and co-workers presented spectroscopic indications (XPS) of the formation of U(V) in the presence of magnetite and explained the stability of U(V) by sorption/incorporation/precipitation in either secondary iron phases or mixed valent U phases (Ilton et al., 2010). Surprisingly, no evidences of U(IV) on basis of XPS and X-ray absorption spectroscopy (XAS) measurements were found. Partner KIT-INE focused within the ReCosy project on the following:

- Provide long-term kinetic data (1d -550d contact time) about U-removal processes for pH 3 to 11.
- Compare the redox capacity of partly oxidized magnetite with a freshly prepared magnetite.
- Examine if thermodynamic calculations based on independent measured Eh-pH conditions are consistent with spectroscopically determined U redox states.

Detailed results can be found in an S&T contribution of the 4<sup>th</sup> Annual workshop proceedings and in (Huber et al., 2012, in review). The interaction of hexavalent U with a fresh synthetic nanoparticulate magnetite (Fe<sup>II</sup>Fe<sup>III</sup>O<sub>4</sub>), a partly oxidized synthetic nanoparticulate magnetite and maghemite nanoparticles under anoxic conditions and exclusion of CO<sub>2</sub> as function of pH, contact time and total U concentration has been examined. Short term kinetic batch experiments (contact time of 90 d) for four different pH values have been conducted. Moreover, classical batch pH sorption edges have been prepared for two different uranium concentrations for a contact time of 550 d.

Here we focus on the presentation of the spectroscopic results. Spectroscopic techniques (XPS, XAS) were applied to probe for the presence and amount of reduced U on the magnetite surface. Batch kinetic studies revealed a fast initial U removal from aqueous solution with > 90% magnetite associated U after 24 hours within the pH range 5-11. Long term contact time batch experiments (550 d) showed neither a U removal below pH < 3 nor a decrease in the magnetite associated U at pH  $\geq$  9. Selected samples were analyzed to determine the Fe(II)/Fe<sub>TOT</sub> ratios by XPS. Since Fe(II) is the only potential redox agent for U reduction present in the experiments, this information is crucial concerning their redox capacity. Several approaches determining the Fe(II) portion by XPS in iron oxides and compounds are reported (Aronniemi et al., 2005; McIntyre and Zetaruk, 1977; Raeburn et al., 1997a; Raeburn et al., 1997b; Yamashita and Hayes, 2006; Yamashita and Hayes, 2008). In this work, the Fe 2p spectra are measured to estimate Fe(II)/Fe<sub>TOT</sub> ratios on the mineral surfaces. More precisely, the intensity of the shoulder on lower binding energy side at the Fe 2p<sub>3/2</sub> elemental line is representative for the amount of Fe(II) present. The intensity of the shoulder is determined within a band of 708.5 eV to 708.7 eV binding energy and set into relation to spectra of a freshly prepared magnetite and a hematite powder (Fe<sub>2</sub>O<sub>3</sub> puratronic, Alfa Aesar) by use of normalized spectra. Error in Fe(II) portion determination in this way is estimated to about  $\pm$  5 %. The Fe(II)/Fe<sub>TOT</sub> ratio of the partially oxidized magnetite range between 10.4 % to 25.4 % with a mean value of 22.9 %, while the fresh magnetite samples range between 24.8 % to 33.3% with a mean value of 30.1 %. The maghemite samples show values of only 0-2 % Fe(II)/Fe<sub>TOT</sub> on the surface which is in the range of the analytical uncertainty. The amount of Fe(II)/Fe<sub>TOT</sub> is clearly a function of pH reflecting the preferential dissolution of Fe(II) out of the magnetite structure at low pH, since the amount of Fe(II)/Fe<sub>TOT</sub> increases with increasing pH (Jolivet and Tronc, 1988; White et al., 1994). This trend follows the general curve of magnetite dissolution which is more pronounced in the acidic pH range. The U 4f<sub>7/2</sub> elemental line was used to determine the redox state of U in the selected batch samples of all three different series by XPS. The binding energy ranges determined in the present study are for U(VI) and U(IV) 381.1 – 381.7 eV and 380.1 - 380.6 eV, respectively. In the present work satellite peaks used by (Ilton et al., 2010) for spectra interpretation are often low intense due to low surface concentrations of U. That is, if the signal to noise ratio is low the intensities of the satellite peaks are within noise level and not resolved. As a “reference” for U(IV) and U(V), we measured U 4f spectra of an oxidized UO<sub>2</sub>-Pd thin film vapour-deposited onto a semiconducting silicon wafer and stored in air (received from Institute of

Transuranium Elements (JRC-ITU), Karlsruhe). Binding energies of  $4f_{7/2}$  elemental lines and satellites spacings coincide with reported values for U(V) and U(IV) (Ilton et al., (2010) (Ilton et al., 2007) and thus confirm the assignments to the 4f main components concerning U valence. To estimate portions of U(IV), U(V), and U(VI) on U reacted magnetite, U  $4f_{7/2}$  spectra are curve fitted by three Gaussian-Lorentzian sum functions with same Gaussian fractions and FWHM. In contrast to reported values of 0.8 eV and 1.04 eV between U(IV) - U(V) and U(V) - U(VI), respectively (best fit derived from a single crystal annite; (Ilton et al., 2005)), in this study, curve fits yield spacing of about 1.1 eV for U(IV) - U(VI). One should keep in mind that U 4f spectra give no further insight how U interacts at the chosen U concentrations on the molecular scale with the magnetite surface. The Fe(II)/Fe<sub>TOT</sub> ratios of all samples are located in the range between 21 % up to 33.2 %. For low Fe(II) amounts (21 % to ~ 23 %), the U speciation determined by XPS is dominated by U(VI) with ~ 65 % - 90 %. With increasing Fe(II) (up to 25 %), the amount of U(VI) decreases to ~ 50 % to 60 % and the amount of U(IV) increases to ~ 40 – 45 % respectively. Concerning the U speciation in the series after 550d contact time, differences arise compared to the results of 90d contact time. Here, the amount of U(IV) is clearly higher ranging between 41.6 % up to 54.6 % despite the lower Fe(II)/Fe<sub>TOT</sub> ratio. This deviation may be explained by the considerably longer contact time indicating that a fast initial U reduction to U(IV) occurs within the first day followed by a subsequent more slowly reduction kinetic with time. The fact that the hexavalent U is not quantitatively reduced to U(IV) after 550 d may again be referred to the lower Fe(II)/Fe<sub>TOT</sub> ratio. To sum up, all data obtained in this study shows that the reduction of U can be correlated to the available Fe(II)/Fe<sub>TOT</sub> ratio on the magnetite surface leading to an increase in U(IV) with rising Fe(II)/Fe<sub>TOT</sub> ratio. Maghemite reacted uranium samples have been probed by XPS after a contact time of 13 d to determine both the Fe(II) content and the U speciation. The ratio of Fe(II)/Fe<sub>TOT</sub> for all three samples is below ~ 2 % within the analytical uncertainty. The U 4f spectra shows up to ~ 8% U(IV) with decreasing U(IV) for increasing pH. This may indicate that a pronounced dissolution of maghemite at more acidic pH releasing bulk Fe(II) which has not been fully oxidized at the synthesis step. To sum up, the removal of U from solution can thus be explained mainly by sorption to the maghemite surface, but minor contributions of reduction to U(IV) are detectable as discussed above. XPS is a surface sensitive technique, whereas XAS in standard transmission or fluorescence detection mode provides bulk information about the U oxidation state and its local coordination in magnetite. We studied with XAS one partially oxidized sample to complement the results obtained with

XPS. The ARTEMIS program package (Ravel and Newville, 2005) was used for EXAFS analyses. The XAFS signal  $[\chi(k)]$  measured at the U  $L_3$ -edge, covering a  $k$  range from 2.7 to  $10.5 \text{ \AA}^{-1}$  was Fourier transformed to  $R$  space using  $k$  weightings of 1, 2, and 3 and a Hanning window with window sills  $dk$  equal to 2. Four U-O/U-Fe single scattering paths (U-O at (ICSD 82477) 1.77, 2.68, (ICSD 26410) 1.89  $\text{\AA}$  and U-Fe at 3.48  $\text{\AA}$ ) were used for the initial model of the po-mag#42 spectral fit. The amplitude reduction factor was held constant to 1.0 ( $S_0^2$ ); the value was obtained from initial fits of the schoepite Fourier-transformed (FT) EXAFS spectrum measured under the same experimental conditions. The energy position of the WL maximum in U  $L_3$ -edge XANES spectra, which describes mainly  $2p \rightarrow 6d$  electronic transitions, shifts towards higher energies with the increase of the formal oxidation state of U (Denecke, 2006). However, its position can also be influenced by the degree of covalency of the U-O bond, i.e., U local symmetry, electronegativity of the U bonding partner and long range geometric structure of the material (Antonio M. R. and Sonderholm, 1994). The po-mag#42 WL exhibits an asymmetric shape. The energy position of its low energy part coincides with the energy positions of the U(IV) and U(V) WL, whereas its high energy part is positioned higher than the WLs of all reference spectra. The po-mag#42 WL broadening and its energy position indicate the presence of mixtures of U oxidation states as expected for the predominant reduction of U(VI) to U(IV). This implies the predominance of a geometric structure different than that of uranyl. We obtain further insights from the characteristic feature, marked with line c, which describes the multiple scattering of the photoelectron from the two axial O atoms (Denecke, 2006), (Antonio M. R. and Sonderholm, 1994). The absence of this feature in the po-mag#42 spectrum suggests U-Os bond longer than about 2  $\text{\AA}$  as confirmed by the EXAFS analysis. The first coordination shell peak of the po-mag#42 EXAFS spectrum is fit with  $0.5 \pm 0.1$  O at  $1.77 \pm 0.01 \text{ \AA}$ ,  $1.6 \pm 0.2$  O at  $2.23 \pm 0.01 \text{ \AA}$  and  $3.3 \pm 0.2$  O at  $2.51 \pm 0.01 \text{ \AA}$ . These results point out that most of the initial U(VI) in linear uranyl geometry reacted with the magnetite nanoparticles and was reduced forming a distorted octahedral oxygen coordination symmetry. One possible reduction mechanism might take place at the  $\text{Fe}^{2+}$  octahedral sites of magnetite. The EXAFS fit yields at average  $5.4 \pm 0.2$  O at 1.75-2.51  $\text{\AA}$  in the first coordination shell (FCS) and  $5.7 \pm 1.5$  Fe atoms at  $3.39 \pm 0.02 \text{ \AA}$  in the second coordination shell (SCS). Therefore incorporation of U in vacant  $\text{Fe}^{2+}$  (FCS: 6 O at 2.056  $\text{\AA}$ , SCS: 6  $\text{Fe}^{2+}$  at 2.97) sites in the bulk part of the particles is likely. In summary, the prevailing study confirmed the reduction of hexavalent U by nanoparticulate magnetite by means of XPS and XAS measurements. A direct proportional correlation between the Fe(II)

content on the surface of magnetite and the amount of tetravalent U was found. Consequently, the highest tetravalent U content was observed in case of the interaction with a freshly prepared magnetite which possesses the highest amount of Fe(II) on the surface underpinning the above mentioned correlation. Removal processes show fast kinetics within 24 h with more than 90 % U associated to the magnetite surface. Specifically, a fast reduction was observed after 1 d contact time with up to 80% reduced U (both pentavalent and tetravalent) on the magnetite surface. XANES results independently revealed the presence of tetravalent U in the magnetite particles. Furthermore, EXAFS results suggest that U incorporates into vacant Fe(II) sites after contact time of 550 d and pH of 5.7. Overall, the results show that magnetite, both partly oxidized or “non-oxidized”, can effectively reduce hexavalent U, thus representing an effective retention pathway.

## 5. Modelling and application

### a. Microscopic modeling: modeling the di-octahedra smectite CEC variation, vs. structural iron level (BRGM)

An important work was devoted to modeling the di-octahedral smectites CEC variation versus structural iron level, in the framework of the PhD position of J. Hadi (Hadi et al., 2010a; 2010b; 2011; 2012). Iron is one of the most common redox species in soils and sedimentary rocks. Amongst iron-bearing phases, phyllosilicates might play key roles in various bio-geochemical processes involving redox reactions, where structural Fe ( $Fe_{str}$ ) acts as a renewable source/trap of electron. A large set of data from kinetics, spectroscopic or electrochemical studies on dioctahedral smectites demonstrate that reduction of  $Fe_{str}$  impacts many clay properties such as color, layer charge, swelling pressure, and colloidal properties that are linked to layer structural changes. Experiments also suggest that this mechanism is partly reversible, depending on type and properties of the primary oxidized clay and on extent of iron reduction level. The complexity of the involved mechanisms makes the prediction of  $Fe_{str}$  redox properties challenging. For instance, only empirical models are currently available to quantify structural changes as a function of reduction level. However, a predictive and mechanistic model of these changes is a prerequisite to develop a thermodynamic model for  $Fe_{str}$  redox properties. In this contribution (Hadi et al. 2012), we propose a mechanistic statistical model to explain 2:1 layer excess negative charge changes induced by chemical (dithionite) or electrochemical reduction of structural Fe(III) to Fe(II).



This model was calibrated on data from our own and from the literature and conclusively agrees and completes this published by Drits and Manceau (2000).

*b. Macroscopic Modelling: distribution of redox elements (Fe, S, Mn and N) and speciation-solubility calculations (UNIZAR)*

Once again, the work carried out on this topic by the Geochemical Modelling Group of the University of Zaragoza (UNIZAR) is based on the observations and interpretations done in the two sites proposed in Sweden for hosting a deep repository for spent nuclear fuel: Forsmark and Laxemar-Simpevarp. The redox-sensitive elements considered in the studied systems are mainly iron, sulphur, manganese and nitrogen. The evolution trends of their dissolved contents with depth are presented in the following subsections in combination with the results of speciation-solubility calculations (with PHREEQC code and a modified version of the WATEQ4F database; Parkhurst and Appelo, 1999, Ball and Nordstrom, 2001, Gimeno et al., 2009b) aimed at identifying some of the effective precipitation/dissolution processes in the studied systems. Dissolved CH<sub>4</sub> (g) and H<sub>2</sub> (g) distribution have also been analysed but they are not presented here due to the scarcity of available data (methane, however, has been used in the redox-pairs calculations).

*6.b.1. Iron and sulphur systems*

As will be seen below, the general redox features observed in both studied systems seem to be determined by the influence of the geochemical processes affecting the mineral phases or dissolved species of iron and sulphur. Therefore, the behaviour and evolution of dissolved Fe(II) and S(-II) are treated together here. In the groundwaters of Laxemar-Simpevarp and Forsmark, Fe(II) shows a rough decreasing trend from the surface down to 700 m. Below that depth, the values are generally lower than 0.2 mg/L, reaching only occasionally values of about 1 mg/L in Forsmark. With regard to the evolution of dissolved S(-II) contents with depth, there are no clear trends either in Laxemar-Simpevarp or in Forsmark. S(-II) contents are mostly below 0.5 mg/L and in many cases below the detection limit. However, there are locally significant amounts of sulphide down to 700 or even 900 m depth (for both, Forsmark and Laxemar-Simpevarp), with maximum dissolved concentrations of 2.5 mg/L (at 700 m depth in Laxemar-Simpevarp). Due to the importance of this parameter, a very thorough

monitoring program is being developed in the two sites for the last two years and the sulphide evolutions is being studied in detail. Speciation-solubility calculations show that the near surface groundwaters (NSGW in the plots) reach equilibrium or oversaturation states with respect to siderite ( $\text{FeCO}_3$ ) suggesting the effective precipitation of this mineral and its involvement in the control of dissolved Fe(II). However, siderite saturation indices decrease in the deep groundwaters with increasing depth and chloride contents, which indicates that this phase is not playing a controlling role on dissolved Fe(II) concentrations in this part of the system. Most of the near surface groundwaters with dissolved sulphide contents greater than 0.04 mg/L, are in equilibrium with respect to “amorphous” FeS. This equilibrium situation can also be observed down to 600 m depth in many samples but it appears to be less frequent at greater depths. The equilibrium with respect to the amorphous and metastable iron monosulphides found in these groundwaters suggests a continuous and present supply of  $\text{H}_2\text{S}$  produced by Sulphate-Reducing Bacteria activity combined with the presence of an iron source.

#### 6.b.2. Manganese system

The distribution of dissolved Mn concentrations with depth shows, in both sites, a similar pattern to that of dissolved Fe(II) also showing variable and high contents down to 600 m depth and very low to undetectable values at greater depths (<0.25 mg/L Mn). This suggests a “simultaneous” control of the dissolved concentrations of both elements by iron phases with traces of manganese (oxyhydroxides, clays) or by surface processes between dissolved manganese and these minerals. However, there exists an additional control in the Mn contents as the highest values are associated with brackish groundwaters with an important marine signature. Mn contents (as well as other components such as  $\text{SO}_4^{2-}$ , Mg,  $\text{SiO}_2$ ,  $\text{HCO}_3^-$ ,  $\text{NH}_4^+$ , etc.) reach high values in the intruding marine waters (Littorina stage; see Gimeno *et al.*, 2008). In spite of the water-rock interaction and mixing processes of these intruding marine waters with the pre-existing groundwaters at depth, some of the resultant brackish marine groundwaters (with chloride about 5,500 mg/L) still show this marine inheritance with variable and high concentrations of these components. For the manganese system, the only mineral that reaches equilibrium in some of the studied groundwaters (the shallowest ones and those deeper but with the highest marine contribution) is rhodochrosite ( $\text{MnCO}_3$ ),

although saturation indices with respect to this mineral generally decrease towards clear undersaturation with depth.

### *6.b.3. Nitrogen system*

The observed evolution in the two studied sites shows the general depletion of nitrogen species usually observed in anoxic groundwater systems as residence time and/or depth increase (not shown). Thus, the higher contents and variability of  $\text{NO}_2^-$ ,  $\text{NO}_3^-$  and  $\text{NH}_4^+$  are associated with the shallowest groundwaters in the overburden, where the oxic/anoxic transition appears to occur. However, already in the shallow groundwaters with a meteoric origin, the low levels found for nitrate and nitrite indicate the presence of reducing conditions suggesting the development of an anoxic environment very soon after groundwater infiltration. Only  $\text{NH}_4^+$  shows high and variable contents in deep groundwaters with clear marine influence also seen in other elements.

### *6.b.4. General conceptual model for the redox control in the studied systems*

Even though the distribution of redox parameters (mainly Eh measurements and dissolved contents of redox-sensitive elements) does not show any evident trend with depth, the existence of very reducing conditions already in the recharge waters with very short residence time has been proven indicating an efficient redox-buffering ability of microbial and water-rock interaction processes. The combined interpretation of all the available data and calculations points towards the probable existence of presently active processes of stable bacterial sulphate reduction. This is supported by the potential presence (according to speciation-solubility calculations) of metastable amorphous iron monosulphides not yet recrystallised to ordered or crystalline mackinawite or pyrite. The existence of equilibrium situations with respect to ferrous iron monosulphides indicates the permanent supply of dissolved Fe(II), without which the concentrations of dissolved sulphide in the groundwaters would not be solubility-limited and could reach much higher values. This interpretation has important implications for performance assessment, since high sulphide concentrations are known to affect very negatively to the safety of canisters owing to corrosion processes. All these results would support the presence of clearly sulphidic environments, consistently with

the good performance of the sulphur redox couples. Furthermore, the results obtained by means of partial equilibrium calculations have allowed appreciating the critical importance of the crystallinity, particle size and surface area of ferric oxyhydroxides on the predominance of iron or sulphate reduction processes and, therefore, in the development of segregated redox zones in natural systems. According to these calculations, the less crystalline ferric oxyhydroxides (e.g. ferrihydrite) constitute the primary source for IRB activity and, therefore, their absence must be an important limitation in the activity of these microorganisms under the pristine highly-reducing conditions of the Laxemar-Simpevarp and Forsmark deep groundwater systems. Thus, all the available data and interpretations suggest that present IRB activity in those systems is restricted to the shallower levels, where a broad spectrum of Fe-oxyhydroxides (including poorly crystalline phases) exists. At deeper levels, the characters of Fe-oxyhydroxides and clays in the fracture fillings do not seem to be suitable to support the active presence of this type of microorganisms. However, under specific evolutionary scenarios (past or future), the presence of IRB is, at least temporally, feasible. This is the case of oxygen intrusion scenarios. All the modelling studies performed on this issue have considered only inorganic redox buffers against penetration of oxygenated waters (Fe(II)-bearing aluminosilicates and sulphides). Although the relevance of microbial activities for maintaining the reducing conditions of a repository, and for buffering the intrusion of O<sub>2</sub>-rich groundwater, has been recognised (e.g. Pedersen and Karlsson, 1995; Banwart, 1999; Trotignon *et al.*, 2002; Puigdomènech, 2001) the effects of microbial activity have not been included in the predictive calculations of the long-term evolution of deep crystalline rock environments (e.g. performance assessment exercises for spent nuclear fuel repositories).

## WP4. Redox reactions of radionuclides

For the long-term safety assessment of deep geological nuclear waste repositories, a detailed knowledge of the processes controlling the chemical speciation of the radionuclide contaminants is essential for predicting their fate and transport in the geosphere. Redox processes play an important role in the speciation of actinides and redox-sensitive fission products present in nuclear waste repositories. Radioelements that undergo redox transformations, behave very differently with regard to reactivity and mobility depending on their redox state.

Under normal conditions, the host rock of a deep geological repository is reducing. The introduction of oxygen and oxidizing waters during the construction and operation will cause oxidation of the exposed rock surfaces. Furthermore the material introduced into the repository for construction and backfill will be completely oxidized. After closure of the repository, the oxygen present in the pore spaces and in the pore solution will slowly be consumed by different kinds of redox processes and, after a while, the repository near-field and the surrounding geosphere will return to their original reduced state. The large amounts of steel present in the repository near-field (originating from steel canisters) will serve as a large source of reducing agents maintaining reducing conditions in the repository near-field. On the other hand, radiolysis reactions of the repository pore water might create oxidizing conditions: Radiolysis of water generates oxidants such as  $H_2O_2$ ,  $O_2$  and OH radicals and reductants, mainly  $H_2$ . As  $H_2$  is relative inert and escapes easily via diffusion through the pore water, the net effect of radiolysis is the generation of an excess of oxidants. In the case steel canisters are used as containment of the radioactive waste, these oxidants will be neutralized by the iron present in the near-field until all of it is oxidized. When copper canisters are used however, the amount of iron present in the repository near-field will much smaller, making the appearance of oxidizing conditions caused by radiolysis, much less improbable. Natural analogues suggest that the redox conditions in a nuclear waste repository might not be as simple as described above; e.g. redox conditions controlled by steel corrosion and radiolysis of pore water. Even when overall redox conditions in a repository are expected to be reducing, locally, oxidizing conditions may prevail.

Finally, many redox reactions occurring in the repository environment may not be at equilibrium with each other due to the very slow kinetics of many oxidation and reduction reactions.

Variations of redox conditions in the repository environment may strongly influence the aqueous speciation, solubility, and sorption behaviour of redox-sensitive radionuclides and thus their mobility in the near-field and in the far-field of a nuclear waste repository. On the other hand side, the presence of complexing ligands in the pore water may influence the redox speciation of the radionuclides due to stabilization of one of the redox states.

Redox-sensitive radionuclides investigated during the course of the Recosy project include fission products such as iodine, selenium, technetium and actinides including uranium, neptunium and plutonium.

Control of the redox conditions in experimental systems can be achieved either by using chemical redox buffers or by the use of an electrochemical cell coupled to a potentiostat. The latter approach avoids chemical disturbance of the experimental system but redox reactions can only occur at the electrode surface. Hence the electrochemical method can only be applied when efficient transport of radionuclides to the electrode surface is ensured. In most studies described below chemical reducing or oxidizing agents were applied. These include, Na-dithionite, hydrazine as reducing agents and Na-hypochlorite as oxidizing agent. It is clear that this type of experiments requires careful analysis of possible unwanted interactions of such chemicals with the experimental system.

Within work package 4 of the Recosy project, several of these radionuclide – redox interactions have been studied: The following topics were addressed: 1. Determination of the redox conditions present in groundwaters with the help of redox-sensitive radionuclides as redox indicators. 2. The influence of complexing ligands on radionuclide redox speciation; 3. The effect of the redox state on processes such as radionuclide solubilities, complexation of radionuclides with organic ligands and radionuclide sorption. 4. Interaction of radionuclides with pyrite, 5. Microbial impact on radionuclide redox behaviour. The outcomes of each of these five topics will be discussed in more detail below.

## ***The use of redox-sensitive radionuclides as redox indicators***

Depending on their redox state, redox-sensitive radionuclides behave very differently with regard to their reactivity and mobility. It is therefore essential to be able to characterize the redox conditions prevailing in the repository environment.

Determination of the redox conditions in environmental samples is usually carried out with the help of electrochemical measurements of redox potentials. Such measurements may provide a direct measure of redox conditions in the system under investigation. However, redox potential measurements have a number of practical and theoretical weaknesses:

1. Reactions at the liquid junction of the reference electrodes (blocking by particulate matter, precipitation,...),
2. Low exchange current densities at the surface of the metal working electrodes due to low concentrations of the redox-sensitive radionuclides,
3. Lack of redox equilibrium at the electrode surface (related to 2)
4. The occurrence of mixed potentials.

Alternative methodologies for the determination of the redox conditions in a repository environment are therefore of interest. One possible alternative methodology has been investigated by CTH in the framework of Recosy. The CTH methodology is based upon the addition of trace amounts of redox-sensitive actinides, such as uranium and neptunium to repository-relevant groundwaters followed by the determination of their redox speciation by solvent extraction. Finally the system redox potential is calculated based upon the measured redox speciation of the two actinides.

Three extraction reagents of the  $\beta$ -diketone type have been used: 0.5 M thenoyltrifluoroacetone (TTA) in xylene, 0.5M dibenzoylmethane(DBM) in chloroform and 0.05 M 4-benzoyl -3-methyl-1-phenyl pyrazol-5-one (PMBP) in xylene.

The extraction efficiency of these reagents and the effect of pH on the extraction efficiency, have been tested on a series of  $\text{NaClO}_4$  solutions ( $I=0.22$ ;  $0.6 \leq \text{pH} \leq 7$ ) spiked with aliquots of either U(IV), U(VI), Np(IV) and Np(V). The reduction of these actinides was carried out by bubbling  $\text{H}_2(\text{g})$  through the solutions in the presence of a Pt net. The redox state after reduction was verified using UV-Vis-NIR spectrometry and solvent extraction. The spectra and the extraction results showed that the uranium reduction was complete after six hours but that complete neptunium reduction could not be achieved.

From the tests with TTA, DBM and PMBP in the pH range  $0.6 \leq \text{pH} \leq 7$ , distribution coefficients (D), representing the distribution between the organic and aqueous phase, were calculated for uranium and neptunium in their different redox states at each pH. These D-values were used to calculate separation factors between couples of redox states (4/5 and 4/6) by simple division of the D-values for each redox state for a given extraction reagent.

Optimum conditions for separation of the actinide (IV) and (VI) states were achieved using 0.5 M DBM at pH 1, resulting in a separation factor of over 1000 (Figure 4.1a). However, recovery of U(IV) with this procedure is only 40%, so the extraction results have to be compensated for this by a corresponding factor. For the separation of the actinide (IV) and (V) states, optimum conditions were achieved using 0.05 M PMBP at pH 2 with separation factor of 1000 and where percentage extraction of (IV) with this system is 100% (Figure 4.1b). However, it is convenient to choose pH 2 for both separations as the separation of (IV) and (VI) with the DBM system is then down slightly from 1000 to 320, while the extraction efficiency has, on the other hand, increased to 65% and extraction results are compensated with a factor of 1.5. By selecting the same pH value, sample handling when measuring actinide oxidation states in groundwater samples is somewhat simplified since the same pH adjustment are made to the groundwater before extraction, irrespective if either U(IV)/(VI) or Np(IV)/(V) is to be measured.

The redox potentials of four synthetic Äspö groundwaters from the Long Term sorption Diffusion Experiment (LTDE) project (Widestrand et al., 2010) were determined both by electrochemical measurements and uranium as redox indicator and the resulting measured redox potentials were compared with theoretical redox potentials calculated from the chemical compositions of the synthetic porewaters. These four porewaters are, 1) the original Äspö porewater (LTDE water), 2) the LTDE water mixed with a small grain of pyrite, 3) LTDE water mixed with 1 g of crushed rock, and 4) the LTDE water mixed with both 1 g of crushed rock and a small grain of pyrite.

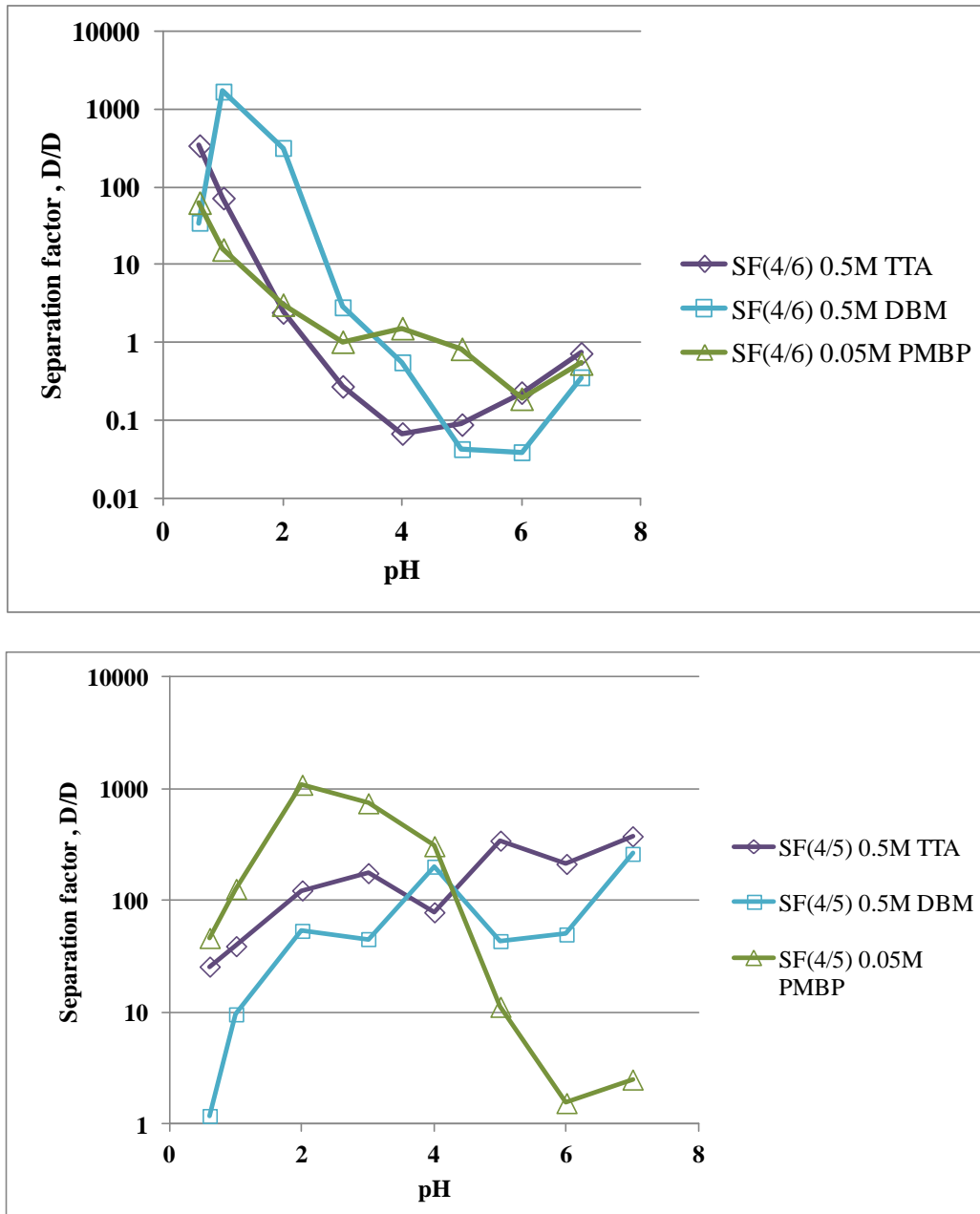


Figure 4.1. Separation factors ( $D/D$ ) for the separation of tetravalent and hexavalent actinides (a) and tetravalent and pentavalent actinides (b) as a function of pH

The theoretical  $E_h$  value derived from the chemical composition of the synthetic LTDE porewater was calculated to be  $-167$  mV versus SHE. The electrochemical measurements carried out with a combined Ag/AgCl/Pt electrode (Mettler Toledo Inlab Redox) gave an  $E_h$  value of  $+30$  mV immediately after preparation of the LTDE water. Redox potentials recorded in the samples spiked with uranium varied between  $+260\text{mV} \leq E_h \leq +320\text{mV}$  versus SHE.

These measurements clearly suggest that the theoretical redox potential of the synthetic LTDE water is not stable in an inert gas atmosphere glove box containing ~1 ppm O<sub>2</sub>, even not in the presence of pyrite. Redox potentials obtained from measured U(IV):U(VI) ratios with the help of speciation calculations using PhreeqC, varied between  $28\text{mV} \leq E_h \leq 69\text{mV}$  versus SHE. These values correspond very well with the  $E_h$  value electrochemically measured immediately after the preparation of the synthetic LTDE water suggesting that the uranium redox speciation method might give a better representation of the initial  $E_h$  value of the synthetic LTDE water. However, an  $E_h$  value of +300mV versus SHE would mean a U(IV)/U(VI) ratio of  $10^{-10}$ , which is far below the sensitivity range of the extraction techniques applied in this study.

In conclusion, redox-sensitive actinides such as uranium, may be employed as redox indicators as a complementary method for the determination of the redox conditions in groundwaters. The application of this method is however limited by the sensitivity of the techniques used to measure the ratios of the different redox states.

### ***The influence of complexing ligands on radionuclide redox speciation***

Complexing ligands in repository pore waters can strongly influence the redox state of radionuclides by stabilizing one of the redox states through complex formation. Organic complexing agents will be present in intermediate level waste (ILW), including decontamination agents such as EDTA and picolinic acid (PA), as well as polyhydroxylated carboxylic acids like  $\alpha$ -isosaccharinic acid (ISA) and gluconic acid (GLU). Such ligands are often strong complexants and can cause significant increases in radionuclide solubility, especially at high pH. In a study carried out by Loughborough University, the effect of the presence of such organic ligands on the redox state of technetium has been investigated. A nuclear waste repository will not be homogenous so there will be areas of reducing and oxidising potential, which could mean both Tc(VII) and Tc(IV) are present. If  $\text{TcO}_4^-$  migrates into an area of reducing conditions, the organics may complex with Tc during reduction to form water-soluble species. Also of relevance is the possibility of increased solubility when organics are in contact with reduced Tc. Studies were undertaken in which  $\text{TcO}_4^-$  was reduced in the presence and absence of the four ligands, to determine whether there was an increase in Tc solubility when  $\text{TcO}_2$  was contacted with the ligand.

### Tc(IV) complexation with organic ligands

Experiments were conducted in an N<sub>2</sub> glove box. Solutions were boiled, N<sub>2</sub> sparged and kept in presence of Fe filings to maintain reducing conditions. The ligands were added to NaOH(aq) in the form of solids at pH 13.3, to give concentrations between 0.4 and 0.001 mol dm<sup>-3</sup>. NH<sub>4</sub>TcO<sub>7</sub> was added and pH and E<sub>h</sub> measured. Reduction was achieved by 3 methods, the addition of 0.7 g of SnCl<sub>2</sub> or FeCl<sub>2</sub> or electrochemically. Five replicates were used. Control experiments showed that reducing conditions were maintained for the required periods of time and that 14 days was sufficient for steady state to be established.

The red data points in Figures 4.2, to 4.4 show the effect of EDTA, ISA and picolinic acid concentration on Tc(IV) solubility. The slopes of close to unity for ISA and picolinate indicate that the increase in solubility of Tc is being controlled by the formation of a 1:1 Tc(IV)-ligand complex. It is difficult to interpret the slope of 1.76 for EDTA.

### TcO<sub>4</sub><sup>-</sup> reduction in presence of ligands

Reduction experiments in presence of ISA indicated a lowering of [Tc](aq) from the initial concentration of 4 x 10<sup>-6</sup> mol dm<sup>-3</sup>, showing that ISA did not prevent reduction taking place (Figure 4.2). If this reduction was to Tc(IV), then the final [Tc](aq) should be the same as that produced by the addition of ISA to Tc(IV) solution, i.e. the Tc(IV)-ISA complex would again be formed, but by 2 different routes at steady state.

For ISA, this would seem to be the case. The presence of EDTA inhibited the reduction of pertechnetate by all three methods tried, i.e. SnCl<sub>2</sub>, FeCl<sub>2</sub> and electrochemically, (Figure 4.3). The presence of PA again inhibited the reduction of pertechnetate by all three reduction methods tried (Figure 4.4).

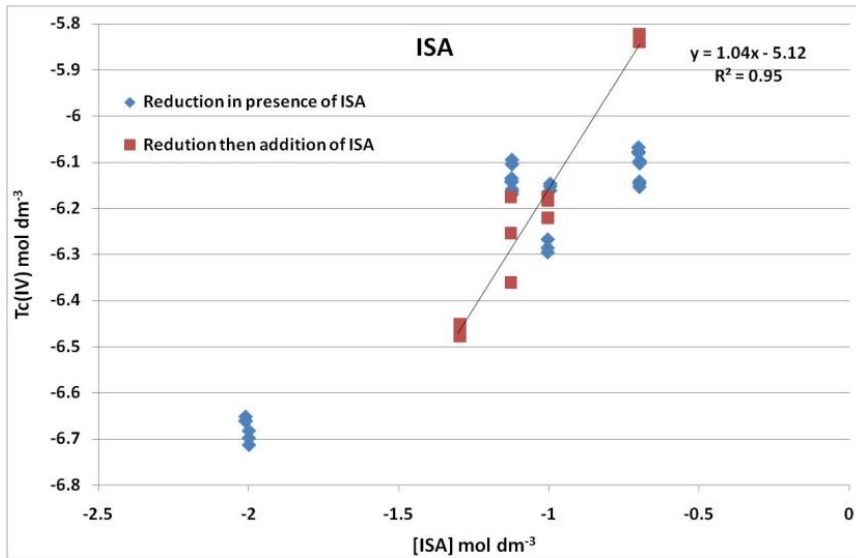


Figure 4.2 Comparison of final [Tc] with ISA at pH 13.3, starting from  $TcO_4^-$  and  $Tc(IV)$ .

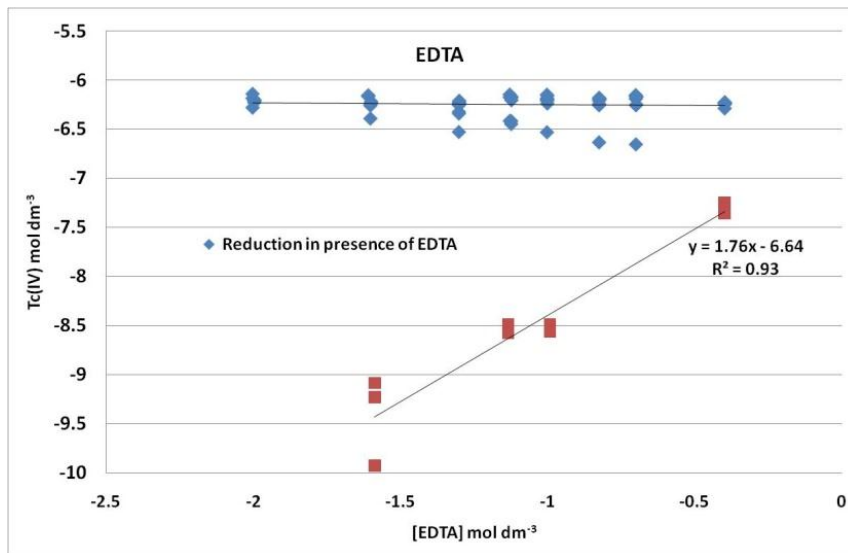


Figure 4.3 Comparison of final [Tc] with EDTA at pH 13.3, starting from  $TcO_4^-$  and  $Tc(IV)$

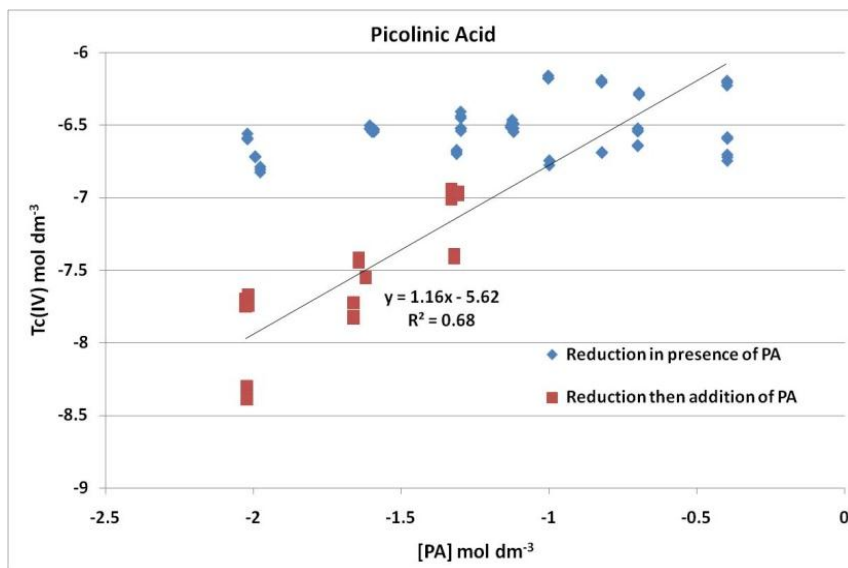


Figure 4.4 Comparison of final [Tc] with of PA at pH 13.3, starting from  $TcO_4^-$  and  $Tc(IV)$

Figure 4.5 shows the effect of increasing GLU concentration on technetium(IV) solubility. The slope of close to unity indicates that the increase in solubility of Tc is being controlled by the formation of a 1:1 Tc(IV)-gluconate complex. This relationship allows the calculation of a conditional stability constant for this complex at pH = 13.3 using the solubility product approach. The conditional stability constant for the Tc(IV) GLU complex was determined to be;  $\beta = 4.0 \times 10^{26}$  or  $\log \beta = 26.6 \pm 0.2$ .

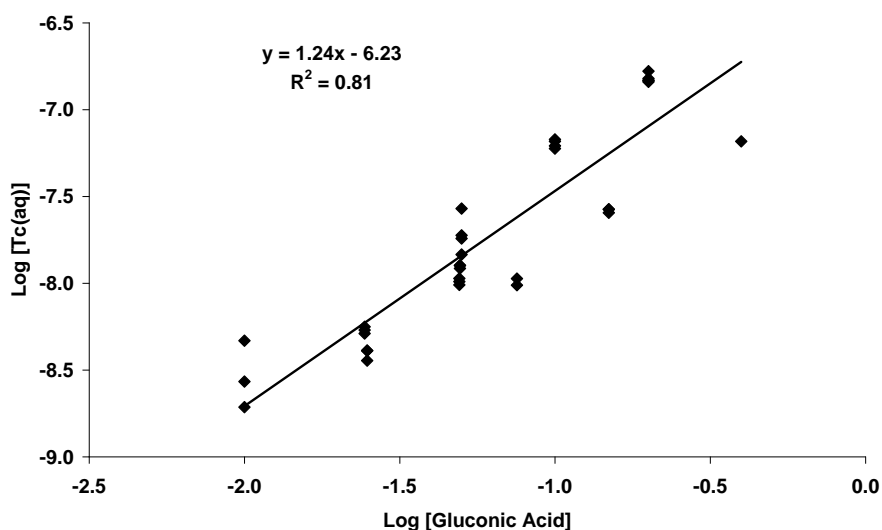


Figure 4.5 Effect of concentration of gluconic acid on aqueous technetium concentration above  $TcO_2(am)$  at pH 13.3.

### ***The influence of the redox conditions on the solubility of radionuclides***

Changes in redox conditions after closure of a nuclear waste repository or at local redox fronts can strongly influence the chemical behaviour of the radionuclides with regard to their solubility, reactivity towards dissolved ligands and solid surfaces and thus their overall mobility. Within work package 4 of the Recosy project, the influence of the redox state on the solubility of uranium has been investigated by AMPHOS. This study has been performed under alkaline conditions ( $10.0 \leq \text{pH} \leq 13.3$ ) reflecting the situation in the near-field of a cement-based low and intermediate level nuclear waste repository. The aim of the uranium solubility study was to explain the commonly observed trend of the measured  $\text{UO}_2$  solubility to increase with pH increasing from 10 to 14 (Gayer and Leider, 1957; Galkin and Stepanov, 1961; Tremaine 1981; Ryan and Rai, 1983; Bruno et al., 1987; Casas, 1989; Rai et al. 1990; Torrero, 1995; Yajima, 1995; Ollila, 2002; Fujiwara et al. 2005).

The solubility of uranium (IV) oxide has been studied in the pH range from 9-12 and using different anoxic / reducing conditions at 25° C in solutions without complexing ligands (carbonate, phosphate, silicate, etc.) where uranium oxides, oxyhydroxides or hydroxides are expected to be the solubility controlling solids.

The  $E_h$  - pH predominance diagram for the uranium system calculated with the ThermoChimie database Parkhurst and Appelo (1999) (as the sit.dat file) under alkaline conditions is shown in Figure 4.6. The Pourbaix diagram indicates  $\text{UO}_2(\text{OH})_3^-$  and  $\text{UO}_2(\text{OH})_4^{2-}$  are the predominant U(VI) complexes under alkaline conditions, and  $\text{U}(\text{OH})_4(\text{aq})$  is the only U(IV) hydrolysis complex under reducing conditions. Despite the fact that the  $\text{U}(\text{OH})_4(\text{aq})$  complex is currently the only U(IV) hydrolysis species accepted by the NEA database (Guillaumont et al. 2003) and included in ThermoChimie, discussion on U(IV) speciation under alkaline conditions has been ongoing for decades (Gayer and Leider, 1957; Galkin and Stepanov, 1961; Tremaine 1981; Ryan and Rai, 1983; Bruno et al., 1987; Casas, 1989; Rai et al. 1990; Torrero, 1995; Yajima, 1995; Ollila, 2002; Fujiwara et al. 2005).

Published experimental data on the aqueous concentration of uranium in equilibrium with a  $\text{UO}_2$  solid phase have been collected and plotted in Figure 4.7. Despite the wide range of experimental conditions ( $E_h$ , ionic strength, reducing agents, crystallinity of the solid) used by the authors, some of the data show a common trend of increasing  $\text{UO}_2$  solubility with pH.

There are currently two explanations for this solubility increase: 1) partial oxidation of the uranium U(IV) to U(VI), 2) formation of anionic species of uranium U(IV) such as  $U(OH)_5^-$  and/or  $U(OH)_6^{2-}$  (see Figure 4.6).

In order to determine if redox reactions are occurring in these systems, increasing uranium solubility under alkaline conditions, AMPHOS has performed  $UO_2$  solubility experiments under well controlled redox conditions; i.e. in the presence of  $H_2$  at different pressures and in the presence of Na-dithionite as a reducing agent.

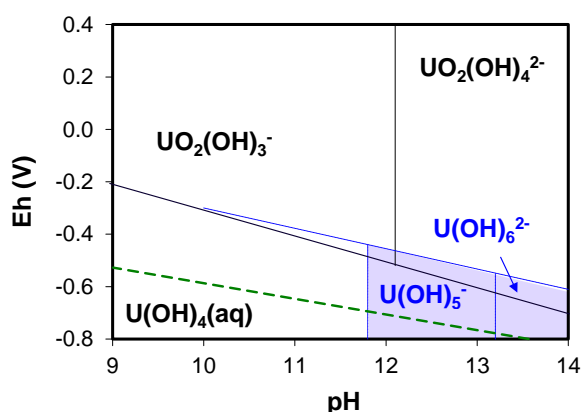


Figure 4.6.  $E_h$ -pH predominant diagram of uranium aqueous species using selected uranium species in ThermoChimie database (Parkhurst and Appelo, 1999) (black lines). The blue dashed lines stand for the simulation using selected uranium species in ThermoChimie database and also including the formation constants of  $U(OH)_5^-$  and  $U(OH)_6^{2-}$  reported in Fujiwara et al. (2005).  $[U]_{TOT} = 1 \cdot 10^{-7} M$ ,  $I=0$

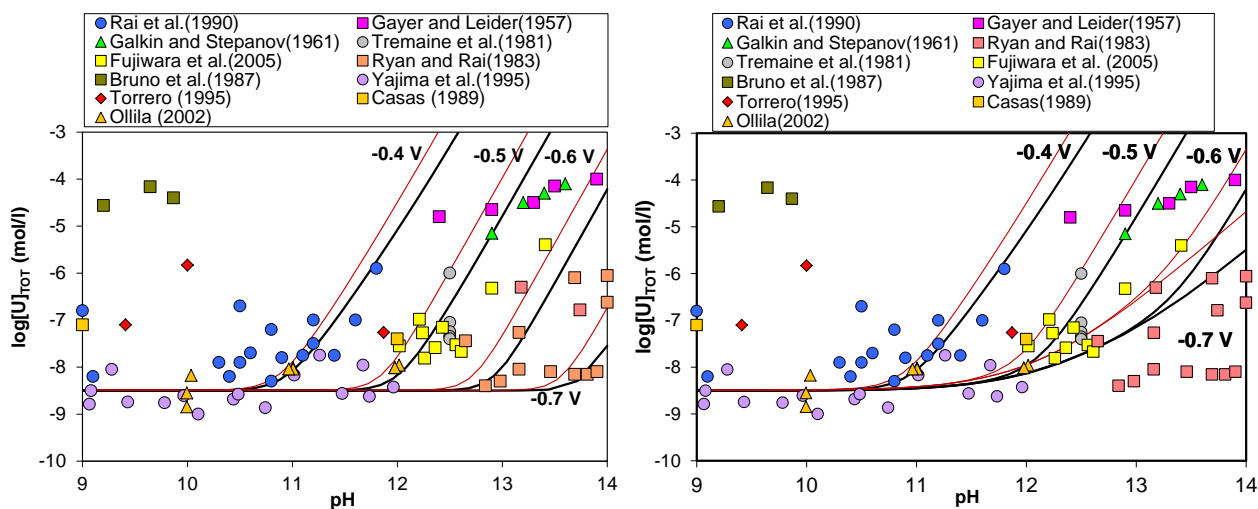


Figure 4.7 Solubility data described in the literature under alkaline conditions for uranium oxide ( $UO_2$ ). (Left) Lines: Calculated solubility at different Eh values using the ThermoChimie database. (Right) Lines: Calculated solubility at different Eh using the ThermoChimie database together with the formation constants of  $U(OH)_5^-$  and  $U(OH)_6^{2-}$  reported in Fujiwara et al. (2005). Black lines,  $I = 0$ . Red lines,  $I = 1M$

$H_2(g)$  is thermodynamically able to generate highly reducing conditions, however, it has been demonstrated that this is only possible in presence of a catalyst. For instance, under repository conditions,  $e$  particles (e.g. Pd, Pt, Mo) generated by fission processes and embedded in the spent fuel matrix can activate  $H_2(g)$  generating highly reducing conditions (Shoesmith, 2008). Also, the catalytic capacity of  $UO_2(s)$  has been proven in a-doped  $UO_2$  and it is known that these properties are promoted by surface density defects (Senanyake et al. 2007).

The first solubility experiments were performed in an autoclave batch reactor under  $H_2(g)$  atmosphere ( $P_{H_2(g)} = 1.8$  atm) with freshly prepared  $UO_2(am)$  in 0.01 M  $NaClO_4$  solution at  $pH = 9.4$ . The autoclave was connected to a Time-resolved Laser-induced Fluorescence Spectrometer (TRLFS) and to a cell designed to measure  $pH$  and  $E_h$  online.

With this experimental set up the formation of  $UO_2(OH)_3^-$  was observed by fluorescence spectroscopy indicating oxidation of  $UO_2(am)$ . These data together with the measured  $pH$ ,  $E_h$  and total U concentration confirmed the oxidative dissolution of  $UO_2(am)$  under anoxic conditions with the  $H_2(g)$  acting as inert gas (Riba et al. 2012).

A second series of solubility experiments was designed to investigate the effect of high  $H_2(g)$  pressure on  $UO_2(s)$  solubility. To this end, a previously washed unirradiated  $UO_2$  pellet was placed in an alkaline ( $pH$  11) 0.1 M  $NaClO_4$  solution in an autoclave under high hydrogen pressure (ca. 9 bars). The system was periodically sampled and at each sampling point the  $H_2(g)$  pressure was allowed to drop. The final  $H_2(g)$  pressure after six sampling operations was 6 bars (the final reaction time was 14 days).

The results indicated that  $pH$  was constant throughout the experiment and the  $E_h$  stabilized at  $\sim 0.25V$  after one day reaction time. This measured  $E_h$  is well above the value corresponding to  $H_2O$  in equilibrium with  $H_2(g)$  at the experimental pressure and also to the one characteristic of the redox pair  $U(IV)/U(VI)$  at the measured  $pH$ . Actually, the measured  $E_h$  is typical of “redox-neutral” conditions described in Neck et al. (2007). However, the total measured U concentration was surprisingly low according to the measured  $E_h$  controlling the oxidative dissolution of  $UO_2$ . The measured  $E_h$  and U concentration in solution was in agreement with the formation of a Na-uranate secondary phase  $Na_2U_2O_7(am)$  controlling the uranium solubility (Yamamura et al., 1998).

The study of  $UO_2(s)$  solubility performed under alkaline conditions and different  $H_2(g)$  pressures corroborates the poor performance of  $H_2(g)$  to keep uranium as a tetravalent state

in absence of a catalyst (Trummer et al. 2008) and the possible transformation of  $\text{UO}_2(\text{s})$  to  $\text{U}(+\text{VI})$  phases depending on the composition of the contacted water (Riba et al. 2012).

Na-dithionite has been used as a reducing agent in order to avoid the oxidative dissolution of  $\text{UO}_2(\text{am})$  under alkaline conditions. In this study, solubility of freshly prepared  $\text{UO}_2(\text{am})$  has been measured at  $\text{pH} = 10, 11$  and  $12$  at ionic strength of  $0.1 \text{ M}$  ( $\text{NaClO}_4$ ) and using two different dithionite concentrations ( $0.001$  and  $0.01 \text{ M}$ ).

In order to understand the dithionite behaviour in these experiments, the predominance species of the sulphur system under different  $\text{pH-E}_h$  conditions has been considered. The sulphur system in aqueous solution has a rather complex chemistry mainly due to the formation of metastable species. The decomposition of  $\text{S}_2\text{O}_4^{2-}$  under acidic conditions has been reported by several authors. Despite its higher stability under alkaline conditions, decomposition has also been observed to occur in high  $\text{pH}$  environments (Lister and Garvie, 1959; Szecsody et al., 2004). According to the literature, the identified coexisting species resulting from  $\text{S}_2\text{O}_4^{2-}$  decomposition are  $\text{S}_2\text{O}_3^{2-}$ ,  $\text{SO}_3^{2-}$ ,  $\text{S}^{2-}$  and  $\text{S}(\text{s})$  (Carvalho and Schwedt 2001).

The general trend in all the performed experiments using dithionite as reducing agent is that despite the redox reading of the systems are characteristic of different sulphur redox pairs (predicting high amounts of uranium in solution) the measured uranium concentration and the thermodynamic study of the systems indicate limited oxidative dissolution of  $\text{UO}_2(\text{am})$  (Riba et al. 2012).

From the current study on the solubility of  $\text{UO}_2(\text{s})$  the following conclusions can be drawn:

- (1) The experiments performed under  $\text{H}_2(\text{g})$  atmosphere indicate that  $\text{H}_2(\text{g})$  behaves as an inert gas without reducing properties. The measured  $E_h$  is in agreement with the occurring uranium processes in the system. At low Na concentration ( $0.01 \text{ M NaClO}_4$ ), the measured redox potential respond to the oxidative dissolution process of  $\text{UO}_2(\text{am})$ . However, at  $0.1 \text{ M NaClO}_4$  the measured redox potential responds to redox-neutral conditions and measured uranium concentration is in agreement with Na-uranate secondary phase controlling the U in solution.
- (2) The experiments performed with Na-dithionite as a reducing agent demonstrate that the  $E_h$  measurements respond to different dithionite processes of oxidation and decomposition as a function dithionite concentration,  $\text{pH}$  and reaction time. Despite the variability in the redox potential, the measured U concentration suggest that sulphide is

controlling the limited extent of oxidative dissolution process of  $\text{UO}_2(\text{am})$ . Therefore, under the experimental conditions, the low concentration of U in solution is associated with the existence of U(VI) aqueous complexes and it cannot be mainly attributed to the formation of  $\text{U}(\text{OH})_5^-$ .

### ***The effect of the redox state on radionuclides sorption processes***

The uptake of redox-sensitive radionuclides by near-field solids and the host rock under varying redox conditions is poorly known (e.g. Wieland and Van Loon, 2003) due to the many experimental difficulties to control the redox conditions during sorption experiments in the laboratory. Many sorption databases used in performance assessment studies for nuclear waste repositories rely on chemical analogies: i.e. the analogy in sorption behaviour of radionuclides having certain similar chemical characteristics such as the electrostatic interaction energy expressed by  $(Z_{\text{eff}}/d)$ ; the ratio of the effective charge ( $Z_{\text{eff}}$ ) and the interatomic distance between the metal cation and the oxygen from the sorption sites ( $d$ ). Furthermore, it is assumed that a positive correlation exists between the sorption strength ( $R_d$  value) and the electrostatic interaction energy (e.g., Wieland and Van Loon, 2003).

### ***Sorption of Am and Pu on Fe(II/III) oxides and natural clays and soils***

The applicability of the chemical analogy approach was tested in a study of the sorption of Pu, Np, Am and U on different iron oxides, Triassic clay and a meadow soil by FMTC.

To investigate of the sorption behaviour of Pu(III) by Fe(II/III) oxides (wustite/magnetite and hematite) as well as by soil, Am (III) was used as a chemical analogue for Pu(III).

Both the batch sorption method and the laboratory column method were applied. The composition of two powdered iron oxides was verified using Mössbauer spectroscopy. One of them showed properties characteristic of hematite ( $\text{Fe}_2\text{O}_3$ ). The Mössbauer spectra of another mineral indicated a Fe(II)/Fe(III) ratio of 50%/50%. Based on SEM analysis, particle sizes of wustite/magnetite were in the range of  $2 \cdot 10^{-6}$ - $2 \cdot 10^{-5}$ m and those of hematite ranged between  $2 \cdot 10^{-6}$ - $1 \cdot 10^{-5}$ m. After partial mixing for 92-hour at a solid:liquid ratio of 0.1 kg/L, the  $^{243}\text{Am}$  activity in both phases was determined using a well-type HPGe detector (the effective crystal - 170  $\text{cm}^3$ , energy resolution - 2.05 keV at 1332.5 keV) coupled to the MCA Inspector 2000 unit with Genie 2000 gamma-ray analysis software (Canberra Industries, USA).  $^{243}\text{Am}$  sorption by the sorbents from 0.1 M  $\text{NaNO}_3$  solution was determined to be pH-dependent (Figure 4.8).

<sup>243</sup>Am sorption onto wustite/magnetite and soil showed a negative correlation with pH, while the sorption of <sup>243</sup>Am ions onto hematite increased with rising pH .

<sup>243</sup>Am sorption onto wustite/magnetite was in the range of 30-40% after a reaction time of 92 hours. The largest amount of <sup>243</sup>Am was sorbed at pH 2.15. On hematite maximum sorption (about 40%) of <sup>243</sup>Am was observed at pH 6.95 and 9.01 indicating that hematite possesses a higher Am sorption capacity at alkaline pH values.

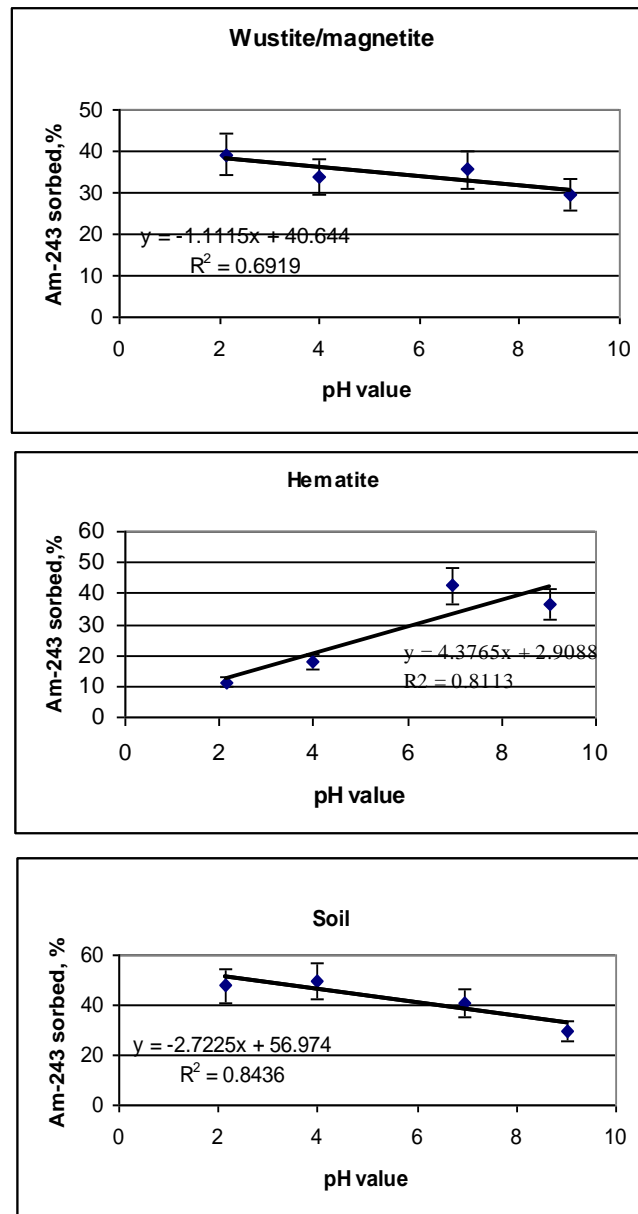


Figure 4.8 <sup>243</sup>Am pH-dependent sorption onto three different sorbents

The soil used in model experiments contained 5.3% of organic matter, 2975 mg/kg Fe, 247 mg/kg Mn, 580 mg/kg Ca and microelements Ni, Cu, Zn, Pb, Cr. Fe and Mn oxides have large sorption capacity for metal cations explaining the higher Am sorption on soil compared to pure hematite or wustite/magnetite. Soil organic matter consists basically of humic substance. Thus, humic substance can enhance Am<sup>3+</sup> cation adsorption at low pH values but reduce the adsorption at high pH values. Enhanced Am sorption in the acidic pH range can occur due to the formation of additional binding sites by humic substance. The formation of soluble Am-humate complexes above 6 pH value in solution could be responsible for the reduction of <sup>243</sup>Am sorption on soil surface.

Thus, it can be speculated that under the present experimental conditions Am(III) and Pu(III) sorption behaviour is similar.

<sup>243</sup>Am distribution in the sorbent column vertical profile at different pH values and 0.5 mL/h flow rate of 0.1 mol/L NaNO<sub>3</sub> aqueous solution was determined. Experimental results suggest <sup>243</sup>Am accumulation in the upper 2 cm layer regardless of geosorbent origin and aqueous solution pH.

In a second sorption study Triassic clay from the industrial exploitation site Šaltiškiai in North Lithuania was used. Iron oxides were synthesized using procedures modified from Cornell and Schwertmann (2003). Sorption experiments were carried out under argon atmosphere. 0.01 – 0.1 M NaNO<sub>3</sub> solutions were used as background electrolyte. Pu(IV), Pu(V) and Am(III) were used in sorption experiments at initial concentrations of Pu isotope mixture and <sup>241</sup>Am of  $1.1 \cdot 10^{-9}$  –  $2.5 \cdot 10^{-11}$  and  $3.2 \cdot 10^{-11}$  mol·L<sup>-1</sup>, respectively. Pu oxidation states were produced electrochemically and/or using nitric acid solutions and very low concentration of hydrogen peroxide. There were no any additional ions in the solutions (Sorin et al., 1972, Orlandini et al., 1986, Perevalov and Molochnikova, 2009). Oxidation state distribution was measured using ultrafiltration and solvent extraction with TTA, HDEHP and DBM.

In the natural clay system in 0.1 M NaNO<sub>3</sub> after 7 days contact time, the Pu oxidation state distribution analysis in the liquid-phase indicated a comparatively high content (up to 75%) of Pu(III/IV) at pH 4.86 – 4.98 while polymeric species of Pu(IV) were found to be the dominant species at pH 5.76 – 8.21. Pu oxidation states in the solid-phase were determined after the desorption step using 3 mol·L<sup>-1</sup> HCl, and Pu(III,IV), Pu(V) and Pu(VI) as well as Pu(IV) at pH=0 were analyzed in parallel. The content of Pu(III) was calculated from mass balance considerations. Pu(III) was not found in the system at pH (5.76 - 8.2) while 4.9% and 10.7%

of Pu(III) were found at  $\text{pH } 4.86 \pm 0.11$  and  $4.98 \pm 0.08$ , respectively. Reduction by iron-bearing minerals such as montmorillonite and siderite detected in the Triassic clay under investigation may explain the presence 10.7 % of Pu(III) in solids because these minerals are known to possess significant reductive capacity.

The oxidation state distribution at trace initial Pu concentrations in liquid- and solid-phase of the natural clay systems was studied. Existing solvent extraction techniques were verified with respect to Pu(III) quantification in the liquid- and solid-phase. Pu(III) was desorbed quantitatively from the solids, no oxidation of Pu(III) and Pu(IV) was observed during desorption procedure. It was found that Pu(IV) was reduced by iron-bearing minerals in the natural clay in the pH range from 4.22 to 4.98. However, no reduction was detected in the near-neutral and high pH range.

After 7 days, sorption experiments showed an increase in the amount of Pu(III) sorbed on the solid phase (up to 11% at  $\text{pH} = 5$ ) in the natural clay suspension in 0.1 M  $\text{NaNO}_3$  labelled with Pu(IV). In the kinetic sorption experiment with goethite suspensions in 0.01 M  $\text{NaNO}_3$ , Pu(V) was mainly reduced to Pu(IV), and a small portion of Pu(III) found at the beginning in the solids (up to 15%) was later oxidized to Pu(IV).

#### *Influence of the redox state on the retention of neptunium by cementitious materials*

Validation of the chemical analogy approach for the actinides was one goal of the studies carried out by PSI in the framework of Reosy. The influence of the redox state of neptunium on its uptake by cementitious materials under hyperalkaline conditions was investigated. Neptunium is commonly believed to exist in oxidation states +IV and +V in a cementitious environment under reducing, respectively oxidizing conditions. However, recent investigations carried out in the framework of Reosy show that the possible formation of anionic Np(VI) species ( $\text{NpO}_2(\text{OH})_3^-$  and  $\text{NpO}_2(\text{OH})_4^{2-}$ ) in oxidizing hyperalkaline environments, in analogy to U(VI), may significantly limit the stability field of Np(V) in favour of Np(VI) species (Gaona, et al., 2012a).

Assuming a correlation between the electrostatic interaction energy and sorption, it may be anticipated that  $R_d$  values for neptunium increase in the series Np(V) ( $Z_{\text{eff}} = 2.2$ ,  $d = 0.25\text{nm}$ ) < Np(VI) ( $Z_{\text{eff}} = 3.0$ ,  $d = 0.242\text{nm}$ ) < Np(IV) ( $Z_{\text{eff}} = 4.0$ ,  $d = 0.24\text{nm}$ ) (Choppin, 1984; Neck and Kim, 2000).

Whereas experimental data concerning the sorption of Np(V) by cementitious materials are scarce, sorption data on Np(IV) and Np(VI) are non-existing in the literature due to the

experimental difficulties to stabilize the +IV and +VI redox states. Therefore, in many sorption databases, sorption values for redox-sensitive actinides such as Np(IV) and Np(VI), are often estimated based on chemical analogy with other tetravalent and hexavalent cations such as Th(IV) and U(VI), for which sorption data are more easily experimentally accessible (e.g., Wieland and Van Loon., 2003).

Batch sorption experiments with Np(IV, V, VI) were carried out on C–S–H phases, the main component of hardened cement paste as well as on hardened cement paste. In addition batch sorption experiments were carried out on titanium dioxide (TiO<sub>2</sub>) in order to determine the effect of the aqueous neptunium speciation on the sorption behaviour of neptunium under hyperalkaline conditions. Finally sorption experiments with Th(IV) and U(VI) were carried out for comparison with the aim of verifying the analogous sorption behaviour of actinides with the same oxidation state. All experiments were carried out in inert atmosphere glove boxes (O<sub>2</sub> and CO<sub>2</sub> concentration < 2 ppm).

The redox state of Np in all the sorption tests was fixed by the addition of Na-dithionite as a reducing agent (Np(IV)) or Na-hypochlorite as an oxidizing agent (Np(VI)). No redox buffer was used for the experiments with Np(V). Preliminary sorption tests with Th(IV) and U(VI) showed that these reducing and oxidizing agent have no influence on the aqueous speciation of tetravalent and hexavalent actinides.

Due to its high stability under hyperalkaline conditions and its very low recrystallisation rate, radionuclide incorporation into the structure of TiO<sub>2</sub> is improbable and sorption is expected to be reversible. Neptunium sorption on this substrate was found to be fast. Furthermore, in view of the very low loadings used in the present studies, it may be safely assumed that the sorption behaviour of Np on TiO<sub>2</sub> is linear. The above listed properties make TiO<sub>2</sub> an ideal substrate for the study of the effect of speciation on the sorption of Np under highly alkaline conditions.

The effect of pH on the Np(IV,V,VI) uptake by TiO<sub>2</sub> was investigated. Overall, the formation of anionic species with progressing hydrolysis of Np appeared to adversely affect the neptunium sorption. In the case of Np(IV), Np(OH)<sub>4</sub> is the only species present in the pH range 10 ≤ pH ≤ 14, resulting in constant sorption values for this tetravalent species (Figure 4.9a). In the case of the neptunyl species (Np(V/VI)), the aqueous Np species become progressively hydrolysed with increasing pH, up to the formation of anionic hydroxy species (Np(V)O<sub>2</sub>(OH)<sub>2</sub><sup>-</sup>, Np(VI)O<sub>2</sub>(OH)<sub>3</sub><sup>-</sup> and Np(VI)O<sub>2</sub>(OH)<sub>4</sub><sup>2-</sup>) at the higher end of this pH range. In

parallel, the sorption of Np(V/VI) decreases significantly, suggesting a much weaker affinity of these anionic hydroxyl species for  $\text{TiO}_2$  (Figure 4.9a). The observed sorption reduction could be described satisfactorily by assuming that the anionic species  $\text{Np(V)O}_2(\text{OH})_2^-$  and  $\text{Np(VI)O}_2(\text{OH})_4^{2-}$  do not sorb and that the formation of these two anionic species in solution competes with the surface complexation reaction on the  $\text{TiO}_2$ .

Sorption experiments with Np(IV,V,VI) were performed on C–S–H phases with varying Ca:Si (C:S) mol ratios in the range  $0.65 < \text{C:S} < 1.65$ . It is known that increasing C:S ratios of C–S–H phases are always accompanied by increasing pH values and increasing Ca concentrations in solution

In Figure 4.9b,  $R_d$  values obtained for Np(IV), Np(V), Np(VI), are plotted against the pH. The large scatter in some of the datasets (e.g. Np(IV) and Np(V)) are attributed to incomplete phase separation. Due to strong sorption of the radionuclides onto colloidal materials, incomplete phase separation may increase the activity in the supernatant and thus result in a significant decrease of  $R_d$  values.

The sorption data indicate a very high affinity of Np(IV) and Np(V) for C–S–H phases characterized by  $R_d$  values in the range of  $10^5 \text{ L kg}^{-1}$  to  $10^6 \text{ L kg}^{-1}$ , independent of the pH. The affinity of Np(VI) for C–S–H phases appears to be high at  $\text{pH} = 10$  with a tendency to decrease with pH values increasing to 12.5.

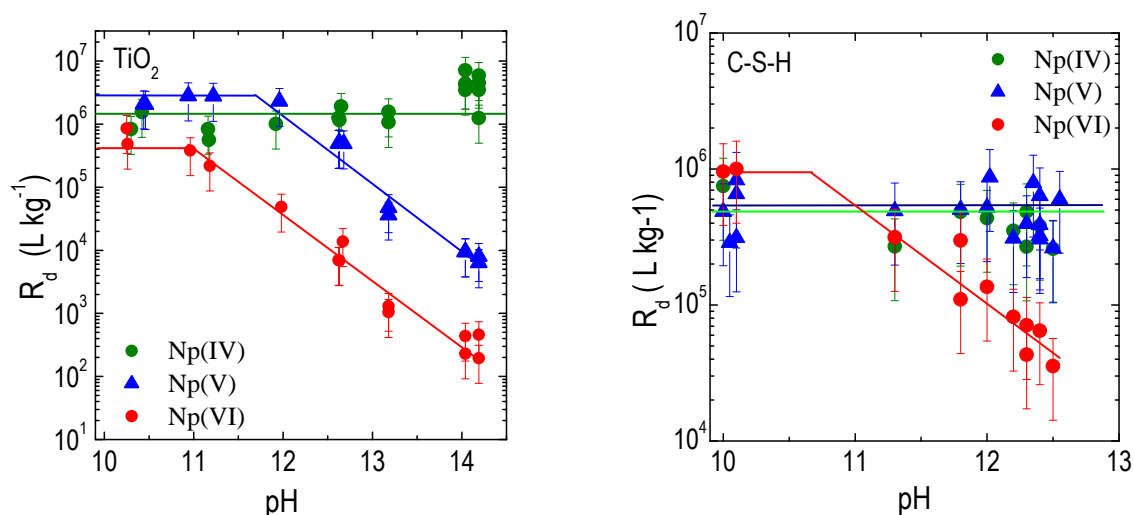


Figure 4.9: Effect of pH on the Np(IV, V, VI) sorption on  $\text{TiO}_2$  (a) and on C–S–H phases (b).

The S:L ratio =  $2 \times 10^{-4} \text{ kg L}^{-1}$ . .  $[^{239}\text{Np}] = 1.5 \times 10^{-10} \text{ M}$ .  $I = 1.0$ .

The sorption behaviour of the tetravalent, pentavalent, and hexavalent actinides on C–S–H phases appears to be very similar to the sorption behaviour observed previously on  $TiO_2$  (Figure 4.9a) and can thus be explained by their speciation behaviour. With rising pH, negatively charged species increasingly dominate the aqueous speciation of the hexavalent actinides, thus resulting in decreasing sorption. In the case of the tetravalent Np, the aqueous speciation is independent of pH in the pH range studied, resulting in constant sorption values with rising pH for this redox state. In the case of Np(VI), anionic species dominate the aqueous speciation starting from pH = 11, resulting in decreasing  $R_d$  values. The constant sorption values observed in the case of Np(V) are explained by its weaker hydrolysis with anionic  $Np(V)O_2(OH)_2^-$  species appearing only above pH = 12; i.e. outside the experimental pH range.

The similar sorption behaviour of the tetravalent, pentavalent and hexavalent neptunium on  $TiO_2$  and C–S–H phases suggest that the variation in the C–S–H composition only has a marginal influence on actinide sorption.

In addition, sorption experiments with Th(IV) and U(VI) were carried out on C–S–H phases with different C:S ratios (pH range:  $10 < pH < 12.5$ ) to compare the sorption behaviour of these actinides with that of Np(IV) and Np(VI). The sorption behaviour of Th(IV) was found to be identical to that of Np(IV), i.e. very high  $R_d$  values and no dependence of pH were observed. U(VI) exhibited a pH dependence similar to Np(VI), i.e. decreasing  $R_d$  values with rising pH. The absolute  $R_d$  values for U(VI) were, however, found to be slightly higher (Factor of 2) than those for Np(VI). Overall, it is concluded that the assumption of analogous sorption behaviour of actinides with the same oxidation state is valid.

In addition to the wet chemistry studies, EXAFS investigations were carried out at the ROBL beamline at the European Synchrotron Radiation Facility (ESRF) in Grenoble (France). C-S-H phases with C:S mol ratios 0.75, 1.07 and 1.65 (synthesized both in Milli-Q water and in artificial cement pore water – ACW), and a hardened cement paste (HCP) of a sulfate resistant Portland cement (CEM I 52.5 N HTS) were spiked with a Np(IV/V) tracer resulting in a final Np concentration of about 8500 ppm (dry weight).  $Na_2S_2O_4$  was added to the suspensions containing Np(IV) to stabilize its tetravalent state and NaClO was added to some suspensions containing Np(V) to oxidize the Np to the hexavalent state.

The EXAFS studies on Np(IV)-doped C-S-H and HCP samples revealed that Np(IV) was predominantly incorporated in the structure of C-S-H phases. The two main species identified correspond to Np(IV) in C-S-H with a C:S mol ratio of 1.65 as in fresh cement and with a C:S mol ratio of 0.75 as in highly degraded cement. The high Si-coordination numbers ( $CN_{Si}$ ) obtained for both Np(IV)-C-S-H species ( $5.0 \pm 1.5$  and  $3.6 \pm 0.7$ , respectively) strongly suggests that an incorporation mechanism in the C-S-H structure is taking place. Amplitude of the Ca-shell for Np(IV)-C-S-H 1.65 was found to be significantly larger than for Np(IV)-C-S-H 0.75, indicating a molecular environment richer in Ca for Np(IV) incorporated in C-S-H with C:S 1.65. Based on this information and considering the structural data reported in Garbev et al. (2008) for micro-crystalline C-S-H phases, two candidates for the Np(IV)-C-S-H end members were identified (Figure 4.10). A detailed description of this study is given in Gaona et al. (2011).

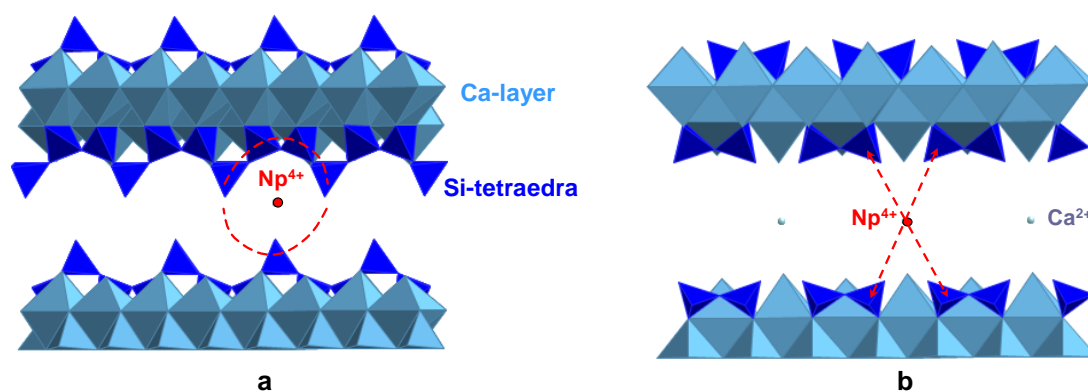


Figure 4.10 Candidates for Np(IV)-C-S-H end members, according with Np structural parameters determined in this work and in agreement with C-S-H structures reported in Garbev et al. (2008) for low (a) and high (b) C:S ratios.

EXAFS measurements on Np(V)-doped C-S-H and HCP samples under anoxic conditions revealed that no reduction to Np(IV) occurred in the course of the uptake process. A rather uniform molecular environment of sorbed Np was observed throughout the complete sequence of cement degradation (HCP/ C-S-H 1.65  $\rightarrow$  C-S-H 0.75), in agreement with the very high sorption values determined and nearly pH independent behaviour observed in wet chemistry experiments. The short Np-O<sub>eq</sub> distances together with the relatively large  $CN_{Si}$  for bicoordinated Si suggest that an incorporation mechanism in the C-S-H structure could control the uptake of Np(V) by cementitious materials.

Both XANES and EXAFS confirmed that Np(VI) exists under oxidizing hyperalkaline conditions. Two different Np(VI) sorbed species were identified by EXAFS, which dominate in HCP/C–S–H 1.65 (fresh cement, pH ~ 12.5 – 13.3, lower  $R_d$ ) or C–S–H 0.75 (degraded cement, pH ~ 10, higher  $R_d$ ), respectively. The latter species may play a role in the early oxidizing stage of a cement-based repository and in oxidizing waste forms (e.g.  $\text{NO}_3$ -rich wastes). Structural data obtained for both Np(V) and Np(VI) sorbed-species can be found in Gaona et al. (2012b).

The following conclusion could be drawn from this work:

- the uptake of Np(IV/V/VI) in cementitious materials takes place on the C–S–H fraction;
- the sorption behaviour of Np(IV/V/VI) on C–S–H phases can macroscopically be interpreted in terms of its aqueous speciation assuming that anionic hydrolysis species do not sorb.
- the sorption of Np(IV) and probably of Np(V/VI) takes place through incorporation in the C–S–H interlayers;
- actinides with the same oxidation state exhibit similar sorption behaviour on cementitious materials (chemical analogy) but the correlation between  $R_d$  values and electrostatic interaction energy could not be confirmed, i.e.  $R_d$  values for Np(V) were much higher than expected.

### ***Influence of the redox state on the formation of ternary complexes***

The redox state may also affect the extent of sorption and the sorption reversibility in humic acid (HA) ternary systems, i.e. systems where humic substances, mineral surfaces and radionuclides are present together. In such systems, the redox state affects both the aqueous speciation (i.e. the complexation with HAs) and the sorption on the solid.

Manchester University studied two types of ternary systems: 1) U/Pu ternary systems of HAs and hematite, bentonite and kaolinite. 2) Th / U / Pu ternary systems of HA and quartz.

### ***Ultra Trace Actinide Behaviour in Ternary Systems using $^{237}\text{U}/^{237}\text{Pu}$***

In collaboration with the Flerov laboratory, Dubna, two new routes to high specific activity uranium and plutonium tracers ( $^{237}\text{U}$ ;  $^{237}\text{Pu}$ ) were developed. These allow U and Pu chemistry to be studied over a wide range of concentrations. They were used to study U/Pu ternary systems of HA and hematite, bentonite and kaolinite. The effect of ionic strength, pH and HA concentration in the U(VI)/humic/bentonite ternary system were investigated (Figure

4.11). Uranyl sorption was strongly dependant on pH and the presence of HA. In the absence of HA, an enhancement in the uptake with increasing pH was observed, and a sharp sorption edge was found to take place between pH 3.2 and 4.2. The presence of HA slightly increases U(VI) sorption at low pH and curtails it at moderate pH. In the basic pH range for both the presence and absence of HA the sorption of uranium was significantly reduced due to the formation of soluble uranyl carbonate complexes. More importantly, the behaviour at trace level concentrations was found to be different to that determined at higher concentrations, showing the importance of the use of high specific activity isotopes to allow studies at low radionuclide concentrations. There was an enhancement in the sorption of HA with increasing ionic strength, but U(VI) sorption was found to be indifferent to ionic strength, both in the absence and presence of HA at  $I < 1$ .

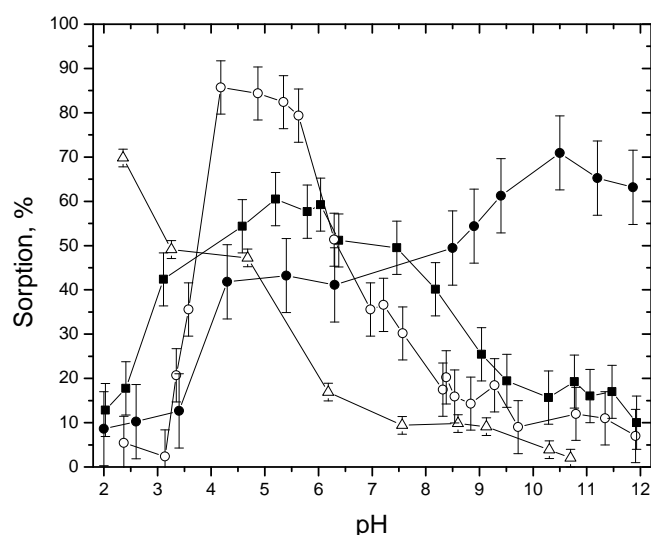


**Figure 4.11** Effect of pH on U(VI) ( $10^{-10}$  M) sorption onto  $1 \text{ g}\cdot\text{L}^{-1}$  bentonite in the absence of HA ( $\circ$ ) and in the presence of  $100 \text{ mg}\cdot\text{L}^{-1}$  HA ( $\blacksquare$ ) and the sorption of HA on bentonite alone ( $\triangle$ ). Filled circles ( $\bullet$ ) represent the sorption of U(VI) at a concentration of  $1 \times 10^{-4}$  M on bentonite in the presence of  $100 \text{ mg}\cdot\text{L}^{-1}$  HA.

The high specific activity  $^{237}\text{U}$  and  $^{237}\text{Pu}$  tracers were also used to study the effect of the order of addition of the system components and sorption kinetics in the Pu(III) and U(VI) HA bentonite ternary systems. The uranyl system revealed reversibility with the same final equilibrium amount of sorbed species obtained (within 1 week), regardless of the order of system components. However, for Pu some irreversibility was observed. For example, for

Pu(III), the amount of Pu sorbed was significantly lower if the Pu were added to the HA first, rather than the mineral surface. Even on a time scale of a few months, there was evidence of irreversibility, and sorption was still reduced if the metal ion was introduced to the HA before the mineral. It is tempting to think that the difference is due to the redox properties of Pu(III) (very likely to change oxidation state) and U(VI) (not).

#### Quartz Ternary Systems of Th, U, Pu

The majority of the studies have involved ternary systems of quartz sand, HA and the actinides U, Th and Pu. The effect of the presence of atmospheric CO<sub>2</sub> and the associated dissolved carbonates was also studied. Simple sorption experiments were performed routinely, i.e. the amount of sorbed actinide determined as a function of time. Such experiments are routinely used to define kinetic and equilibrium sorption parameters. For some systems, once (apparent) equilibrium was reached, the supernatant was separated from the mineral phase and replaced with a fresh electrolyte containing the same concentration of HA, but no actinide. The original supernatant was also added to a fresh sample of quartz sand. The distribution of actinide between solid and solution was then monitored in both new experiments with time. The objective of the replacement experiments was to provide a more rigorous test of speciation models. Also, the replacements were designed to determine the ability of HA to re-mobilise radionuclide that has been sorbed to a mineral surface, and to simulate the processes that will take place as an actinide containing solution encounters fresh mineral surfaces as it migrates.

A simple mathematical model was developed to predict the behaviour of both metal ion and HA. The interaction of metal ions with the HA can be described using two components with initial uptake to an exchangeable fraction, which is assumed to be instantaneous, and simulated with a single equilibrium constant. Subsequent transfer to and from the non-exchangeable fraction is a first-order kinetic (slow) process described with a single kinetic reaction and forward and backward rate constants. The interaction of metal ion with the quartz surface is also described with a single kinetic reaction with forward and backward rate constants. For the sorption of the HA itself, the model assumes that the surface is the source of the heterogeneity. There is a single type of HA species in solution and two surface sites. Kinetic reactions with separate forward and backward rate constants were used to describe HA sorption. The model further assumes that the metal ion interaction with the HA is the

same for HA in solution and sorbed on the mineral surface. Figure 4.12 shows example experimental data for Pu(IV).

**Th(IV):** in many ways, the Th systems display fairly simple ternary system behaviour. As the concentration of the HA increases, the amount of Th sorbed to the mineral surface decreases. Hence, in this system, the main effect of the HA is to act as a competing solution phase ligand, which holds the actinide in solution. The results suggest that the presence of HA could increase Th mobility, since even low concentrations of HA (e.g. 10 ppm), which could be found at a real site, can increase Th solubility.

**U(VI):** For uranyl, the effect of the HA is more subtle. The presence of the HA actually increases the sorption of uranyl. This can happen in systems where the interaction of the metal ion with the mineral surface is weak compared to that with the HA. In that case, ternary complex formation is particularly favourable for the metal ion, and the presence of HA enhances sorption. There is also evidence that the sorbed HA has an enhanced affinity for the uranyl, which is probably due to fractionation of the HA. The importance of the HA to the distribution of uranium in this system was shown by the effect of the addition of fresh HA solution to a uranyl/HA/quartz sand system. A significant reduction in sorption was observed after the addition of fresh HA as it removes uranium from the surface by competition. With time, however, the amount of uranium sorbed increased. This probably represents slow exchange between solution and sorbed HA species, which results in a return of U to the surface as a ternary complex. The results suggest that although HA may promote sorption in a static system, in one where there is flow of groundwater introducing fresh material, competition may result in a resuspension of uranium. Whether this would result in increased mobility would depend upon the relative magnitudes of the time taken for re-adsorption and the residence time of the groundwater in the contaminated region.

**U(IV):** Like Th(IV), U(IV) shows a simple ternary system behaviour.

**Pu(IV):** The behaviour in the Pu(IV)/quartz sand ternary system appears simple, with the HA appearing to act largely as a competing solution phase ligand, and Pu sorption decreases with increasing HA concentration for all systems. The sorption behaviour appears to be reversible.

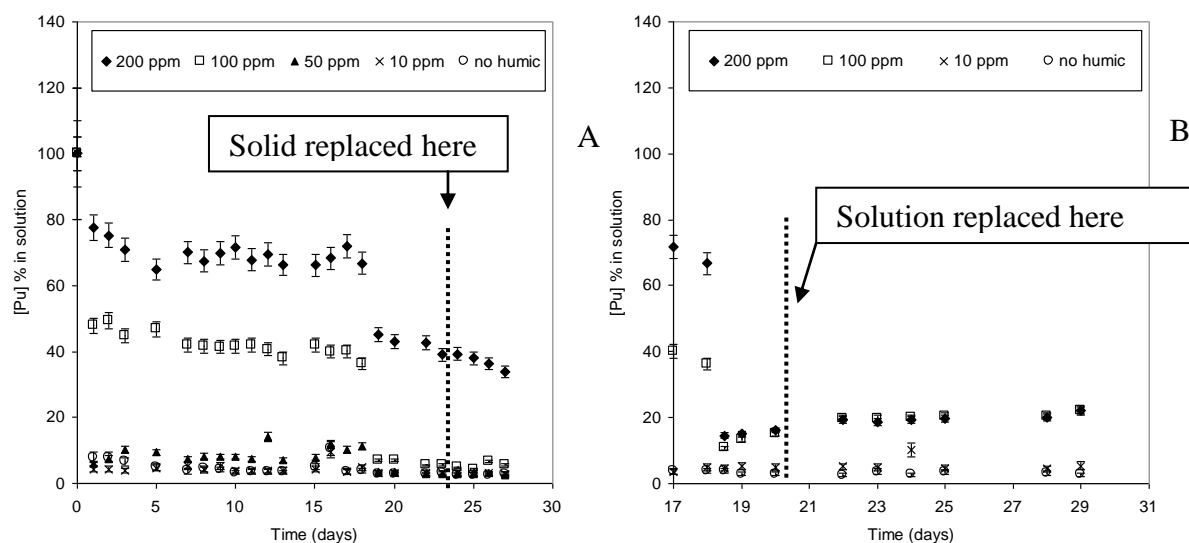


**Figure 4.12:** Results for ternary HA/quartz sand system  $^{239}\text{Pu}(\text{IV})$ ,  $1.22 \text{ kBq ml}^{-1}$ ,  $I = 0.1$ ,  $\text{pH} = 6$ , as a function of total HA concentration. **A:** Pu concentration in solution following exposure to 2 successive samples of mineral. **B:** Pu concentration in solution before and after replacement of the solution for the same sample of mineral.

**Pu(VI):** Like Th(IV) and U(IV), Pu(IV) shows a simple ternary system type of behaviour.

**Pu(V):** The behaviour of Pu(V) is more similar to that of U(VI) than that of the other Pu oxidation states that were studied. The presence of HA at low concentrations actually enhances sorption, and so ternary complexes are very important. Unlike the uranyl systems, higher concentrations of HA do reduce sorption.

**Modelling:** The model performed reasonably well for a simple representation of a complex and heterogeneous system in predicting the partition of the HA and that of the metal ions in the systems that showed simpler ternary behaviour (Th(IV); U(IV); Pu(IV); Pu(VI)). However, in the systems where ternary complexes were very significant (i.e. those where the HA was able to increase sorption at any concentration: U(VI); Pu(V)), the situation was always more complex and the model could not simulate that behaviour. In a system where the HA binding strength dominates, if it behaves like a simple homogeneous ligand, then the metal ion should 'follow' the HA: that is the solid/solution partition of the metal should approach that of the HA. However, it was found that in all of these systems, the HA sorbed on the surface had a higher affinity for the metal ions than that left in solution, which must be due to fractionation

of the heterogeneous HA population that accompanies sorption. The model shows that even in the systems that appear to show simpler ternary behaviour, e.g. Pu(IV) and Pu(VI), ternary complexes are significant, and that the surface HA ternary complexes are still significantly stronger than the binary solution phase complexes. These effects will make radionuclide behaviour hard to predict in some circumstances.

### ***Influence of changing redox conditions on the sorption of radionuclides***

It is one thing to know the influence of the redox state of a radionuclide on its sorption properties. Another thing is to know whether the sorption of a radionuclide effectively changes with changing redox conditions. This is not obvious. A redox-sensitive radionuclide is not necessarily in equilibrium with other redox couples in the system and often the redox reaction kinetics of a radionuclide are too slow to react immediately on a change in the redox conditions in its environment. Furthermore, for a redox-sensitive radionuclide to adapt to changing redox conditions, a process is needed to bring electrons from the reductant to the radionuclide or away from the radionuclide to the oxidant. In the case of e.g. sorbed or incorporated radionuclides, such a process is not always active.

KIT has investigated the sorption of neptunium, plutonium and technetium on two natural clay rocks, Opalinus clay (OPA) (Van Loon et al., 2009) and Callovo-Oxfordian argillite (COx, Bure, France) (Latrille et al., 2006) as well as the influence of a disturbance of the existing redox conditions on the sorption behaviour of these three radionuclides. A disturbance of the redox state was obtained by the addition of either magnetite or hydroquinone.

Sorption experiments have been performed with Np, Pu, and Tc suspensions of crushed OPA and COx clay rocks mixed with their respective artificial pore water (Van Loon et al., 2003). The reaction times varied between 1 week and 1 year.

For the experiments under disturbed redox conditions, either 3.0-4.5 mg of magnetite (mag, Alfa Aesar) or  $3.0 \times 10^{-3}$  M hydroquinone (HQ) were added to the samples. Np/Pu/Tc redox speciation in clay/pore water system were performed by capillary electrophoresis, TTA/PMBP liquid-liquid extraction at low concentration ( $<10^{-6}$  M), and spectroscopy (X-ray absorption fine structure (XAFS), UV-Vis/NIR absorption (UV-Vis), X-ray photoelectron spectroscopy (XPS)) at high concentrations ( $>10^{-5}$  M).

The sorption of Np, Pu, and Tc was observed to increase with increasing solid to liquid (S/L) ratio and with increasing contact time. For a total Np(V), Pu(V), and Tc(VII) concentration of  $3.0 \times 10^{-7}$  M, the  $K_d$  values were 35, 303, and 8.0 mL/g at pH 7.6 for OPA; 40, 367, and 4.5 mL/g at pH 7.2 for COx, at S/L ratio of 50 g/L for 6 weeks contact time. Our  $K_d$  values of Np(V) and Pu(IV) for both clay rocks shows a good agreement with literature values [Latrille et al., 2006, Wu et al., 2009]. The sorption maximum of Pu (85% for 10 g/L OPA) was reached after several days, whereas the sorption for Np increased from 25% after 6 weeks to 85% after several months at S/L of 10 g/L OPA. At higher S/L ratios the kinetic of Np was faster and the maximum of 85% was already reached after 6 weeks. Tc showed only a small increase from 25% after 4 weeks to 30% after 4 months at S/L of 10 g/L OPA. The same kinetic was observed at higher S/L ratios of OPA but the percentage of the sorption was higher: 60 to 65% for contact time of 4 weeks to 4 months.

The sorption of Pu, Np, and Tc increased with time suggesting that they are slowly reduced to the tetravalent oxidation state. This was confirmed by a steadily decrease of the  $E_h$  from an initial value of about +250 mV to values between -100 mV (Pu-OPA), +50 mV (Np-OPA), and -80 mV (Tc-OPA) after 4 months. However, a constant value was not reached after this long reaction time, meaning that the system did not reach equilibrium.

R reduction of the metal ions was also confirmed by liquid-liquid extraction with TTA. In the solution at low metal concentration ( $\sim 10^{-7}$  M), after separating the clay mixtures, Np(V), a mixture of Pu(IV/V) and Tc(VII) were found after 1 week contact time, while after 4 months Np(IV/V), Pu(IV/V) and Tc(IV/VII) mixtures were detected. Only the Pu(V) was reduced after the short reaction time of 1 week, whereas Np(V) and Tc(VII) were reduced at a much slower rate. After 4 months the dissolved species for all three elements consisted of 50% of the tetravalent oxidation state. The amount of reduced species on the clay could not be detected at these low concentrations. However, these experimental data are in qualitative agreement with equilibrium modelling performed with existing thermodynamic data.

The experiments in the presence of magnetite and hydroquinone did not show any significant difference regarding the sorption behaviour of the metal ions and the evolution of the average  $E_h$  values ( $E_h = -52$  mV (COx-mag), +80 mV (COx-HQ), and -60 mV (OPA-mag), +70 mV (OPA-HQ) independent of metal ions after 4 months contact time. Surface analysis of the magnetite – a commercial compound from Alfa Aesar – showed that the surface of this material was covered with a layer of oxidised Fe(III). Reduction by contact of the metal ion with the magnetite surface was therefore very improbable. An explanation for the failing

reduction in presence of hydroquinone cannot be given. Maybe the kinetic is much slower in the ternary system than in the binary system.

The experiments at high metal concentrations, in the absence of magnetite and hydroquinone revealed a somewhat different picture. The XAFS and XPS measurements of the clay paste after ultrafiltration with 10 kD filters at  $10^{-4}$  M showed that Np is sorbed on both solid phases in the form of Np(V), Pu was sorbed as Pu(IV), and Tc as Tc(VII) after 1 week contact time. XPS measurements detected a satellite at about 6.5 eV higher binding energy indicating Pu(IV) oxide, presumably due to Pu eigencolloids, whereas satellite at about 6.5 eV higher binding energy was not detected for Np indicating absence of Np(IV) oxide or Np(IV) eigencolloids. In solution Np(V), Tc(VII) was measured by UV-Vis/NIR spectroscopy, and Pu(IV) was confirmed by liquid-liquid extraction. This result agrees well with the  $E_h$  values after one week and thermodynamic calculations. The surface speciation of Np and Tc on clay rocks after 4 or 8 months contact time, did not reveal any reduction of Np(V) and Tc(VII) on either clay rocks even after 4 or 8 months contact time. This might be explained by slow reduction kinetic due to limited available reaction sites on clay surfaces for Np and Tc. The amount of pyrite site on the surface of clay rock was estimated to be in the range of  $10^{-8}$  mol/g, too low for a direct reduction of Np(V) and Tc(VII). Why was Pu(V) reduced at higher concentrations? Thermodynamic calculations show that our clay system has  $E_h$  values corresponding to the stability field of Pu(IV)/Pu(III). Hence, species – on the surface or in solution – with lower reducing strength can reduce Pu(V). Additionally, Pu(V) disproportionates easily to Pu(IV) and Pu(VI) at higher concentrations easily and therefore is not stable with time.

A detailed analysis of the EXAFS results shows that outer sphere complexes dominate at the beginning of the reaction. The appearance of a new weak shell signal from Si/Al neighbours at a distance of 3.75 Å after 8 months contact time, ascribed to a Np-O-Si distance (s. Figure 4.13), indicate that Np inner sphere complexes become dominant with time.

To summarize, the experiments clearly show that redox processes of redox sensitive radionuclides like Np, Pu, and Tc have an impact on the sorption on clay rock. However, the redox mechanisms are not yet unravelled, because the component on the clay surface that is responsible for the reduction process could not clearly be identified. Recent surface characterisation of the magnetite from Alfa Aesar showed that the surface was highly oxidised. This magnetite had almost no Fe(II) on the surface. This result explains why no

influence of the magnetite was observed and that magnetite from Alfa Aesar is not suitable for reduction experiments. First thermodynamic solution speciation and surface speciation with the 2 site protolysis non-electrostatic surface complexation and cation exchange (2SPNE SC/CE) sorption model from Bradbury & Baeyens (2009) – not shown here – qualitatively describes the experiments. However, the model has to be improved and adapted regarding the redox reactions in future research programs.

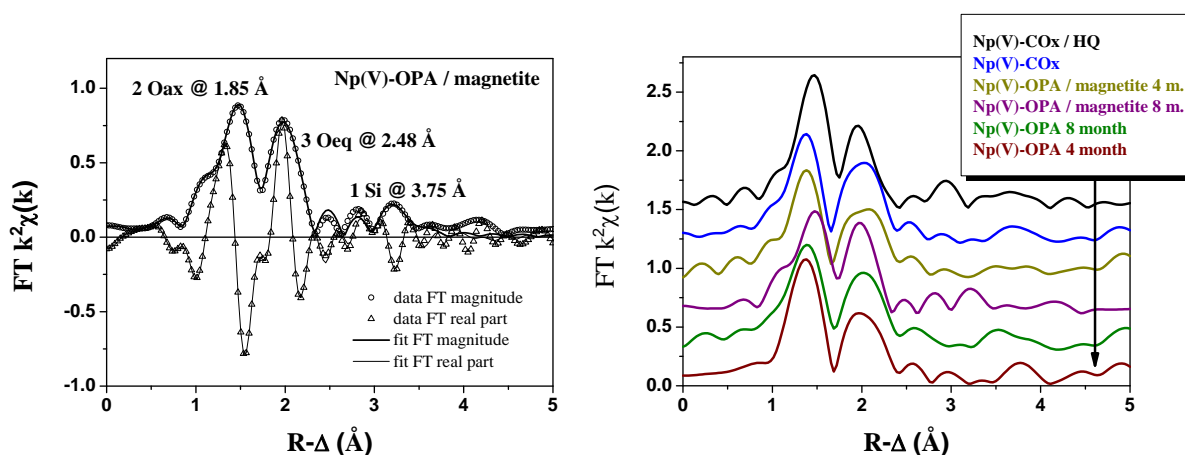


**Figure 4.13:** Fourier transforms of the Np LIII-edge  $k^2$ -weighted EXAFS spectra of Np-OPA and COx samples, without and with magnetite or hydroquinone after 4 or 8 months contact time (right graph). In the left graph the Fourier transforms of one samples is shown including the classification of the different shells, especially the Si/Al shell at 3.75 Å.

### Interaction of redox-sensitive radionuclides with pyrite

Pyrite ( $\text{FeS}_2$ ) is known to be present in significant quantities in many clay rocks such as OPA and Cox. Pyrite is known to buffer reducing conditions in clay formations (e.g. Gaucher et al., 2006, Beaucaire et al., 2008). Pyrite exhibits a high affinity for cations partially explained by its very low zero point of charge (ZPC) having a value lower than 2 (Bebié et al., 1998). Sorption combined with reduction was observed to take place with redox-sensitive radionuclides such as U(VI) (e.g. Descostes et al., 2010).

In the framework of Recosy CNRS/LCPME investigated the interaction of long-lived fission products with pyrite by means of electrochemical methods. Pyrite is an electric semiconductor and  $\text{FeS}_2$  electrodes can thus be used to monitor its electrochemical reactivity. The interactions of pyrite with elemental iodine as well as with iodate, iodide, selenate and selenite ions were investigated in acidic, neutral, and alkaline solutions.

The CNRS/LCPME activities consisted essentially of (i) electrochemical measurements performed in acidic, neutral and alkaline media using massive pyrite electrodes in the presence of iodine and iodate, selenite and selenate ions, (ii) the chemical conditioning at different pH values of pyrite microparticles with solutions of iodine, iodide, iodate, selenite and selenate ions (solution aliquots were sampled during the conditioning and analyzed by ICP-OES, ion chromatography and UV-visible spectroscopy), (iii) the characterization of the reacted pyrite microparticles by SEM, XPS, voltammetric and dielectric measurements, (iv) the dielectric monitoring of dry pyrite during its exposure to air or pure oxygen.

*Electrochemical measurements with pyrite electrodes in the presence of iodine, iodide, iodate, selenite and selenate*

Voltammograms were recorded at pH 1, 3, 7 and 12 using massive rotating pyrite electrodes immersed in 1 mM solutions of iodate, selenite and selenate ions as well as in a saturated solution of elemental iodine. The measurement of the corrosion currents gives insight in the kinetics of oxidation of  $\text{FeS}_2$  by the different oxidizing species. The corrosion currents were also visualised (only in acidic media) using the Scanning Reference Electrode Technique (SRET).

The experiments performed using the rotating pyrite electrode with  $\text{I}_2$  in acidic and neutral media ( $\text{I}_2$  is not stable in alkaline media) showed the existence of important corrosion currents. This result was confirmed by the pyrite surface mapping by SRET at pH 3. These corrosion maps showed anodic and cathodic areas confirming the localized nature of the corrosion.

The voltammetric experiments performed with  $\text{IO}_3^-$  ions at pH 1 and 3 also showed the presence of corrosion currents that seem to be less intense than those recorded in the presence of  $\text{I}_2$ . SRET maps confirmed the presence of a localized corrosion process. Because the oxidizing properties of iodate ions decreased with rising pH, no corrosion currents were observed at pH 7. On the other hand, the voltammograms testify for the presence of a corrosion process at pH 12.0 (probably because of the very high oxidizability of pyrite in alkaline media).

The experiments performed with selenite ions at pH 1 showed the presence of an extremely low corrosion in acidic media. No corrosion currents were observed at pH 3 neither voltammetrically nor using SRET. In neutral medium, the i-E curves were highly disturbed by

the presence of a cathodic peak that is located very close to the rest potential ( $\text{Fe}_2(\text{SeO}_3)_3$  precipitate?). The voltammograms recorded in alkaline medium were not exploitable. No corrosion currents were observed with selenate ions whatever the pH.

The experiments performed with  $\text{I}_2$  and  $\text{IO}_3^-$  species revealed the electrochemical nature of their interaction with  $\text{FeS}_2$  and predict relatively rapid redox kinetics, whereas the absence of a detectable corrosion current in the case of  $\text{SeO}_3^{2-}$  and  $\text{SeO}_4^{2-}$  excludes an interaction electrochemical in nature unless the electrochemical kinetics are extremely slow.

#### Chemical conditioning at different pH of pyrite microparticles with soluble iodine and selenium species

The pyrite samples were dry grinded in air in a porcelain mortar just before use in order to limit their oxidation by the atmospheric oxygen. Surface analyses by XPS of the grinded pyrite particles indicated essentially pure material with no evidence of surface oxidation products. Only the particles between 40 and 80  $\mu\text{m}$  (surface area  $\sim 0.1 \text{ m}^2/\text{g}$ ) were selected. Sorption experiments were performed under argon atmosphere at room temperature by shaking the containers with the pyrite suspensions in the dark on a come and go movement shaker. The solution pH was adjusted to 3.0, 7.0 and 12 at the beginning of the experiment with HCl and NaOH. The solid/liquid ratio was 5g/L and  $[\text{I}^-] = [\text{IO}_3^-] = [\text{SeO}_3^{2-}] = [\text{SeO}_4^{2-}] = 1.0 \text{ mM}$  or 0.1 mM. In the case of elemental iodide, either a saturated  $\text{I}_2$  solution (solid  $\text{I}_2$  was always present) was used or a sample of the liquid phase from an iodine suspension in 1 mM  $\text{I}^-$ .

The reactivity predicted electrochemically (section 4.8.1) was in general confirmed by solution analyses. Some analysis are still in progress. The most important and relevant results derived from the analyses are the following: (i) when pyrite is treated with water adjusted at pH 12 it releases continuously sulphide ions ( $\text{S}^{2-}$ ) in the solution, (ii) iodide ion is sorbed at the "pyrite" surface at pH 12, (iii) the reaction of iodate ions is extremely rapid in acidic media and slow at pH 12, (iv) iodine quantitatively reacts with pyrite in acidic and neutral media.

## Characterization of pyrite microparticles after contact with soluble iodine and selenium species

The results of the characterization of the pyrite microparticles with SEM, XPS, Raman microscopy and the "Voltammetry of MacroParticles" (VMP) technique were rather disappointing. With XPS, SEM, SEM-EDX and Raman microscopy, selenium and iodine were only detected on oxidized iron surfaces for the samples that were conditioned in neutral or alkaline media. No Se or I species were detected on clean pyrite surfaces. The samples exhibited etched pyrite containing some silicate; especially when the conditioning operations were performed in the presence of iodine species. Similar results were obtained from analysis from electrochemical measurements carried out with the VMP technique, using a 5 mV/ scan rate, both in acidic, neutral or alkaline media. (VMP allows the characterization of electroactive microparticles, conducting or not conducting after their immobilization on the surface of a graphite electrode). Recent XPS characterizations performed with extremely fine microparticles sampled after the reaction of  $\text{FeS}_2$  with selenite or selenate ions in neutral and alkaline media revealed the presence of elemental selenium. The corresponding voltammograms showed an additional voltammetric signal at about -0.7 V vs. SCE. Experiments are in progress in order to confirm the absence of any photochemical origin of the observed selenium.

Applying VMP at an extremely slow scan rates (0.1 mV/s) delivered much more promising results. However, the duration of the voltammetric sweeps, that is about 12 hours, seriously limited the number of experiments performed. Therefore only pyrite grains conditioned in acidic media were characterized in this way. When Voltammograms were recorded using such a slow scan rate, all the electroactive matter immobilized at the graphite is electrochemically transformed. Thus, after the electro-oxidation of all the pyrite, species that have higher oxidation potentials than that of pyrite, can be explored. In this way it was found that: (i) when pyrite is conditioned only with deionised water, the voltammograms show only a main peak at about 0.95 V vs. SCE, (ii) when pyrite is conditioned with iodine or iodate ions this peak is followed by another at about 1.12 V vs. SCE that is strong and sharp in the case of iodine and broader in the case of iodate, (iii) when pyrite is treated with iodide, selenite or selenate ions, the main peak of pyrite is shifted by about 100 mV to lower potentials (0.85); that means that the electrochemical oxidation of pyrite became easier.

Interesting results were also obtained after the treatment of the raw dielectric data obtained after the dielectric characterization of the pyrite particles recovered after conditioning with soluble species of iodine and selenium. More particularly, the Nyquist plots showed that: (i) when pyrite is conditioned only with deionised water, iodide or iodate, the resistance  $Z'$  of the particles is about 1500 ohm and the  $Z''=f(Z')$  plots maximum corresponds to values acquired at a frequency of about 7.5 MHz (ii) when pyrite is conditioned with iodine, the maximum of the Nyquist plot corresponds to values acquired at a frequency of about 0.24 MHz and the resistance  $Z'$  is quite higher than 20,000 ohm (the domain of frequencies of the impedancemeter used does not allow this determination) and (iii) when pyrite is conditioned with selenite or selenate, the domain of frequencies available does not allow to determine neither the resistance nor the  $Z''=f(Z')$  plots maximum; however, both samples are more resistive than all the others (and  $\text{FeS}_2$  treated with selenate is much more resistive than  $\text{FeS}_2$  treated with selenite).

We tried to correlate these observations after performing the voltammetric and dielectric experiments with the observation of Demoisson et al. (2008) who investigated the oxidation processes of pyrite by dissolved oxygen using Raman spectroscopy. Especially, these authors have observed a drift of the vibration modes  $E_g$  and  $A_g$  of  $-3$  and  $-6 \text{ cm}^{-1}$  respectively. Our investigations clearly demonstrate that this drift was an artefact due to the heating of the samples by the laser beam. The reactivity predicted electrochemically was in general confirmed by solution analyses The reactions of  $\text{I}_2$  and  $\text{IO}_3^-$  species with pyrite are rapid and lead to the formation of the soluble species  $\text{I}^-$  and  $\text{SO}_4^{2-}$ ; however, dielectric and particular electrochemical measurements revealed noticeable but yet unexplained changes in pyrite properties. As regards the pyrite– $\text{SeO}_3^{2-}/\text{SeO}_4^{2-}$  interactions the phenomena are complex: the kinetics are slow, the reaction products do not adhere on the pyrite surface and the absence of any photochemical origin for the elemental selenium detected must be confirmed

*Dielectric measurements with dry pyrite microparticles during their stepwise exposure to air or pure oxygen (S+T contribution)*

This study was initiated after an attempt to use dielectric spectroscopy to in-situ monitor the interactions of pyrite with soluble selenium and iodide species. We observed that once dry pyrite was exposed to air for a short time its impedance rose rapidly. However, during its stay in a hermetically closed dielectric cell, its impedance progressively decreased and finally

became almost the same as that before the exposure to air. It was as if pyrite had “repaired” the damage induced by its exposure to air. We considered that the observed phenomenon was worth being explored further: (i) because of the importance of the pyrite oxidation during the mining works in relation to the underground installations construction and (ii) for avoiding the misinterpretation of dielectric data obtained during the in-situ monitoring of the interactions in liquid phase of pyrite with soluble selenium and iodide species.

The work performed using pyrite microparticles put in a dielectric cell under alternative flows of dry argon and ambient air (or dry oxygen) confirmed the preceding observation. The observed changes in the dielectric spectra are probably due to extremely fine transformations on the pyrite surface that cannot be detected with usual spectroscopic techniques (Raman microscopy). If the ambient air is used as the oxidizing agent, the presence of moisture renders the phenomena more complex. Even if this work is quite long, it must be considered as a preliminary approach; its main objective was to check the reproducibility of the measurements and if no artefacts occurred. The systematic study of other parameters as the particles size, the temperature, moisture degree... as well as the use of a well-suited and complementary technique would bring essential information in order to understand the observed phenomena.

In general, the interaction of  $I_2$  and  $IO_3^-$  species with pyrite undergoes through a rapid electrochemical process leading to the formation of  $I^-$  and  $SO_4^{2-}$ . The pyrite– $SeO_3^{2-}/SeO_4^{2-}$  interactions are more complex: their electrochemical nature could not be established, the kinetics are slow, the reaction products are submicrometric and do not adhere on the pyrite surface and the absence of any photochemical origin for the elemental selenium detected must be confirmed.

### ***Chemical and redox behaviour of radionuclides in different systems through microbial mediated processes***

#### *Uranium redox speciation in biofilms*

The studies performed by HZDR within the framework of ReCosy clearly demonstrated that biological systems must be considered as a part of natural systems that can significantly influence radionuclide behaviour. The results improve our understanding of the mechanisms of biofilm response to radionuclides

---

(D-N°:1.2) – [Report on the scientific state of the art](#)

Dissemination level :PU

Date of issue of this report : **03/09/2012**

*Multispecies biofilms grown in the laboratory:*

At the beginning of our research work of HZDR in collaboration with UPPC it was shown that the application of electrochemical and laser-based fibre-optic oxygen microsensors to biological systems, e.g. multispecies biofilms grown in the laboratory and exposed to environmentally relevant uranium concentration, offer two methods that allow the measurements of oxygen with comparable good results. Both sensor methods showed almost identical curve progressions.

*Radionuclide contaminated environments:*

In a next step the improved miniaturized laser-based fibre-optic oxygen microsensors and the electrochemical sensors were used for field-measurement in radionuclide contaminated environments, e.g. in the former uranium mine Königstein (Germany), where the mining activities had been stopped in 1990 and the uranium mine was partially flooded for remediation. The aim of the study was to verify redox processes in in-situ biofilms. First comparative studies were carried out in stalactite-like biofilms. In the acidic, sulphate-rich waters with high concentration of heavy metals and radionuclides (uranium) as contaminants, biofilms are formed and occur as gelatinous filaments, and as stalactite-like snotites. Fibre-optic oxygen microprofiles, carried out in these snotites were found to be in good agreement with electro-chemical measurements. The oxygen concentration decreased slowly from the edge versus centre of the snotite biofilm. Electrochemical redox potential microprofilings were carried out in these biofilms using a miniaturized platinum redox electrode with a tip diameter of 10  $\mu\text{m}$ . In the bulk solution a redox potential of  $728 \text{ mV} \pm 9.5 \text{ mV}$  was measured in comparison to an increased redox potential of  $834.5 \text{ mV} \pm 10.21 \text{ mV}$  within the biofilm. We assume that the different geochemical conditions are due to the oxidation of ferrous iron catalyzed by Fe(II) oxidizing bacteria and that they will have an influence on the uranium speciation. A pH-Eh diagram for the U-S-O-H-C system at 15 °C was constructed using the geochemical speciation code "Geochemist's Workbench" Version 8.0.8 / ACT2 Version 8.0.8 and the most recent NEA database for uranyl silicates and solid uranates, supplemented with solubility data for uranophane and  $\text{CaU}_2\text{O}_7 \cdot 3\text{H}_2\text{O}_{(\text{s})}$  and the analytical data of the bulk water for the calculation of the field stability boundaries of different uranium species. The plotting of the measured pH and  $E_h$  values into this diagram showed

that the theoretical stability fields of U species are defined in areas characterized by higher pH or lower Eh. The measured values indicate that aqueous uranium(VI) sulfate complexes were formed in the biofilm as well as in the bulk solution. Changes of the local conditions (e.g. closure of the underground galleries) will lead to substantial changes and the formation of solid uranium(IV) species.

*In-situ U sorption experiments:*

In further studies microsensor measurements were performed in biofilms grown at site 2200 A of the Äspö Hard Rock Laboratory, Sweden and in the underground rock characterization facility, ONKALO (Finland) in collaboration with MICANS and POSIVA. Biofilm samples were removed from the tunnel wall at the 777 m position and exposed into a rectangular cell with an outer dimension of 121 x 42 x 15 mm. 150 ml of the groundwater as a blank solution from the site was pumped through the cell in a closed circuit. U in ecologically relevant concentrations ( $4 \times 10^{-5}$  M) was added to the groundwater solution for 42 hours. Samples of the U contaminated groundwater were taken at the end of the experiments and analyzed for determination of the inorganic and organic elements. The analytical data of the groundwater sample was used for the calculation of the predominance fields of different uranium species in the pH- $E_h$  diagram at 25°C by using the geochemical speciation code “Geochemist’s Workbench” Version 8.0.8 / ACT2. The database used was the thermo.dat accompanying the code, supplemented by the most recent NEA database for aqueous uranium species and by solubility data for the minerals rutherfordine, uranophane and uraninite and for the aqueous species  $\text{Ca}_2\text{UO}_2(\text{CO}_3)_{3(\text{aq})}$ . When plotting the measured pH and  $E_h$  values of the contaminated groundwater in the pH- $E_h$  diagram, the formation of an aqueous calcium uranyl carbonates species ( $\text{Ca}_2\text{UO}_2[\text{CO}_3]_3$ ) was predicted. In addition to the thermodynamic calculation, the uranyl species formed in the U contaminated groundwater was identified, using spectroscopic methods. The results of the time-resolved laser induced spectroscopy (TRLFS) studies are in excellent agreement with the thermodynamic calculations of the theoretical predominance fields of the uranium species formed in the uranium-contaminated groundwater. In addition, the spectra of aqueous alkaline earth uranyl carbonate species were obtained for comparison displayed similar luminescence emission bands. The results were compared with the luminescence properties of the uranyl carbonate species  $\text{Ca}_2\text{UO}_2(\text{CO}_3)_3$ , which displays band positions similar to those of our studied groundwater. In addition, the luminescence spectrum of the  $\text{MgUO}_2(\text{CO}_3)_3^{2+}$  species can be considered as a

possible species as well. The considerable amounts of magnesium and calcium in the contaminated groundwater suggest that aqueous calcium and aqueous magnesium uranyl carbonate species could have formed in the contaminated groundwater during the experiments. In contrast, the results of energy-filtered transmission electron microscopy (EF-TEM) and electron energy-loss spectroscopy (EELS) provide spectroscopic evidence that uranium in the biofilm was immobilized intracellularly in microorganisms by the formation of metabolically mediated uranyl phosphate, similar to needle-shaped autunite ( $\text{Ca}[\text{UO}_2]_2[\text{PO}_4]_2 \cdot 2-6 \text{H}_2\text{O}$ ) or meta-autunite ( $\text{Ca}[\text{UO}_2]_2[\text{PO}_4]_2 \cdot 10-12\text{H}_2\text{O}$ ). Analysis of the elongated particles, formed in the cytoplasm of bacteria provide spectroscopic evidence for the presence of uranium immobilization. The distribution analysis of uranium, phosphorus and calcium clearly showed, that a solid uranium mineral has formed intracellular, which indicates the formation of a solid U-phosphate mineral similar to autunite

#### Effect of microorganisms on the redox behaviour and sorption of plutonium and technetium

The studies performed by FTMC within the framework of ReCosy were focussed on 1) effects of microorganisms on redox behaviour of plutonium, 2) evaluation of Fe(III) biogenic transformations by the ferrozine method and UV-vis spectrophotometry, 3) combined effect of microorganisms and iron-bearing mineral hematite on Tc(VII) sorption

#### Effects of microorganisms on redox behaviour of plutonium

At the beginning the methodology to monitor the Pu oxidation state was developed. Separation of individual Pu oxidation states, Pu (IV), Pu (III) and oxidized fraction Pu (V, VI), was accomplished using a combination of the neodymium fluoride co-precipitation method and the improved two column anion exchange separation. Out of microorganisms detected in the low-level radioactive waste repository in the Ignalina NPP territory, microorganisms which demonstrated properties to participate in reduction reactions were selected for the investigations. Pu oxidation states after Pu (IV) interaction with microorganisms under aerobic conditions at low pH (2.7-2.9) were studied using radiochemical analysis. The highest effect in a change of Pu(IV) to Pu(III) at low pH under aerobic conditions was demonstrated by gram-positive bacterium *Bacillus mycoides* (strain DPKI-01) and Gram-negative bacterium *Serratia marcescens* (strain DPKI-06). The amount of reduced Pu(III) in brine solution was determined to be 15%. Tested fungi *Absidia spinosa* var. *spinosa* (strain DPKI-25) and *Paecilomyces lilacinus* (strain DPKI-12) showed no pronounced influence on

the redox process in the used experimental system under aerobic conditions (Druteikienė et al., 2010; Lukšienė et al., 2012). Hence, bioreduction makes it possible to control the solubility and mobility of redox-sensitive radionuclides at contaminated environmental sites. The efficient method to determine the Pu oxidation states in the tested matrices enhances the probability to model the fate and transport of plutonium in the environmental systems. Therefore, the models used should take into account the different chemical plutonium species as well as their biogeochemical behaviour due to the microbial activity.

#### *Evaluation of Fe(III) biogenic transformations by the ferrozine method and UV-vis spectrophotometry*

The objective of this study was adaptation of the ferrozine method to perform iron oxidation state analysis by the UV-vis spectrophotometric method after exposure of aqueous solution with Fe(III) to different microorganisms, isolated from soil and groundwater. Ferrozine forms magenta complex of Fe(II) with maximum absorbance at 560 nm while Fe(III) solutions show absorbance at 330 nm.

Experiments provided a two-month interface of microorganisms from groundwater and water-logged soil to 0.08 mol/L NaCl aqueous solution with Fe(III) at 30°C temperature under aerobic conditions. Experimental studies have shown that microorganisms from groundwater (*Streptomyces* sp., *Aspergillus niger*, *Bacillus mycoides*, *Penicillium* sp., *Rhodococcus* sp., *Spicaria* sp.) caused bioreduction of Fe(III) at a larger extent compared to microorganisms from water-logged soil (*Arthrobacter globiformis*, *Cellulomonas cellulans*, *Fusarium oxysporum*).

#### *Combined effect of microorganisms and iron-bearing mineral hematite on Tc(VII) sorption*

Results of the combined effect of microorganisms and iron-bearing mineral hematite on Tc (VII) sorption peculiarities using batch-type experiments showed that after exposure of Tc(VII) for 144 hours with bacteria *Arthrobacter globiformis* and *Cellulomonas cellulans* 78 and 98% of Tc remained in solution. Micromicete *Fusarium oxysporum* of the same substrate altered sorption to approximately 85% compared to that in the system without microorganisms. Differences in Tc(VII) sorption processes onto hematite due to microbial activity of microorganisms isolated from the groundwater borehole were observed as well. Presence of microorganisms *Penicillium* sp., *Rhodococcus* sp. and *Streptomyces* sp. in the

tested system induced Tc(VII) sorption onto hematite up to 71-82%. After interaction of Tc(VII) with microorganisms *Penicillium* sp., *Rhodococcus* sp. and *Streptomyces* sp. 24, 18 and 29% of Tc, respectively, remained in solution. The effect of microbial activity of *Bacillus mycoides*, *Aspergillus niger* on Tc(VII) sorption onto hematite was less, 54% and 18%, respectively. Micromicete *Spicaria* sp. had practically no influence on the sorption of Tc onto hematite, because approximately 98% of Tc remained in solution.

Additional experiments with only microorganisms and without Fe-oxides were performed. Microorganisms which showed the highest influence on Tc(VII) sorption onto hematite were used for additional experiments. Sorption results obtained from these additional experiments (Table 1) showed that sorption of Tc(VII) by microorganisms is lower compared to that when the experimental system consisted of hematite and microorganisms. The results showed that microorganisms could have some reductive effect on Fe<sub>2</sub>O<sub>3</sub> and its sorption capability.

Distribution coefficients ( $K_D$ ) were calculated to describe the adsorption behaviour of Tc in the experimental systems in presence of iron oxide and microorganisms (Fig. 1, 2). The  $K_D$  is defined as

$$K_D = (A_i - A_e) / A_e * V/m$$

Here  $A_i$  is the initial activity of the solution and  $A_e$  is the activity of the solution after the adsorption.  $V$  is the volume of the solution and  $m$  is the mass of the solid (Vejsada, 2006).

**Table 1.** Behaviour of Tc (VII) in aqueous solutions in the presence of iron oxides and microorganisms

Medium from which microbes were isolated	Microorganism	Tc in solution/in Fe <sub>2</sub> O <sub>3</sub> , %	Tc in solution/in biomass, %
Soil	<i>Arthrobacter globiformis</i>	78/24	-
	<i>Cellulomonas cellulans</i>	98/2	-
	<i>Fusarium oxysporum</i>	15/85	59.9/40.1
Groundwater	<i>Aspergillus</i>	82/18	-
	Bacterium No1	49/51	-
	<i>Bacillus mycoides</i>	46/54	-
	<i>Streptomyces</i> sp.	29/71	56.3/43.7
	<i>Penicillium</i> sp.	24/76	37.1/62.9
	<i>Rhodococcus</i> sp.	18/82	50.8/49.2
	<i>Spicaria</i> sp.	98/2	-

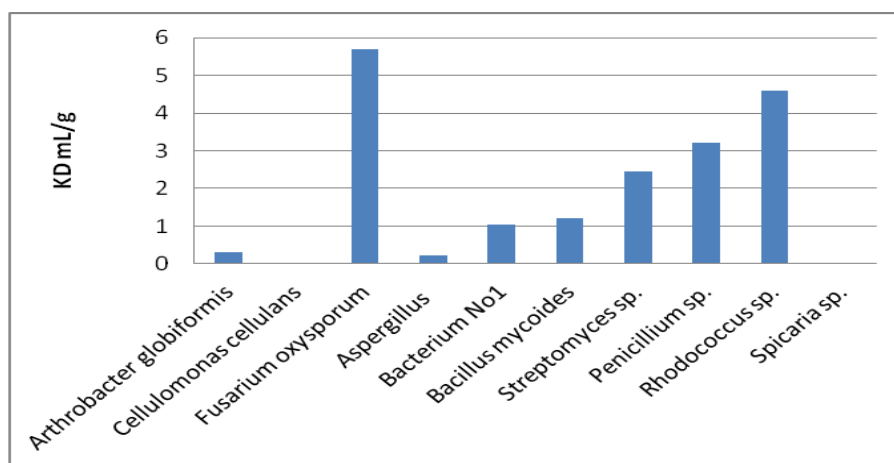


**Figure 4.14.**  $K_D$  of Tc(VII) in the system aqueous solution-hematite-microorganisms

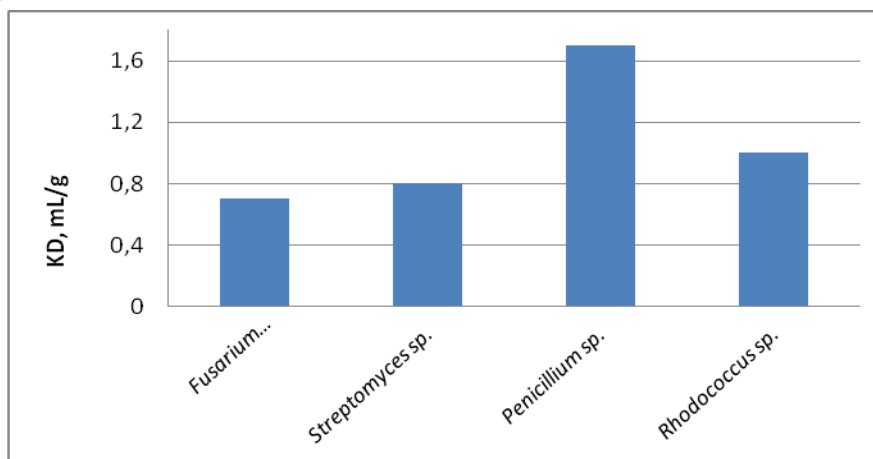


**Figure 4.15:** .  $K_D$  of Tc(VII) in the system aqueous solution –microorganism

## References

- Beaucaire, C., Michelot, J.-L., Savoye, S., Cabrera, J. (2008) Groundwater characterisation and modelling of water-rock interaction in an argillaceous formation (Tournemire, France). *Applied Geochem.* 23, 2182-2197.
- Bebié, J., Schoonen, M.A.A., Fuhrmann, M., Strongin, D.R. (1998) Surface charge development on transition metal sulfides: an electrokinetic study. *Geochim. Cosmochim. Acta*, 62, 633-642.
- Berner, U. (2003) Project Opalinus Clay: Radionuclide Concentration Limits in the Cementitious Near-Field of an ILW Repository; PSI report 02-26; Paul Scherrer Institut: Villigen, Switzerland.
- Bradbury, M.H., Baeyens, B., (2009) Sorption modelling on illite. Part II: Actinide sorption and linear free energy relationships, *Geochim. Cosmochim. Acta* 73, 1004–1013.
- Bruno, J., Casas, I. Lagerman, B., Muñoz, M. (1987) The determination of the solubility of amorphous  $UO_2(s)$  and the mononuclear hydrolysis constants of uranium(IV) at 25°C. *Sci. Basis Nucl. Waste Management X, Symp. Proceedings*, 84, 153-160.
- Carvalho, L.M., Schwedt, G. (2001) Polarographic determination of dithionite and its decomposition products: kinetic aspects, stabilizers, and analytical application. *Analytica Chimica Acta*, 436, 293-300.
- Casas, I. (1989) Estudios Físico-Químicos de la disolución del  $UO_2$ . Universitat Autònoma de Barcelona, Thesis.

- Choppin, G. R. (1984) Complexation of pentavalent and hexavalent actinides by fluoride. *Radiochim. Acta*, 37, 143-146.
- Cornell R.M., Schwertmann U. (2003) *The Iron Oxides*. Wiley-VCH, Weinheim, pp. 694.
- Demoisson, F., Mullet, M., Humbert, B. (2008) Pyrite oxidation in acidic medium: overall reaction pathway. *Surf. Interface Anal.* 40: 343–348.
- Descostes, M., Schlegel, M.L., Eglizaud, N., Descamps, F., Miserque, F., Simoni, E. (2010) Uptake of uranium and trace elements in pyrite (FeS<sub>2</sub>) suspensions. *Geochim. Cosmochim. Acta*, 74, 1551-1562.
- Druteikienė, R., Lukšienė, B., Pečiulytė, D., Baltrūnas D. (2010) Interaction of biomass of aerobic bacteria and fungi with Pu(IV) at low pH. *J Radioanal Nucl Chem*, 286, 387-391.
- Fujiwara, K., Yamana, H., Fujii, T., Kawamoto, K., Sasaki, T., Moriyama, H., (2005) Solubility of uranium(IV) hydrous oxide in high pH solution under reducing conditions. *Radiochim. Acta.*, 93, 347-350.
- Garbev, K., Bornefeld, M., Beuchle, G., Stemmermann, P. (2008) Cell dimensions and composition of nanocrystalline calcium silicate hydrate solid solutions. Part 2: X-ray and thermogravimetry study. *J. f Am. Ceram. Soc.*, 91, 3015-3023.
- Gaona, X., Dähn, R., Tits, J., Scheinost, A., Wieland, E. (2011). Uptake of Np(IV) by C–S–H phases and cement paste: An EXAFS study. *Environ. Sci. Technol.*, 45, 8765-8771
- Gaona, X., Tits, J., Dardenne, K., Liu, X., Rothe, J., Denecke, M.A., Wieland, E., Altmaier, M. (2012a) Spectroscopic investigations of Np(V/VI) redox speciation in hyperalkaline TMA-OH solutions. *Radiochim. Acta*. Accepted for publication.
- Gaona, X., Wieland, E., Tits, J., Scheinost, A., Dähn, R. (2012b) Np(V/VI) redox chemistry in cementitious systems: XAFS investigations on the speciation under anoxic and oxidizing conditions. Submitted to *Applied Geochem*.
- Gayer, K. H., Leider, H. (1957) The solubility of uranium(IV) hydroxide in solution of sodium hydroxide and perchloric acid at 25°C, *Can. J. Chem*, 35, 5-7
- Galkin, N. P., Stepanov, M. A. (1961) Solubility of uranium(IV) hydroxide in sodium hydroxide. *At. Energ.*, 8, 231-233
- Gaucher, E., Blanc, P., Bardot, F., Braibant, G., Buschaert, S., Crouzet, C., Gautier, A., Girard, J.-P., Jacquot, E., Lassin, A., Negrel, G., Tournassat, C., Vinsot, A., Altmann,

- S. (2006) Modelling the porewater chemistry of the Callovian-Oxfordian formation at a regional scale. *C.R. Geosci.*, 338, 917-930.
- Guillaumont, R., Fanghänel, J., Neck, V., Fuger, J., Palmer, D.A., Grenthe, I., Rand, M.H. (2003) *Chemical Thermodynamics 5. Update on the Chemical Thermodynamics of Uranium, Neptunium, Plutonium, Americium and Technetium*. NEA OECD, Elsevier.
- Latrille, C.; Herbette, J. Ly. M. (2006) Retention of Sn(IV) and Pu(IV) onto four argillites from the Callovo–Oxfordian level at Bure (France) from eight equilibrated sedimentary waters. *Radiochim. Acta.*, 94, 421–427.
- Lister, M. W., Garvie, R. C. (1959) Sodium dithionite, decomposition in aqueous solution and in the solid state. *Can. J. Chem.*, 37, 1567 – 1574.
- Lukšienė, B., Druteikienė, R., Pečiulytė, D., Baltrūnas, D., Remeikis, V., Paškevičius, A. (2012) Effect of microorganisms on the plutonium oxidation states, *Appl Radiat Isot*, 70, 442-449.
- Neck, V. and Kim, J. I. (2000) An electrostatic approach for the prediction of actinide complexation constants with inorganic ligands - application to carbonate complexes. *Radiochim. Acta*. 88, 815-822.
- Neck V., Altmaier M., Fanghänel T. (2007) Solubility of plutonium hydroxides/hydrous oxides under reducing conditions and in the presence of oxygen. *C. R. Chimie*, 959-977.
- Ollila K. (2002) Uranium solubility. In: *Nuclear Waste Managements in Finland. Finalreport of Public Sector's Research Programme, JYT 2001* (Ed. K. Rasilainen), Ministry of Trade and Industry, Helsinki, Finland, pp. 77-79
- Orlandini K.A., Penrose W.R. and Nelson D.M. (1986) Pu(V) as the stable form of oxidized plutonium in natural waters. *Marine Chemistry*, 18, 49-57
- Parkhurst, D.L. Appelo, C.A.J, (1999) PHREEQC v. 2.17.5: User's guide to Phreeqc (version 2) - A computer program for speciation, batch-reaction, one-dimensional transport, and inverse geochemical calculations. *Water-Resources Investigations Report 99-4259*.
- Perevalov. S.A., Molochnikova N.P. (2009) Sorption of Pu in various oxidation states onto multiwalled carbon nanotubes. *J. Radioanal Nucl Chem* 281, 603-608.
- Rai, D., Felmy, A. R., Ryan, J. L. (1990) Uranium (IV) hydrolysis constants and solubility product of  $UO_2 \cdot xH_2O(am)$ . *Inorg. Chem.*, 29, 260-264.

- Riba, O., Montoya, V., Grivé, M., Duro, L. (2012) Uranium solubility under alkaline conditions using different reducing agents. Scientific and Technical Contribution, Recosy (in preparation).
- Ryan, J. L., Rai, D. (1983) The solubility of uranium(IV) hydrous oxide in sodium hydroxide solutions under reducing conditions. *Polyhedron*, 2, 947-952
- Shoesmith, D.W. (2008) The role of dissolved hydrogen on the corrosion/dissolution of spent nuclear fuel. Nuclear Waste Management Organization Report, Toronto, Canada, NWMO TR-2008-19.
- Senanayake, S.D., Waterhouse, G.I.N., Chan, A.S.Y, Madey, T.E., Mullins, D.R. Idriss, H. (2007) The reactions of water vapour on the surfaces of stoichiometric and reduced uranium dioxide: a high resolution XPS study. *Catalysis Today*, 120, 151-157.
- Sorin T., Amamoto T., Motojima K. (1972) Study of oxidation state of plutonium in solution by flow-colometric method. *Talanta*, 19, 329 - 340.
- Szecsody, J. E., Fruchter, J. S.; Williams, M. D.; Vermeul, V. E.; Sklarew, D. (2004) In situ chemical reduction of aquifer sediments: Enhancement of reactive iron phases and TCE dechlorination. *Environ. Sci. Technol.* 38, 4656-4663.
- Torrero, M. E. (1995) Estudio de la disolución del  $UO_2$  como análogo químico de la matriz del combustible nuclear gastado. Influencia de los principales parámetros fisicoquímicos que definen los repositorios en medios salinos y granítico. Universidad de Barcelona, Thesis.
- Tremaine, P. R., Chen, J. D., Wallace, G. J., Boivin, W. A. (1981) Solubility of uranium (IV) oxide in alkaline aqueous solution to 300°C, *J. Solution Chem*, 10, 221-230
- Trummer, M., Nilsson, S., Jonsson, M. (2008) On the effects of fission product noble metal inclusions on the kinetics of radiation induced dissolution of spent nuclear fuel. *Journal of Nuclear Materials*, 378, 55.
- Van Loon, L. R., Soler, J. M., Bradbury, M. H. (2003) Diffusion of HTO, Cl-36(-) and I-125(-) in Opalinus Clay samples from Mont Terri - Effect of confining pressure. *J. Contamin. Hydrol.* 61, 73-83.
- Van Loon, L. R.; Baeyens, B.A.; Bradbury, M. H. (2009) The sorption behaviour of caesium on Opalinus Clay: A comparison between intact and crushed material, *Applied Geochem.* 24, 999-1004.

- Vejsada, J. (2006) The uncertainties associated with the application of batch technique for distribution coefficients determination—A case study of cesium adsorption on four different bentonites. *Appl. Radiat. and Isot.* 64, 1538-1548.
- Widestrand, H., Byegård, J., Selnert, S., Skålberg, S., Höglund, S. and Gustafsson, E. (2010) Long Term Sorption Diffusion Experiment (LTDE-SD) Supporting laboratory program – Sorption diffusion experiments and rock material characterisation. With supplement of adsorption studies on intact rock samples from the Forsmark and Laxemar site investigations, Geosigma AB. SKB Report R-10-66.
- Wieland, E., Van Loon, L. R. (2003) Cementitious near-field sorption data base for performance assessment of an ILW repository in opalinus clay. PSI Report. Nr. 03-06, Paul Scherrer Institute, Villigen-PSI, Switzerland and Nagra Technical Report NTB 02-20, Nagra, Wettingen, Switzerland.
- Wu, T.; Amayri, S., Drebert, J., Van Loon, L. R., Reich, T. (2009) Neptunium(V) sorption and diffusion in Opalinus clay. *Environ. Sci. Technol.*, 43, 6567–6571.
- Yajima, T., Kawamura, Y., Ueta, S. (1995) Uranium(IV) solubility and hydrolysis constants under reduced conditions. *Sci. Basis Nucl. Waste Management XVIII, Symp. Proceedings*, 353, 1137-1142.
- Yamamura, T., Kitamura, A., Fukui, A., Nishikawa, S., Yamamoto, T., Moriyama, H. (1998) Solubility of U(VI) in highly basic solutions. *Radiochim. Acta*, 83, 139 – 146.

## WP5. Redox processes in radionuclide transport

Many countries have chosen deep underground disposal to take care of storage of their nuclear wastes. The concept relies on various favourable characteristics of the host rock formation to assure that harmful release of radionuclides would not occur. The confidence to the concept is based on capability to demonstrate that the models used to predict radionuclide transport through the respective host rock formations are based on a scientifically sound understanding of contributing phenomena. In clayrocks due to very compact homogeneous texture of the formations diffusion-driven transport models are not difficult to justify whereas in heterogeneous crystalline rocks advective flow and natural hydrogeological disturbances have to be taken into account in safety case which largely complicates radionuclide transport modelling. Crucial for both concepts is the long-term redox-stability of the host formations. In clayrocks this is usually the case but in crystalline rocks (Finnish and Swedish disposal concepts) redox-stability is threatened due to foreseeable glacial melt water and sea water intrusions which can carry oxygen along the flow paths hundreds of meters into the bedrock. The aim of WP 5 was to increase process understanding of the transport of redox-sensitive nuclear waste radionuclides through clayrocks and crystalline rocks with eye on uncertainties still exist in the disposal concepts. Key questions addressed were:

- Do we have coherent conceptual models describing transport of redox-sensitive nuclear waste radionuclides?
- Do redox-reactions take place during diffusion and do radionuclides take part in redox-reactions?
- Do natural changes in redox-conditions affect radionuclide mobility?
- Do we know sufficiently of the redox-impact glacial melt water intrusion?

Material to answer or at least to discuss these questions was collected from (i) laboratory diffusion experiments with samples from potential host clayrock formations (Collovo-Oxfordian in France and Boda Claystone in Hungary), (ii) studies on the behaviour of waste actinides in natural crystalline environment (natural uranium at Olkiluoto) and in near natural conditions in laboratory with samples from Äspö Hard Rock Laboratory, and (iv) from studies

on behaviour radionuclides in contaminated areas in Cyprus and Russia. Major attention was paid to radionuclide immobilisation processes because redox transformations into lower valence states are known to immobilise radionuclides. Required reducing potential is provided by Fe(II)-containing mineral phases abundantly found in clay and crystalline rocks. It should be bore in mind, however, that redox-reactions can transform radionuclides into higher valence states thus promoting their mobility. This is possible e.g. under natural redox-disturbances such as glacial melt water intrusion which is expected at the repository sites in Finland and Sweden. Redox response of melt water intrusion is not known which complicates long-term predictions of radionuclides redox state.

During the four years ReCoSy time some new information was created the results being mostly illustrative. Key questions could be answered only partly and indirectly. Clear radionuclide reduction-like retention was observed both in laboratory and natural conditions but whether the retention was due to redox transformations remained still unclear except in case of Se where direct redox-state determination of retarded Se could reveal reduction as retention mechanisms.

Research teams involved were from different organisations in six participating countries: KIT-INE (Germany) and UH (Finland) studied issues related to the influence of natural redox-disturbances including a small scale method development by UH. CEA (France) and ITHAS (Hungary) studied diffusion in clayrocks, UC (Cyprus) and MSU (Russia) studied the behaviour of radioactive contaminants. Posiva Oy who manages nuclear wastes from the Finnish nuclear power plants participated in WP5 by providing matching funding and sample material to UH. The research was done mainly independently by the organisations. Small scale collaboration in the form of analytical help and interpretation was performed between UH and UC concerning U behaviour within phosphogypsum stack and between ITHAS and UH concerning characterisation of immobilised U. In the following topic specific activities are summarised and discussed.

### **Diffusion studies**

CEA studied diffusion of U(VI), Se(IV,VI) and I(-I,V) in Callovo-Oxfordian (CO<sub>x</sub>) argillite samples. Investigations were performed using through-diffusion and batch experiments with physico-chemical conditions as close as possible to those prevailing *in situ* by means of

$N_2/CO_2$  glove-box. A single reservoir method with decreasing source concentration for a semi-infinite case was used to model the results (Shackelford, 1991). Data analysis of the results was based on the second Fick's law for one-dimensional reactive transport. Modelling details can be found in Savoye et al. (2012) and in references therein. The experiments with U(VI) showed that U diffuses into the rock sample mainly as oxyanion forms (carbonate and calcium complexes evidenced by TRLFS in the high-concentration container), with no or less retardation but strong steric and anion exclusions. The behaviour of Se was particularly studied (Savoye et al., 2011). The results from the through-diffusion experiments showed that Se(+VI) activity in the upstream reservoir remains relative constant throughout the experiment, while the total activity can clearly be related to the decrease of the  $^{75}Se(+IV)$  activity (Fig. 1). The respective concentration profile in sample disc in Fig. 2 shows that the global pattern of the  $^{75}Se$  profile cannot be accounted for only by a pure diffusion process with a reversible sorption. Other processes, possibly redox-transformation into lower valence state, may have involved.

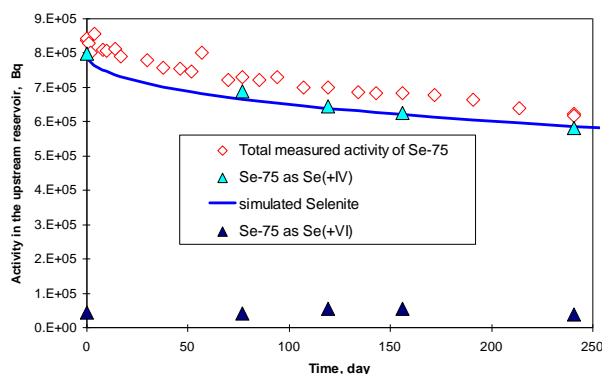


**Figure 1:**  $^{75}Se$  activity in the upstream reservoir spiked with  $Se(+IV) = 10^{-3} mol L^{-1}$  as a function of time. The curve was calculated using the corresponding analytical solution with given parameters (Savoye et al., 2012). Closed symbols denote the results of the fractionation. Open symbols denote the activity of total Se determined from the total radioactivity in the solution samples.

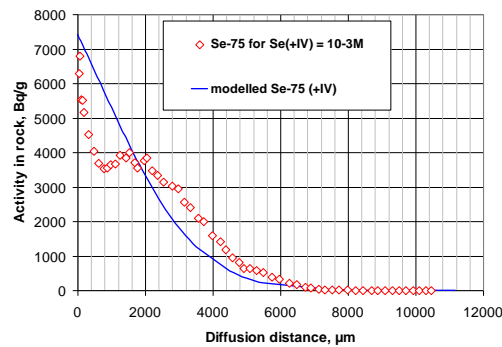


**Figure 2:** Concentration profile of  $^{75}\text{Se}(\text{IV})$  in sample disk. Symbols represent experimental data. The curve has been constructed using the best fit.

The evolution of the selenite concentration as a function of time in the upstream reservoir was given in the Figure 3. Even though the scattering is more pronounced than for the radioactive cell, the global tendency is quite the same, given the associated uncertainties.

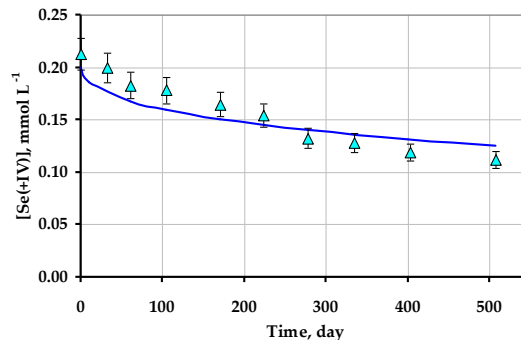


**Figure 3:** Measured and modelled evolution of selenite concentration in the upstream reservoir.

The distribution of the total selenium content within the sample disk (Fig. 4) was acquired by means of  $\mu\text{XRF}$  analyses at an energy of 12,800 eV (Charlet et al., 2007 and Frasca, 2011). Distribution shows a relative homogeneous decrease from upstream reservoir to downstream reservoir with some isolated hot-spots. The total Se profile calculated from this mapping (Fig. 4B) exhibits a global pattern very similar to the  $^{75}\text{Se}$  profile given in Figure 4, with a rapid drop down to 1 mm into the sample, an increase at about 2 mm, and thus, a relative regular decrease.

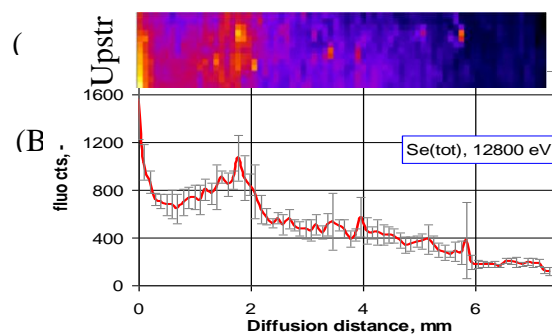


**Figure 4:** (A)  $\mu$ XRF mapping of the selenium distribution concentration at 12800 eV. The resolution is for one pixel: 100  $\mu$ m in X-axis and 50  $\mu$ m in Y-axis. (B) Average values of total selenium as a function of the diffusion distance. Error bars correspond to the standard deviation.

Se K-edge XANES spectra at an energy range from 12645 eV to 12670 eV were measured to study selenium redox-state (Charlet et al., 2007; Frasca, 2011). The spectra demonstrate the occurrence of some reducing phenomena of selenium during diffusion in indurate clay rock sample. The  $\mu$ XRF mapping carried out allowed to contour Se(red) (Fig. 5A) and selenite (Fig. 5B). The Se(red) map exhibits several hot-spots, especially at about 2 mm from the interface (Fig. 5A), while the selenite map shows a relatively smooth diffusion profile, even though the zone at 2 mm looks selenite-depleted. Nevertheless, given the very rough approach used, only the global pattern can be discussed. These tendencies were confirmed when considering the associated profiles and normalizing by the total selenium (Fig. 5D). The two approaches gave consistent results. While the monitoring of the selenium concentration in solutions could be roughly reproduced by a pure diffusion model with a reversible sorption ( $D_e = 4 \times 10^{-12} \text{ m}^2 \text{ s}^{-1}$  and  $R_d = 12 \text{ mL g}^{-1}$ ), the total selenium rock profiles exhibited irregular shapes, requiring more complicated models. Determination of Se oxidation states revealed (1) a relative regular diffusion profile for selenite and (2) the presence of some areas rich in selenium reduced forms (Se(red)  $\sim$  Se (0), S(-I) and/or Se(-II)), especially located at about 2 mm from the interface. Some correlation was found between the Se(red) hot-spots and the iron content, suggesting a role of iron-rich minerals, such as pyrite. However, the larger Se(red)-rich area at 2 mm (Fig. 5A) could not be accounted for by some mineralogical heterogeneities. Other explanations have to be proposed, such as the existence of reducing front located deeper in the sample because of some redox perturbations near the interface.

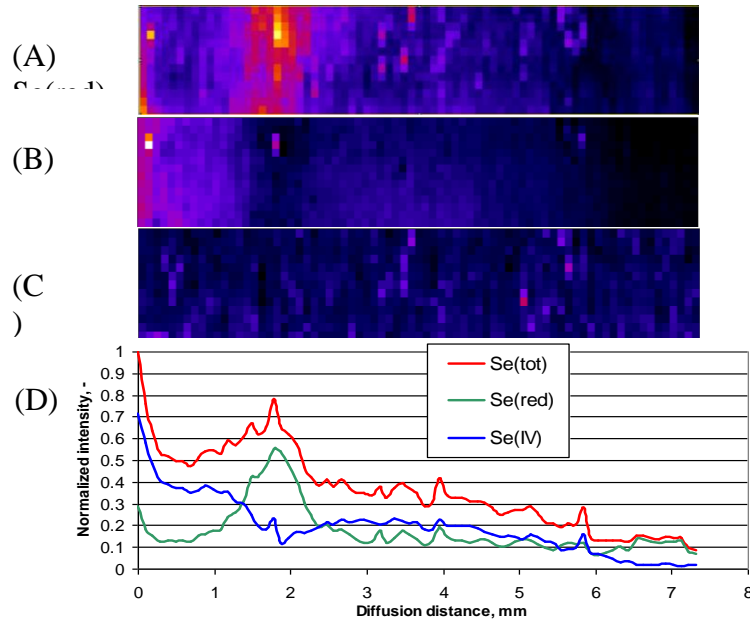


**Figure 5:** (A)  $\mu$ XRF mapping of the Se reduced forms acquired at 12.66 keV. (B)  $\mu$ XRF mapping of the Selenite. (C)  $\mu$ XRF mapping of Fe acquired at energies ranging from 6.1 to 6.7 keV. The resolution is for one pixel: 100  $\mu$ m in X-axis and 50  $\mu$ m in Y-axis. (D) Normalised average values as a function of the diffusion distance.

II-HAS studied U(VI) diffusion in Boda Claystone samples. The aim was to see whether migration of U(VI) through Boda Claystone borecore samples can be coupled with simultaneous  $\text{Fe}^{2+} \Rightarrow \text{Fe}^{3+}$  oxidation taking place in the layered clay minerals of the rock. Break through measurements were applied. Uranyl acetate solution (7.7 g /100 ml) in the upstream reservoir was contacted 8 mm thick bore core samples. Break through was monitored in the groundwater in downstream reservoir for five years. The concentration of uranyl ions decreased in the upstream reservoir but did not appear in the downstream reservoir (Fig. 6 and Lázár et al., 2011) indicating strong retardation of uranyl ions compared to anionic tracers  $^{125}\text{I}^-$ ,  $^{99}\text{TcO}_4^-$ ,  $\text{H}^{14}\text{CO}_3^-$  (Lázár et al, 2009).

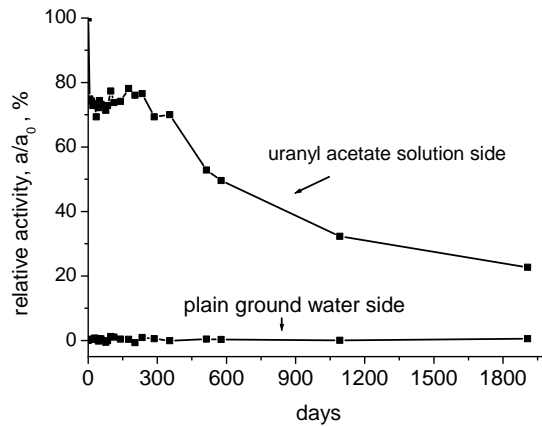


**Figure 6:** Decrease of the concentration of uranium in the uranyl acetate solution in the upstream reservoir (upper curve) and lack of break-through in the downstream reservoir (lower curve).

Mössbauer spectroscopy was used to determine  $\text{Fe}^{2+}/\text{Fe}^{3+}$  ratio in the 2 mm thick surface layers on both sides of the borecore samples. No apparent changes in the  $\text{Fe}^{2+}/\text{Fe}^{3+}$  ratios were observed. The spectra are the same within the accuracy of measurements in the both sides of the discs, regardless whether the sample was taken from the surface contacted with the saturated uranyl acetate solution or from the surface in contact only with ground water. Uranium ( $^{235}\text{U}$  and  $^{238}\text{U}$ ) concentration profile across the sample disk was determined with LA-ICP-MS measurements (Fig. 7). The profile obtained was described by  $C = C_0 e^{-kx}$ , ( $C_0$  is U concentration at the surface,  $x$  is the distance from the surface exposed to the uranyl acetate solution,  $k$  is constant).

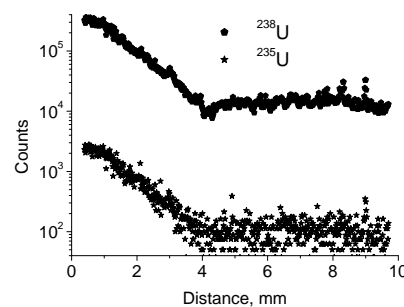


**Figure 7:** U concentration profiles in logarithmic scale along the migration path perpendicular to the surface of the borecore disc

Value of  $C_0$  was also determined by chemical analysis and 1.85 wt % of U was obtained. The amount of the sorbed uranium was estimated with rough calculations which gave 36 mill equivalent of uranium per 100 g of clay. This can be compared with sorption capacity values reported for clay minerals, typically for montmorillonite 50 mill equivalent / 100 g montmorillonite (Tsunashima et al., 1981; Akcay, 1998). The rough comparison shows that sorption probably dominate the sorption of uranium, regardless to the iron content. U oxidation states were also determined and over 99 % of U was found in the U(VI) form. Due to lack of U(IV) it was concluded that sorption of uranium on Boda Claystone is not promoted by redox processes, i.e. the expected coupled simultaneous redox processes  $U(VI) \leftrightarrow U(IV)$  and  $Fe^{2+} \leftrightarrow Fe^{3+}$  do not take place during sorption.

### **Radionuclide mobility under the influence of glacial melt water intrusion**

**KIT-INE** studied simulated glacial melt water intrusion on the mobility of redox sensitive radionuclides in crystalline rock. In the simulation glacial groundwater from the Grimsel Test Site (GTS, Switzerland) and granodiorite from Äspö were used in batch-experiments. Crushed and sieved granodiorite material was pre-equilibrated for 50 days with Grimsel groundwater. All the data from the earlier studies with the Äspö system showed a contact time/residence time dependent retardation and/or reduction kinetic for U(VI), Np(V) and Tc(VII) ([Kienzler et al., 2003](#); [Kienzler et al., 2009](#)). Prior to the start-up of the new experiments, a thorough characterization of the granite material derived from Äspö Hard Rock Laboratory (HRL) and fracture filling material (FFM) from the Grimsel granodiorite (GTS, Switzerland) was performed. More details can be found in Huber et al. (2010 and 2011).

The redox potential  $E_{h(SHE)}$  values at the beginning of the experiments was ~50 mV and dropped in the course of the experiments to values around -100mV (7500h contact time). The aqueous speciation modeling using the code Hydra/Medusa ([Puigdomenech, 2004](#)) implementing only NEA-TTB constants predicted no reduction of U(VI) under the experimental conditions. In the case of Tc the experimental pH/pe conditions are near the borderline of the  $TcO_4^-/TcO_{2(s)}$  transition and a kinetically controlled Tc(VII) reduction is therefore feasible. As shown in Fig. 8 for Tc(VII) and U(VI) the concentration trend is very similar (independent of the granite material) and shows a decrease after ~313 days potentially indicating a sorption/reduction of both radionuclides. The role of colloids was found insignificant.

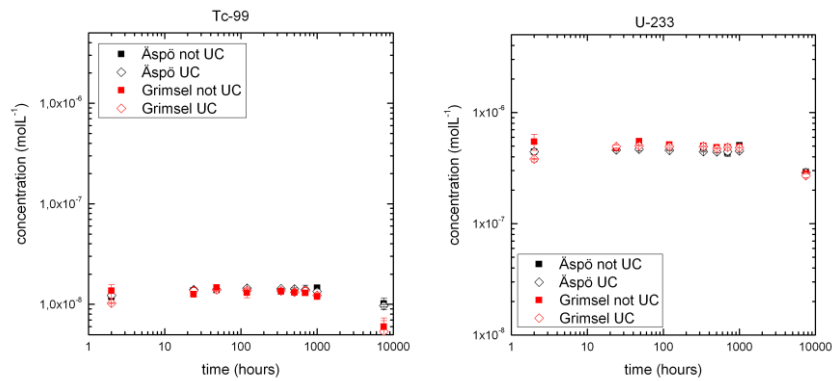


**Figure 8:** Time dependent concentration change for Tc-99 (left) and U-233 (right) over a period of 313 days. Compared are data sets for spiked Grimsel groundwater in presence of Grimsel FFM or Äspö granodiorite and samples ultracentrifuged (UC; open symbols) with not ultracentrifugated samples (filled symbols).

Concerning the Np(V) sorption experiments (Fig. 9) again the concentration decreases over time indicating slow Np(V) reduction in accordance with the pH/pe conditions and an absence of differences between UC and not-UC samples could be observed. Here, the  $K_a$  (surface normalized distribution coefficient) value after 2h is  $\sim 2.4 \cdot 10^{-6}$  m and increases to  $K_a \sim 4.1 \cdot 10^{-4}$  m after 313 days, respectively. The experimental results were directly compared with migration studies on a well characterized core (Huber et al., 2012). Considerable higher retention was obtained for Np in the migration experiments compared to the batch type studies.

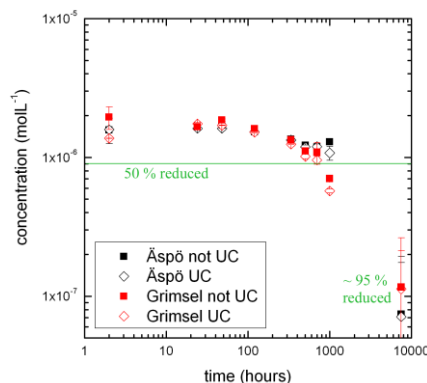


**Figure 9:** Time dependent concentration change for  $^{237}\text{Np(V)}$  with an initial concentration of  $2E-6$  mol/L over a period of 313 days. Compared are data sets for spiked Grimsel groundwater in presence of Grimsel FFM or Äspö granodiorite and samples ultracentrifuged (UC; open symbols) with not-UC samples (filled symbols).

Tc migration experiments revealed migration behavior similar to conservative tracers in line with the batch-type studies and previous work on pertechnetate migration. A very low mobility of U(VI) could be observed in the migration studies (< 1% recovery) which might be related to a secondary phase formation of unknown composition that could not be characterized within the project duration. Furthermore, for the colloid associated tri- and tetravalent radionuclides, Th, Pu and Am, no breakthrough was detected within the experimental duration, although the groundwater conditions are assumed to be unfavourable for colloid attachment. However, stop-flow experiments revealed an admixture of matrix water with significant higher divalent cation concentration which could be a reason for the colloid retention (Ca changing the attachment probability as working hypothesis).

The experimental results obtained under Grimsel groundwater conditions mimicking glacial melt water intrusion scenario clearly show a considerable kinetic controlled retention of Np(V), U(VI), Tc(VII) and colloid associated tri- and tetravalent radionuclides. Future studies have to focus on the detailed mechanistic understanding for the unexpected high retention of U and colloid associated tri- and tetravalent actinides under these geochemical conditions.

UH used observations of U leaching and deposition in fracture network as a tracer to study past redox-processes. Investigations were made in connection to the site characterisation in Olkiluoto, south-west coast of Finland. Information of U behaviour was derived with the help of U series disequilibrium method which can reveal the movement of U isotopes ( $^{238}\text{U}$  and  $^{234}\text{U}$ ) relative to immobile  $^{230}\text{Th}$ , i.e. U leaching and deposition which can be regarded as a sign of redox-processes triggered by a change in hydrochemical conditions that has caused by a change in local hydrology. Currently most geochemical reactions at the site occur along the first few tens of metres of recharge path, in an interface between anaerobic and aerobic conditions (Pitkänen et al., 2008). Aggressive agents  $\text{CO}_2$  and  $\text{O}_2$  in the infiltrating water are consumed and the hydrogeochemistry stabilises to neutral and anaerobic conditions as a result of weathering processes. As a consequence of this evolution, reaction fronts are formed in the flow routes between acid-neutral and aerobic-anaerobic interfaces. It is evident that transient glacial/postglacial evolution in the Baltic Sea region during the Holocene has influenced the current groundwater chemistry Posiva, (2009). The latest deglaciation started 11500 years ago. The cover of ice retreated from Olkiluoto site about 11000 years ago but Olkiluoto remained under the mildly saline Yoldia Sea water which infiltrated into the

bedrock. Also glacial melt water close to the retreating ice margin infiltrated the bedrock under considerable pressure. According to groundwater stable isotopic data (Pitkänen et al. 2004) melt water may have penetrated at least to the depths of 200 to 300 m being able to transport oxygen deeper than Yoldia Sea water and meteoric infiltrations. The site also remained submerged during the stages of the fresh water Ancylus Lake (started some 10800 years ago) and saline Littorina Sea (started around around 8500-8000 years ago). The denser seawater of the Littorina Sea could have infiltrated into the bedrock by gravity and penetrated deeply mixing with the glacial and preglacial groundwaters, which were already present in the bedrock. Infiltration of melt and marine waters most probably affected the flow paths and groundwater composition at least in the most conductive hydrogeological features. Based above description it is possible that the shift in the redox environment also occurred during infiltrations. Steady-state infiltration of fresh meteoric water started after Olkiluoto Island begun to emerge from the Baltic Sea about 3000-2500 years ago. Due to planar topography of Olkiluoto Island the flushing of the bedrock is limited ranging from the surface down to a few tens of meters. Infiltration of carbonic acid and oxygen containing meteoric water is aggressive inducing weathering processes along the flow paths. In the central part of the site fresh water infiltration seems to be limited to the depth of main hydrogeological zone system HZ19 and mostly above it from where the samples to this study were obtained.

Over 40 fracture surface samples from close to ground surface (3 – 120 m) were studied for U leaching/deposition. Respective U series data was analysed using a model presented in Osmond et al. (1983). The model is based on U/Th geochemistry and the known behaviour of the U series isotopes  $^{238}\text{U}$ ,  $^{234}\text{U}$  and  $^{230}\text{Th}$  in redox-frontal system where U series nuclides produce characteristic distribution across the redox-front (Fig. 10). In the upstream side of the redox-front (sector I in the model) U leaching produces  $^{230}\text{Th}$  excess in the fracture surface material because Th is immobile. Correspondingly, in the downstream side of the redox-front U depositions of different ages produce activity ratios with excess of U isotopes (sectors II-V). Therefore, determination of U series activity ratios in fracture surface material allows easy recognition of redox-front.

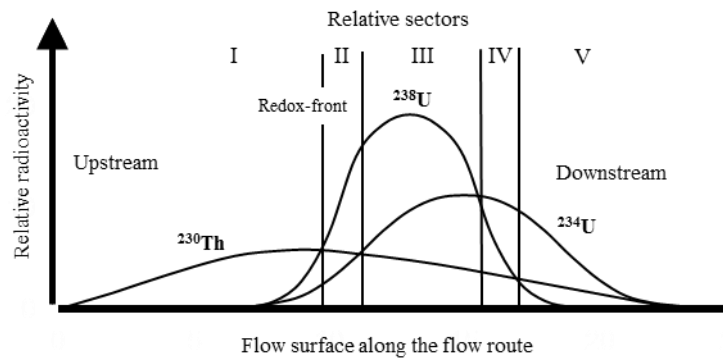


**Figure 10:** Development of  $^{238}\text{U}$ ,  $^{234}\text{U}$  and  $^{230}\text{Th}$  activities on flow surfaces along the flow route under steady-state flow field (modified from Osmond et al. 1983). Nuclide activity ratios obtained from the respective activity curves define sectors from I to V which contain information of flow process. At the beginning U is leached leaving immobile  $^{230}\text{Th}$  behind (sector I). Redox-front occurs between sectors I and II where  $^{238}\text{U}$  activity exceeds  $^{230}\text{Th}$  activity indicating U deposition. Due to enhanced mobility of  $^{234}\text{U}$  it moves ahead of  $^{238}\text{U}$ . In the downstream side of the redox-front deposition and decay of U isotopes modify activity ratios which typify the sectors.

For the analysis of the U series data measured activity ratios  $^{234}\text{U}/^{238}\text{U}$  and  $^{230}\text{Th}/^{238}\text{U}$  were plotted in a diagram (Fig. 11). The horizontal line at  $^{234}\text{U}/^{238}\text{U}=1.0$  separates upstream samples from the downstream samples. The diagonal line  $^{230}\text{Th} = ^{234}\text{U}$  divides samples into upstream (lower right) and downstream (upper left) sets. The meaning of the vertical  $^{230}\text{Th}/^{238}\text{U} = 1.0$  line varies: at the top of the diagram samples plotting to the right (sector V) are from further downstream while at the bottom samples plotting to the right (sector I) are from further upstream until to the ground surface. Samples plotting in the upper right sector cannot form under steady-state flow, i.e. nuclide activity curves in Figure 10 do not form any activity ratio to be found in this sector.

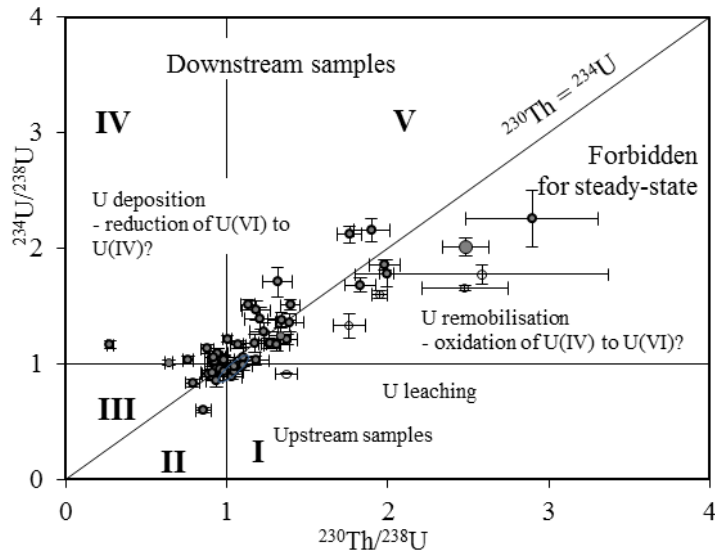


**Figure 11:** U series disequilibrium records presented according to the model in Osmond et al. (1983). Large number of samples plot in recent U deposition sectors IV and V. Is the U deposition a result of U reduction? Number of samples plots in the sector which is forbidden in steady-state flow field. Pathway to this sector via leaching of deposited U, mainly from sector V. If U deposition is a result U(VI) reduction to U(IV), is U leaching from deposited U a result of oxidation?

Leaching of U was observed in a very limited number of samples which suggests that infiltrated waters promoting U mobilisation have flowed through specific routes. Most of the samples showed U deposition indicating that infiltration rapidly turns to anoxic (in agreement with hydrochemistry) triggering U deposition. In a significant part of the samples U series results were not consistent with the steady-state flow model suggesting that respective fracture surfaces have experienced infiltration that is different from the steady-state meteoric recharge. Forbidden U series records were found close to the ground surface mostly in the first 30 m the deepest observation being from the depth of 120 m. Formation of forbidden U series records was studied in detail with model calculations. Possible evolutionary pathways were simulated under different U mass flow scenarios. According to the results forbidden U series records can be created only if deposited U remobilises and considerable U mass is leached which would be hardly possible under reducing conditions. Outcrop rock samples from around the infiltration area were studied as a reference for oxidative leaching. Outcrops (bald bedrock) have been under current conditions since Olkiluoto Island emerged from the Baltic Sea about 3000-2500 years ago. All U series data from outcrop samples plotted in

sector I manifesting leaching of U in oxidising conditions. More details can be found in Suksi and Salminen (2010) and Suksi and Pitkänen (2012).

Findings of recent (in last glaciation time-scale) U leaching and depositions suggest that above mentioned infiltrations have affected redox-conditions in the bedrock. Future prospects include determination of U oxidation states in U depositions plotted in sectors IV and V (Fig. 11). Methodology for that is under development (next chapter).

### **Method development for analysing U oxidation states in solid U compounds**

Finding of recent U depositions in fracture surfaces in U poor environment raised a question of whether deposition could be due to U(VI) reduction to U(IV). Due to low U concentration of depositions (few ppm) instrumental XAS, XPS etc. methods were not able to apply which gave a good reason to develop wet chemical method. It is known that U oxidation states can be determined reliably by chemical method provided that original U oxidation forms composition is not disturbed during U dissolution from the sample material. However, U redox-balance is known to disturb because ferric and ferrous mineral phases in the sample material are dissolved at the same time (Ervanne and Suksi, 1996; Ervanne, 2003). Within WP 5 a series of experiments were carried out with a certified reference U/Th ore as a test material. The main U minerals in the material are uraninite  $UO_{2+x}$  ( $0 < x < 0.25$ ) and brannerite  $(U,Ca,Ce)(Ti,Fe)_2O_6$ . Uranium concentration is 116  $\mu\text{g/g}$ . Material contains 0.9% Fe and 0.45% S, the elements which may disturb U redox state during U dissolution. Main rock forming mineral components were identified as quartz, muscovite (mica), pyrite and iron oxides. For the extraction of U from the sample material pure 4.5 M HCl and mixed with 0.03 M HF were prepared using commercial acids, and then bubbled with Ar gas during several minutes to remove dissolved oxygen. Two redox tracers  $^{232}\text{U}^{4+}$  and  $^{236}\text{U}^{6+}$  were used to monitor redox-change during extraction.  $\text{U}^{4+}$  and  $\text{U}^{6+}$  fractions were separated from each other in an anion exchange column (Dowex 1 $\times$ 4, 50-100 mesh) regenerated with 4.5 M HCl. Extraction solution was loaded into the column and  $\text{U}^{4+}$  was collected in the first 20 ml because respective chloro complexes do not fix in the column.  $\text{U}^{6+}$  chloro complexes fixed in the column was eluted with 20 ml of 0.1 M HCl. U isotope concentrations were measured by  $\alpha$ -spectrometry. Uranium L<sub>III</sub> XANES (ANKA, Karlsruhe Institute of Technology) with  $\text{UO}_2$  and schoepite as references was used for comparison (Pidchenko et al. 2012a and 2012b).

The amount of undissolved U was 10-18% of the total and was considered  $U^{4+}$ . XANES results confirmed that U in residue is in  $U^{4+}$  state. Different results obtained for varying sample masses indicate disturbance of redox balance which was found to relate to different concentrations of  $Fe^{2+}$  and  $Fe^{3+}$  fractions. The amount of Fe in  $U^{4+}$  and  $U^{6+}$  fractions measured by atomic absorption spectrometry showed that the amount of  $Fe^{2+}$  coming with  $U^{4+}$  fraction, is up to eight times higher than that for  $Fe^{3+}$ , which is coming with  $U^{6+}$  fraction eluting with 0,1 M HCl. High  $Fe^{2+}$  concentration in extraction solution creates reducing conditions which become more reducing with larger sample amounts promoting faster  $U^{6+}$  reduction kinetics.  $^{232}U^{4+}$  and  $^{236}U^{6+}$  tracers behaviour was studied using two different sample material and with varying masses. In the first experiments only the behavior of  $^{232}U^{4+}$  was studied. The results showed that no significant oxidation of  $^{232}U^{6+}$  tracer occurred; less than 2% of total  $^{232}U$  was found in  $U^{6+}$  fraction irrespective of the samples material, i.e. extraction system is stable against U tracer oxidation. It has to be taken into account that  $U^{4+}$  and  $U^{6+}$  fractions have a slight overlap in the anion exchange step (Hussonnois et al., 1989), which would explain 1-3% leak of “wrong” fraction. On the other hand, the reduction of  $U^{6+}$  to  $U^{4+}$  is quite dramatic at least with the largest sample mass.  $^{236}U^{6+}$  tracer is reduced up to 80% with 500 mg of the sample. U redox effects can be quantitatively estimated for a few minutes extraction time using ion-exchange chromatography. Application of U redox tracers made possible to transfer leaching experiment results to the original solid material. Results from the wet chemistry were to some extent in agreement with those obtained for XANES measurements. Application of synchrotron radiation methods for U oxidation forms analysis in U low samples can be complicated because to get sufficient statistics very long measurement times are needed.

### **Study of radionuclide behaviour in contaminated areas**

**UCyprus** studied the behaviour of U within a phosphogypsum (PG) disposal site in a coastal area in front of a former fertilizer plant in Cyprus. Among the physicochemical parameters such as pH,  $E_H$ , ionic strength, chemical composition (Papanicolaou et al., 2009), the redox potential ( $E_H$ ) may significantly affect the chemistry and hence stability and leachability of PG. Generally, an enormous drop in the redox potential takes place due to restricted oxygen diffusion within the stack, organic matter disintegration and proceeding microbial activity, which leads eventually to reduction of sulphate S(+VI) to sulphide S(-II) (Luo et al., 2007));

Papanicolaou et al., 2010)). Regarding the geochemistry of PG there are several studies on acidic runoff and hazardous material dispersion in the near-field of PG stacks. These studies show that groundwater pollution under a PG stack is possible (Rutherford et al., 1994).

In the present study several observation boreholes were drilled into the stack (to a maximum depth of 5 meters) and stack solutions were sampled from the boreholes using a submersible pump and filtered in the field immediately after collection. Since spring 2008, the stack has been covered by 1-meter topsoil and dense vegetative cover, which will affect the redox conditions within the stack. Because the cover is relatively young the effects due to the soil/vegetative cover are observed only close to the soil-PG interface. Therefore, solid samples were obtained from PG adjacent to the topsoil and affected by organic run-offs. The respective samples have in contrast to non-affected PG, which is white coloured, pale-brown to dark-brown colour.  $E_H$ , pH, and solubility experiments were performed in-situ and in laboratory systems. Uranium concentration measurements as well as  $^{230}\text{Th}/^{238}\text{U}$  ratios show higher uranium retention under anoxic conditions, which could be ascribed to the lower solubility and mobility of U(IV). Uranium series nuclides  $^{238}\text{U}$ ,  $^{234}\text{U}$  and  $^{230}\text{Th}$  were analysed to obtain information of U behaviour in the system. Sample materials were extracted in *aqua regia* and U series nuclides were analysed using ion exchange chromatography and  $\alpha$ -spectrometry.

**Table 1.** U series nuclide concentrations and activity ratios in sample materials.

Sample material	U [mg/kg]	$\pm\delta$	$^{234}\text{U}/^{238}\text{U}$	$\pm\delta$	$^{230}\text{Th}/^{234}\text{U}$	$\pm\delta$
PG	4.9	0.2	0.97	0.04	9.62	0.49
PRock	73	2	1.04	0.03	1.05	0.05
PGNOM	12.5	0.4	1.03	0.04	4.46	0.22

As was expected the highest U concentration was found in phosphate rock (PRock). Nuclide activity ratios show also radioactive equilibrium in this material. PG with NOM shows elevated U concentration compared to PG. If the latter acts as a U source from where U is leached and PGNOM collects U the observed decrease in the  $^{230}\text{Th}/^{234}\text{U}$  activity ratio from around 10 in PGypsum to 5 explains the process. It is also possible that fixing the phosphogypsum stack with the soil/vegetative cover may have added some U in phosphogypsum which can explain the decrease in the  $^{230}\text{Th}/^{234}\text{U}$  activity ratio as well.

Uranium redox-state was studied by determining U oxidation states in the sample material. U(IV) and U(VI) fractions were determined as described above (e.g. Hussonnois et al. 1989; Ervanne and Suksi, 1996). For quantitative determination  $\alpha$ -spectrometry was used.

Table 2. U oxidation state distribution in sample materials.

Sample	U(IV) [mg/kg]	$\pm\delta$	$^{234}\text{U}/^{238}\text{U}$	$\pm\delta$	U(VI) [mg/kg]	$\pm\delta$	$^{234}\text{U}/^{238}\text{U}$	$\pm\delta$	% U(IV)
PRock1	35.3	0.7	0.92	0.02	33	1	1.08	0.0	51
								3	
PRock2	41.0	0.6	0.92	0.02	31	1	1.09	0.0	57
								3	
PGypsum	0.20	0.0	0.99	0.09	11.2	0.4	1.03	0.0	1.8
NOM		2						2	

Non-affected PG did not contain U(IV). Some 50 % of U in the phosphate rock (duplicate samples) occurs in U(IV) fraction. The lower  $^{234}\text{U}/^{238}\text{U}$  activity ratio of U(IV) is explained by transfer of  $^{234}\text{U}$  from the U(IV) pool to U(VI) pool due to radioactive decay which causes  $^{234}\text{U}$  to be born in higher oxidation (VI) state. Different  $^{234}\text{U}/^{238}\text{U}$  activity ratios in U(IV) and U(VI) can also be considered a kind of success in oxidation state separation. Some U(IV) was found in NOM containing phosphogypsum suggesting U(VI) reduction to U(IV) during U accumulation in this material.

**MSU** has studied behaviour of radionuclides in contaminated soil and lake environment in industrial reservoirs at PA “Mayak” (Russia) in collaboration with KIT-INE. It has been estimated that about 20 quintillions Bq of radionuclides were disposed of and 4-5 millions m<sup>3</sup> of contaminated solutions were penetrated into groundwater system at the site providing a unique natural laboratory to develop link between field and laboratory data. The methods included (1) redox speciation of actinides (U and Pu) by spectroscopic methods (XPS, XAFS) and membrane extraction, (2) study of possibility of formation of An(IV) eigencolloids by alpha track analysis, TEM, STEM-HAADF, EELS and XAFS and their evolution upon redox transformations, dilution, changes of pH, Eh, ionic strength, interaction with NOM, (3) study of preferential binding of actinides to different colloids by nano-SIMS and their redox speciation by membrane extraction. In particular, the role of humics in actinide redox-speciation has been studied. Some of the Pu is bound to the organic nanoparticles that are

stable within long period of time and can therefore be mobile. Redox-state of Pu is still unknown and would be studied using “chemical” methods.

Uranium was found to occur as isolated uranium particles with no associations with other elements  $\geq$ Ca, neither evenly distributed within the particles nor as agglomerate that would imply U sorption on a mineral surface that nucleated further growth of a U-containing precipitate on the surface. The XANES and the EXAFS spectra and curve-fit results unambiguously show that the particles consist of chemically homogeneous  $UO_{2+x}$ ,  $U_3O_8$ , and schoepite  $(UO_2)_8O_2(OH)_{12}(H_2O)_{12}$  with metrical parameters within the range exhibited by these compounds within the lab and other environmental and geological sources. There are no indications even after several decades of environmental exposure of any convergence of these species towards the most stable schoepite form. It can therefore be safely assumed that these species are the original source terms from multiple waste streams and that they unexpectedly were highly inert under these conditions.

More details from studies above can be found in Batuk et al. (2011), Kalmykov et al. (2011) and Romanchuk et al. (2011).

## References

Akcay, H., (1998) Aqueous speciation and pH effect on the sorption behaviour of uranium by montmorillonite, *J. Radioanalytical and Nuclear Chemistry*, 237, 133-137.

Batuk D.N., Shiryayev A.A., Kalmykov S.N., Batuk O.N., Romanchuk A.Yu., E.A. Shirshin, Zubavichus Ya.V., 2011. Sorption and Speciation of Uranium on Silica Colloids. In: *Actinide nanoparticleresearch*. In: S. Kalmykov and M. Denecke (Editors), Springer. 2011, p. 315-332

Charlet L., Scheinost A, Tournassat C., Greneche J., Gehin A, Fernandezmartinez A, Coudert S., Tisserand D., Brendle J. (2007). Electron transfer at the mineral/water interface: Selenium reduction by ferrous iron sorbed on clay. *Geochimica et Cosmochimica Acta*, 71(23), 5731-5749.

Ervanne, H. and Suksi, J. (1996). Comparison of Ion-Exchange and Coprecipitation Methods in Determining Uranium Oxidation States in Solid Phases. *Radiochemistry* **38**, 306-309.

---

(D-N°:1.2) – [Report on the scientific state of the art](#)

Dissemination level :PU

Date of issue of this report : **03/09/2012**



Frasca B. (2011). Migration de l'iode et du sélénium au travers de roches argileuses. Thèse de L'université Paris-Sud, Orsay.

Huber, F., Kunze, P., Geckeis, H., Schäfer, T., 2010. Sorption/sorptive reduction studies on the interaction of radionuclides with FEBEX bentonite colloids/nanoparticles under Grimsel groundwater conditions in the presence of fracture filling material. In: Buckau, G., Kienzler, B., Duro, L., Grivé, M., Montoya, V. (Editors), 2<sup>nd</sup> Annual Workshop Proceedings 7<sup>th</sup> EC FP – Recosy CP, Larnaca (Cyprus) 16-19<sup>th</sup> March 2010, pp. 122-129.

Huber, F., Kunze, P., Geckeis, H., Schäfer, T., 2011. Sorption reversibility kinetics in the ternary system radionuclide–bentonite colloids/nanoparticles–granite fracture filling material. *Applied Geochemistry*, 26(12): 2226-2237.

Huber, F. et al., 2012. Natural micro-scale heterogeneity induced solute and nanoparticle retardation in fractured crystalline rock. *Journal of Contaminant Hydrology*, 133(0): 40-52.

Hussonnois, M., Guillamont, R., Brillard, L., Fattahi, M. (1989). A method for determining the oxidation state of uranium at concentration as low as 10<sup>-10</sup> M, in: W. Lutze and R.C. Ewing (Eds.), *Mater. Res. Soc.* 127, 979-984.

Kalmykov S.N., Zakharova E.V., Novikov A.P., Myasoedov B.F., Utsunomiya S., 2011. Effect of Redox Conditions on Actinide Speciation and Partitioning with Colloidal Matter. In: Actinide nanoparticle research. In: S. Kalmykov and M. Denecke (Editors), Springer. 2011, Springer, 2011, p. 361-375.

Kienzler, B. et al., 2003. Swedish-German actinide migration experiment at ASPO hard rock laboratory. *Journal of Contaminant Hydrology*, 61(1-4): 219-233.

Kienzler, B., Vejmelka, P., Romer, J., Schild, D., Jansson, M., 2009. Actinide Migration in Fractures of Granite Host Rock: Laboratory and in Situ Investigations. *Nuclear Technology*, 165(2): 223-240.

Lázár K., Megyeri J., Parneix, J-C., Máthé Z., Szarvas T., (2009) Diffusion of anionic species ( $^{99}\text{TcO}_4^-$ ,  $\text{H}^{14}\text{CO}_3^-$ ) and HTO in Boda Claystone borecore samples, in: 4th Annual Workshop Proceedings, FUNMIG, Eds: G. Buckau et. al, Forschungszentrum Karlsruhe, Wissenschaftliche Berichte, FZKA 7461, 199-204.

Lázár K., Megyeri J., Mácsik Zs., Széles É., Máthé Z., (2011) Migration of uranyl ions in Boda Claystone samples, In: M. Altmaier, B. Kienzler, L. Duro, M. Grive, V. Montoya (Editors), 3<sup>rd</sup> Annual Workshop Proceedings 7<sup>th</sup> EC FP – Recosy CP, Balaruc-les-Bains (Sète – Languedoc – Rousillon, France) 21<sup>th</sup> – 24<sup>th</sup> March 2011, pp. 91 – 97.

Luo J., Weber F.-A., Cirpka O. A., Wu W.-M., Nyman J. L., Carley J., Jardine P. M., Criddle C. S., Kitanidis P. K. (2007), Modeling in-situ uranium(VI) bioreduction by sulfate-reducing bacteria, J. Contam. Hydrol., 92, 129-148.

Osmond, J. K., Cowart, J. B. and Ivanovich, M. (1983). Uranium isotopic disequilibrium in groundwater as an indicator of anomalies. Int. J. Appl. Radiat. Isot. 34, No. 1, 282-308.

Posiva 2009. Olkiluoto site description 2008. Posiva 2009-01.

Pashalidis, I. and Suksi, J., 2012. Redox Chemistry and Mobility of Uranium in Phosphogypsum. 4<sup>th</sup> Annual Workshop Proceedings of the Collaborative Project “Redox Phenomena Controlling Systems” (7<sup>th</sup> EC FP CP RECOSY).

Papanicolaou, F., Antoniou, S., Pashalidis, I. (2010), Redox chemistry of sulphate and uranium in a phosphogypsum tailings dump, J. Environ. Radioact., 101, 601-605.

Pidchenko, I., Salminen-Paatero, S., Vitova, T. and Suksi, J., 2012. Study of U oxidation states in natural geological material. 4<sup>th</sup> Annual Workshop Proceedings of the Collaborative Project “Redox Phenomena Controlling Systems” (7<sup>th</sup> EC FP CP RECOSY).

Pidchenko, I., Salminen-Paatero, S., Vitova, T. and Suksi, J., 2012. Study of U oxidation states in low U geological material. Submitted to Journal of Environmental Radioactivity.



Pitkänen, P., Korkealaakso, J., Löfman, J., Keto, V., Lehtinen, A., Lindgren, S., Ikonen, A., Aaltonen, I., Koskinen, L., Ahokas, H., Ahokas, T. and Karvonen, T., 2008. Investigation plan for infiltration experiment in Olkiluoto. Working Report 2008-53, 38 p.

Puigdomenech, I., 2004. HYDRA and MEDUSA chemical equilibrium software. Software and documentation. <http://web.telia.com/~u15651596/>

Romanchuk, A.Yu., Kalmykov S.N. and Aliev R.A., 2011. Plutonium sorption onto hematite colloids at femto- and nanomolar concentrations. Radiochim. Acta 99, p. 137–144.

Rutherford, M.J., Dudas, P.M., Samek, R.A. (1994), Environmental impacts of phosphogypsum, Sci. Total Environ., 149, 1-38.

Savoye S., Frasca B., Grenut B., Fayette F., Radwan J. (2011). Study of the Diffusive behaviour of selenite and selenate through the Callovo-oxfordian claystones (France): effect of the initial selenite concentration. 3<sup>rd</sup> Annual Workshop Proceedings of the 7<sup>th</sup> EC FP

Savoye, S., Schlegel, M., Frasca, B., Fayette, A. and Grenut, B., 2012. How mobile is selenite diffusing through the Callovo-Oxfordian claystones? Insights given by radiochemistry and x-ray absorption spectroscopy. 4<sup>th</sup> Annual Workshop Proceedings of the Collaborative Project “Redox Phenomena Controlling Systems” (7<sup>th</sup> EC FP CP RECOSY).

Schackelford C.D. (1991). Laboratory diffusion testing for waste disposal: A review. Journal of Contaminant Hydrology 7, 177-217.

Suksi, J. and Salminen, S., 2010. Study of U oxidation states in U deposited on fracture lining rock. 2<sup>nd</sup> Annual Workshop Proceedings 7<sup>th</sup> EC FP - Recosy CP, Larnaca (Cyprus), p. 229-236.

Suksi, J. and Pitkänen, P., 2012. U series disequilibrium records in active hydrogeological zone – a case study. To be submitted to Applied Geochemistry.

Tsunashima A., Brindley G.W., Bastovanov M., (1981), Adsorption of uranium from solutions by montmorillonite; compositions and properties of uranyl montmorillonites, Clays and Clay Minerals, 29, 10–16.

## WP6. Redox reactions affecting the spent fuel source-term

The source term from spent fuel dissolution is subject to considerable uncertainties, both with respect to the presence and extent of oxidative dissolution processes of the spent fuel itself and the coupling with processes associated with the iron canister. Related problems to be examined in this work package are the representativeness and reliability of laboratory data with respect to the impact of unavoidable minor concentrations of oxygen also in inert-gas boxes used, the potential reactivity and its outcome of hydrogen from container corrosion in combination with high burn-up spent fuel, possible galvanic coupling of spent fuel and container material and the retention of redox sensitive radionuclides by relevant minerals, especially by steel container corrosion products.

A set of investigations has been conducted with the aim of getting better insight into redox processes determining spent fuel and iron canister corrosion. The following summary covers the activities conducted between 2008 and 2012 (BUCKAU G., KIENZLER B., DURO L., GRIVÉ M., MONTOYA V. (EDS.) (2009), BUCKAU G., KIENZLER B., DURO L., GRIVÉ M., MONTOYA V. (EDS.) (2010), ALTMAIER M., KIENZLER B., DURO L., GRIVÉ M., MONTOYA V. (EDS.) (2011), ALTMAIER M., KIENZLER B., DURO L., GRIVÉ M., MONTOYA V. (EDS.) (2012)). **ITU** reports on *studies on spent fuel in presence of corroding Fe, on corrosion of spent fuel in presence of H<sub>2</sub> and on fuel corrosion studies on thin film model systems. The redox reactivity of doped UO<sub>2</sub> in view of effects on the reactivity towards H<sub>2</sub>O<sub>2</sub>* has been studied at **KTH**. *The reductive trapping of actinides in container corrosion products during spent fuel corrosion* is investigated by **INE**. **Studsvik** reports on *the redox chemistry at the near field of repository and the influences of iron canister material and hydrogen. Redox conditions near waste packages* were studied by **NRI**.

## Studies on Spent Fuel in Presence of Corroding Fe and on Thin Film Model Systems (JRC-ITU)

### Introduction

Underground storage of spent nuclear fuel is a generally accepted strategy for final disposal. In many European countries the disposal concept foresees a storage of spent fuel in a cast iron, stainless steel or carbon steel container with an overpack of copper or carbon steel [BENNETT D.G., GENS R. (2008); FÉRON D., CRUSSET D., GRAS J.-M. (2008)]. In such a container spent fuel is in direct contact with the cladding material e.g. Zircaloy and steel. The principle of galvanic coupling of spent fuel with metals has been discussed at the example of defect spent fuel electrodes immersed in synthetic groundwater and 5 M NaCl solution [GRAMBOW B. ET AL. (2000)]. Studies on the effect of carbon steel and Zircaloy-4 in direct contact with  $UO_{2+x}$  have been carried out in salt brines and bentonite porewater under oxidising conditions. It was shown that in case of Zircaloy-4  $UO_2$  dominates the contact potential and the corrosion behaviour [KUPFER A. (2000)] while in the pair carbon steel and  $UO_2$  the steel is dominating. In the latter case the corrosion of  $UO_2$  is reduced when in direct contact with steel. This effect is enhanced in cases where less iron corrosion products were detected which form a passive layer on the steel surface [ENGELHARDT J., MARX G. (1999)]. The stability of this passive layer is influenced by hydrogen [YU J.G., LUO J.L., NORTON P.R. (2002)]. Hydrogen promotes the susceptibility of the passive film on iron to pitting corrosion especially under lower chloride ion concentrations. Therefore studies on the behaviour of  $UO_2$  electrically connected to carbon steel in presence of hydrogen have been carried out.

### Experimental

The experiments have been carried out with a new developed electrochemical cell for thin film applications [BUCKAU G., KIENZLER B., DURO L., GRIVÉ M., MONTOYA V. (EDS.) (2010)]. This cell (Figure 1) is connected to the vacuum system of a XPS/UPS spectrometer. The construction allows a transfer of electrodes from the spectrometer into the cell and vice versa without any exposure to air. The setup also allows a pre-purging of the stock solution and after transfer into the cell gaseous and liquid phase can be purged separately with gas. The samples have been prepared by coating of specially made carbon steel plates (ST37-2)

with  $\text{UO}_2$  thin films. The latter are prepared by reactive sputter deposition from a uranium metal target with  $\text{Ar}/\text{O}_2$  mixtures as sputter gas. The plasma in the diode source is maintained by injection of electrons of 50 - 100 eV energy. This allows reaching a sputter gas pressure below 5 Pa in absence of stabilizing magnetic fields (magnetron setup). Ultrahigh purity argon and oxygen (99.9999% each) are used for the experiments. Films have a mass of typically 100 - 200  $\mu\text{g}$  (corresponding to a film thickness of around 100 - 200 nm). XPS spectra are recorded with a Leyboldt EA-10 hemispherical analyzer, using  $\text{Al K}\alpha$  (1486.6 eV) and  $\text{Mg K}\alpha$  (1253.6 eV) excitation radiation. Calibration is done on the  $\text{Au-4f}_{7/2}$  level of a sputter cleaned polycrystalline Au standard, set to a binding energy (BE) of 84.0 eV. The Fermi-level cut-off of the metal is set to 0.00 eV BE in UPS. Those films have shown their ability to act as a simplified model for single parameter studies on the electrochemical behaviour of spent fuel [WEGEN D.H., GOUDER T., ECKLE M., WISS T., GLATZ J.-P. (2004); SEIBERT A. ET AL. (2011)]. An important advantage of those films for electrochemical studies is their low resistance which makes in many cases  $iR$ -drop corrections superfluous [MISERQUE F., GOUDER T., WEGEN D.H., BOTTOMLEY P.D.W. (2001)]. On the other hand there is a risk of  $\text{O}_2$  leakage because it was not possible to install the electrochemical cell inside a glove box. Experiments under  $\text{Ar}/\text{H}_2$  were run under oxygen monitoring by a NeoFox phase measurement system equipped with a FOXY-R optical sensor with FOSPOR coating (Ocean Optics).

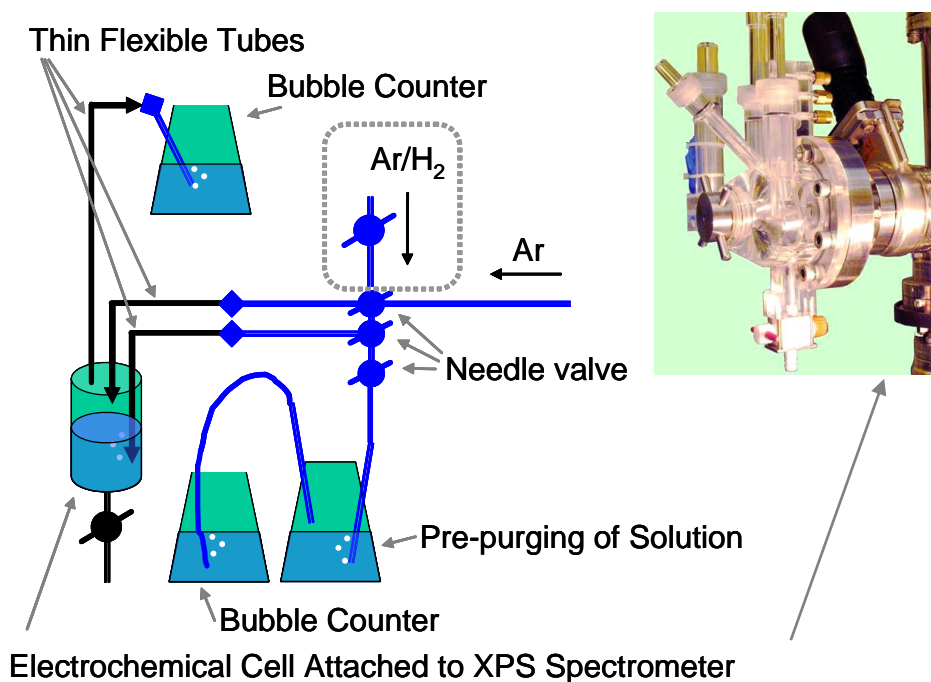


**Figure 1:** Schematic experimental set-up.

Special manufactured carbon steel supports were fully or partially coated with  $\text{UO}_2$  by reactive sputtering and then used as electrodes. The stoichiometry of the films was checked by XPS analysis before and after the experiments. The experimental conditions are summarised in Table 1.

Open circuit potentials (OCP) were measured in experiments A1-A3 after 2 minutes pre-cathodisation at  $-1.3\text{ V}$  over 20 hours on uncoated, partially coated and fully coated carbon steel specimen in  $10\text{ mM NaCl}$  solution under Ar-purging at  $19^\circ\text{C}$ - $22^\circ\text{C}$  (Figure 2). In all other experiments the pre-cathodisation was dropped and the polished, cleaned and then uranium oxide coated steel samples were used directly after sputter deposition (and pre-corrosion) for OCP measurements (IM6 Zahner Elektrik). Further  $E_h$  (Mettler-Toledo InLab®501 redox combination electrode), pH (WTW Sentix 97) and temperature were recorded (WTW Multiline 340i). Impedance spectra were recorded in situ at distinct time intervals to investigate ongoing processes. After exposure the solution was collected and analysed by ICP-OES and ICP-MS. The coated steel electrode was dried under inert gas and vacuum and directly introduced into the XPS-spectrometer for analysis. Then the specimen were optically examined and in some cases they were analysed by Raman spectroscopy (Horiba Scientific T64000).

### Results

The measured OCP is shown in Figure 2. At the times where the shown curves are interrupted impedance measurements have been carried out. During experiment C the recorder failed to start which results in a large gap in curve C. Generally the OCP were in good agreement with those measured by Smart et al. on carbon steel in artificial groundwater [SMART N.R., BLACKWOOD D.J., WERME L. (2001)].

In case A (precathodisation) the measured mean OCP are for carbon steel (A1)  $-450\text{ mV}_{\text{SHE}}$  ( $E_h=+490\text{ mV}_{\text{SHE}}$ ) and for the half with  $\text{UO}_2$  covered carbon steel (A3)  $-480\text{ mV}_{\text{SHE}}$  ( $E_h=+440\text{ mV}_{\text{SHE}}$ ).

**Table 1:** Summary of the experimental conditions.

Conditions for all experiments	<ul style="list-style-type: none"> <li>• carbon steel (ST37-2)</li> <li>• 10 mM NaCl , initial pH 7</li> <li>• 20-22 hours duration</li> <li>• RT (19°C – 22°C)</li> </ul>
Variation of conditions	
A)	<ul style="list-style-type: none"> <li>• initial uranium oxide film (with slight ~3 at-%Th contamination from sputter source): none (A1), fully coated with UO<sub>2</sub> (A2) and half coated with UO<sub>2+x</sub> (A3) <ul style="list-style-type: none"> <li>• continuous Ar purging</li> <li>• prior to OCP 2min at -1.3 V</li> </ul> </li> </ul>
B)	<ul style="list-style-type: none"> <li>• initial film: UO<sub>2+x</sub> <ul style="list-style-type: none"> <li>• continuous Ar purging</li> <li>• no precathodisation</li> </ul> </li> </ul>
C)	<ul style="list-style-type: none"> <li>• initial film: UO<sub>2</sub> <ul style="list-style-type: none"> <li>• continuous Ar/5%H<sub>2</sub> purging</li> <li>• no precathodisation</li> </ul> </li> </ul>
D)	<ul style="list-style-type: none"> <li>• initial film: in humid atmosphere pre-corroded electrode <ul style="list-style-type: none"> <li>• continuous Ar/5%H<sub>2</sub> purging</li> <li>• No precathodisation</li> </ul> </li> </ul>

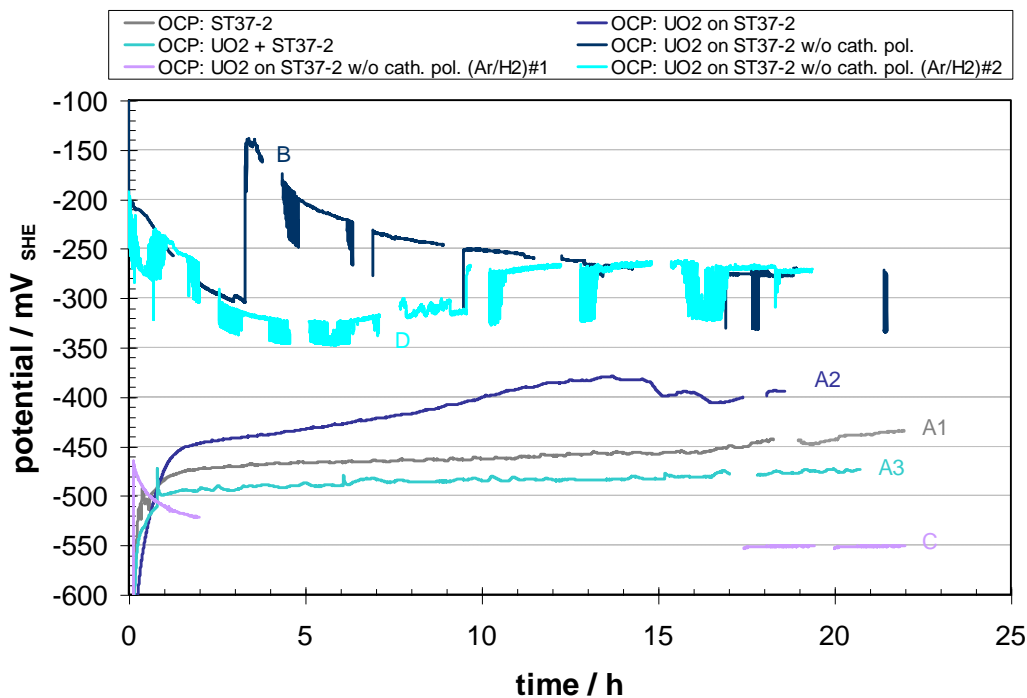


**Figure 2:** Open circuit potentials (OCP) measured on carbon steel (A1) and on fully (A2, B, C, D) and partially (A3) UO<sub>2</sub> coated carbon steel in Ar-purged (A1, A2, A3, B) and Ar/H<sub>2</sub>-purged (C, D) 10 mM NaCl solution at RT with (A1, A2, A3) and without (B, C, D) pre-treatment (cathodic polarisation).

Taking into account the slightly more oxidising condition in case of the steel the measured OCP are comparable. A still negative but clearly more anodic OCP of ~-400 mV<sub>SHE</sub> ( $E_h = +460$  mV<sub>SHE</sub>) was found for the fully UO<sub>2</sub> covered steel sample (A2). Microscopic examination of the UO<sub>2</sub> film after the experiment show defects in the UO<sub>2</sub> film accompanied with a localised attack of the steel. The system shows a galvanic coupling, where the UO<sub>2</sub> is cathodically polarised by the corroding steel which predominates the measured OCP in all three cases. The potential at the UO<sub>2</sub>/solution interface is shifted into the cathodic (reducing) regime, this protects the UO<sub>2</sub> surface to be oxidised.

XPS surface analysis done immediately after exposure supports this. No oxidation of the UO<sub>2</sub> surface could be detected and it seemed that the uranium oxide films after the experiments were more UO<sub>2</sub> like, i.e. they were slightly reduced. It could not be distinguished if this reduction occurred during the pre-cathodisation or due to the galvanic coupling with iron. Therefore the experiment was repeated with a fully UO<sub>2+x</sub> covered carbon steel sample without pre-cathodisation. The OCP (B) is 150 to 200 mV higher than in the former

measurements. An air leakage occurred after ~3.5 hours and results in a sharp increase of the potential ( $E_h = +600 \text{ mV}_{\text{SHE}}$  to  $+800 \text{ mV}_{\text{SHE}}$ ). After 4 hours the potential became unstable and showed scattered data. This was a first hint for ongoing localised corrosion processes. During the time where the OCP curves show gaps impedance measurements were performed. They show pseudo inductive behaviour of the corroding sample which is also a sign for localised corrosion. The final proof was the optical examination after the experiment (Figure 3). There are three zones which also reflect the influence of the experimental set-up on the corrosion processes. In the outer zone I the sample surface was touched by the sealing (O-ring) of the measurement cell. In the 12 to 3 o'clock position slight crevice corrosion is visible which occurred in the very narrow gap between the inner part of the O-ring and the sample surface. The next inner zone II is characterised by a gap formed between the acrylic glass of the cell and the sample (some tenth millimetres) with much more pronounced crevice corrosion. Depth profiles show here a loss of 3 – 5  $\mu\text{m}$ . In the central zone III contact between surface and solution is not hindered. Here localised pitting corrosion occurred with pit depth up to 40  $\mu\text{m}$ .

In experiments C and D To the oxygen content in solution was followed by an optical sensor system. In both cases the oxygen partial pressure was below 2 mbar with an uncertainty of 2 mbar. The OCP of  $-550 \text{ mV}_{\text{SHE}}$  (and  $E_h = -320 \text{ mV}_{\text{SHE}}$ ) measured at the fully  $\text{UO}_2$  coated carbon steel sample under  $\text{Ar}/5\%\text{H}_2$  purging after 17 h is very low. Under these conditions both steel and  $\text{UO}_2$  are corrosion protected. Consequently, the optical examination showed no major onset of corrosion and this behaviour is also reflected in the results of the solution analysis (Table 2). Furthermore was the measured pH ( $7 \pm 0.5$ ) here constant while it in all other experiments dropped from pH 7 to pH ( $5 \pm 0.5$ ). This pH drop can be attributed to an increase of Fe(II) in solution which is here much smaller. Also XPS analysis showed that the uranium oxide film after the experiment was compared to the initial film slightly more reduced.

A completely different behaviour was found under conditions D. Here a freshly on steel deposited and characterised uranium oxide film was oxidised in humid atmosphere prior to the OCP measurement. In this case the OCP was very similar to that measured in case B. The OCP was after 15 hours around  $-270 \text{ mV}_{\text{SHE}}$  ( $E_h = -200 \text{ mV}_{\text{SHE}}$ ) but here an oxygen intrusion can be excluded taking the measured  $E_h$  and oxygen partial pressure into account. The sample was very strongly attacked and showed heavy local defects in the uranium oxide

film and steel combined with slight crevice corrosion at the parts that were covered by the sealing during the experiment. XPS analysis on the uranium oxide after the experiment gave the same result as for the freshly sputtered  $\text{UO}_2$  film, i.e. any higher uranium oxide produced by pre-corrosion was reduced or dissolved.

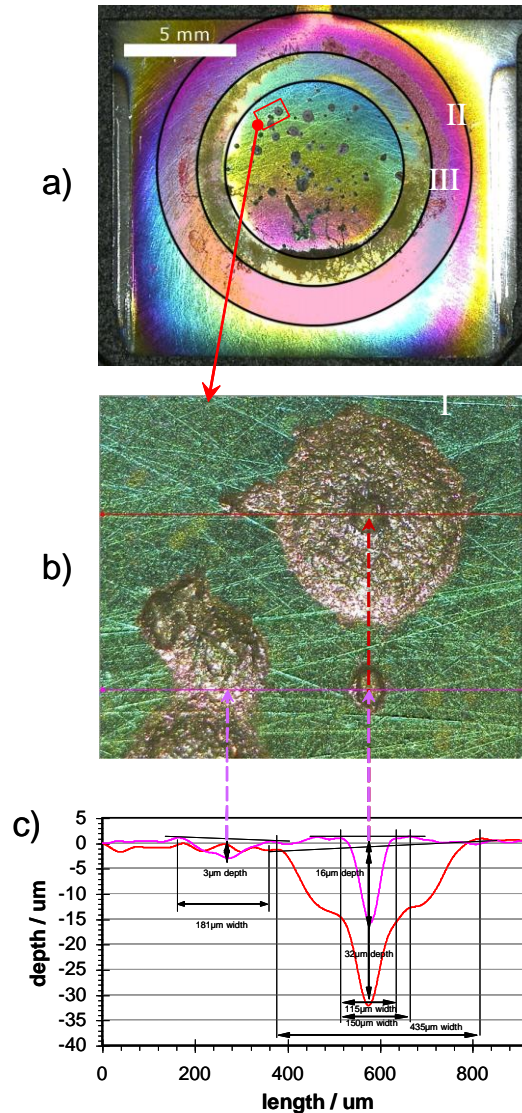


**Figure 3:** Optical microscopy of the  $\text{UO}_2$  coated carbon steel (B) after the experiment (a). The outer reddish zone I marks the area where the sealing (O-ring) touched the sample surface. In the second yellowish zone II a crevice was formed between the cell and the sample surface. The inner ring III shows the area where the surface was in direct contact with the solution. The macrograph b) shows pits which have formed and the related depth profile in c).

Furthermore indicate Fe 2p XPS-spectra measured on the specimen after treatment under conditions C and D different iron oxides on the surface. In case C the iron oxide contains a higher amount of Fe(II) (e.g.  $\text{Fe}(\text{OH})_2$ ) formed by anaerobic corrosion while on the preoxidised sample (aerobic corrosion) Fe(III) (e.g.  $\text{Fe}(\text{OH})_3$ ) is the main part.

ICP-MS and ICP-OES analysis (Table 2) shows much more iron than uranium in solution. This means that the ongoing processes and also the OCP are governed by steel corrosion. The measured OCP is in all cases below the potential of surface oxidation for  $\text{UO}_2$  (of around  $-150 \text{ mV}_{\text{SHE}}$ ).

**Table 2:** Solution analysis results obtained by ICP-OES and ICP-MS from experiments with fully  $\text{UO}_2$  covered carbon steel samples.

pre-cathodisation/ purge gas	OCP [ $\text{mV}_{\text{SHE}}$ ]	ICP-MS [U]	ICP-OES	
			[U]	[Fe]
Yes / Ar (A2)	-400		< 5 $\mu\text{g/l}$	0.1 mg/l
No / Ar (B)	-270	4 $\mu\text{g/l}$	< 5 $\mu\text{g/l}$	22 mg/l
No / Ar/ $\text{H}_2$ / pre-corr. (D)	-270	4 $\mu\text{g/l}$		14 mg/l
No / Ar/ $\text{H}_2$ (C)	-550	0.05 $\mu\text{g/l}$		0.007 mg/l

### Conclusions

The first experiments were conducted under Ar purging. Under these conditions the Pt-electrode of the redox combination electrode acts mainly as an oxygen electrode. The  $E_h$  is dominated by the oxygen activity. The OCP measured (Figure 2) after pre-cathodisation of the samples show for the fully  $\text{UO}_2$  coated steel (A3) a potential shift of 50 mV in anodic direction compared to pure steel (A1). This shift is attributed to a galvanic coupling effect where  $\text{UO}_2$  is the more anodic part. At the same time the OCP of the half  $\text{UO}_2$  covered electrode was found to be 30 mV more cathodic than pure steel. This is explained by the facts that due to the surface ratio of  $\text{UO}_2$  to steel in this case the influence of  $\text{UO}_2$  decreases and is surpassed by decreased oxygen content in solution derived from a 30 mV lower  $E_h$ . Therefore the cathodic partial current densities governed by the oxygen reduction are smaller and the OCP is shifted cathodically.

The next experiment (B), now without pre-cathodisation, shows the opposite behaviour. The  $E_h$  is 200 – 300 mV higher indicating oxygen intrusion into the system and consequently also

the OCP is shifted about 200 mV into anodic direction. As a result of the increasing cathodic processes also the anodic corrosion processes must increase and the sample shows heavy corrosion pattern combined with localised pitting attack.

Under Ar/5% $H_2$  the Pt-electrode of the redox combination electrode acts mainly as a hydrogen electrode and  $E_h$  cannot be used as qualitative parameter for the oxygen content. Therefore oxygen was measured with an optical sensor. The partial pressure was during experiments always below  $(2 \pm 2)$  mbar. Here a very low OCP of  $-550 \text{ mV}_{\text{SHE}}$  was measured for a fully  $UO_2$  coated steel sample (C). Consequently this sample showed no major corrosion attack. The solution contained after the experiment approximately 100 times less uranium and 3000 – 14 times less iron in solution. Even the pH remains constant at pH 7 while in all other cases it dropped to  $\sim$ pH 4.5 due to Fe(II) in solution.

In case of a pre-oxidised uranium oxide coated steel sample under Ar/5% $H_2$  (D) the same final OCP of  $-270 \text{ mV}_{\text{SHE}}$  was found as in the case of oxygen intrusion (B). Here the reason for this large potential shift must be different because no increase of the oxygen partial pressure could be detected. But differently to other experiments a Fe(III) (hydr)oxide layer was found by XPS. The reduction of this Fe(III) layer is coupled to the corrosion process and shifts as cathodic process the OCP into anodic direction and increases at the same time the metal corrosion [SMART N.R., BLACKWOOD D.J., WERME L. (2002)].

Remarkable was the finding by XPS measurements that after all experiments the uranium oxide film on the steel surface was reduced to  $UO_2$  and the  $UO_2$  layer was in contact with steel stabilized even in the case of pre-oxidation.

The experiments have shown that the corrosion processes are ruled by iron corrosion and in contact with iron is a reduction of  $UO_{2+x}$  to  $UO_2$  possible.

## Thin Films as Spent Fuel Models for Surface Corrosion (JRC-ITU)

### Introduction

In order to understand SNF corrosion the elucidation of the involved single processes is indispensable. In this context, the impact of individual fuel components on fuel corrosion has to be clarified. To achieve this, thin films are used as model systems for spent nuclear fuel, to

investigate the surface reactions of these films in single effect studies (i.e. isolating one single parameter like  $f_p$ , stoichiometry, etc.). In the present contribution, we investigated the inhibition of surface corrosion by molecular hydrogen, generated for example during corrosion of the iron canisters. We focussed on the contribution of the  $\alpha$ -particles to the activation of the hydrogen.

To investigate the catalytic properties of the noble metal particles in the single effect approach, we studied actinide oxide thin films ( $\text{UO}_2$ ) doped with the pure noble metals. In this work, we concentrate on the Pd, which is a known hydrogenation catalyst and thus very efficient in activating hydrogen. We first determined the optimal conditions for thin film preparation. In particular we investigated, under what deposition condition U was oxidised to  $\text{UO}_{2+x}$ , while the metallic inclusions stayed reduced. Also, the size of the metallic particles as function of deposition temperature was an issue, Goal was to simulate the real  $\alpha$ -particles, which have a size of about 0.1 to 1  $\mu\text{m}$  – being composed of smaller grains [CUI D., LOW J., SJÖSTEDT C.J., SPAHIU K. (2004)].

#### Thin film deposition study

First experiments of the co-deposition of U and Pd at room temperature in presence of oxygen showed that  $\text{UO}_2$  films containing different Pd concentrations can be produced. The oxygen content can be varied, allowing to obtain stoichiometric or hyperstoichiometric  $\text{UO}_{2+x}$ , as confirmed by the XPS-U4f lines (Figure 4, right graph). The Pd content is controlled by varying the U and Pd deposition rates, via adjustment of the respective target voltages/currents. For room temperature deposition, Pd is partially oxidized to  $\text{PdO}_2$  at low Pd concentrations (Figure 4, left graph). Uranium obviously plays an active role in the oxidation of the Pd – which is probably related to the dispersion of Pd in the  $\text{UO}_2$  oxide lattice.

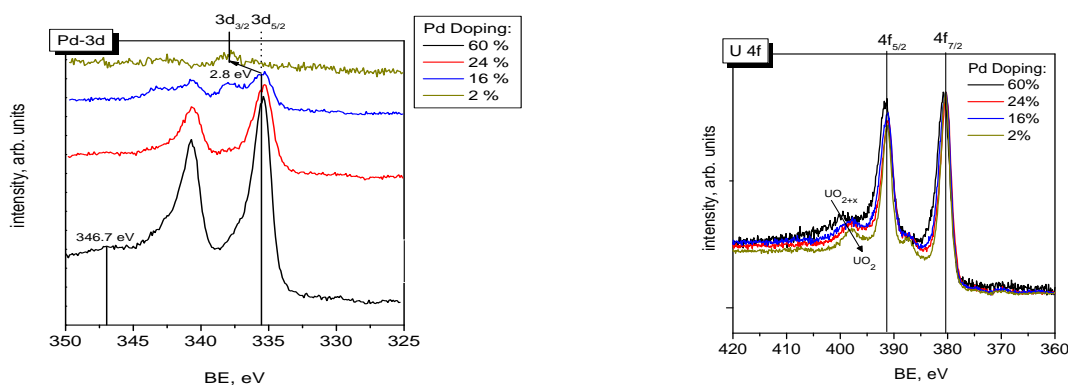


**Figure 4:** Pd-3d spectra (left graph) and U4f spectra (right graph) for different  $\text{UO}_2/\text{Pd}$  compositions.

XRD was used to check the formation of metallic particles and the presence of oxidic matrix. It was found that only above 70% Pd, characteristic Pd diffraction patterns appear, while simultaneously  $\text{UO}_2$  diffraction lines disappear. Already for low Pd concentration,  $\text{UO}_2$  diffraction patterns are suppressed and the lattice parameter is decreased. AFM (A) and SEM (B) pictures show homogeneous deposits with small crystallite sizes ( $\sim 150$  nm). The homogeneous dissolution of Pd in  $\text{UO}_2$  is interpreted as a result of the method of sputter deposition. Due to the low substrate temperature ( $\sim$  room temperature) U-Pd-O-clusters from the plasma are instantaneously cooled at the surface and the components are "frozen" in the deposited film.

To favour diffusion of the film components after deposition, and a relaxation of the system into a thermodynamically stable state, the substrate was heated during or after the deposition process [STUMPF S., SEIBERT A., GOUDER T., HUBER F., WISS T., RÖMER J. (2012)]. It was hoped, that Pd would segregate into larger metallic particles, more representative of the  $\square$ -particles. Some of the sputtered films were repeatedly heated after deposition at moderate conditions (several heating cycles for maximum 2 minutes at temperatures  $\sim 150^\circ\text{C}$  to  $200^\circ\text{C}$ ). For the compounds with a Pd concentration of about 16 % the heating process leads to the decomposition of the oxidic Pd, which can be easily followed by XPS from the Pd-3d lines that show a BE shift back to the position characteristic for the metallic Pd and the appearance of the satellite at  $\sim 346.7$  eV.

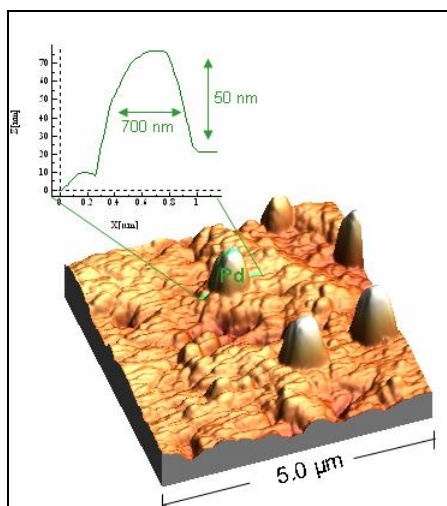


**Figure 5:** AFM image of a  $\text{UO}_2$  thin film surface doped with Pd ( $\epsilon$ -particles).

This indicates that even at such low temperatures (compared to the substance melting points) diffusion and rearrangement of the film components is allowed. As a result Pd oxide transforms into a metallic Pd phase. Agglomerates of spherical particles with a diameter of 0.3  $\mu\text{m}$  to 1  $\mu\text{m}$  form on top of the film surface. These are easily detected in the SEM images. The agglomerates are as well observed in the EDX mappings where a Pd accumulation in some regions is significant. The size of these regions of about 10  $\mu\text{m}$  corresponds to the size of the agglomerates seen in the SEM pictures. Indeed these structures resemble very well the results of Cui et al. [CUI D., LOW J., SJÖSTEDT C.J., SPAHIU K. (2004)] who investigated structure, morphology and composition of mixed alloy particles ( $\epsilon$ -particles) extracted from spent fuel. In the cited study, the  $\epsilon$ -particles are described as agglomerates of micrometer sized spheres ( $\sim 0.7 \mu\text{m}$ ).

### Electrochemical investigations

The thin film surface corrosion behaviour in aqueous environment was investigated by electrochemical tools. Two sets of experiments were performed: CV measurements under oxidizing conditions and open circuit potential measurements under oxidizing and reducing conditions. The influence of Pd on the surface corrosion behaviour was determined by comparing  $\text{UO}_2$  to  $\text{UO}_2/\text{Pd}$  doped films.

The normalized voltammograms of  $\text{UO}_2$  and  $\text{UO}_2$  doped with 2% and 16% Pd are compared in Figure 6a (0.01 M NaCl, pH  $\sim 5$ , scan rate  $10 \text{ mVs}^{-1}$ ). In  $\text{UO}_2$ , three stages of oxidation are observed on the anodic scan. At low potentials (region A: -1.0 to -0.4 V) a shoulder appears

that can be attributed to a reversible oxidation process. Region B to region C is attributed to the oxidation of the  $\text{UO}_2$  electrode matrix involving the incorporation of  $\text{O}^{2-}$  ions leading to a stoichiometry of the oxide close to  $\text{UO}_{2.33}$ . With increasing Pd concentration new features appear in the oxidative as well as reductive path of the voltammogram (A, E1) whereas C shows a change in its intensity. Without going into more detail, we note that Pd has an impact on the overall redox behaviour of  $\text{UO}_2$  and propose, according to literature, dissociative sorption processes at Pd sites as being responsible for such effect. In respect of feature C, we observe a decreased current with increasing Pd concentration. The current decrease indicates a less extensive oxidation of the matrix which is in good agreement with results described in [NAOHARA H., YE S., UOSAKI K. (2000)]. Assuming the adsorption and reaction of redox active species at the Pd particles as cited above, the activated components obviously couple more readily to recombination and reduction processes than to the oxidation of  $\text{UO}_{2.33}$ .

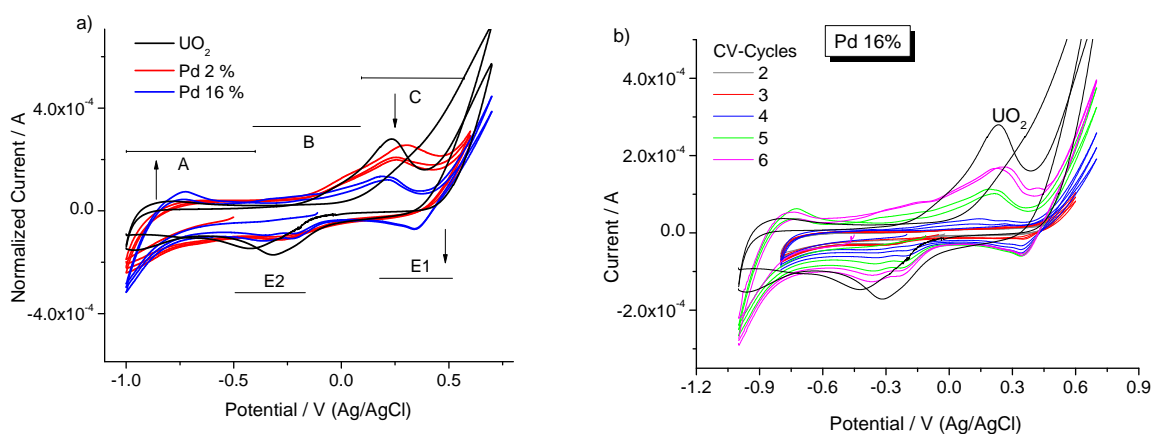


**Figure 6:** Normalized voltammograms of  $\text{UO}_2$  doped with a) 0%, 2% and 16% Pd in a comparative diagram and doped with b) 16% Pd whereas the CV is run for several cycles.

This interpretation of experimental data is supported by theoretical studies on the recombination of  $\text{OH}_{\text{ads}}$  to form  $\text{H}_2\text{O}_{\text{ads}}$  on a Pd(111) surface performed by Cao and Chen [CAO Y., CHEN Z.-X. (2006)] who predict such reaction path as being very likely from an energetic point of view.

With increasing number of voltammetric cycles (exemplarily shown for the 16% Pd sample in Figure 6b) the electrode response resembles more and more the pure  $\text{UO}_2$  case, except the

distinct feature seen in region E1. Such effect indicates the passivation of Pd particles towards dissolution inhibition. Shoemith et al. [SHOESMITH D.W. (2000); SHOESMITH D.W., SUNDER S., HOCKING W.H. (1994)] propose the formation of secondary phases as being responsible for the blockage of donor-acceptor sites at the  $UO_2$  surface.

Open circuit potential (OCP) measurements of  $UO_2$  and  $UO_2/Pd$  were performed under oxidizing (air), neutral (Ar) and reducing (Ar/ $H_2$ ) redox conditions. The corrosion processes consists in a series of different electrochemical reactions occurring on the surface of the corroding material. The potential at which the anodic and cathodic reaction currents are of equal magnitude (therewith producing a net current of 0) is named corrosion potential for homogeneous material. For heterogeneous materials the measured (steady-state) potential is a mixed potential depending on all the anodic and cathodic reactions. In literature the corrosion behaviour of  $UO_2$  surfaces as function of the surface redox conditions is often described by means of this open circuit potential, OCP. Shoemith et al. developed the Mixed-Potential Model which is most reliable under oxidizing conditions [SHOESMITH D.W., SUNDER S., TAIT S. (1998)]. The same model can also predict the dissolution rate under reducing conditions, because the dissolution rate should be related to the potential also in this case.

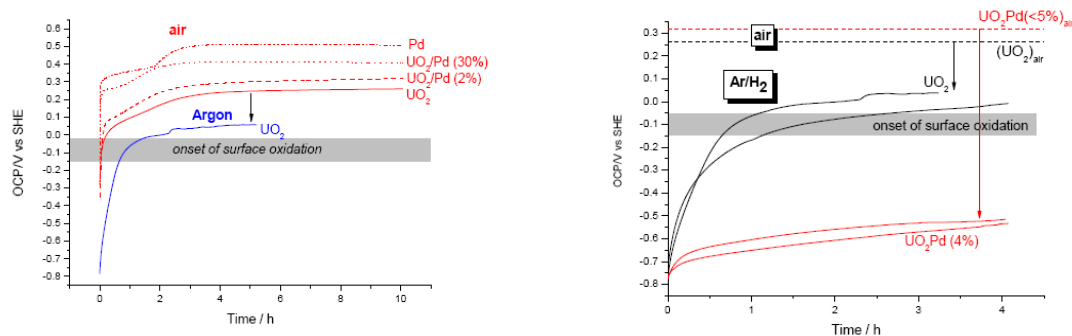


**Figure 7:** OCP of  $UO_2$  and  $UO_2/Pd$  under oxidizing and neutral conditions (left) and under reducing conditions (right).

In a first set of experiments, the reactivity of SNF model surfaces ( $UO_2/Pd_x$  thin films) was investigated in electrochemical experiments under oxic conditions. The corrosion of  $UO_2$  in (aerated) aqueous solution is decreased (lower anodic currents / less dissolution observed in cyclic voltammetry) when Pd is incorporated into the oxide surface. The formation of

secondary phases on the  $\text{UO}_2$  surface (built up in subsequent cathodic scans) disabled this inhibiting effect of Pd.

The influence of Pd doping on the OCP of  $\text{UO}_2$  under air was investigated by using the freshly prepared films as working electrode. Figure 7, left summarises the measurements for thin film electrodes ( $\text{UO}_2$ , and  $\text{UO}_2/\text{Pd}$  with different Pd content) and a Pd metal electrode under oxidizing and neutral conditions. For a pure  $\text{UO}_2$  film the OCP reaches a steady state after 6 hours at about  $250 \text{ mV}_{\text{SHE}}$  which is similar to results found for SIMFUEL (without  $\epsilon$ -particles) under oxygen. With increasing palladium amount the open circuit potential increases, shifting closer to the value of a pure Pd metal electrode. Even the 2% doped film shows an increase of the potential ( $\sim 50 \text{ mV}_{\text{SHE}}$ ) which is thought to be due to the noble metal doping. For the literature data (SIMFUEL with and without  $\epsilon$ -particle doping under  $\text{O}_2$ ) no significant change of the OCP is observable.

The measured potential is always a combination of single potentials therefore the mixed potentials of  $\text{UO}_2/\text{Pd}$  are placed between pure  $\text{UO}_2$  and pure Pd electrodes.

Experiments under reducing conditions were carried out under  $\text{Ar}/\text{H}_2$  (5%  $\text{H}_2$ ); results are summarised in Figure 7, right. For the pure  $\text{UO}_2$  film a potential of around  $0 \text{ mV}_{\text{SHE}}$  is measured which is 250 mV lower compared to the one obtained under air. The absolute value is similar to measurements under Argon. This indicates a decrease of the corrosion potential due to very low concentrations of oxidants. A much stronger response to the presence of  $\text{H}_2$  is shown by the  $\text{UO}_2/\text{Pd}$  electrodes. Here the potential after 4 h is still below the threshold for surface oxidation of  $\text{UO}_2$ . These findings correspond to the trend reported in literature (the given absolute values are higher). Although the steady state was not reached during the experiment the clear effect of  $\text{H}_2$  in presence of Pd could be demonstrated. The different possible explanation is that  $\text{H}_2$  is activated on Pd, which is acting as galvanically coupled anode within the  $\text{UO}_2$  matrix and is leading to a decrease of the corrosion potential and inhibition of  $\text{UO}_2$  oxidation. But also reduction of dissolved oxidants or the surface itself by surface hydrogen is possible, as described in the introduction.

The reversibility of the redox reactions was checked by experiments under changing redox conditions. The OCP of  $\text{UO}_2/\text{Pd}$  (5% Pd) was measured first under  $\text{Ar}/\text{H}_2$ , then the atmosphere was switched to pure Ar and vice versa. Figure 8-left shows that after half an hour the system reacts strongly to the changed conditions. The OCP increases from around  $-500 \text{ mV}_{\text{SHE}}$  to  $0 \text{ mV}_{\text{SHE}}$  after 12 h. The initial delay may be explained by the time needed to

remove the remaining  $H_2$  from solution and the dissociated H from surface. Figure 8-right shows the results of the reverse experiment: starting under anoxic (Ar) and switching to reducing conditions (Ar/ $H_2$ ).

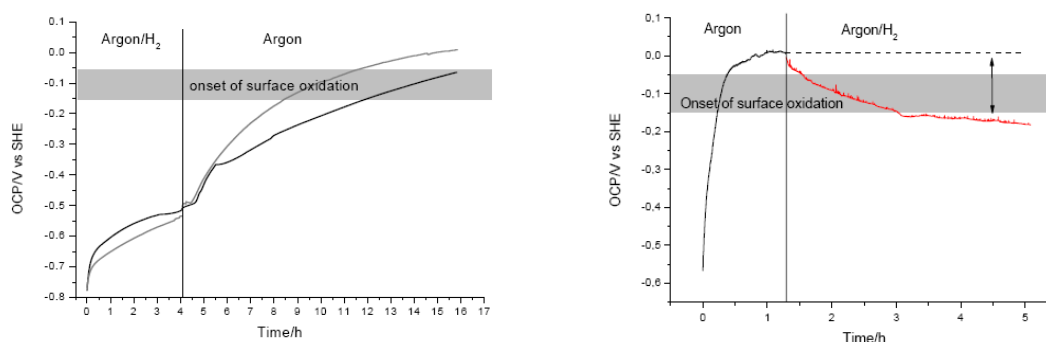


**Figure 8:** OCP under switching redox condition: left (reducing to neutral), right: neutral to reducing

Under Argon the OCP reaches a steady state at about 0 mV<sub>SHE</sub> after ~ 1 h. After switching to Ar/ $H_2$  the potential immediately decreases. At the end of the experiment (after nearly 5 h) the potential has dropped to -177 mV<sub>SHE</sub>. But it does not reach a value as low as in the experiments started directly under Ar/ $H_2$ .

### Gas adsorption experiments

In order to simulate one conceivable heterogeneous redox reaction, such as the oxide reduction by hydrogen,  $UO_2$ -Pd thin films are exposed to  $H_2$  gas. The corresponding XPS spectra of a pure  $UO_{2+x}$  surface are shown in Figure 9a. The U4f spectrum of  $UO_{2+x}$  is characterized by two main peaks with peak maxima at 380 eV and 391 eV binding energy. Two satellites at 7 eV higher binding energy are characteristic for the actinide dioxides. For the hyperstoichiometric oxide these satellites are broadened. The treatment with  $H_2$  gas does not result in a change of the U4f electronic structure and the  $UO_{2+x}$  reduction can be therefore ruled out. These changes when doping the  $UO_{2+x}$  matrix with Pd (Figure 9b). Already at very low pressures of about  $1.3 \cdot 10^{-5}$  mbar  $H_2$  (x 5 min), the treatment of the mixed film induces a narrowing of the main peaks as well as of the satellites. The calculation of the U/O ratio from the corresponding U4f and O1s spectra after 15 minutes  $H_2$  treatment gives a stoichiometry of  $UO_2$ . Obviously, the activation of  $H_2$  is solely due to the presence of Pd. We conclude as a first result, that the catalytic properties of the uranium oxide matrix can be

ruled out (at least at the  $H_2$  pressure used) and that the activating effect is exclusively attributed to the noble metal incorporation instead. The mechanism of  $H_2$  activation is deduced from another series of experiments where pure  $UO_{2+x}$  is treated with atomic H. At comparable hydrogen pressures such treatment results in the reduction of the hyperstoichiometric oxide (not shown here). From this we conclude that the activation of  $H_2$  is consistent with a dissociative sorption process and with the formation of atomic H at Pd active sites. The only possible reaction path to further reduce uranium oxide in the doped oxide films is the diffusion of hydrogen atoms at the  $UO_{2+x}$ -Pd surface.

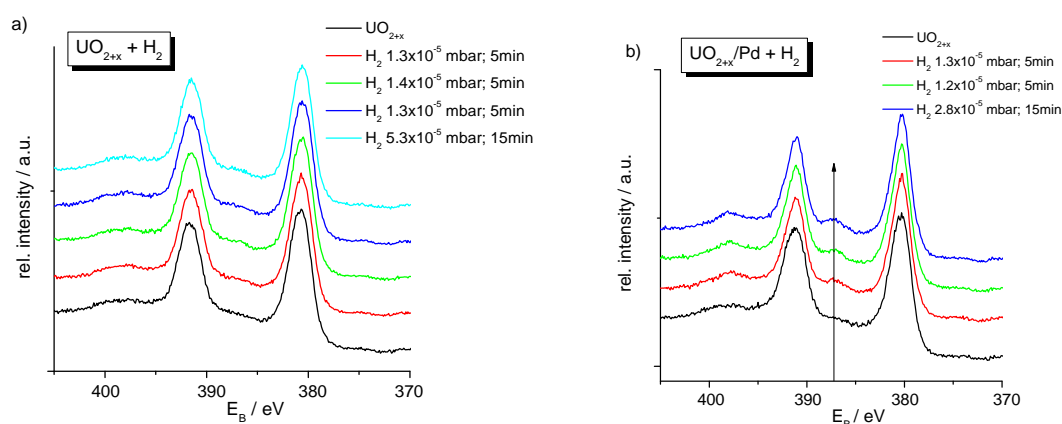


**Figure 9:**  $U4f$  spectra of a)  $UO_{2+x}$  thin film, b)  $UO_{2+x}$ -Pd mixed thin film exposed to molecular hydrogen. Growth of the satellites at 397 and 387 eV BE indicates surface reduction to  $UO_{2.0}$ .

Such process is known in literature as spillover reaction [TEICHNER S.J. (1990); GORODETSKII V.V., SAMETOVA A.A., MATVEEV A.V., TAPILIN V.M. (2009)] which is defined as migration of a sorbed species, such as hydrogen, from one solid phase, such as a metal where it is easily adsorbed and dissociated, onto another solid phase, such as uranium oxide, in contact with the first.

## Redox Reactivity of Doped $UO_2$ (KTH)

### Introduction

$UO_2$  has been used as a model for spent nuclear fuel in numerous experimental studies. Rates and rate constants for oxidation as well as dissolution of the oxidized  $UO_2$  matrix of spent nuclear are derived from experiments on pure  $UO_2$  powder or pellets [ROTH O.,

(D-N°:1.2) – Report on the scientific state of the art

Dissemination level :PU

Date of issue of this report : 03/09/2012

JONSSON M. (2008)]. On the basis of these results the relative impact of radiolytic oxidants have been assessed and also employed in simulations of spent nuclear fuel dissolution under deep repository conditions [EKEROTH E., ROTH O., JONSSON M. (2006)]. One important conclusion from these studies is that  $\text{H}_2\text{O}_2$  is the major oxidant responsible for radiation induced oxidative dissolution of spent nuclear fuel under deep repository conditions.  $\text{H}_2\text{O}_2$  can react with  $\text{UO}_2$  by catalytic decomposition and by oxidizing U(IV) to U(VI). Since spent nuclear fuel can be regarded as highly doped  $\text{UO}_2$ , the effects of the presence of dopants in the  $\text{UO}_2$  matrix should be regarded as key-knowledge in the field of spent nuclear fuel dissolution. To elucidate this we have studied the dissolution yield in reactions between  $\text{H}_2\text{O}_2$  and doped  $\text{UO}_2$  and the reactivity of a number of oxidants towards doped  $\text{UO}_2$  materials. In parallel we have studied the catalytic formation of hydroxyl radicals (upon reaction with  $\text{H}_2\text{O}_2$ ) on the doped  $\text{UO}_2$  materials.

### Experimental

The experiments are described in detail in the publications [TRUMMER, M. (2011); LOUSADA, C. M., TRUMMER, M., JONSSON, M. (2011)].

### Results

#### *Dissolution yield*

Experiments performed at KTH have shown that the oxidative dissolution yield, i.e. the amount of dissolved uranium per consumed  $\text{H}_2\text{O}_2$  varies dramatically between different  $\text{UO}_2$ -based materials [TRUMMER M., DAHLGREN B., JONSSON M. (2010); NILSSON S., JONSSON M. (2011)]. It has not been clear whether this variation can be attributed to changes in redox reactivity or in the catalytic ability of the material.

#### *Rate of $\text{H}_2\text{O}_2$ consumption*

The rate of  $\text{H}_2\text{O}_2$  consumption has been measured in a number of previous studies [ROTH O., JONSSON M. (2008); TRUMMER M., DAHLGREN B., JONSSON M. (2010); NILSSON S., JONSSON M. (2011)]. The rate constant for  $\text{UO}_2$  oxidation by  $\text{H}_2\text{O}_2$  was obtained in experiments on  $\text{UO}_2$  powder suspensions. This rate constant can be used to make fairly reasonable predictions of the rate of oxidation for  $\text{UO}_2$  pellets as well as for doped  $\text{UO}_2$  pellets. Hence, the overall rate of  $\text{H}_2\text{O}_2$  consumption on  $\text{UO}_2$  surfaces is relatively insensitive

to the presence of dopants. However, noble metal particles have been shown to catalyze oxidation to some extent [TRUMMER M., ROTH O., JONSSON M. (2009)].

#### *Hydroxyl radical formation*

Hydroxyl radicals formed as a primary product in metal oxide catalyzed decomposition of  $H_2O_2$  can be detected using a modified version of the Hantzsch method [LOUSADA C. M., JONSSON M. (2010)]. In short, tris-buffer is added to the system. Upon reaction with hydroxyl radicals (or other hydrogen abstracting radicals), formaldehyde is produced. The formaldehyde concentration is the used to monitor the accumulated hydroxyl radical production in the system.

It can clearly be seen that the consumption of  $H_2O_2$  is accompanied by production of OH. For  $UO_2$  powder, the dissolution yield, expressed as the ratio between dissolved U(VI) and consumed  $H_2O_2$ , has been determined to 80% [JONSSON M., EKEROTH E., ROTH O. (2004)]. The present experiments on hydroxyl radical production confirms this as the hydroxyl radical production corresponds to ca 20% of the  $H_2O_2$  consumption. The rate of hydroxyl radical production varies by less than 30 % for  $UO_2$ , SIMFUEL,  $Y_2O_3$  doped  $UO_2$ , Pd-doped  $UO_2$  and  $Y_2O_3$ /Pd-doped  $UO_2$ .

#### *Reactivity of different oxidants towards doped $UO_2$*

If differences in the ability to catalyze decomposition of  $H_2O_2$  cannot explain the observed differences in dissolution yield, the rationale must be differences in the redox reactivity of the doped materials. In order to elucidate this possibility we performed experiments using pure oxidants that cannot undergo catalytic decomposition. In addition to  $H_2O_2$ , which has already been studied quite extensively, we used  $IrCl_6^{2-}$  and  $MnO_4^-$  to monitor the redox reactivity of the doped  $UO_2$  materials. In Figure 10 the reactivity of the different pellets towards these oxidants can be seen.

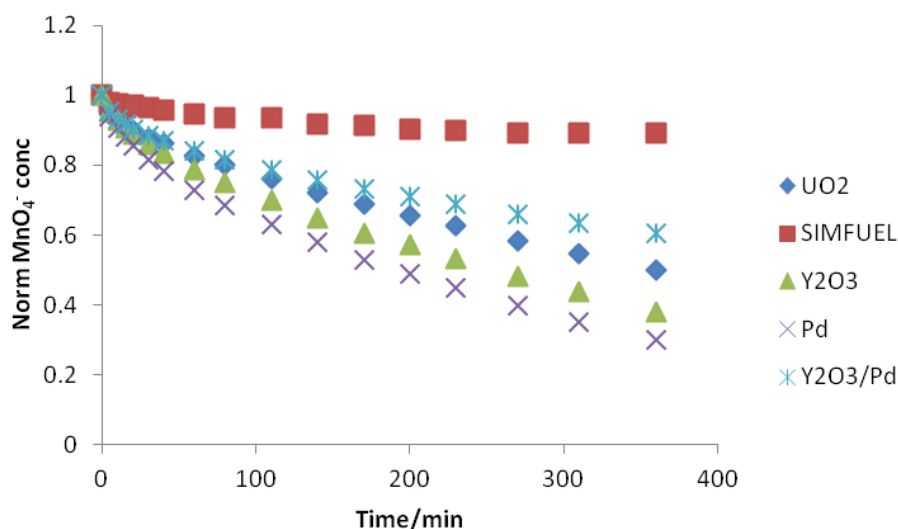


**Figure 10:** Normalized  $MnO_4^-$  concentration as a function of reaction time in pellet experiments.

What can clearly be seen here is that the redox reactivity of the doped materials differs significantly for the weaker oxidant ( $MnO_4^-$ ) while the reaction with the stronger oxidant ( $IrCl_6^{2-}$ ) is much faster and the difference between the doped materials is also less pronounced. Furthermore, experiments (kinetics as a function of temperature) show that the activation energy for oxidation of  $UO_2$  by  $MnO_4^-$  is lower than the activation energy for oxidation of SIMFUEL by  $MnO_4^-$ . The measured activation energies are  $7.4$  and  $12.9$   $\text{kJ}\cdot\text{mol}^{-1}$ , respectively. This shows that the redox reactivity is significantly influenced by doping [PEHRMAN R., TRUMMER M., LOUSADA C. M., JONSSON M. (2011); PEHRMAN R., TRUMMER M., LOUSADA C. M., JONSSON M. (2012)].

### Conclusions

From our work we can conclude the following:

- The dissolution yield in the reaction between  $H_2O_2$  and  $UO_2$  decreases with rare earth oxide doping.
- The catalytic decomposition of  $H_2O_2$  on  $UO_2$  initially produces hydroxyl radicals (adsorbed)
- The overall rate constant for the reaction between  $H_2O_2$  and  $UO_2$  is fairly insensitive to rare earth oxide doping.

- The rate constant for the catalytic decomposition of  $\text{H}_2\text{O}_2$  on  $\text{UO}_2$  is fairly insensitive to rare earth oxide doping.
- The redox reactivity of  $\text{UO}_2$  pellets decrease significantly with upon rare earth oxide doping. This effect is more pronounced for weaker oxidants than for strong oxidants.

### Acknowledgement

The Swedish Nuclear Fuel and Waste Management Company (SKB) is gratefully acknowledged for financial support.

## **Reductive Trapping of Actinides in Container Corrosion Products during Spent Fuel Corrosion (INE)**

### Introduction

The source term from spent nuclear fuel (SNF) dissolution is highly dependent on oxidative dissolution of the fuel matrix. Various experimental data on the dissolution behaviour of the spent fuel matrix itself and in some cases in presence of container material (initial metallic Fe powder) as well, and the associated releases of radioelements were already obtained by extensive laboratory test programs and reported e.g. in [SHOESMITH D.W. (2000); FERRY C., POINSSOT C., BROUQUIE V., CAPPELAERE C, DESGRANGES L., ET AL. (2005); LOIDA A., GRAMBOW B., GECKEIS H. (1996)]. The capacity of corroded canister iron phases to incorporate radionuclides is under investigation within the European collaborative project “ReCosy”. The stable corrosion product of steel canister material under reducing disposal conditions is magnetite. In the present study, it was intended to investigate the reductive trapping of actinides in metallic corrosion products, which may provide for a driving force for SNF dissolution. Over almost 10 years, an experiment (“denoted as K14Mt”) was carried out to study the effect of magnetite on the overall corrosion behaviour of SNF in NaCl solution. Unexpected was the measured rather high U solution concentration of  $\sim 1 \cdot 10^{-4}$  M at the end of the experiment, in association with an at first unexplainable  $\text{CO}_2$  content of 0.8 vol % in the gas phase. Additionally, first studies by means of optical microscopy (SNF sample, corroded magnetite), SEM/EDS (corroded magnetite), XPS (corroded magnetite), Raman

spectroscopy were carried out. Further characterization work upon the corroded magnetite was focused on its mineralogical phase composition and on possible impurities by carbon. Additionally, the distribution of radioelements released from the SNF sample in the course of almost 10 years of corrosion over the magnetite, the container wall and the aqueous phase was determined.

### Experimental

The corrosion experiment was performed by using a pellet sized segment of high burnup SNF (50 MWd/kg U, linear power 260 W/m), 6.6 g fuel, and 10 mm in length together with commercial available magnetite (ALFA 012962, grain size ~ 5 µm). SNF sample and magnetite were immersed simultaneously in 5 mol/L NaCl solution (initial volume 200 mL, under Ar-atmosphere), using a glass vessel. During the initial phase of the experiment, the leachant was replaced entirely by fresh solution for four times until total 65 days. This procedure reduced effectively the "initial release fraction (IRF)", such as Cs and fission gases in the gap and on grain boundaries. Afterwards the experiment was continued without replacing the solution (static), lasting over 3562 days. The gas phase and solution were sampled at 78, 215, 349, 771, 1895 and 3562 days after start of the static phase. The analytic procedures are described detailed in [GRAMBOW B., LOIDA A., DRESSLER P., ET AL. (1996)]. After termination of the experiment, fractions of the magnetite were removed and analyzed. Various methods have been applied: SEM/EDX, XRD, Raman spectroscopy, XPS, digestion in HCl, or stripping by HNO<sub>3</sub> and following radiochemical analyses.

### Results

#### *Release of radionuclides during 10 years corrosion of SNF in 5M NaCl solution in presence of magnetite*

**Gases:** In the observation period, only a slight release of Xe of < 0.01 vol.% was found. Until 10 years, the H<sub>2</sub> concentration in the leaching vessel amounted to 18.5 vol.% and O<sub>2</sub> to 5.4 vol.%. After the first year, the CO<sub>2</sub> concentration raised from 0.1 to 0.8 vol.%, a value which cannot be explained by contact with air.

**Solution concentrations:** Figure 11 shows the measured concentrations of the fission products Sr, Tc, Cs and the actinides U, Np, Pu, Am during the "static phase". Additionally, measured pH is also shown (right axis).

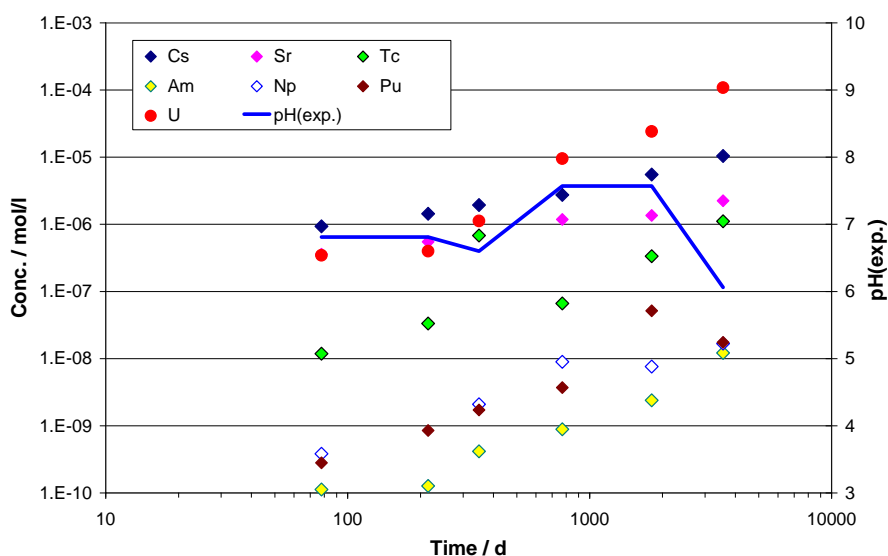


**Figure 11:** Dissolved element concentrations of the experiment K14Mt. Solid line: measured pH.

Figure 11 shows considerable differences in the temporal evolution of the released radionuclides. Between 215 and 3562 days, the Sr concentration increases from  $6 \cdot 10^{-7}$  to  $2 \cdot 10^{-6}$  mol/L. Release of Cs is slightly faster, whereas the mobilization of U is at the highest rate. The final U concentration was measured up to  $1 \cdot 10^{-4}$  mol/L. The other radionuclides (Tc, Np, Pu and Am) are released at an intermediate rate. In total, fission gas release was >16%, Cs ~ 0.7%, Sr ~ 0.3%, and the actinides <0.1% of the inventory. After one year, the measured pH increased to 7.6 and dropped after 10 years to ~ 6.

Model calculations for 5 mol/L NaCl solution in contact with the measured  $p(\text{CO}_2)$  revealed a decrease of the pH and the presence of dissolved carbonate. Under these conditions, initially generated solid  $\text{Na}_2\text{U}_2\text{O}_7$  is dissolved forming U carbonato complexes in the range of the observed concentration of  $1 \cdot 10^{-4}$  mol/L. Vice versa, at  $\text{pH}_{\text{exp}} \sim 7.6$  in combination with the measured  $\text{CO}_2$  partial pressure, the calculated Sr concentration is in equilibrium with solid  $\text{SrCO}_3$  (strontianite).

#### *Phase composition of the corroded magnetite*

To verify the phase composition of the corroded magnetite a sample of this material was used for XRD measurements. Diffraction patterns of the untreated Fe-oxide powder as fabricated and the sample recovered from the leaching experiment show essentially the same reflexes. In both samples magnetite ( $\text{Fe}_3\text{O}_4$ ) and hematite ( $\alpha\text{-Fe}_2\text{O}_3$ ) are detected as

major phases. Though weak reflexes at 33.9°, 47.2° and 59.8° indicate traces of an unidentified phase, but no reflexes of a Fe-carbonate mineral are observed.

Small samples of the reacted magnetite, as well as reference materials (hematite, goethite and magnetite) were analyzed by Raman spectroscopy. In the spectra measured upon the corroded magnetite sample material after the experiment no magnetite, but only hematite was detected by Raman spectroscopy. It is known that magnetite may undergo a phase transformation by the high laser irradiation used in Raman spectroscopy [DE FARIA D. L. A., VENAÜNCIO S., SILVA M. T., DE OLIVEIRA M.T. (1997)]. Therefore low laser energy was applied and magnetite spectra could be measured with the reference samples. Due to the fact that (a) magnetite was detected with the reference sample and (b) the black colour of the magnetite increased the surface sensitivity of Raman spectroscopy, it is concluded that hematite covers the surfaces of the magnetite. By means of XPS spectroscopy U peaks were detected indicating its presence in the hexavalent state only.

#### *Magnetite dissolution experiments*

To find an explanation of the unexpected high CO<sub>2</sub> content of the gas phase encountered at the end of the SNF-magnetite corrosion experiment and eventually to identify the CO<sub>2</sub> source, magnetite dissolution experiments were carried out. An amount of 5 g magnetite as fabricated (ALFA 012962) was inserted in 30 ml HCl (30% ultrapure) under pure Ar atmosphere using a 250 mL autoclave. The gas phase was sampled after 74 days and replaced by Ar. After additional 31 days gas was sampled again. The gas was analyzed by mass spectrometry. The results are shown in Table 3. The fraction of Ar was found to decrease to 33 or 26.3 vol. %, whereas H<sub>2</sub> was formed up to percentages of 66.8 or 73.5 vol.%, respectively. The percentage of CO<sub>2</sub> was found to be 0.106 vol% after 74 d and 0.082 vol.% after 31 days, respectively. With regard to the measured N<sub>2</sub> contamination of 0.07 vol.% (air contamination over valves and fittings) the CO<sub>2</sub> percentage from air should not exceed 0.3·10<sup>-4</sup> vol%. Even in the case of a complete exchange of the Ar atmosphere by air the maximum possible amount of CO<sub>2</sub> would be about 0.03 vol.%, only. After the end of both reaction intervals the original magnetite was found to be completely dissolved.

**Table 3:** Composition of the gas phase after dissolution of 5 g magnetite (ALFA 012962) in 30 mL HCl.

	1 <sup>st</sup> Interval 74 d Percentage	2 <sup>nd</sup> Interval 31 d Percentage
Ar	33.011	26.343
CO <sub>2</sub>	0.106	0.082
H <sub>2</sub>	66.803	73.504
N <sub>2</sub>	0.076	0.069
O <sub>2</sub>	0.004	0.002
<b>Total</b>	<b>100.000</b>	<b>100.000</b>

Thus, these results support the assumption that the reason of the unexpected high CO<sub>2</sub> percentage in the atmosphere of the long-term SNF-magnetite corrosion experiment is the carbon/carbonate content of the magnetite. The relevant phase is a minor component and was not observed by XRD. During magnetite dissolution CO<sub>2</sub> will be formed by reactions between carbon impurities and released O<sub>2</sub>.

#### *Radioelement distribution*

The amounts of retained radionuclides upon the magnetite and the vessel wall were obtained after dissolution of 230 mg magnetite in 30% HCl and acid stripping of the vessel wall (5 M HNO<sub>3</sub>) followed by radiochemical analysis of related aliquots. The results show that the total releases of Cs, Sr and Tc (in solution + on the vessel wall + on the magnetite) were measured at  $1.48 \cdot 10^{-6}$  M,  $3.04 \cdot 10^{-7}$  M and  $1.52 \cdot 10^{-7}$  M, where parts of 95%, 99% and 98.5 % were found in the aqueous phase. U was released in total at  $5.1 \cdot 10^{-5}$  Mol, where of 70% was found upon the magnetite. The total measured amount of Am was determined to be  $3.56 \cdot 10^{-8}$  M, where a percentage of 95% upon the magnetite was encountered. The Pu release was measured to be  $2.3 \cdot 10^{-8}$  Mol, whereof 90% was re-immobilized upon the magnetite. The retention of radioelements upon the glass vessel wall does not play a significant role except for plutonium. Figure 10 shows the distribution of released radioelements between the aqueous phase, the glass vessel wall and the magnetite.

The related Kd values of Cs, Sr, Tc, Np, Am, Pu and U are compiled in Table 4. With respect to U a Kd value of 41.3 mL/g was found. This is a factor of about more than 10 higher as found in the frame of U (VI) sorption studies upon magnetite by [MISSANA T., GARCIA-GUTHIERRES M., FERNANDEZ V. (2002)], which is indicated as Kd (U VI) 4 mL/g.

**Table 4:** *K<sub>d</sub> values of radionuclides sorbed upon the magnetite after 3562 days co-dissolution of SNF and magnetite in 5 M NaCl solution.*

Nuclide	K <sub>d</sub> (mL/g)	Nuclide	K <sub>d</sub> (mL/g)
Cs	0.9	Np	10.5
Sr	0.1	Am	344.5
Tc	0.2	Pu	140.4
		U	41.3

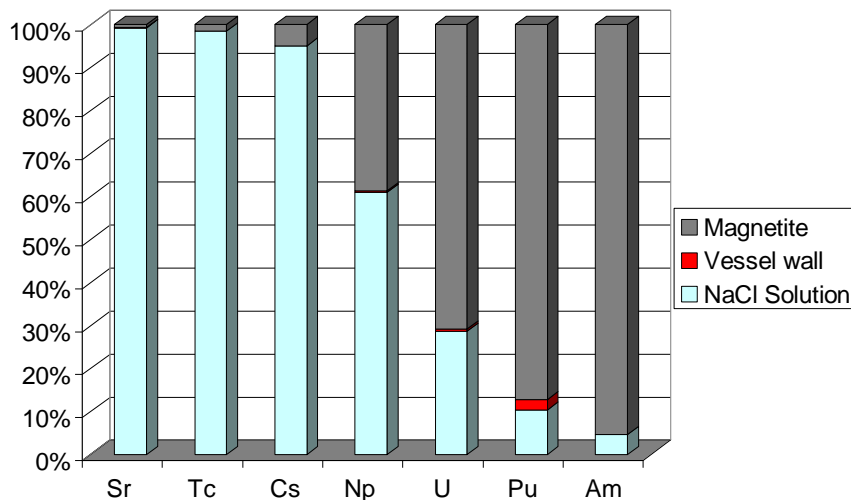


**Figure 12:** *Distribution of released radionuclides between the aqueous phase, the magnetite and the glass vessel wall in terms of percentage.*

### Conclusions

In the glass vessel used for SNF corrosion experiments over almost 10 years the atmospheric conditions were not sustained. The presence of CO<sub>2</sub> and O<sub>2</sub> explained the observed U and Sr concentrations. Under these conditions, Sr cannot be used as indicator for SNF matrix dissolution.

The unexpected high CO<sub>2</sub> content in the gas phase at the end of the corrosion experiment might be explained by the carbon/carbonate content of the magnetite as fabricated, reacting with oxygen released during magnetite dissolution. The relevant carbon-containing phases are of minor concentration in the ALFA 012962 magnetite and could not be detected by XRD and Raman spectroscopy.

In spite of the accelerated release of radioelements in particular U due to the high CO<sub>2</sub> content in the gas phase, considerable amounts of radioelements were retained upon the magnetite. With respect to Am, Pu, U and Np about 95, 87, 71 and 39 % of the released measured amounts were found to be re-immobilized upon the magnetite.

Due to the Raman findings, which are corroborated by XRD, a hematite layer is present onto the surfaces of this material. Therefore, the trapping of the actinides cannot be attributed to reductive process alone, but sorption reactions may influence the retention, too. The ALFA 012962 magnetite plays a significant role in retaining the redox sensitive actinides.

## **Corrosion of spent fuel in presence of H<sub>2</sub> (JRC-ITU)**

### Introduction

The aim was to study the influence of dissolved H<sub>2</sub> on corrosion of the high burn-up rim fraction of spent nuclear fuel. The rim fraction was selected as it contains a higher concentration of Pu, as well as, fission products and the first water will contact in case of container penetration in a spent fuel disposal. The experimental conditions were selected to imitate crystalline rock disposal environment. A titanium autoclave is used to avoid presence of atmospheric oxygen and to study the interaction of spent fuel (UO<sub>2</sub> matrix, ε-particles, fuel gap inventory and grain boundaries), water (composition in respect to concentration of carbonate and α-radiolysis) and hydrogen (originating from corrosion of carbon steel containers). Titanium was selected to minimise the influence of iron which is known to react with oxidants formed by α-radiolysis. The final goal was to perform a mass balance of reductants and evolved oxidants.

### Results

The details concerning the experiment are published elsewhere [FORS P., CARBOL P., VAN WINCKEL S., SPAHIU K. (2009), BUCKAU G., KIENZLER B., DURO L., GRIVÉ M., MONTOYA V. (EDS.) (2010)]. The result, in relevance to the ReCosy project, is the behaviour of fission products (<sup>137</sup>Cs, <sup>129</sup>I), redox sensitive actinides (U and Pu) and natural elements (Ti, Cr, Mn, Fe, Ni, Cu and Mo) in the leachate in contact with the rim structure of

spent  $\text{UO}_2$  fuel. The study is divided into three parts: the period 0-313 days, the wash-out action during the days 313-314 and the samplings made in the period 314-1435 days.

A noticeable observation is the high correlation between the measured redox potential and the concentrations changes of redox sensitive elements, verifying that the observed concentration changes mainly occurs when oxygen intrudes the autoclave. The results from these two independent measurement techniques, redox potential and SF-ICP-MS analysis, support each other and give confidence in the results.

### Redox potential

The measured redox potential correlates strongly with the operations of the autoclave (Figure 13). Operations such as leachant refill, leachate sampling, rinse actions and un-tight valves results in rapid redox potential increase indicating  $\text{O}_2$  (air) intrusion into the autoclave. It is noticeable that despite all precautions taken to avoid air intrusion during the different manipulations (such as purging of leachant with  $\text{H}_2$ -gas) always a small amount of oxygen enters the autoclave. Some more conclusions can be deduced from the redox potential measurements, seen in Figure 13. Firstly, in between the autoclave operation the redox potential stabilises within a range of -0.375 to -0.450 V. This redox potential range is representative for disposal conditions.

Secondly, it can be observed that after an autoclave operation, for example during the initial 20 days of the experiment or after the rinse action, the redox potential rapidly decreases back to the steady state level. The rapid decreases of the  $E_h$  indicate a fast consumption of intruded  $\text{O}_2$ , during this initial time the total amount of radiolytically produced  $\text{H}_2\text{O}_2$  is negligibly small.

The co-variation of  $E_h$  and the redox sensitive elements in the leachate can be observed comparing Figure 13 and Figure 14. In order to extract redox relevant data, three criteria were applied. Firstly, the elemental concentration must have a significant variation to be able to be used as redox indicator, for simplicity a variation larger than one order of magnitude.

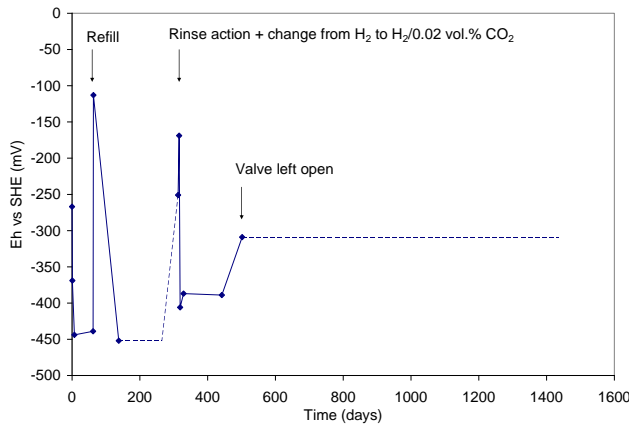


**Figure 13:** Redox potential variation in the autoclave as a function of time during corrosion experiment. A valve mistakenly left open after ~500 d from the start of the experiment caused the  $E_h$  value in the redox measurement chamber (isolated from the autoclave) to increase as a result of air ingress. As a consequence no stable redox potential measurement could be obtained during the short measurement time (leachate sampling time) at the sampling point 1435 days after start of the experiment.

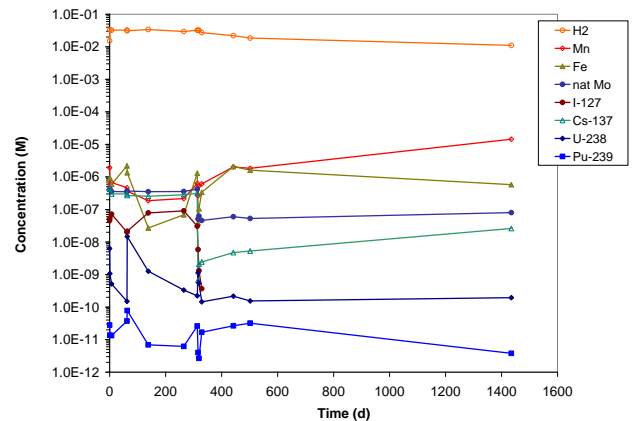


**Figure 14:** Concentration of radionuclides and stable elements in leachates during the entire  $UO_2$  fuel corrosion experiment.

Secondly, the lowest values must be checked against detection limit of that element. Thirdly, the stable redox concentration, absence of intruding oxygen (which is in reality an experimental error), are used for determination of the redox state of that element. Applying these criteria does reduce the number of presented elements, to the ones shown in Figure 14.

Each change of the  $E_h$  corresponds to a concentration change in U, Pu, Fe, Mn and natural Mo. Changes in Cs concentration indicate dissolution of fresh matrix or newly opened grain boundaries and functions as a type of matrix dissolution indicator. The fact that uranium and plutonium can not be, exclusively, used as matrix indicators is due to their cycled oxidation/dissolution and reduction/re-precipitating behaviour. The concentration changes of different elements are shown in Figure 14.



### *Hydrogen*

The decrease of dissolved hydrogen during the last part of the experiment, 316-1435 days, is due to stopped refilling after each leachant sampling. It can be concluded that there is no influence of dissolved hydrogen concentration on the redox sensitive elements in the studied  $H_2$  concentration range of 30-11 mM range during the experiment duration of 1435 days.

### *Manganese*

Manganese is the one of the elements that is relatively uncomplicated to analyse by SF-ICP-MS as there is no mass interferences at mass 55. The concentration profile of natural Mn in the leachate, present as an impurity in the autoclave, correlates with  $^{239}\text{Pu}$ . The Mn-concentration variation is more than one order of magnitude and it seems to be a reasonable redox indicator. The detection limit for Mn is  $1 \cdot 10^{-9}$  M.

### *Molybdenum*

Figure 14 also show the behaviour of natural Mo, which is present as an impurity in the autoclave, from the start of the corrosion experiment. It remains at a concentration of  $4 \cdot 10^{-7}$  M during the period 0-313 days. Except for the small concentration variations due to dilutions during refilling of the autoclave the Mo behaves as an inactive element. After the rinse action it stabilises at a new concentration level of  $4 \cdot 10^{-8}$  M. The detection limit for Mo is  $4 \cdot 10^{-9}$  M.

### *Iodine*

Two iodine isotopes were measured during the corrosion experiment:  $^{127}\text{I}$  and  $^{129}\text{I}$ . The low total leachate concentrations of  $\text{I}^-$  ( $1 \cdot 10^{-7}$  M) results in only a small amounts of formed  $\text{I}_2$  which remains dissolved in the acidified solution. This observation is based on of  $^{137}\text{Cs}/^{127}\text{I}$  ratio calculated for the fuel and compared with the analysed ratio in the leachate. Assuming that there are no losses of  $^{137}\text{Cs}$  during sample preparation, observing the calculated, by ORIGEN, molar ratio of  $(^{137}\text{Cs}/^{127}\text{I})_{\text{fuel}} = 21.4$  and compared it with the average ratio found in the leachate of  $8.3 \pm 4.4$ , indicates that there is 2.6 times more  $^{127}\text{I}$  in the leachate compared to the amount expected in the rim fraction of the HBU fuel with a burn-up of 67 GWd/tHM.

The HBU-fuel has an average burn-up of 59.1 GWd/tHM and give a calculated ratio of  $(^{137}\text{Cs}/^{127}\text{I})_{\text{fuel}} = 21.7$ . The small difference between the two ratios, 21.4 and 21.7, indicate that an increased transport of I during reactor irradiation from the pellet centre to the rim is not a

plausible explanation for the 2.6 times higher concentration of  $^{127}\text{I}$  in the leachate. The results imply that I and Cs are present in different chemical compounds in the HBU-rim, with different leachability under reducing conditions. This can be observed, analysing the leaching behaviour of Cs and I at the time period 0-13 days when Cs concentration decreases while I increases and during the period 265-313 days when again Cs increase while I decreases. The detection limit of  $^{127}\text{I}$  is  $1 \cdot 10^{-8}$  M.

#### *Iron, uranium and plutonium*

The origin of iron in the leachate is due to its presence in the titanium grade II autoclave material, with a content of 0.25 wt.-% Fe [FORS P., CARBOL P., VAN WINCKEL S., SPAHIU K. (2009)]. The redox couple  $\text{Fe}^{2+}/\text{Fe}^{3+}$  is sensitive to redox changes. The concentration behaviour of Fe should be inverted to U. This means that when U(IV) is oxidised to U(VI) and its concentration increase due to complexation of U(VI) with carbonate, the simultaneous oxidation of  $\text{Fe}^{2+}$  to  $\text{Fe}^{3+}$  gives a  $\text{Fe}(\text{OH})_3(\text{s})$  with a very low solubility and therefore a low total Fe concentration. On the other hand, reduction reactions in the autoclave are not so easy to interpret. Reduction of U(VI) to U(IV) on the fuel surface gives at the same time reduction of Fe(III)hydroxide present on fuel surface to  $\text{Fe}^{2+}$  which can be co-precipitated with U(IV) hydroxide. The discussion on stable colloidal  $\text{Fe}(\text{OH})_3$  in the solution is contradicted by the orders of magnitude variation in the solution. This means that if all  $\text{Fe}^{2+}/\text{Fe}^{3+}$  reactions with intruding oxygen would take place in the solution, functioning as a redox buffer, no changes would be expected at the fuel surface. This is contradicted by the two orders of magnitude uranium concentration changes when oxygen intrudes the autoclave (for example at day 63 and 313). Nevertheless, one have to remember that the total concentration of Fe, mainly as  $\text{Fe}^{2+}$  as concluded above, is 2-3 order of magnitude higher than for U. The HR-ICP-MS detection limit for Fe is  $5 \cdot 10^{-8}$  M.

The behaviour of  $\text{Fe}^{2+}$  is similar to Pu, but different from U (Figure 14). The interpretation of the Fe changes during the time period 0-63 days show that initially, at  $t=0$ , Fe present in the leachant added to the autoclave had a concentration of  $7 \cdot 10^{-8}$  M, while U and Pu were in the range of  $10^{-12}$  M and  $10^{-13}$  M, respectively. After one day of fuel corrosion the [Fe] increased one order of magnitude to  $9 \cdot 10^{-7}$  M while [U] increased four order of magnitude to  $6 \cdot 10^{-9}$  M and [Pu] increased 2.5 orders of magnitude to  $3 \cdot 10^{-11}$  M.

The ratio  $(^{238}\text{U}/^{239}\text{Pu})_{\text{leachate}} = 4 \cdot 10^{-3}$  is similar to the same ratio in fuel ( $6 \cdot 10^{-3}$ ) and prove congruent fuel oxidation/dissolution and therefore a proof of dissolution of a pre-oxidised layer,  $\alpha$ -radiolysis has not produced enough of oxidants during this short time.

During the period 1-63 days, U(VI) in solution was reduced to U(IV) by two orders of magnitude reaching a [U]  $1 \cdot 10^{-10}$  M. The reduction reaction/precipitation occurs on the fuel surface. Contrary to [U] during the period 7-63 days, [Fe] and [Pu] increases as expected if highly reducing conditions prevail at the fuel surface, reducing Pu(IV) to Pu(III) which has a higher solubility than Pu(IV) and reducing Fe(III) to Fe(II) also with a higher solubility than  $\text{Fe}(\text{OH})_3(\text{s})$ .

After a large  $\text{O}_2$  intrusion into the autoclave on day 63 (see Figure 13), the uranium which originated from the pre-oxidised fuel layer and had been reduced on the fuel together with additional fresh fuel (confirmed by the increase of  $[^{239}\text{Pu}]$  and  $[^{137}\text{Cs}]$ , Figure 2) was dissolved and yielded in a two order of magnitude increase in [U].

The increase of  $[^{239}\text{Pu}]$  occurred due oxidation/dissolution of fresh fuel and can be observed through the ratio  $(^{238}\text{U}/^{239}\text{Pu})_{\text{leachate}} = 5.3 \cdot 10^{-3}$  (Figure 15). At this occasion [Fe] decreased due to oxidation of  $\text{Fe}^{2+}$  to  $\text{Fe}^{3+}$  followed by Fe(III)hydroxide precipitation.

During the period 63-265 days the highly reducing conditions at the fuel surface again reduces [U] by two orders of magnitude to [U] of  $3 \cdot 10^{-10}$  M, while [Pu] only one order giving a  $(^{238}\text{U}/^{239}\text{Pu})_{\text{leachate}} = 2 \cdot 10^{-2}$ .

This indicates that U is more easily reduced than Pu. The only reasonable explanation for the decreasing [Fe] is that the reducing conditions at the fuel surface reduces  $\text{Fe}^{3+}$  to  $\text{Fe}^{2+}$  which is then co-precipitated with U on the fuel surface.

The period 265-313 days show the same pattern as the time period 7-63 days: while highly reducing conditions prevail at the fuel surface seeing by a decrease in [U] to  $2 \cdot 10^{-10}$  M while [Pu] and [Fe] increases, through the same reactions as proposed above (( $\text{Pu}^{4+}$  reduced to  $\text{Pu}^{3+}$  and  $\text{Fe}^{3+}$  reduced to  $\text{Fe}^{2+}$ , see Figure 17).

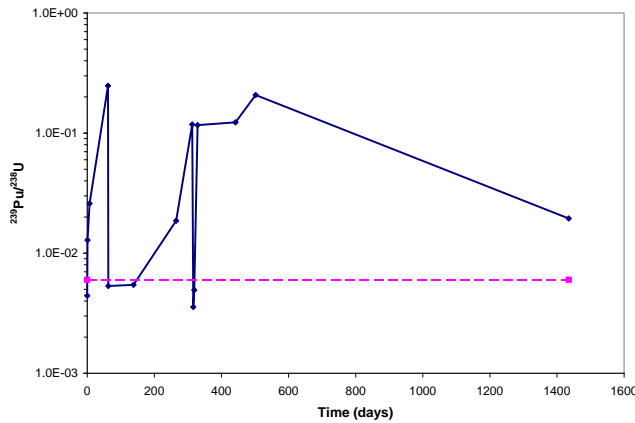


**Figure 15:** Molar ratio  $^{239}\text{Pu}/^{238}\text{U}$  in the leachate during corrosion experiment. The dotted line represents the  $^{239}\text{Pu}/^{238}\text{U}$  ratio in the rim fraction of the  $\text{UO}_2$  fuel with a burn-up of 67 GWd/tHM after 2920 days of cooling.

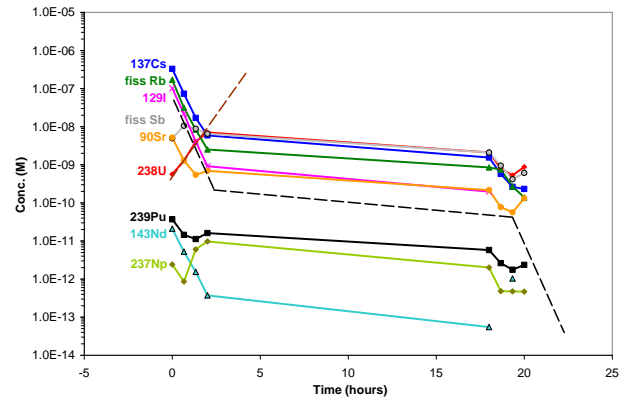


**Figure 16:** Concentration of elements (FP and Ac) in the leachate during the rinse action (days 313-314). The black dotted line represents the calculated dilution factor of 3.1. The brown dotted line shows the oxidation of uranium.

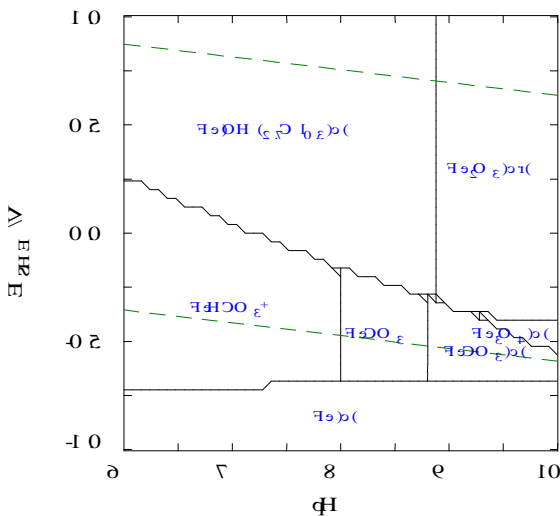


**Figure 17:** Predominance diagram of Fe in leachate during the experiment, at 25 °C, using the following concentration:  $[\text{Fe}^{2+}]_{\text{tot}} = 1 \cdot 10^{-6} \text{ M}$ ,  $[\text{CO}_3^{2-}]_{\text{tot}} = 2 \cdot 10^{-3} \text{ M}$ ,  $[\text{Na}^+] = 1 \cdot 10^{-2} \text{ M}$ ,  $[\text{Cl}^-] = 1 \cdot 10^{-2} \text{ M}$ ,  $[\text{U}^{4+}] = 1 \cdot 10^{-10} \text{ M}$ .

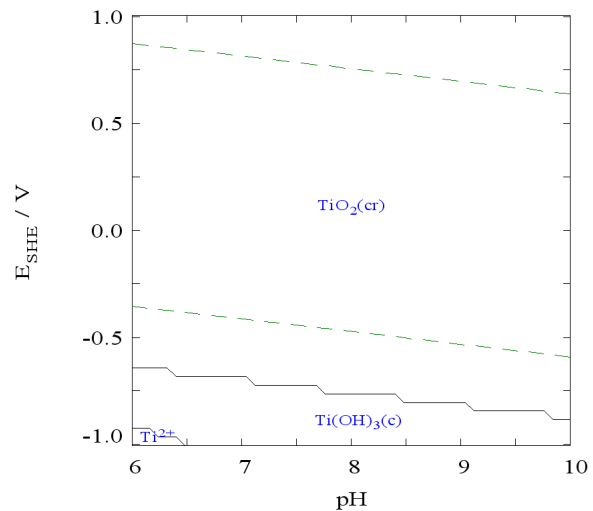


**Figure 18:** Stability range of Ti in the leachate during the experiment, at 25 °C, using the following concentration:  $[\text{Ti}^{4+}]_{\text{tot}} = 1 \cdot 10^{-7} \text{ M}$ ,  $[\text{CO}_3^{2-}]_{\text{tot}} = 2 \cdot 10^{-3} \text{ M}$ ,  $[\text{Na}^+] = 1 \cdot 10^{-2} \text{ M}$ ,  $[\text{Cl}^-] = 1 \cdot 10^{-2} \text{ M}$ ,  $[\text{U}^{4+}] = 1 \cdot 10^{-10} \text{ M}$ .

### *Actinides and FP behaviour during rinse action*

During the period 313-316 days the rinse action was performed. The fission products and actinides measurable above their detection limits are given in Figure 16. The concentration profile of  $^{238}\text{U}$ , fission Sb,  $^{237}\text{Np}$  and  $^{239}\text{Pu}$  during the first four leachant exchanges (brown dotted line) deviates from the calculated dilution (black dotted line). The increased concentration of uranium show that re-precipitated U(IV) ( $[\text{U}]$  of  $5.6 \cdot 10^{-10}$  M) was oxidised to U(VI) during this phase. The simultaneous increase of fission Sb,  $^{237}\text{Np}$  and  $^{239}\text{Pu}$  at the same time show that these elements were incorporated in the reduced precipitated uranium layer on the fuel surface. The time period 2-18 hours was enough to revert to reducing conditions at the fuel surface and to stop further oxidation of uranium. The leachant exchanges 5-7 decreased the concentration of all elements with the expected dilution factor indicating absence of fuel oxidation. The last leachant exchange indicates an oxidation of the fuel. Anyhow, the purpose of the rinse action was to decrease the  $[\text{}^{137}\text{Cs}]$  to be able to observe the oxidation of the fuel. A comparison of the  $[\text{}^{137}\text{Cs}]$  before and after the rinse action showed a decrease by a factor of 1415, but the  $(\text{Cs}_{\text{tot}}/\text{U}_{\text{tot}})_{\text{leachate}}$  was 0.62, which is still far higher than the same ratio in the fuel of 0.0092. It indicates that Cs is mainly leached from the grain boundaries which contain a much higher Cs/U ratio than the average fuel matrix, probably close to the ratio  $(\text{Cs}/\text{U})_{\text{leachate}}/(\text{Cs}/\text{U})_{\text{fuel}}$  of 67.

The molar ratio  $^{90}\text{Sr}/^{137}\text{Cs}$  in the leachate during the rinse action in comparison to the calculated ratio in the fuel is shown in Figure 19. Solubility calculations show that no  $\text{SrCO}_3(\text{s})$  was formed ( $[\text{Sr}]_{\text{tot}} 1 \cdot 10^{-7}$  M,  $[\text{CO}_3^{2-}]_{\text{tot}} 2 \cdot 10^{-2}$  M, pH 8.1,  $E_h$  -0.169 V). The initially low  $^{90}\text{Sr}/^{137}\text{Cs}$  ratio can be explained by a larger inventory of Cs in comparison to Sr in the grain boundaries. The  $(\text{Sr}_{\text{tot}}/\text{U}_{\text{tot}})_{\text{leachate}}$  was 0.27 which is still far higher than the same ratio in the fuel of 0.00412.

Applying the same calculation as above, for the last leachant exchange, show a  $(\text{Sr}/\text{U})_{\text{leachate}}/(\text{Sr}/\text{U})_{\text{fuel}}$  ratio of 65, which is similar to the ratio calculated, above in the text, for Cs. This means that Cs and Sr in the leachate are congruently released with U when less reducing conditions occur at the spent fuel surface observed by the relatively positive  $E_h$  of -0.169 V on day 316 in Figure 13,  $(^{238}\text{U}/^{239}\text{Pu})_{\text{leachate}} = 3 \cdot 10^{-3}$  on day 316 in Figure 15, and the last value in Figure 16 indicating a molar ratio similar to the one expected in virgin fuel. For the first time, on day 316, in this experiment a relatively un-oxidised virgin fuel surface is available for corrosion study.

As mentioned above a slight oxidation (Figure 13,  $E_h$  -0.169 V on day 316) occurred during the leachant change 7 and 8. This can also be observed in Figure 16 where the concentrations of  $^{238}\text{U}$ ,  $^{237}\text{Np}$  and  $^{239}\text{Pu}$  should have decreased with a factor of 3.2, but instead increased, although at a very low concentration levels. Even though it is speculative, a comparison of the concentration changes of  $^{238}\text{U}$ ,  $^{237}\text{Np}$ ,  $^{239}\text{Pu}$  between rinse 7 and 8 can be used to study their oxidation behaviour. Calculating the  $dC/dt$ , taking into account their abundance in the fuel, show that the oxidation rate gives the following order:  $^{238}\text{U} \approx ^{239}\text{Pu} > ^{237}\text{Np}$ .

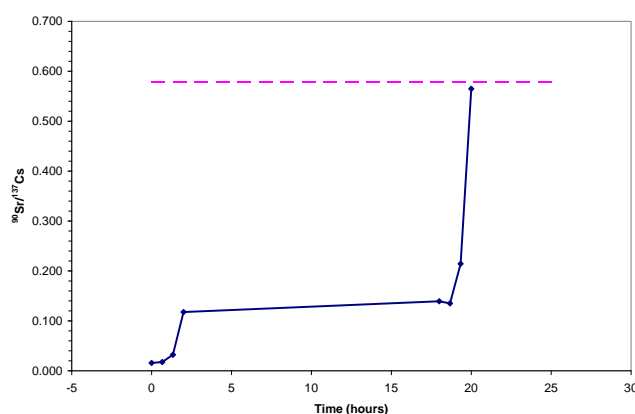


**Figure 19:** Molar ratio  $^{90}\text{Sr}/^{137}\text{Cs}$  in the leachate during rinse action (days 313-314). The dotted line represents the  $^{90}\text{Sr}/^{137}\text{Cs}$  ratio in the rim fraction of the  $\text{UO}_2$  fuel with a burn-up of 67 GWd/tHM after 2920 days of cooling

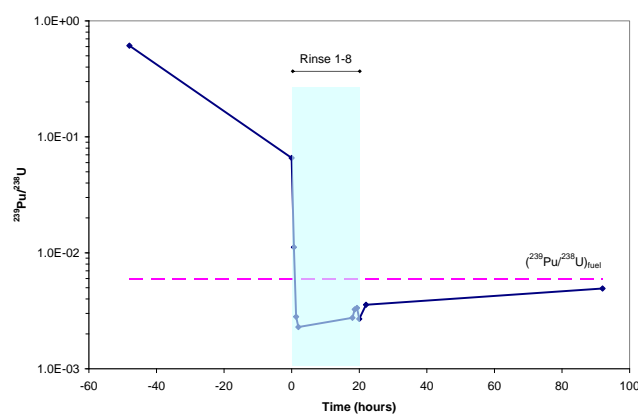


**Figure 20:** Molar ratio  $^{239}\text{Pu}/^{238}\text{U}$  in the leachate before the rinse action (48 hours), during rinse action (on days 313-314, period 0-20 hours) and after the rinse (2 and 70 hours after last rinse). The dotted line represents the  $^{239}\text{Pu}/^{238}\text{U}$  ratio in the rim fraction of the  $\text{UO}_2$  fuel with a burn-up of 67 GWd/tHM after 2920 days of cooling.

#### Stable elements behavior during rinse action

The changes in concentration of natural elements Fe, Zn, Cu, Ti, Cr and Y correlate with each other. This general behavior of the stable elements in the leachate is that they behave similarly indicating either presence of small particles with a certain metallic composition in the leachate or that the autoclave walls dissolve/re-precipitate the elements depending on the redox potential.

During the rinse action the concentration changes of the elements; Mn, natural Mo, Ni, natural Sr and Cd show a different behavior than the elements Fe, Zn, Cu, Ti, Cr and Y.

This can also be noticed in calculations of the elements co-variation. Four groups could be identified and within each group the co-variation was high:

- Zn, Sr, Rb, Y, Cd, Mo and Cu
- Ti, Fe and Cr
- Ni
- Mn

The first group consists of non-redox sensitive elements in the experimental  $E_h$  range of -0.1 to -0.5 V. The second group contains redox sensitive elements. Ti originates from the titanium autoclave and possibly also Fe (as an impurity in titanium grade-II material) even though the molar concentration levels deviates strongly,  $(\text{Ti}/\text{Fe})_{\text{leachate}}$  is 0.27 while  $(\text{Ti}/\text{Fe})_{\text{autoclave}} = 465$ . Within the studied redox range of -0.1 to -0.5 V and pH 8.2, metallic titanium reacts with water and forms a passivated layer of  $\text{TiO}_2(\text{s})$  (Figure 18).

In order to determine the elements steady-state concentration levels in the autoclave the concentration levels were studied before and after the rinse action. Considering the  $^{239}\text{Pu}/^{238}\text{U}$  molar ratio in the leachate in comparison to the same ratio in the fuel during the rinse action is shown in Figure 20. During the two first rinses the ratio rapidly decreases due to the fact that the Pu in solution is diluted at the same time as re-precipitated U, with low Pu-content, is dissolved. During rinse 4-8 to five the ratio is lower than found in the fuel, thus indicating that uranium is slightly easier to oxidise than Pu.

Three conclusions can be made, firstly, the initial  $(^{239}\text{Pu}/^{238}\text{U})_{\text{leachate}}$  ratio of 0.6 indicate a slower reduction rate for Pu than for U and, secondly, the rinse action have brought the leachate to conditions close to congruent dissolution of the fuel and finally, that uranium is easier to dissolve from the fuel matrix than Pu.

The steady-state concentration of the stable elements in the leachate could be established observing the change in the concentration levels before and after the rinse action. The theoretical dilution, through the seven leachate exchanges, each with a dilution factor of 3.16, is 3166. The calculated dilution factor of  $^{137}\text{Cs}$  for the seven rinses is 1415 indicating a slight release of Cs from the fuel during each rinse step. In any case, the expected dilution of the stable elements should have been in the range of 3000. In Table 1 one can easily

observe that, even though the leachates were diluted, the concentration of the stable elements before (day 311) and after the rinse action (day 319), are as most one order of magnitude lower (Fe, Zn, Cu, Cr, Mo, Ni, Cd) and in some case unchanged (Ti, Mn, Sr and Rb).

It can be concluded that the stable elemental concentrations, given in Table 5, are the steady-state concentrations in the leachate (on day 319 since lowered by rinse action and then increased to a steady state).

**Table 5:** Concentration of stable elements in the leachate before the rinse action (48 hours, day 311), after the last rinse (2 hours) and after 72 hours after last rinse (day 319).

Elements	Concentration (M)			
	Blank, 10mM NaCl + 2mM NaHCO <sub>3</sub>	Day 311	Day 314	Day 319
Fe	$5 \cdot 10^{-8}$	$1.3 \cdot 10^{-6}$	$3.8 \cdot 10^{-8}$	$1.1 \cdot 10^{-7}$
Zn	$5 \cdot 10^{-8}$	$3.2 \cdot 10^{-7}$	$6.5 \cdot 10^{-8}$	$5.7 \cdot 10^{-8}$
Cu	$2 \cdot 10^{-9}$	$1.1 \cdot 10^{-7}$	$1.5 \cdot 10^{-8}$	$5.1 \cdot 10^{-8}$
Ti	$2 \cdot 10^{-8}$	$9.8 \cdot 10^{-8}$	$1.3 \cdot 10^{-8}$	$5.4 \cdot 10^{-8}$
Cr	$7 \cdot 10^{-9}$	$3.6 \cdot 10^{-9}$	$3.1 \cdot 10^{-9}$	$1.4 \cdot 10^{-8}$
Y	$5 \cdot 10^{-13}$	n.d.	n.d.	n.d.
Mn	$1 \cdot 10^{-9}$	$6.3 \cdot 10^{-7}$	$2.6 \cdot 10^{-7}$	$5.3 \cdot 10^{-7}$
Mo	$4 \cdot 10^{-9}$	$4.2 \cdot 10^{-7}$	$5.1 \cdot 10^{-8}$	$6.2 \cdot 10^{-8}$
Ni	$1 \cdot 10^{-8}$	$3.0 \cdot 10^{-6}$	$3.6 \cdot 10^{-7}$	$5.2 \cdot 10^{-7}$
Sr	$2 \cdot 10^{-9}$	$7.1 \cdot 10^{-8}$	$9.2 \cdot 10^{-9}$	$4.4 \cdot 10^{-8}$
Cd	$1 \cdot 10^{-10}$	$4.1 \cdot 10^{-9}$	$3.9 \cdot 10^{-10}$	$9.1 \cdot 10^{-10}$
Rb	$2 \cdot 10^{-8}$	$3.0 \cdot 10^{-7}$	$6.8 \cdot 10^{-9}$	$2.0 \cdot 10^{-7}$

n.d. no data

Only those elements that are redox sensitive will change when the redox potential changes, mainly through oxygen intrusion.

In order to understand the leachate chemistry in relation to the presence of the stable elements some simplified speciation calculations were performed and are presented in Table 6. The identified redox sensitive elements within the  $E_h$  interval -0.167 to -0.5 V, defined by the highest and lowest measured  $E_h$  in the autoclave, are; Fe, Cu, Ti, Cr, Mo(natural) and U. Only U is part of the spent fuel while the other originates from the autoclave setup. It can be noticed that the concentration of Cu, Ti, Cr and Mo(natural) in the leachate is several magnitudes higher than calculated indicating that a large fraction of the elements exists as fine particulates (colloids) in the leachate. This might well be since the leachates are not filtrated or centrifuged before ICP-MS analysis. The large discrepancy between measured

elemental concentrations and calculated concentrations, taking into account speciation, questions the relevance of these data for the interpretation of the redox potential. This statement is based on the large errors in the concentration of stable elements originating from used mQ-water, start chemicals and preparation vials (reflected by the Blank leachant in Table 5). As well as contribution from walls of refill autoclave, transfer tube (with a length of 25 m), valves, tube connections and the autoclave itself. Additional error contributions come from preparation of the leachate sample before ICP-MS analysis.

Anyhow, observing the steady state  $E_h$  range measured in the autoclave, -0.375 to -0.45 V, as shown in Figure 13; Fe should exist mainly in the reduced form as  $Fe^{2+}$ , Cu exist at such low concentration that it has negligible influence on the redox potential; Ti exists in autoclave material and could influence the redox, Cr exists in low concentrations and is therefore considered as having low impact on redox; Mo should mainly exist in its tetravalent state, as  $MoO_2(cr)$  with low solubility; U exists in its tetravalent state as predicted.

Analyzing the concentration variation of the elements and the redox potential during the experiment together with the results of the speciation calculations, the following conclusions could be made:

- Mn is correlated mainly with Pu. The Mn concentration has a significant variation with changes in  $E_h$ . Speciation calculation show that manganese exist as  $Mn^{2+}$ . Co-variation with Pu could possibly be explained by co-precipitation.
- Natural Mo exists in the autoclave from the start and its concentration variation is small indicating a weak correlation with neither U nor Pu.
- The concentration variations of U and Pu during the experiment are different, see Figure 14 and Figure 15. Congruent dissolution of the matrix or re-precipitated U/Pu layer occurs only when there is an  $O_2$  intrusion or when all previously dissolved U is re-precipitated and is Pu co-precipitated (Figure 15).
- Fe behaves similarly to Pu, but not as U (Figure 14). The speciation indicates that Fe exist as  $Fe^{2+}$  on a borderline to  $Fe(OH)_3(s)$  (Figure 17). Through its relatively high concentration ( $10^{-6}$  M) it seems to buffer a part of the redox system.

- Ti exist as  $\text{Ti}(\text{OH})_4(\text{aq})$  in contact with the autoclave walls in the form of an passivate layer of  $\text{TiO}_2(\text{s})$  (Fig. 7). The solubility product of  $\text{TiO}_2(\text{s})$  is  $10^{-5.5}$  M [BAES C.F., MESMER R.E. (1976)] according to the reaction:



The equilibrium  $\text{TiO}_2(\text{s})/\text{Ti}(\text{OH})_4(\text{aq})$  gives a Ti concentration of  $3 \cdot 10^{-6}$  M which is comparable to the measured concentrations in the leachate.

**Table 6:** Results of speciation calculation of stable elements and U in leachate during the corrosion experiment. All calculations are made in presence of  $[\text{CO}_3^{2-}]_{\text{tot}} = 2 \cdot 10^{-3}$  M,  $[\text{Na}^+] = 1 \cdot 10^{-2}$  M,  $[\text{Cl}^-] = 1 \cdot 10^{-2}$  M,  $[\text{U}^{4+}] = 1 \cdot 10^{-10}$  M,  $[\text{Fe}^{2+}] = 1 \cdot 10^{-6}$  M and a leachate pH of 8.1. The concentrations are given for the solubility limiting compound.

Elements	$C_{\text{tot}}$ in leachate (M)	Redox potential, $E_h$ (V)		
		-0.169	-0.3	-0.5
<i>Redox couple</i>				
$\text{Fe}^{2+}/\text{Fe}^{3+}$	$1 \cdot 10^{-6}$	$\text{Fe}^{2+}(\text{aq})/$ $\text{Fe}(\text{OH})_{2.7}\text{Cl}_{0.3}(\text{cr})$ $5 \cdot 10^{-9}$ M	$\text{Fe}^{2+}(\text{aq})/$ $\text{Fe}(\text{OH})_{2.7}\text{Cl}_{0.3}(\text{cr})$ $5 \cdot 10^{-9}$ M	$\text{Fe}^{2+}(\text{aq})$ $1 \cdot 10^{-6}$ M
$\text{Cu}/\text{Cu}^+$	$5 \cdot 10^{-8}$	$\text{Cu}/\text{Cu}^+(\text{aq})$ $2 \cdot 10^{-7}$ M	$\text{Cu}/\text{Cu}^+(\text{aq})$ $<10^{-11}$ M	$\text{Cu}/\text{Cu}^+(\text{aq})$ $<10^{-11}$ M
$\text{Ti}^{2+}/\text{Ti}^{4+}$	$1 \cdot 10^{-7}$	$\text{Ti}(\text{OH})_4(\text{aq})/$ $\text{TiO}_2(\text{cr})$ $3 \cdot 10^{-6}$ M	$\text{Ti}(\text{OH})_4(\text{aq})/$ $\text{TiO}_2(\text{cr})$ $3 \cdot 10^{-6}$ M	$\text{Ti}(\text{OH})_4(\text{aq})/$ $\text{TiO}_2(\text{cr})$ $3 \cdot 10^{-6}$ M
$\text{Cr}^{3+}/\text{Cr}^{6+}$	$4 \cdot 10^{-9}$	$\text{Cr}(\text{OH})_3(\text{aq})/$ $\text{FeCr}_2\text{O}_4(\text{cr})$ $4 \cdot 10^{-11}$ M	$\text{Cr}(\text{OH})_3(\text{aq})/ \text{FeCr}_2\text{O}_4(\text{cr})$ $5 \cdot 10^{-11}$ M	$\text{Cr}(\text{OH})_3(\text{aq})/$ $\text{FeCr}_2\text{O}_4(\text{cr})$ $8 \cdot 10^{-10}$ M
$\text{Mo}^{6+}/\text{Mo}^{4+}$	$6 \cdot 10^{-8}$	$\text{MoO}_4^{2-}(\text{aq})/$ $\text{MoO}_2(\text{cr})$ $1 \cdot 10^{-7}$ M	$\text{MoO}_4^{2-}(\text{aq})/$ $\text{MoO}_2(\text{cr})$ $1 \cdot 10^{-11}$ M	$\text{Mo}(\text{OH})_4(\text{aq})/$ $\text{MoO}_2(\text{cr})$ $<1 \cdot 10^{-11}$ M
$\text{U}^{4+}/\text{U}^{6+}$	$2 \cdot 10^{-10}$	$\text{UO}_2(\text{CO}_3)_3^{4-}(\text{aq})$ $2 \cdot 10^{-6}$ M	$\text{UO}_2(\text{am})/$ $\text{U}(\text{OH})_4(\text{aq})$ $2 \cdot 10^{-10}$ M	$\text{UO}_2(\text{am})/$ $\text{U}(\text{OH})_4(\text{aq})$ $2 \cdot 10^{-10}$ M
<i>Non-redox couple</i>				
Zn	$2 \cdot 10^{-7}$	$\text{ZnOH}^+(\text{aq})$	$\text{ZnOH}^+(\text{aq})$	$\text{ZnOH}^+(\text{aq})$
Y	$1 \cdot 10^{-10}$	$\text{Y}(\text{CO}_3)_2^-(\text{aq})$	$\text{Y}(\text{CO}_3)_2^-(\text{aq})$	$\text{YOH}^{2+}(\text{aq})$
Mn	$6 \cdot 10^{-7}$	$\text{Mn}^{2+}(\text{aq})/\text{Mn}(\text{OH})_2(\text{aq})$	$\text{Mn}^{2+}(\text{aq})$	$\text{Mn}^{2+}(\text{aq})$
Ni	$1 \cdot 10^{-6}$	$\text{NiCO}_3(\text{aq})$	$\text{Ni}^{2+}(\text{aq})$	$\text{Ni}^{2+}/\text{Ni}(\text{cr})$
Sr	$1 \cdot 10^{-7}$	$\text{Sr}^{2+}(\text{aq})$	$\text{Sr}^{2+}(\text{aq})$	$\text{Sr}^{2+}(\text{aq})$
Rb	$2 \cdot 10^{-7}$	$\text{Rb}^+(\text{aq})$	$\text{Rb}^+(\text{aq})$	$\text{Rb}^+(\text{aq})$

Out of the inactive elements studied: Fe, Zn, Cu, Ti, Cr, Y, Mn, Mo, Ni, Sr, Cd and Rb only two elements are feasible candidates, as concluded from the reasoning made above, to influence the redox conditions in the autoclave, namely Ti and Fe.

The presence of Ti and Fe in the autoclave material, and their relatively high concentration of Fe ( $1\text{-}100\cdot 10^{-8}$  M) and Ti ( $1\text{-}10\cdot 10^{-8}$  M) in the leachate, together with their co-variation with Pu, but no co-variation with U, indicate their importance.

#### *Mass balance*

The stable redox sensitive elements active in the studied redox potential range of -0.375 to -0.45 V were taken into account when calculating the mass balance of reducing and oxidizing species (Table 7). The table comprise of the two time periods: 0-313 days and 314-1435 days. At the end of the first period a gas sample was sampled and analysed which gives relatively accurate information of the amount intruded air. No gas sample has been sampled during the second period and therefore the amount of oxidative species is an estimate.

Anyhow, it can be noticed that the concentration of oxidised redox sensitive elements such as Fe, Mo and U are not in parity with the sum of intruded  $O_2$  and radiolytically produced oxidants (Table 7) during the first study period.

For the second period (314-1435 days) the estimations was based on the amount of released Cs. It was assumed that during the initial period 0-313 days all Cs in the instant release fraction was dissolved, 3.5 % of total inventory [FORS P., CARBOL P., VAN WINCKEL S., SPAHIU K. (2009)]. It can also be observed that no more Cs was dissolved at the end of the initial period (Figure 14). The amount of released Cs, in the second period, will be mainly due to corrosion of fuel grains and possibly grain boundaries. In a first iteration we assume that  $\alpha$ -radiolysis does not contribute. The amount of oxidised U, and indirect the amount of in-leaked  $O_2$ , corresponds therefore to the amount of dissolved Cs, taking into account Cs fraction of inventory (0.0058). It can be seen that the  $O_2$  in-leakage is of the same order as the amount of oxidants produced by  $\alpha$ -radiolysis. Since it is not possible to distinguish whether in-leaked  $O_2$  or oxidants produced by  $\alpha$ -radiolysis caused the release of Cs, the higher of these two numbers was taken as maximal amount of oxidants.

**Table 7:** Mass balance of oxidative and reducing species.

Reactants	Period (days)	
	0-313	314-1435
<i>Oxidative species</i>		
O <sub>2</sub> , in-leakage (mol)	0.23	6.4·10 <sup>-6(a)</sup>
O <sub>2</sub> , α-radiolysis (mol)	1.6·10 <sup>-6</sup>	5.6·10 <sup>-6</sup>
Σ Oxidants (mol)	0.23	6.4·10 <sup>-6</sup>
<i>Reducing species</i>		
Fe (mol)	1.1·10 <sup>-7</sup>	6·10 <sup>-8</sup>
Mo (mol)	5·10 <sup>-9</sup>	8·10 <sup>-9</sup>
U (mol)	6·10 <sup>-11</sup>	5·10 <sup>-11</sup>
Σ Reductants (mol)	2·10 <sup>-7</sup>	1·10 <sup>-7</sup>
ΣO <sub>x</sub> / ΣRed	1·10 <sup>6</sup>	6.4·10 <sup>1</sup>

(a) estimated from Cs concentration

It can be concluded that in the first period of the experiment the amount of oxidative species exceeds by a factor of at least 10<sup>6</sup> the amount of reducing species. In the second period of the experiment (314-1435 days) the differences is small and shows that by avoiding refilling the autoclave with leachant or gas and only make leachate sampling, greatly reduces in-leakage of O<sub>2</sub> (Table 7). But, the main advantage is that by lowering the Cs concentration long-time corrosion of the fuel, using Cs as fuel corrosion indicator, can be correctly monitored. It shows that during a period 993 days the Cs concentration increased slightly from 1.1·10<sup>-8</sup> M to 6.1·10<sup>-8</sup>, mainly due to an open valve (experimental error, Figure 14).

### Summary

This 1435-days long study aimed to investigate the corrosion of fragments isolated from the rim of high burn-up UO<sub>2</sub> in a slightly saline leachate containing 2 mM carbonate under a pressure of 14-41 bar H<sub>2</sub>. The main task is to perform a mass balance in respect to reducing and oxidising species.

Despite the fact that 0.23 mol of atmospheric O<sub>2</sub> intruded the autoclave on day 63 [FORS P., CARBOL P., VAN WINCKEL S., SPAHIU K. (2009)] and additional O<sub>2</sub> was produced in the autoclave during the period of 0-313 days, as a result of α-radiolysis of water, low steady state concentration levels were reached for U and Pu of 1.5·10<sup>-10</sup> M and 7·10<sup>-11</sup> M, respectively. The release of Cs almost stopped which indicate an almost insignificant corrosion of grain boundaries and the UO<sub>2</sub> matrix (which contains 97 wt% of the total Cs).

Having exchanged the leachant during the rinse action, the Cs concentration was lowered by a factor of 1415, thus removing the instant release fraction, made it possible to monitor the spent fuel corrosion. During the period of almost 3 years of corrosion (442-1435 days) the Cs concentration increased by a factor of 5. The concentration of U and Pu remained, after a corrosion time of 1121 days (314-1435 das) at the same steady state level as during the initial period of  $2 \cdot 10^{-10}$  M and  $8 \cdot 10^{-12}$  M, respectively.

These results confirm that in the studied  $\text{UO}_2\text{-H}_2\text{-H}_2\text{O}$  system, within the range of 10-33 mM dissolved  $\text{H}_2$ , radiolytically induced  $\text{UO}_2$  corrosion is inhibited by hydrogen and that the rim high burn-up structure of the 67 GWd/tHM fuel did not enhance fuel dissolution.

For the first time, to the knowledge of the authors, the variation of redox sensitive natural elements, present in the leachate as contaminants from the autoclave setup, are studied in order to confirm the redox state of redox sensitive actinides and fission products. Out of the inactive elements studied: Fe, Zn, Cu, Ti, Cr, Y, Mn, Mo, Ni, Sr, Cd and Rb, only Ti and Fe seems to be able to influence the redox conditions. The redox-sensitive natural elements; Fe, Ti, Mn, Mo behave more similarly to Pu than U.

After having identified the redox sensitive elements that influence the redox in the studied system made it possible to perform a mass balance of reducing and oxidising species during the corrosion experiment. The results of the mass balance calculation showed that during the period 0-313 days more than  $10^6$  times more oxidants were present in the autoclave and must have been reduced in the system since no  $\text{O}_2$  or  $\text{H}_2\text{O}_2$  could be detected and the U concentration was in the range of  $10^{-10}$  M, which indicates a non-oxidised spent nuclear fuel. The discussion on different possible mechanisms are outside the scope of this work but are discussed elsewhere [ERIKSEN T.E., SHOESMITH D.W., JONSSON M. (2012); CARBOL P., WEGEN D.H., WISS T., FORS P. (2012); METZ V., GECKEIS H., GONZÁLEZ-ROBLES E., LOIDA A., BUBE C., KIENZLER B. (2012)].

Additionally, the co-variation of redox sensitive natural elements with redox elements originating from the fuel was used to support the measured redox potential in the bulk leachate which is coupled to the oxidative-dissolution process at the  $\text{UO}_2\text{-H}_2\text{O}$  interface.

The results presented gives a better understanding of the redox processes occurring at the  $\text{UO}_2\text{-H}_2\text{O}$  interface and is crucial for the understanding of the spent fuel corrosion which is

directly applicable to the conceptual model of the spent fuel corrosion used in safety assessments.

## **On the redox chemistry at the near field of repository, the influences of iron canister material and hydrogen**

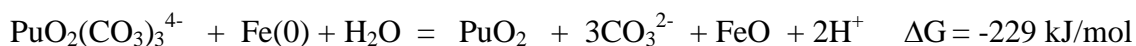
### *Pu reductive immobilization by iron canister material(JRC-ITU, Studsvik)*

#### *Introduction*

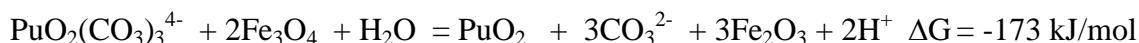
<sup>239</sup>Pu is one of the most radiotoxic radionuclides contained in high level nuclear waste due to its long half live and chemical properties. The environmental behaviour of plutonium is the most difficult to predict due to its multi-valence state in the subsurface environment [RONDINELLA V. V. (2011)]. Pu(III)/(IV) are the predominant valence states at low pH and strongly reducing conditions while Pu(V)/(VI) is favoured in oxidative and high pH systems.

Previous studies have shown that aqueous Pu(V) can be reduced to sorbed Pu(IV) by Fe(II) containing SRS sediments [HIXON A.E., HU Y.-J., KAPLAN D.I., KUKKADAPU R.K., NITSCHKE H., QAFOKU O., POWELL B.A. (2009)]. Pu(VI) reduction by Fe(0) and Fe(II) phases has been investigated [LUCCHINI J.F., KHAING H., RICHMANN M.K., BORKOWSKI M., REED D.T. (2008)], however, the authors did not show the stability of Pu(V)/(VI) in water solution, neither gave the ratio of Pu(V) /Pu(VI) in the solution.

A calculation of Gibbs free energy of redox reaction between Pu(VI) and metallic iron or Fe<sub>3</sub>O<sub>4</sub> shows that the process is in both cases possible. The reaction of plutonyl carbonate with Fe gives, for a groundwater with pH 10 (25 °C);



and the reaction between plutonyl carbonate and magnetite;



The relative small negative values of  $\Delta G$  for both reactions suggest that these two redox reactions may be feasible but the driving force is not very large. In comparison,  $\Delta G$  for a very slow redox reaction between Se(VI) and Fe(0) at repository conditions (pH 8.5) is -278 kJ/mol [CUI D., PURANEN A., SCHEIDEGGER A., GROLMUND D., WERSIN P., LEUPIN O., SPAHIU K. (2007)].

It is relatively difficult to convert Pu(IV), in mg-amount, to Pu(VI) in absence of  $\text{NO}_3^-$  and stabilise Pu at pH 8.2-8.5, for a time period of months. Only a relatively small number of publications exist which describe the conversion of Pu(IV) to Pu(VI) [FEDOSEEV A.M., SHILOV V.P. (2010); TAIT C.D., EKBERG S.A., PALMER P.D., MORRIS D.E. (1995); REILLY S.D., NEU M.P. (2006); REILLY S.D., RUNDE W., NEU M.P. (2007); NEWTON T.W., HOBART D.E., PALMER P.D. (1986); GHOSH MAZUMDAR A.S., SIVARAMAKRISHNAN C.K. (1964)].

Based on the publications concerning the oxidation of Pu(IV) to Pu(VI), the best method, which is also suitable for glovebox work, is to oxidise Pu with fuming  $\text{HClO}_4$  and then add the Pu(VI) solution to 0.5 M  $\text{Na}_2\text{CO}_3$  solution. The high  $\text{Na}_2\text{CO}_3$  concentration was selected to ensure that there is enough of carbonate to form Pu(VI) carbonate. The pH should be in the range of 9-10 (Figure 21).

The experiment aims are: a) to investigate the stability of  $10^{-5}$  M Pu(VI) in a synthetic groundwater solution (a 10mM NaCl and 84mM  $\text{Na}_2\text{CO}_3$  solution, a pH of 10 gives a  $[\text{CO}_3^{2-}]$  of ~20mM, Figure 21) and b) to investigate the possibility of a redox reaction between Pu(VI) and iron canister surface, i.e. Fe(0) surface or  $\text{Fe}_3\text{O}_4$  (magnetite) coated Fe(0) surface.

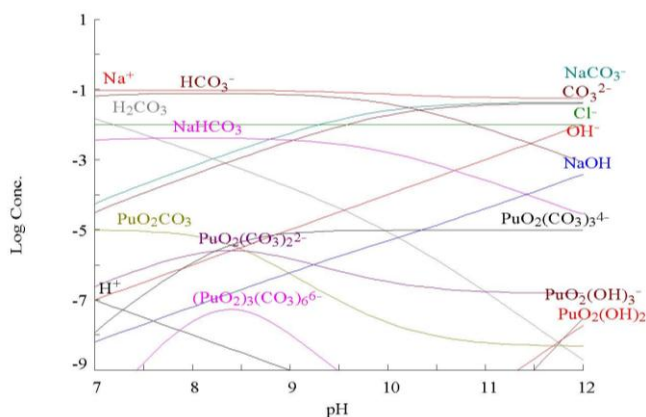


**Figure 21:** Pu speciation in 0.084 M  $\text{Na}_2\text{CO}_3$  solution under oxidative conditions. The total concentrations used for the speciation calculation were:  $[\text{Na}^+] = 0.1 \text{ M}$ ,  $[\text{CO}_3^{2-}] = 0.084 \text{ M}$ ,  $[\text{PuO}_2^{2+}] = 10 \mu\text{M}$  and  $[\text{Cl}^-] = 0.01 \text{ M}$

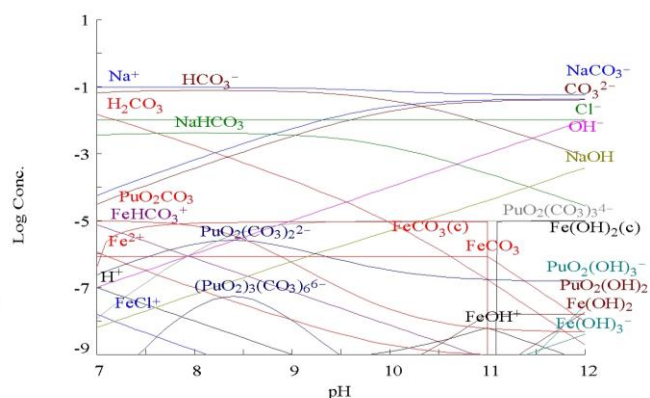


**Figure 22:** Speciation calculations of Fe and Pu in solution after termination of the experiment (114 days). The total concentrations used in the speciation were:  $[\text{Na}^+] = 0.1 \text{ M}$ ,  $[\text{CO}_3^{2-}] = 0.084 \text{ M}$ ,  $[\text{Fe}^{2+}] = 10 \mu\text{M}$ ,  $[\text{PuO}_2^{2+}] = 10 \mu\text{M}$  and  $[\text{Cl}^-] = 0.01 \text{ M}$ .

### Experimental

The preparation of the Pu(VI) solution and of the steel and steel/magnetite coupons has been described extensively in [ALTMAYER M., KIENZLER B., DURO L., GRIVÉ M., MONTOYA V. (EDS.) (2012)].

The reaction vessel was equipped in a  $\text{N}_2$  purged glovebox with a holder for five LSC vials, and an oxygen trap was placed in the middle of the reactor,. The oxygen trap consisted of freshly mixed  $\text{CaCO}_3$  and  $\text{FeSO}_4$ . MilliQ-water was added at the bottom of the reactor to get water vapour saturated atmosphere and thereby avoiding Pu-solution evaporation.

The filtered Pu-solution was poured into new 20ml glass liquid scintillation counting (LSC) vials. The vials were placed in the holder in the reactor and the iron and magnetite coupons were added into labelled Pu-vials, respectively. The reactor was purged with a gas mixture (Basi Schröbert GmbH, Germany) of  $0.0302 \pm 0.0006 \text{ vol-\% CO}_2$  (quality 4.5) and the rest Ar (quality 5.0) at high throughput for 20 minutes. After this time period the gas purging was set to 3 bubbles/s and kept at this purge-rate for the rest of the experiment. The experiment was run at a temperature of  $23 \pm 2 \text{ }^\circ\text{C}$ .

The Pu-solutions were sampled after 0, 1, 7, 37, 77, and 114 days. The sampling was made with a long steel cannula inserted through the rubber sealing located at the top of the reactor vessel. The solution was sucked up into a disposable 2-ml syringe. The syringes were exchanged between each sampled Pu-vial and the cannula cleaned. During sampling, additional surgical gloves were used on the inside of the glovebox to avoid contamination of the Pu-samples.

The experiment was run continuously, without opening the reactor or gas supply interruption. The oxygen trap became darker with increasing experimental time. Optical inspection of the vials containing the Pu-solution and the coupons showed a reddish colour appearing on the vial bottom and surrounding each coupon. The first appearance occurred after approximately 50 days of experiment.

The experiment was terminated after 114 days. Still under gas purging and with an glovebox atmosphere of 0.32 vol-% O<sub>2</sub>, 12 ppm H<sub>2</sub>O and the rest N<sub>2</sub>, the reactor was opened. The <sup>239</sup>Pu-solution, in contact with the iron coupon, was transferred from 20ml glass vials, into new 20ml plastic LSC vials, leaving the iron coupon in the glass vial. The iron coupon was taken out of the vial, dried on a tissue paper (Kleenex) and rinsed twice for 2 seconds in freshly prepared 10ml 10mM NaCl + 2mM NaHCO<sub>3</sub> solution. The coupon was dried in 0.03vol% CO<sub>2</sub> /Ar gas stream. The iron coupon was transferred to the original vials used before the start of the experiment.

Two of the coupons (Fe coupon 1 and Fe magnetite 1) were prepared for SEM-EDX analysis while the other two coupons (Fe coupon 2 and Fe magnetite 2) were bagged out from the glovebox and used for  $\alpha$ -track analysis.

The <sup>239</sup>Pu solutions obtained after terminating the experiment was used for different analyse: SF-ICP-MS analysis,  $\gamma$ -spectrometry, Transmission electron microscope coupled to energy dispersive Y-ray spectroscopy (TEM-EDX), pH measurement and absorption spectrometry.

#### *$\alpha$ -track analysis of Fe and magnetite coupon surfaces*

The  $\alpha$ -track analysis was performed on both sides of the two iron coupons (Fe coupon 2 and Fe magnetite 2). The surface of the coupon was placed in contact with an  $\alpha$ -sensitive cellulose nitrate film (CN85, Kodak, France). Four squares, with the dimensions similar to the coupons, were engraved in the film with a sharp-edge pincette. The individual squares were

used for different pellet exposure times, varying between 10 sec and 1000 sec. The purpose of this procedure was to find an appropriate exposure time for each intensity of the  $\alpha$ -spots since highly active  $\alpha$ -spots made so many  $\alpha$ -tracks that the tracks overlap each other. The background  $\alpha$ -radiation in the glove box was monitored by observing the area beside the exposed squares.

After the exposure the film was etched in 6.5M NaOH at 60°C for 15 min. Subsequently, the etched film was rinsed for 10min in milliQ-water. In order to identify the intensive  $\alpha$ -radiation spots the etched film was investigated with an optical microscope (AxioPlan 2, Zeiss AG, Germany) equipped with a camera. In order to be able to count individual  $\alpha$ -tracks the films were searched with a magnification of 5x, 10x, 20x, and 50x. An area of the same size as the iron coupon surface was searched for  $\alpha$ -spots and average  $\alpha$ -track density.

Four developed films were searched under the microscope: the exposed front (upper) and back of the coupons "Fe coupon 2" and "Fe magnetite 2". The maximal exposure time of 1000 s gave optimal  $\alpha$ -track density and all of the following results are based on images for this exposure time.

Firstly, the optical inspection in the microscope showed that only the upper side of coupon "Fe magnetite 2" showed  $\alpha$ -tracks. We assume that the upper surface received more Pu-deposition than the one directed towards the bottom of the glass vial, as a consequence of restricted exchange of solution.

Secondly, the upper surfaces of Fe magnetite 2 showed 15 hotspots with different  $\alpha$ -track density, here denominated as  $\alpha$ -spots (Figure 23, Figure 24). The  $\alpha$ -track densities in the hotspots varied from 1 to 10  $\alpha$ -track/100 $\mu\text{m}^2$ .

Using the  $\alpha$ -track density on the exposed CN-85 film the surface deposition of  $^{239}\text{Pu}$  could be determined (counting efficiency 40% [DURRANI S.A., BULL R.K. (1987)]). The calculation shows that the  $^{239}\text{Pu}$  activity in the 15  $\alpha$ -spots (0.17 Bq) is negligible in comparison to the average surface  $^{239}\text{Pu}$  activity (1390 Bq) measured on the entire Fe magnetite coupon upper surface. The amount of  $^{239}\text{Pu}$  deposited on the coupon was  $2.5 \cdot 10^{-9}$  mol and should be compared to the amount of  $^{239}\text{Pu}$  added to each 20ml LSC vial of  $2.1 \cdot 10^{-7}$  mol.

This means that approximately 1 % of the total amount of  $^{239}\text{Pu}$  is deposited on the Fe magnetite 2 coupon surfaces. Assuming a homogenous coverage of the surface

approximately 6 atomic  $^{239}\text{PuO}_2$  layers were deposited and should be compared with 470 layers that could be formed in case all  $^{239}\text{Pu}$  added to the 20ml LSC vial would have been precipitated. The absence of  $\alpha$ -spots on the Fe coupon implies that there are no larger colloidal  $\text{PuO}_2$  aggregates formed and deposited during the duration of the experiment.

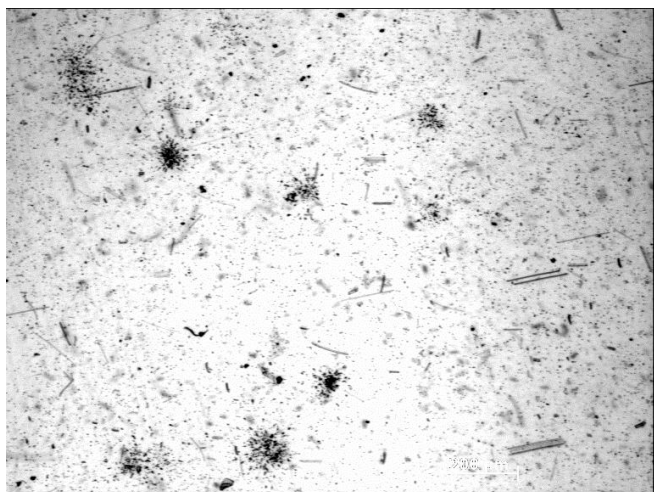


**Figure 23:** Distribution of  $\alpha$ -tracks from film exposed to Fe Magnetite 2 coupon (exposure time 1000 s, magnification 5x). A number of  $\alpha$ -spots (accumulation of  $\alpha$ -tracks) are easily visible on the left side of the picture.

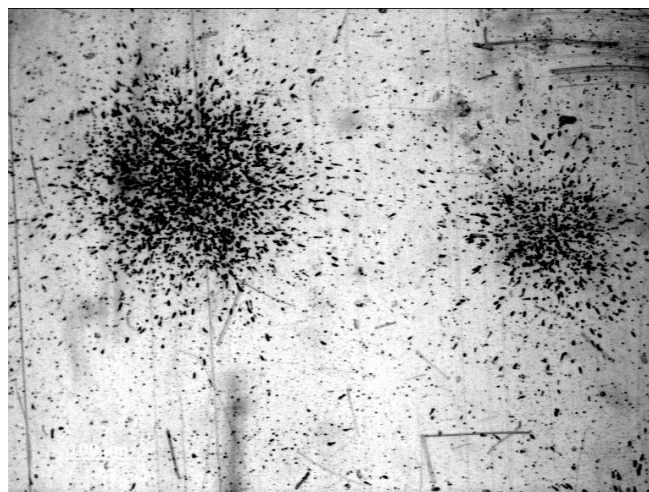


**Figure 24:** The image shows the most intensive  $\alpha$ -spot observed on the Fe Magnetite 2 coupon (exposure time 1000 s, magnification 10x).

#### *SF-ICP-MS and $\gamma$ -spectrometry analysis of $^{239}\text{Pu(VI)}$ samples*

Sector field inductively coupled plasma mass spectrometry, SF-ICP-MS (Element2, Thermo Scientific, Germany), measurements were made on all samples, except for the sampling during termination of the experiment (114 days), to determine the concentration of Fe and Pu. The sampled  $^{239}\text{Pu}$ -solutions (approximately 1ml) from the on-going experiment were diluted 1:10 with 1M  $\text{HNO}_3$ . This low dilution factor was selected to be able to run the SF-ICP-MS in medium resolution so that  $^{56}\text{Fe}$  can be resolved from the interference of  $^{40}\text{Ar}+^{16}\text{O}$ .

All samples were analysed in duplicates, one with and one without internal standard addition. The elements Co and Ho (0.30ml 20ppb Co and 0.15ml 20ppb Ho) were used as internal standards. All samples were acidified to 1 M  $\text{HNO}_3$ . At the start of each measurement, a multi-element calibration was made using certified standards (Agilent Life Sciences/Chemical Analysis GmbH, Germany). Calibration standards with the concentrations 0, 50, 200, 1000,

(D-N<sup>o</sup>:1.2) – [Report on the scientific state of the art](#)

Dissemination level :PU

Date of issue of this report : **03/09/2012**

5000, 20000, 50000 and 100000 ppt were prepared. Two quality-check solutions, each containing 1 ppb of one of the multi-element standards plus 1 ppb of the internal standard, were run to monitor the ICP-MS performance. The estimated uncertainty in the SF-ICP-MS determination of the concentrations of  $^{239}\text{Pu}$  is ~10% and for Fe approximately 20%.

The elemental Fe results are based on the low resolution measurements of  $^{57}\text{Fe}$  and the medium resolution measurements of  $^{56}\text{Fe}$  and  $^{57}\text{Fe}$ . Both  $^{57}\text{Fe}$  results did confirm each other nicely and also the  $^{56}\text{Fe}$  vs.  $^{57}\text{Fe}$  results were in agreement with the natural isotopic composition.

The  $\gamma$ -measurements were made using a high-purity Ge-detector in  $2\pi$ -geometry (EG&G Ortec Inc., USA). The standard used for the  $\gamma$ -spectrometric measurement of un-separated dilutions was the mixed radionuclide standard solution PD954 (QSA Global GmbH, Braunschweig, Germany). The expanded uncertainty ( $k=2$ ) on each radionuclide in this mixed standard is 5%.

The samples collected after 114 days of experiment were measured with  $\gamma$ -spectrometry (reference date: 2011-06-01) without dilution, together with background samples. Contribution from the background measurement was negligible. The expanded uncertainty ( $k=2$ ), by  $\gamma$ -spectrometry, of the concentrations of  $^{239}\text{Pu}$  is <6%.

The results indicated that the Fe concentration is approximately the same in all samples (0-77 days), even though there is a certain spread, averaging at  $5 \cdot 10^{-6}$  M (Figure 25). The Fe(II) concentration also suggested that our experiment was at well controlled reducing conditions.

The  $^{239}\text{Pu}$  concentration during the experiment is shown in Figure 26. The concentrations during the time period 0-77 days were measured by SF-ICP-MS while the last values (at 114 days) are measured by  $\gamma$ -spectrometry. It can be concluded that the  $^{239}\text{Pu}$  concentration is similar in all samples and independent of the measurement technique. Taking into account the measurement uncertainty there are no  $^{239}\text{Pu}$  concentration differences between the samples and the reference. The  $^{239}\text{Pu}$  concentration converges towards an average concentration of  $0.9-1 \cdot 10^{-5}$  M.

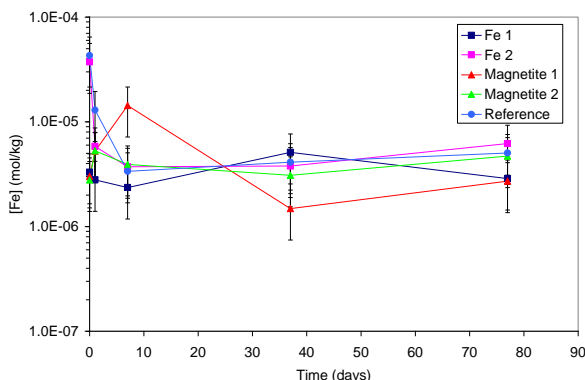


**Figure 25:** Concentration of Fe in Pu(VI)-solution during the experiment (0-77 days).

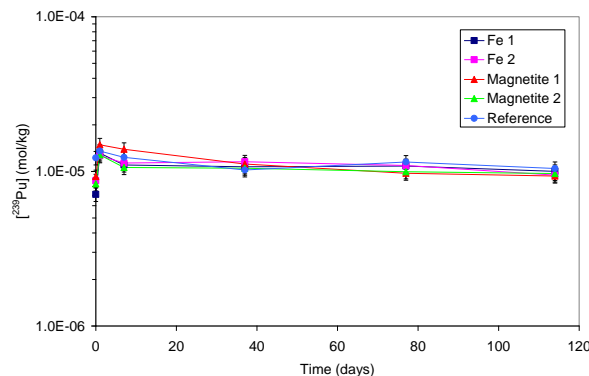


**Figure 26:** Concentration of  $^{239}\text{Pu}$  in Pu(VI)-solution during the experiment (0-114 days). The results during the time interval 0-77 days are measured by SF-ICP-MS and the last values (114 days) by  $\gamma$ -spectrometry.

### Summary and conclusions

The experiment started with preparation of a Pu(VI) carbonate solution. Speciation showed that  $\text{PuO}_2(\text{CO}_3)_3^{4-}$  is stable at pH higher than 9. Without direct evidence if Pu exists as Pu(VI) in the solutions four indirect proofs were used as evidence for the existence of Pu(VI)-carbonate as the dominating Pu species. Firstly, only Pu as Pu(VI) is stable, for longer periods at a Pu-concentration of  $10^{-5}$  M Pu in air atmosphere and in 20mM carbonate solution at pH 10. Normally, Pu(IV) precipitates as  $\text{Pu}(\text{OH})_4(\text{s})$  at  $\text{pH} > 5$ . In highly concentrated carbonate solutions (1-2.5 M) tetravalent Pu can form  $\text{Pu}(\text{CO}_3)_4^{4-}$  and  $\text{Pu}(\text{CO}_3)_5^{6-}$  complexes (MORSS L.R., EDELSTEIN N.M., FUGER J. (2006)).

Anyhow, in our experiment the formation of Pu(VI) was clearly visible during the Pu(IV) oxidation with fuming  $\text{HClO}_4$ . Over a period of 114 days there were no changes of the Pu concentration in the reference solution indicating a stable Pu(VI) solution (at pH 10,  $[\text{CO}_3^{2-}]$  of  $\sim 20\text{mM}$ , Figure 22). Secondly, the fact that all Pu-solutions, before the experiment start, were centrifuge-filtrated through a 3000 Dalton filter without reduction in Pu concentration indicate that if colloids are present they must consist of aggregates  $< 11 \text{ PuO}_2$  molecules. Thirdly, the

TEM investigation of Pu-solution collected after experiment termination showed no Pu-particles (even at a size level of 10Å). Fourthly, there were no evidence of larger Pu-agglomerates on the Fe coupon indicating Pu(VI) hydroxide precipitates.

The study of Pu(VI) reduction by Fe or Fe<sub>3</sub>O<sub>4</sub> in 20 ml of a solution 0.1M NaCl + 0.084M Na<sub>2</sub>CO<sub>3</sub> solution at pH 10 (with a CO<sub>3</sub><sup>2-</sup> concentration of ~20mM, Figure 22) showed that Pu deposition occurred only on Fe<sub>3</sub>O<sub>4</sub> surfaces. Despite the fact that the calculations give negative  $\Delta G$ -values for the reactions between Pu(VI) and Fe or Fe<sub>3</sub>O<sub>4</sub>, only approximately 1% of the added <sup>239</sup>Pu was found on the Fe<sub>3</sub>O<sub>4</sub> surface after 114 days contact time.

The concentration of Fe was similar in all solutions including the reference. Calculations show that FeCO<sub>3</sub>(s) is the solubility limiting phase at pH 10 (Figure 22).

#### Mechanisms of the hydrogen influence on radionuclide migration by D/H isotope exchange method (Studsvik)

a) It was observed that isotope exchange between D in D<sub>2</sub> gas (11 bar) and H in water solution does slowly occur with the presence of SIMFUEL pellet, (a spent fuel simulator containing UO<sub>2</sub> and noble metal fission product particles) through the reaction  $D_2 + H_2O \Rightarrow D_2O + H_2$ , but not significant occurs in the blank experiment.

b) An increase of N<sub>2</sub>/O<sub>2</sub> ratio in the gas mixture of air and D<sub>2</sub> in autoclave containing water solution and the SIMFUEL pellet, but not in blank experiment without SIMFUEL.

c) The D/H ratio in water solution that interacted with a 11.3 bar gas mixture of D<sub>2</sub> + 0.14% O<sub>2</sub> with the presence of SIMFUEL pellet for 2 months was found to be (7157 dD per mil) 1270 ppm (isotopic ratio). It is about three times higher than the calculated value according to the O<sub>2</sub> added in the system. It proves that beside the deoxygenation reaction,  $2D_2 + O_2 \Rightarrow 2D_2O$ , there should be an isotope exchange reaction  $D_2 + H_2O \Rightarrow D_2O + H_2$ .

#### *Acknowledgement*

The Swedish Nuclear Fuel and Waste Management Company (SKB) is gratefully acknowledged for financial support.

## The Effect of Iron Corrosion on Redox Potential (NRI)

### Introduction

Spent fuel dissolution and mobility of radionuclides in the near field of a deep geological repository is significantly affected by reactions of iron from disposal canisters with water. A large number of studies have been devoted to investigate iron reactions in repository conditions. The results are, however, often ambiguous. The problem is that reactions of iron with water are affected by a great variety of factors such as pH, temperature, water composition, radiation or the amount of oxygen in the water. The investigation conducted in the Nuclear Research Institute Rez (NRI) within the ReCosy project has been carried out to clarify some uncertainties concerning the effect of iron and carbon steel on redox conditions developed in or around spent fuel canisters.

### Experimental

The conditions of the experiments were based on the Czech repository concept for disposing spent fuel assemblies in multilayer canisters with a thick carbon steel overpack surrounded by compacted bentonite in a granite host rock structure. The experiments were conducted with carbon steel or iron powder samples under various conditions covering a range of temperatures, different oxygen contents or the presence of solid bentonite in reaction vessels.

A combined platinum electrode was used to measure  $E_h$  in the system with steel plates and iron powder. An electrochemical noise measurement system with three home-made electrodes, two steel working electrodes and one reference electrode were used to measure corrosion potentials. An ECM 8 Electrochemical Multiplexer Analyser with evaluation software ESA 400 Electrochemical Signal Analyser version 2.01 from Gamry Instruments was used to evaluate the results. The corrosion rate was determined by measuring the hydrogen evolved from the corroding iron using equipment developed in NRI. This device allows hydrogen evolution to be continuously measured at different temperatures and at a constant pressure in the water. The volume measurement is based on detecting the piston position, which depends on the medium volume. Corrosion products on the carbon steel plates were measured by Raman spectrometer LabRam with two lasers (He – Ne and Ar), by

X-ray diffraction Philips-Xpert PRO and by ESC Probe P in the CAE mode (Constant Analyser Energy). The concentration of  $\text{Fe}^{2+}$  and  $\text{S}^{2-}$  ions in the solution after the experiments was measured by UV/Vis spectrometry and the total iron concentration in the solution was determined by atomic absorption spectroscopy.

### Results

In all experiments the  $E_h$  decreased after immersing the carbon steel plates or iron powder in the bentonite water solution. The extent of decrease depends primarily on the surface to volume ratio of the metal to the solution and the temperature. The greater the surface to volume ratio is the greater is the decrease of  $E_h$ . The same applies to the effect of temperature. In experiments with one carbon steel plate immersed in 2 L of water, the  $E_h$  decreased to  $-150 \text{ mV}_{\text{SHE}}$  to  $-300 \text{ mV}_{\text{SHE}}$  against standard hydrogen electrode depending on the temperature of water. In experiments with 10 carbon samples immersed in the same volume of water, the decrease of  $E_h$  was much faster and the final values were ranging from  $-220 \text{ mV}_{\text{SHE}}$  to  $-350 \text{ mV}_{\text{SHE}}$  depending on the temperature of water. The most rapid decrease of  $E_h$  was observed after adding iron powder with high surface to volume ratio. Here the  $E_h$  decreased to values lower than  $-550 \text{ mV}_{\text{SHE}}$ . The higher the temperature the higher is the decrease of  $E_h$ . After immersing one carbon steel sample to the water at  $40^\circ\text{C}$ , the  $E_h$  decreases to  $-150 \text{ mV}_{\text{SHE}}$ , but at  $70^\circ\text{C}$  this decrease is to  $-300 \text{ mV}_{\text{SHE}}$ . After the initial decrease, the  $E_h$  increases over time due to the oxidation of iron (II) ions to iron (III) ions and the precipitation of iron oxides on the surface of the carbon steel plates. The largest increase was seen at the end of experiments with 10 carbon steel samples. The  $E_h$  increased from the range  $-220 \text{ mV}_{\text{SHE}}$  to  $-350 \text{ mV}_{\text{SHE}}$  to approximately  $-120 \text{ mV}_{\text{SHE}}$  to  $-230 \text{ mV}_{\text{SHE}}$  in 30 days. Only a very slight increase of  $E_h$  after an initial decrease was observed in experiments with iron powder (from  $-550 \text{ mV}_{\text{SHE}}$  to  $500 \text{ mV}_{\text{SHE}}$  in 30 days).

A noticeable decrease of pH over time was observed in all the experiments with carbon steel, while with pure iron powder no such decrease was observed in solution of the same composition. The reason for this difference could be seen in the release of carbon steel impurities into water.

The corrosion potential between the carbon steel electrodes and the reference electrodes was measured at  $40^\circ\text{C}$  to  $70^\circ\text{C}$  during electrochemical noise measurements, which allows monitoring corrosion processes in free corrosion conditions and avoids a perturbation of the

test system by externally imposed polarization. The measurements were conducted with and without an addition of iron powder. The latter was done to simulate very low  $E_h$  values that could evolve in the near field of a repository. Without iron powder addition, the carbon steel corroded at 70 °C at a higher corrosion potential than in the case of lower temperatures. This indicates assuming the same of cathodic reaction rates that the anodic reaction rate of carbon steel at 70 °C is higher than at 40°C to 60°C. By adding iron powder to the solution,  $E_h$  decreased to values lower than -500 mV<sub>SHE</sub> and accordingly the rate of cathodic reactions. Despite this, the corrosion potential of carbon steel electrodes increased. This indicates that the corrosion rate of carbon steels at very low values of  $E_h$  can be higher than at a higher level of  $E_h$ , probably due to the loss of the protective character of the corrosion product layers.

In experiments with carbon steel samples it was found that the most rapid hydrogen generation is at the beginning of corrosion and it then slows down over time. This decrease is connected with the formation of protecting corrosion product layers formed on the surface of carbon steel samples. The character of the corrosion product layers on the surface of the metal was investigated by Raman spectroscopy and X-ray diffraction. The corrosion product layers on the samples corroded at 40°C and 50°C were under the detection limit of Raman spectroscopy and X-ray diffraction. This suggests that these layers were very thin. This result is consistent with ESCA measurements where practically no iron oxide was detected on the samples corroded at 40°C and 50°C. The corrosion product layer on the samples treated at 60°C and 70°C was also below the detection limit of X-ray diffraction but by Raman spectroscopy magnetite/maghemite (band 676 cm<sup>-1</sup>), maghemite (band 1430 cm<sup>-1</sup>) and hematite bands (band 220 cm<sup>-1</sup>) were detected.

Iron powder with a large surface was used to accelerate the corrosion process. The first experiments with iron powder were not conducted in an anaerobic box but under normal laboratory conditions in a bentonite water solution bubbled with nitrogen to remove free oxygen. The hydrogen generation accumulation curve obtained under these conditions was similar to the curves obtained with carbon steels in which after a very fast period of hydrogen generation at the beginning of corrosion, hydrogen generation slows down over time. In these experiments it is not possible to guarantee that all initial oxygen was completely removed. We suppose that the remaining oxygen could accelerate the corrosion process and

the coupled hydrogen generation at the beginning leading to the formation of protecting corrosion product layers resulting in slowing down of the corrosion process.

Further experiments with iron powder were conducted in the anaerobic box with oxygen content less than 0.1 ppm. Bentonite water was taken into the anaerobic box 14 days before the experiment to remove oxygen from the solution.  $E_h$  and pH were measured during the experiments. The hydrogen accumulation curves obtained look very different compared to those measured outside the anaerobic box. The hydrogen generation rate in the experiment with 30 g of iron powder in 2 L of water was first very slow and then after several days it increased to higher values ( $\sim 1 \text{ mol H}_2/\text{m}^2\text{yr}$ ). This could be explained by the hypothesis that at the beginning of corrosion the corrosion rate is affected by a thin corrosion layer formed under atmospheric conditions on the surface of the iron powder. Under strongly reducing conditions, after adding 30 g of iron powder to the solution, this layer is reduced to pure iron and no further protective layer can be reproduced under these conditions. After adding 5 g of iron powder to the solution in the anaerobic box, the  $E_h$  decreases less than in the previous case and hydrogen generation rate is lower than in the case the experiment with 30 g of iron powder.

The effect of solid bentonite on the conditions evolved near to a repository was simulated by adding solid bentonite in a permeable bag to the solution of synthetic bentonite water. No difference in the change of  $E_h$  or pH of the solution was observed contrary to experiments without bentonite. The hydrogen generation rate increased in a comparison to the experiments without solid bentonite.

To simulate  $E_h$  evolution during the corrosion processes the geochemical code PHREEQC was used. Firstly, iron was kinetically added to the bentonite porewater solution according to the measured corrosion rate and based on speciation in the solution and Fe(II)/Fe(III) activities the  $E_h$  was calculated. The species of iron is assumed to be a main redox couple in the system. Secondly, the solution was equilibrated with Fe-bearing minerals (magnetite,  $\text{Fe}(\text{OH})_2$ ) and the  $E_h$  was recalculated.

The redox potential simulation showed different results for the experiments with carbon steel plates and iron powder. With the carbon steel plates, the simulations and experimental data were not consistent. However, with iron powder a good agreement between both the experimental and simulated data was demonstrated. To summarise, the redox potential of all experiments is driven by the main redox couple Fe(II)/Fe(III). But with carbon steel plates,

other redox elements present could participate in the redox potential. Thus, the model values of the redox potential differ from the actual measurements. Also the evolution of pH is not consistent with the model. With iron powder, the model values of redox potential decreased to -546 mV and came closer to the measured experimental values. The pH values (around 8) are similar in the model and the experiments. The model for both cases showed that almost all Fe is precipitated as  $\text{Fe}(\text{OH})_2$  or magnetite, but the equilibrium concentrations of Fe(II)/Fe(III) in the solutions did not follow the actual measured values. The kinetics of corrosion products should be incorporated in the models. This finding confirmed the different behaviour of carbon steel and iron powder under the same conditions.

### Conclusions

To summarise the results obtained, it was found that the firmly adhering corrosion product layers formed on the carbon steel surface, containing a high amount of oxygen and carbon, have an important impact on the development of geochemical conditions in a repository. These layers protect the carbon steel against fast corrosion, but data about their long term stability are rare. No or very thin layers of corrosion products were formed on iron powder at very low  $E_h$ . This leads surprisingly to a higher corrosion rate of iron powder at lower  $E_h$  values. The presence of solid bentonite can lead to an increase of the corrosion rate of iron, possibly due to the faster sorption (exchange) of ferrous ions on the bentonite leading to a higher concentration gradient between the metal and the solution.

Laboratory experiments conducted in this work contributed to a deeper knowledge of the effect of iron corrosion on redox evolution, but did not remove all uncertainties concerning this issue. For reliable predicting and ascertaining the behaviour of canisters in a repository and their influence on the evolution of geochemical conditions in a repository a more systematic programme involving both laboratory and in situ experiments should be started in future to verify the results obtained.

### References

ALTMAYER M., KIENZLER B., DURO L., GRIVÉ M., MONTOYA V. (EDS.) (2011): *3<sup>rd</sup> Annual Workshop Proceedings of the Collaborative Project "Redox Phenomena Controlling*



*Systems*” (EC 7th FP CP RECOSY), Karlsruhe Institute of Technology, KIT Scientific Reports 7603, Germany.

ALTMAIER M., KIENZLER B., DURO L., GRIVÉ M., MONTOYA V. (EDS.) (2012): *4<sup>th</sup> Annual Workshop Proceedings of the Collaborative Project “Redox Phenomena Controlling Systems”* (EC 7th FP CP RECOSY), Karlsruhe Institute of Technology, KIT Scientific Reports, Germany. In press.

BAES C.F., MESMER R.E. (1976): *The hydrolysis of cations*. John Wiley & Sons, New York, USA.

BUCKAU G., KIENZLER B., DURO L., GRIVÉ M., MONTOYA V. (EDS.) (2009): *Collaborative Project “Redox Phenomena Controlling Systems” - 1st Annual Workshop Proceedings*, Forschungszentrum Karlsruhe, Wissenschaftliche Berichte, FZKA 7466, Karlsruhe, Germany.

BUCKAU G., KIENZLER B., DURO L., GRIVÉ M., MONTOYA V. (EDS.) (2010): *2<sup>nd</sup> Annual Workshop Proceedings of the Collaborative Project “Redox Phenomena Controlling Systems”* (EC 7th FP CP RECOSY), Karlsruhe Institute of Technology, KIT Scientific Reports 7557, Germany.

BENNETT D.G., GENS R. (2008): *Overview of European concepts for high-level waste and spent fuel disposal with special reference waste container corrosion*, J. Nucl. Mater. **379**, 1-8.

CAO Y., CHEN Z.-X. (2006): *Theoretical studies on the adsorption and decomposition of H<sub>2</sub>O on Pd(111) surface*. Surf. Sci. **600**, 4572-4583.

CARBOL P., WEGEN D.H., WISS T., FORS P. (2012): *Spent Fuel as Waste Material*. In: Konings R.J.M., (ed.) *Comprehensive Nuclear Materials*, volume 5, pp. 389-420 Elsevier, Amsterdam, Netherlands.

CUI D., LOW J., SJÖSTEDT C.J., SPAHIU K. (2004): *On Mo-Ru-Tc-Pd-Rh-Te alloy particles extracted from spent fuel and their leaching behaviour under Ar and H<sub>2</sub> atmosphere*. Radiochimica Acta **92**, 551.

CUI D., PURANEN A., SCHEIDEGGER A., GROLMUND D., WERSIN P., LEUPIN O., SPAHIU K. (2007): *On the interaction between iron canister material and fission products*

79Se and 99Tc under simulated deep repository conditions. NF-PRO report Contract Number: FI6W-CT-2003-02389, RTDC 2-WP 2.5 Task 7.

DE FARIA D. L. A., VENAÜNCIO S., SILVA M. T., DE OLIVEIRA M.T. (1997): *Raman microspectroscopy of some iron oxides and oxyhydroxides*. J. Raman Spectr. **28**, 873-878.

DURRANI S.A., BULL R.K. (1987): *Solid state nuclear track detection*. In: Principles, Methods and Applications. Pergamon Press, Oxford, England.

EKEROTH E., ROTH O., JONSSON M. (2006): *The relative impact of radiolysis products in radiation induced oxidative dissolution of UO<sub>2</sub>*. J. Nucl. Mater. **355**, 38-46.

ENGELHARDT J., MARX G. (1999): *Contact corrosion measurements on the pair UO<sub>2+x</sub> and carbon steel 1.0330 in brines and bentonite porewater with respect to direct waste disposal*, J. Nucl. Mater. **264**, 161-168.

ERIKSEN T.E., SHOESMITH D.W., JONSSON M. (2012): *Radiation induced dissolution of UO<sub>2</sub> based nuclear fuel –A critical review of predictive modeling approaches*. J. Nucl. Mater. **420**, 409-423.

FEDOSEEV A.M., SHILOV V.P. (2010): *Oxidation of Am(III) to Am(IV) with ozone in solutions of heteropolyanions*. Radiochemistry **52(1)**, 40-42.

FERRY C., POINSSOT C., BROUDIQUÉ V., CAPPELAERE C, DESGRANGES L., ET AL. (2005): *Synthesis of the Spent Fuel Long-Term Evolution*, Rapport CEA-R--6084.

FÉRON D., CRUSSET D., GRAS J.-M. (2008): *Corrosion issues in nuclear waste disposal*, J. Nucl. Mater. **379**, 16-23.

FORS P., CARBOL P., VAN WINCKEL S., SPAHIU K. (2009): *Corrosion of high burn-up structured UO<sub>2</sub> fuel in presence of dissolved H<sub>2</sub>*. J. Nucl. Mater. **394** (2009) 1-8.

GORODETSKII V.V., SAMETOVA A.A., MATVEEV A.V., TAPILIN V.M. (2009): *From single crystals to supported nanoparticles in experimental and theoretical studies of H<sub>2</sub> oxidation over platinum metals (Pt, Pd): Intermediates, surface waves and spillover*. Catalysis today **144**, 219-234.

GHOSH MAZUMDAR A.S., SIVARAMAKRISHNAN C.K. (1964): *A study of the nitrate and the chloride complexes of plutonium(VI) by solvent extraction technique using TTA as the chelating agent.* J. Nucl. Chem. Proc. **27**, 2423-2427.

GRAMBOW B., LOIDA A., DRESSLER P., ET AL. (1996): *Long-Term Safety of Radioactive Waste Disposal: Chemical Reaction of Fabricated and High Burnup Spent UO<sub>2</sub> Fuel with Saline Brines.* Wissenschaftliche Berichte FZKA 5702.

GRAMBOW B. ET AL. (2000): *Source term for performance assessment of spent fuel as a waste form,* Report No. EUR 19140, 82-101, Luxembourg.

HIXON A.E., HU Y.-J., KAPLAN D.I., KUKKADAPU R.K., NITSCHKE H., QAFOKU O., POWELL B.A. (2009): *Influence of iron redox transformations on plutonium sorption to sediments.* Radiochimica Acta **98**, 685-692. doi: 10.1524/ract.2010.1769.

JONSSON M., EKEROTH E., ROTH O. (2004): *Dissolution of UO<sub>2</sub> by one- and two-electron oxidants.* Mat. Res. Soc. Symp. Proc. **807**, 77-82.

KUPFER A. (2000): *Radiochemische Korrosionsuntersuchungen an Urandioxid und Cladding-Materialien von Kernbrennstoffen in praxisrelevanten Salzlaugen als Beitrag zur direkten Endlagerung,* Dissertation, Freie Universität Berlin, Berlin.

LOIDA A., GRAMBOW B., GECKEIS H. (1996): *Anoxic corrosion of various high burnup spent fuel samples.* J. Nucl. Mater. **238**, 11-22.

LOUSADA C. M., JONSSON M. (2010): *Kinetics, Mechanism and Activation Energy of H<sub>2</sub>O<sub>2</sub> Decomposition on the Surface of ZrO<sub>2</sub>.* J. Phys. Chem. C. **114**, 11202-11208.

LOUSADA, C. M., TRUMMER, M., JONSSON, M. (2011): *Reactivity of H<sub>2</sub>O<sub>2</sub> towards different UO<sub>2</sub>-based materials: The relative impact of radiolysis products revisited.* J. Nucl. Mater. In press doi: 10.1016/j.jnucmat.2011.06.003.

LUCCHINI J.F., KHAING H., RICHMANN M.K., BORKOWSKI M., REED D.T. (2008): *Plutonium (VI) and Uranium (VI) reduction by iron (II) at high pH under subsurface conditions.* Plutonium Futures Conference "The Science". Dijon, France, July 7-11, 2008, LA-UR-0808-04292.

METZ V., GECKEIS H., GONZÁLEZ-ROBLES E., LOIDA A., BUBE C., KIENZLER B. (2012): *Radionuclide behaviour in the near-field of a geological repository for spent nuclear fuel*. Radiochimica Acta, In press doi: 10.1524/ract.2012.1967.

MISERQUE F., GOUDER T., WEGEN D.H., BOTTOMLEY P.D.W. (2001): *Use of UO<sub>2</sub> films for electrochemical studies*. J. Nucl. Mater. **298**, 280–290.

MISSANA T., GARCIA-GUTHIERRES M., FERNANDEZ V. (2002): *Uranium (IV) sorption on colloidal magnetite under anoxic environment: Experimental study and surface complexation modelling*. Geochimica et Cosmochimica Acta **67**, 2543-2550.

MORSS L.R., EDELSTEIN N.M., FUGER J. (2006): *The chemistry of the Actinide and Transactinid Elements*. Springer, Dordrecht, the Netherlands.

NAOHARA H., YE S., UOSAKI K. (2000): *Electrocatalytic reactivity for oxygen reduction at epitaxially grown Pd thin layers of various thickness on Au(111) and Au(100)*. Electrochimica Acta 45, 3305-3309.

NEWTON T.W., HOBART D.E., PALMER P.D. (1986): *The formation of Pu(IV)-colloid by the alpha-reduction of Pu(V) and Pu(VI) in aqueous solution*. Radiochimica Acta **39(3)**, 139-147.

NILSSON S., JONSSON M. (2011): *H<sub>2</sub>O<sub>2</sub> and radiation induced dissolution of UO<sub>2</sub> and SIMFUEL pellets*. J. Nucl. Mater. **410**, 89-93.

PEHRMAN R., TRUMMER M., LOUSADA C. M., JONSSON M. (2011): *Redox reactivity of doped UO<sub>2</sub> - Effects on the reactivity towards H<sub>2</sub>O<sub>2</sub>*, RECOSY 3<sup>rd</sup> Annual Workshop Proceedings of the Collaborative Project “Redox Phenomena Controlling Systems” (EC 7th FP CP RECOSY), Karlsruhe Institute of Technology, KIT Scientific Reports 7603, Germany, pp. 241 – 249.

PEHRMAN R., TRUMMER M., LOUSADA C. M., JONSSON M. (2012): *On the redox reactivity of doped UO<sub>2</sub> pellets – Influence of dopants on the H<sub>2</sub>O<sub>2</sub> decomposition mechanism*. Submitted to J. Nucl. Mater.

REILLY S.D., NEU M.P. (2006): *Pu(VI) hydrolysis: Further evidence for a dimeric Plutonyl hydroxide and contrasts with U(VI) chemistry*. Inorg. Chem. **45**, 1839-1846.

REILLY S.D., RUNDE W., NEU M.P. (2007): *Solubility of plutonium (VI) carbonate in saline solutions*. Geochim. et Cosmochim. Acta **71**, 2672-2679.

RONDINELLA V. V. (2011): *Failure mechanisms of high level nuclear waste forms in storage and geological disposal conditions*. Handbook of advanced radioactive waste conditioning technologies. Edited by M. I. Ojovan, Woodhead Publishing Series in Energy: Number 12, Woodhead Ltd, Philadelphia, USA.

ROTH O., JONSSON M. (2008): *Oxidation of UO<sub>2</sub>(s) in aqueous solution*. Cent. Eur. J. Chem. **6**, 1-14.

SEIBERT A. ET AL. (2011): *The use of the electrochemical quartz crystal microbalance (EQCM) in corrosion studies of UO<sub>2</sub> thin film models*. J. Nucl. Mater. **419**, 112–121.

SERRANO-PURROY D., CLARENS F., GLATZ J.-P., WEGEN D., CHRISTIANSEN B., DE PABLO J., GIMÉNEZ J., CASAS I., MARTÍNEZ-ESPARZA A. (2009): *Leaching of 53 MWd/kgU spent nuclear fuel in a flow-through reactor*. Radiochimica Acta **97**, 491-496.

SHOESMITH D.W., SUNDER S., HOCKING W.H. (1994): in *Electrochemistry of Novel Materials*, edited by J. Lipowski and P.N. Ross, VCH Publishers, New York, pp. 297-337

SHOESMITH D.W., SUNDER S., TAIT S. (1998): *Validation of an electrochemical model for the oxidative dissolution of used CANDU fuel*. J. Nucl. Mater. **257**, 89 98.

SHOESMITH D.W. (2000): *Fuel corrosion processes under waste disposal conditions*. J. Nucl. Mater. **282**, 1-31.

SMART N.R., BLACKWOOD D.J., WERME L. (2001): *The anaerobic corrosion of carbon steel and cast iron in artificial groundwaters*. SKB Technical Report TR-01-22.

SMART N.R., BLACKWOOD D.J., WERME L. (2002): *Anaerobic corrosion of carbon steel and cast iron in artificial groundwaters: Part 1 – Electrochemical Aspects*. Corrosion **58**, 547-559.

STUMPF S., SEIBERT A., GOUDER T., HUBER F., WISS T., RÖMER J. (2012): *Development of fuel-model interfaces: Characterization of Pd containing UO<sub>2</sub> thin films*. To be submitted to J. Nucl. Mater.

TAIT C.D., EKBERG S.A., PALMER P.D., MORRIS D.E. (1995): *Plutonium carbonate speciation changes as measured in dilute solutions with photoacoustic spectroscopy*. Yucca Mountain Site Characterization Program, Milestone Report 3350, LA-12886-MS, UC-802, Los Alamos, National Laboratory, Los Alamos, New Mexico 87545, USA.

TEICHNER S.J. (1990): *Recent Studies in Hydrogen and Oxygen Spillover and their Impact on Catalysis*. Appl. Catalysis **62**, 1-10.

TRUMMER M., ROTH O., JONSSON M. (2009): *H<sub>2</sub> Inhibition of Radiation Induced Dissolution of Spent Nuclear Fuel*. J. Nucl. Mater. **383**, 226-230.

TRUMMER M., DAHLGREN B., JONSSON M. (2010): *The effect of Y<sub>2</sub>O<sub>3</sub> on the dynamics of oxidative dissolution of UO<sub>2</sub>*. J. Nucl. Mater. **407**, 195-199.

TRUMMER, M. (2011): *The effect of solid state inclusions on the reactivity of UO<sub>2</sub>. A kinetic and mechanistic study*. Doctoral Thesis in Chemistry, KTH, Stockholm, Sweden.

WEGEN D.H., GOUDER T., ECKLE M., WISS T., GLATZ J.-P. (2004): *Microgravimetric corrosion studies on UO<sub>2</sub>*. Mat. Res. Soc. Symp. Proc. Vol. **807**, 101-106.

YU J.G., LUO J.L., NORTON P.R. (2002): *Electrochemical investigation of the effects of hydrogen on the stability of the passive film on iron*, Electrochimica Acta **47**, 1527-1536.